INL/MIS-22-66343-Revision-0

MECHANISTIC MULTIPHYSICS MODELING OF CLADDING RUPTURE IN NUCLEAR FUEL RODS DURING LOSS-OF-COOLANT ACCIDENT CONDITIONS

Kyle Allan Lawrence Gamble

Idaho National Laboratory

INL is a U.S. Department of Energy National Laboratory operated by Battelle Energy Alliance, LLC

INL/MIS-22-66343-Revision-0

MECHANISTIC MULTIPHYSICS MODELING OF CLADDING RUPTURE IN NUCLEAR FUEL RODS DURING LOSS-OF-COOLANT ACCIDENT CONDITIONS

Kyle Allan Lawrence Gamble

July 2022

Idaho National Laboratory
Idaho Falls, Idaho 83415

http://www.inl.gov

Prepared for the
U.S. Department of Energy
Under DOE Idaho Operations Office
Contract DE-AC07-05ID14517, DE-AC07-05ID14517, DE-AC07-05ID14517, DE-AC07-05ID14517, DE-AC07-05ID14517

Mechanistic Multiphysics Modeling of Cladding Rupture in Nuclear Fuel Rods during Loss-of-Coolant Accident Conditions

by

Kyle Allan Lawrence Gamble

Bachelor of Science
Queen's University, 2012

Master of Applied Science
Royal Military College of Canada, 2014

Submitted in Partial Fulfillment of the Requirements

for the Degree of Doctor of Philosophy in

Nuclear Engineering

College of Engineering and Computing

University of South Carolina

2022

Accepted by:

Travis W. Knight, Major Professor

Elwyn Roberts, Committee Member

Jamil A. Khan, Committee Member

Jason D. Hales, Committee Member

Tracey L. Weldon, Interim Vice Provost and Dean of the Graduate School

DEDICATION

To my fiancé Nicole and our son Duncan.

ACKNOWLEDGMENTS

First and foremost, I thank my employer Battelle Energy Alliance (BEA), LLC the current contractor to the United States Department of Energy managing Idaho National Laboratory (INL) for allowing me to pursue further education through their Employee Education Program (EEP). In particular, I extend my thanks to my manager Dr. Jason D. Hales for recommending me to use the EEP program, willing to be a member of my dissertation committee, and allowing flexibility in my schedule to balance work and school obligations as required. Since this research work was supported by the EEP program of Battelle Energy Alliance, LLC, the submitted dissertation has been authored by a contractor of the U.S. Government under Contract DE-AC07-05ID14517. Accordingly, the U.S. Government retains a non-exclusive, royalty free license to publish or reproduce the published form of this contribution, or allow others to do so, for U.S. Government purposes. Moreover, some of the work developed as part of this dissertation was supported by funding from the Nuclear Energy Advanced Modeling and Simulation (NEAMS) and the Consortium for Advanced Simulation of Light Water Reactor (CASL) programs through the U.S. Department of Energy.

Secondly, I thank my major professor and faculty advisor Dr. Travis W. Knight at the University of South Carolina (UofSC) for agreeing to take me on as a student through the UofSC's APOGEE distance program. His guidance and thoughtful suggestions have greatly shaped the outcome of this work. In addition, I thank Dr. Elwyn Roberts, another committee member who had an active interest in the research throughout the whole process providing thoughtful suggestions and insight into additional scenarios/phenomena to consider as part of the research. I also appreciate Dr. Jamil A. Khan for serving as the final member of my

dissertation committee.

As an employee of the Computational Mechanics and Materials department at INL I also thank my co-workers in the development team of the Bison fuel performance code for their thoughtful discussions, suggestions, and review of code prior to inclusion in the stable released version of Bison. In addition, many of the simulations completed as part of this work utilized the HPC resources available at INL, namely, the Falcon and Sawtooth machines. As such, this research made use of the resources of the High Performance Computing Center at Idaho National Laboratory, which is supported by the Office of Nuclear Energy of the U.S. Department of Energy and the Nuclear Science User Facilities under Contract No. DE-AC07-05ID14517.

Last but not least, I extend my thanks to my family, whose encouragement and reassurance throughout this process has been unprecedented. In particular, I thank my fiancé Nicole Mitchell who tolerated my long weeknights and weekends at the office to complete this work as well as our son Duncan whose smile kept me going when the times were tough.

ABSTRACT

The Loss of Coolant Accident (LOCA) is a design basis accident that is included as part of the safety analysis of nuclear power plants. As the nuclear industry desires to increase the cycle length and discharge burnup of existing nuclear power plants they must demonstrate safe operation during a LOCA on high burnup fuel. During a LOCA transient on high burnup fuel rods, the rods may undergo a process known as fuel fragmentation, relocation, and dispersal (FFRD). To permit dispersal, the cladding encapsulating the fuel must rupture with an opening size large enough to allow the fragmented fuel particles to release. Current licensing tools used by industry and the United States Nuclear Regulatory Commission are limited in geometric fidelity and materials that can be analyzed. These simulation tools generally employ a quasi-two-dimensional (1.5D or Layered1D) or 2D-RZ axisymmetric geometric representations exclusively. While a valid approach under some instances, there are times when important physics have an asymmetric behavior in the fuel rod. Examples include fuel fragmentation, thermal-hydraulic boundary conditions, and cladding rupture, all of which are important for LOCA analysis.

As industry pursues burnup extensions it must be demonstrated that fuel dispersal can be mitigated or eliminated. To do this, an understanding of the rupture opening after cladding failure is required. This work presents the development of a model for predicting the size and location of the rupture opening in failed fuel rods during LOCA conditions using advanced modeling and simulation tools. In order to supply the rupture model with appropriate boundary conditions, improvements to fuel fragmentation, axial relocation and oxidation modeling were required.

First, the eXtended Finite Element Method (XFEM) is used to mechanistically predict

the number of fuel fragments that form due to material strength randomization, criteria for strength randomization, mesh density, power ramping rates and irradiation effects. These predictions with associated uncertainty were compared to empirical correlations developed for UO_2 verifying that they can be used with increased confidence in subsequent axial relocation analyses. Secondly, a new first-of-its-kind Layered2D computational framework was developed that provides the ability to apply azimuthally varying boundary conditions while providing discrete layers to track fuel movement during the LOCA. An existing fuel axial relocation model developed for Layered1D was extended to work within the Layered2D framework. A large sensitivity study was performed on the initial version of the model to identify modeling parameters of particular importance, with the emissivity used for radiation after blowdown being the primary source of uncertainty. Then, a simplistic approach to incorporate mechanical degradation of the cladding due to oxidation was also developed to investigate the impact of reduced cladding thickness on predictions of the time to failure of cladding tubes. It was found that the cladding will typically rupture prior to a reduction in thickness that is sufficient to impact the rupture behavior. A model was then developed for predicting cladding rupture that transfers the cladding surface temperatures, rod internal and external pressures, fast neutron fluence, and fast neutron flux from a more detailed Layered1D, Layered2D, or 2D-RZ analysis to a 3D cladding only analysis. Comparisons of the rupture model to a few experiments indicate reasonable predictions. The rupture model was then applied to two accident tolerant fuel concepts (FeCrAl and Cr-coated Zircaloy) where it predicted that both ATF concepts would have smaller rupture openings and delayed rupture times than the standard Zircaloy-4 cladding material under identical loading conditions.

TABLE OF CONTENTS

List of Tables

LIST OF FIGURES

CHAPTER 1

INTRODUCTION

The Loss of Coolant Accident (LOCA) is a design basis accident (DBA) that must be taken into account as part of the safety analysis for nuclear power plants. In the United States, depending upon whether the reactor being analyzed is a pressurized water reactor (PWR) or boiling water reactor (BWR) the limiting LOCA investigated is different. For PWRs the limiting case is a large break loss of coolant of accident (LBLOCA) resulting from a double-ended rupture of the cold-leg main feedwater pipe, whereas for BWRs the limiting case is a double-ended rupture of a recirculation loop. The difference in worst case scenarios between the two reactors can be attributed to their design.

In a PWR the large break LOCA consists of five primary stages including, blowdown, bypass, refill, reflood (quench), and long-term cooling. The blowdown phase (∼0-20 s) occurs at the onset of the LOCA where rapid depressurization of the core results in the formation of a two-phase water-steam mixture. During the bypass phase (∼20-30 s) the pressure of the steam is still large enough to prevent Emergency Core Cooling (ECC) from entering the lower plenum of the core. Once the steam pressure has decreased to atmospheric levels, the ECC cooling can now enter the lower plenum of the core during the refill phase (∼30-40 s). Following the refill, reflooding can now occur. The reflooding phase (∼40-250 s) is the rewetting of the exposed fuel rods from the bottom of the core to the top. Once reflooding has occurred, the long-term cooling of the core can be maintained. A similar procedure occurs in a BWR except that the depressurization is slower because the pipe diameters are smaller. Figure 1.1 illustrates the evolution of the reactor coolant system pressure during a representative LOCA.

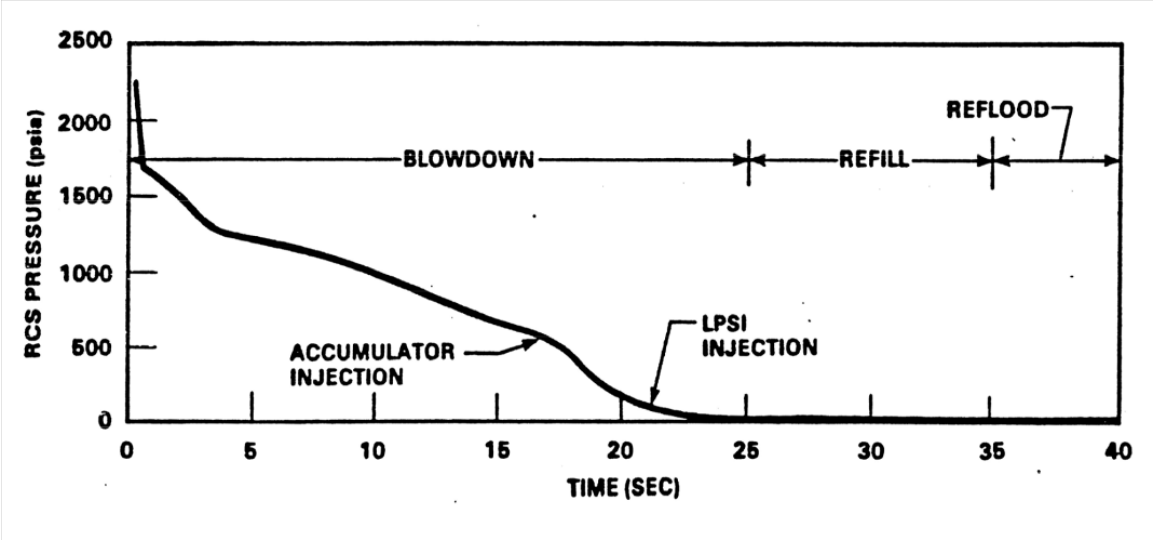

Figure 1.1: An illustration of the reactor coolant system pressure as a function of time during the various stages of a LOCA. Reproduced from [117].

For licensing purposes in the United States, the Nuclear Regulatory Commission (NRC) has published acceptance criteria that must be satisfied by the licensee in regards to the ECC system in a light water reactor (LWR) during a LOCA. These criteria are published in a Code of Federal Regulations (CFR) identified as 10 CFR 50.46(b). This regulation lists five standards that must be maintained and demonstrated using fuel performance, thermal-hydraulic, or system analyses. These standards are reproduced from the NRC's website [24] in Table 1.1.

According to Raynaud and Porter [90] rupture of traditional fuel rods (i.e., UO_2 fuel inside a zirconium-based cladding) typically occur during either the blowdown or reflooding phases. In the blowdown phase the fuel and cladding temperatures rapidly rise and large inelastic strains are generated in the cladding potentially leading to rupture. In the reflooding phase failure can occur due to thermal shock of the cladding by the sudden injection of the cooling water. The rupture of the cladding may lead to fuel dispersal into the primary coolant loop with subsequent radioactivity release to the environment if the containment is breached. Cladding rupture is necessary for the fuel dispersal to occur. Fuel dispersal is the last stage of a process known as fuel fragmentation, relocation, and dispersal (FFRD).

Table 1.1: NRC acceptance criteria for emergency core cooling systems for light-water reactors: 10 CFR 50.46(b) [24].

Criteria	**Description**
Peak temperature	The calculated maximum fuel element temperature shall not exceed 2200°F (1477.6 K).
Maximum oxidation	The calculated total oxidation of the cladding shall nowhere exceed 0.17 times the total thickness before oxidation.
Maximum hydrogen generation	The calculated total amount of hydrogen generated from the chemical reaction of the cladding with water or steam shall not exceed 0.01 times the hypothetical amount that would be generated if all the metal in the surrounding the fuel, excluding the surrounding the plenum volume, were to react.
Coolable geometry	Calculated changes in core geometry shall be such that the core remains amenable to cooling.
Long-term cooling	After any calculated initial operation of the ECC system, the calculated core temperature shall be maintained at an acceptable low value and decay heat removed for the extended period of time required by the long-lived radioactivity remaining in the core.

Irradiated fuel experiencing the formation of the high burnup structure (HBS) ($>\sim$70 MWd/kgU) can undergo fuel fragmentation and pulverization (also known as fine fragmentation) resulting in crumbling of the fuel stack during a LOCA transient. It should be mentioned that larger fuel fragments form from the onset of irradiation during the first rise to power and throughout normal operation because of the thermal gradient throughout the pellet. As the temperature increases and the heat transfer coefficient reduces on the cladding waterside surface due to the formation of steam, the cladding will tend to balloon outward. If the inelastic hoop strain experienced by the cladding is sufficiently large ($\sim 5\%$) the small fuel fragments will be able to leave their cylindrical shape and relocate axially to fill the ballooned region. This mass relocation redistributes the heat load due to residual decay heat in the rod resulting in increased temperatures locally leading to further distention. In addition, the rapid release of fission gases (e.g., xenon and krypton) during the transient will increase the rod internal pressure. This process is known as transient fission

gas release (tFGR). Associated with the interaction with steam, significant oxidation occurs in zirconium-based cladding resulting in a large inventory of volatile hydrogen gas being produced in the core. At high temperatures the oxidation process reduces the thickness of the metal making up the cladding and therefore reduces its strength. The time to rupture of the cladding is dependent on all of these factors. Depending upon the size of the rupture opening compared to the size of the fuel particles in the ballooned region, fuel may be released into the reactor core leading to potential radiological consequences. Figure 1.2 presents radiographs reproduced from [102] that illustrate examples of fuel fragmentation, fuel pulverization, fuel axial relocation, and cladding rupture.

Even if rupture of the cladding does not occur during the blowdown phase the ballooning of adjacent rods in an assembly can lead to rod-to-rod contact affecting the core coolability during the reflooding phase. The rod-to-rod contact can create local hotspots on the rods leading to faster oxidation and rupture due to thermal shock.

Over the years numerous experimental programs have been developed to investigate integral rod behavior and thermal-hydraulic consequences during a LOCA for BWRs and PWRs. The experimental programs are covered in great detail in one of two (or both) extensive reviews of the FFRD phenomenon by Raynaud [91] and the Organisation for Economic Co-operation and Development (OECD) through its Nuclear Energy Agency (NEA) Committee on the Safety of Nuclear Installations (CSNI) [102]. The more well known experimental programs include the Power Burst Facility tests at Idaho National Engineering Laboratory (INEL), the FLASH tests at Commissariat a l'Energie Atomique (CEA) in France, the Argonne National Laboratory (ANL) LOCA test program, the Halden Reactor LOCA Test Series (Norway), and the Studsvik LOCA test program (Sweden).

The results of these experiments have been used to develop empirical thresholds and models for fuel fragmentation, relocation, rupture and fuel dispersal or to validate the existing thresholds developed by earlier test series. These thresholds and models have been incorporated into fuel performance codes for modeling and simulation of LOCA transients.

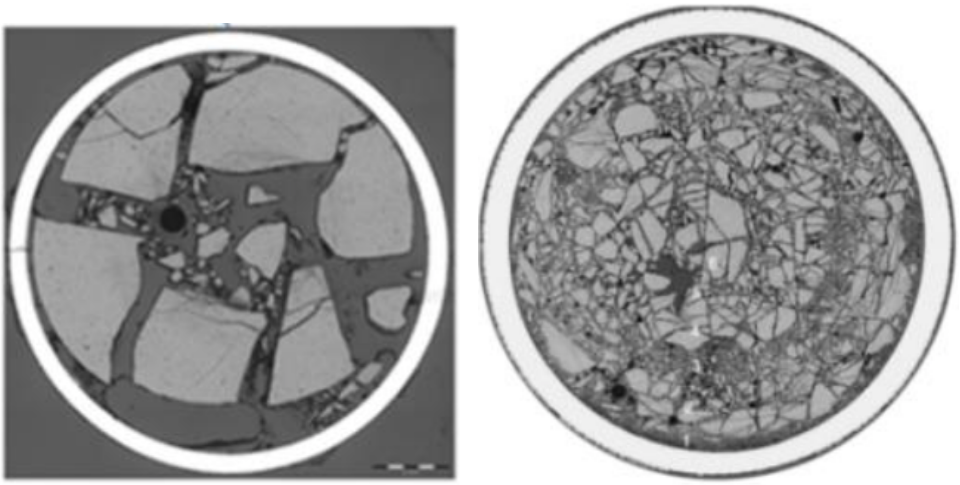

(a) (b)

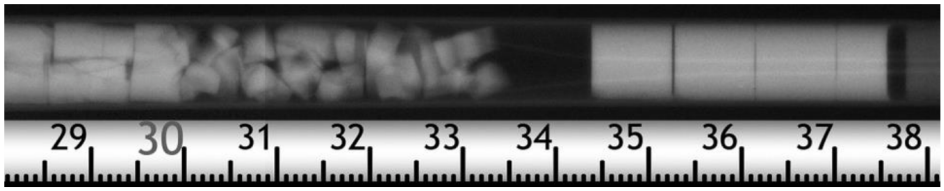

(c)

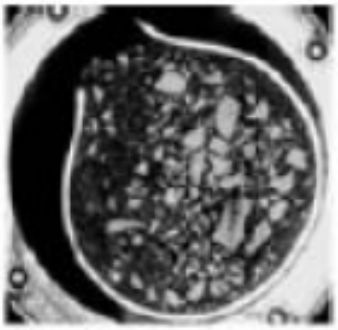

(d)

Figure 1.2: Radiographs from various experiments illustrating (a) fragmentation, (b) pulverization, (c) axial relocation, and (d) rupture. Figures reproduced from [102].

Unfortunately, empirical thresholds have limited ranges of applicability (i.e., the experimental conditions on which they are based) or may disregard certain physics entirely. Over the years, computing resources have increased dramatically allowing the development of more complex predictive modeling and simulation capabilities. Having a predictive capa-

bility that contains correlations that are informed from the underlying physics allow for investigations into new operational conditions, analysis of new materials for which experimental data may be limited, and provide additional insight into existing phenomena. In cases where limited knowledge of the underlying physics or existing experimental data is available, sensitivity analyses can be used to help guide further experiments and determine which parameters are of particular importance.

The authors of the OECD NEA CSNI report [102] state that the prediction of ballooning and rupture (size and location) is of great importance because of their impact on flow blockage (coolability) and equivalent reacted (ECR) post rupture. Recall that core coolability and maximum oxidation, which is related to ECR, are two of the criteria that must be met during the licensing process as per Table 1.1. The authors further state that some of the existing models in the literature, which are reviewed in subsections of Chapter 3 through Chapter 6 of this dissertation, are empirical and overly conservative in predicting FFRD behavior in fuel rods. Therefore, a more mechanistic approach to predicting the effect of FFRD on design basis LOCA accidents may provide improved margins for utilities as these best-estimate models are typically less conservative. Moreover, as utilities and fuel vendors desire to request burnup extensions up to 75 MWd/kgU, understanding of the FFRD phenomenon is of great importance.

Further complicating the issue of fuel and cladding behavior during LOCAs was the events that occurred at the Fukushima Daiichi nuclear power plant (NPP) in March of 2011. A magnitude 9.0 earthquake resulted in a tsunami causing flooding of the backup generators at the plant. The loss of power resulted in a station blackout resulting in loss of coolant flow, causing high temperatures leading to significant oxidation of zirconium-based alloys within the core, producing significant hydrogen gas, which ultimately resulted in hydrogen explosions breaching the containment. It was mentioned previously, that the oxidation behavior of the cladding may effect the ballooning and rupture characteristics. In addition, the rupture affects the total oxidation as the inner surface will begin to oxidize if the

coolant is able to enter through the rupture. As a result, there has been significant research at universities, national laboratories, and fuel vendors on alternative cladding concepts with improved oxidation kinetics including chromium coated zirconium alloys [13, 14], iron-chromium-aluminum (FeCrAl) alloys [29, 34, 37, 83, 106, 116, 135], and silicon carbide composites [4, 26, 31, 59, 107, 115, 136].

Bragg-Sitton et al. [15] provides a broader definition for materials to be considered accident tolerant. They state that accident tolerant materials are defined as those that provide significantly increased response time during accident conditions while providing similar or improved performance during normal operation. This definition requires that fuel performance and thermal-hydraulic assessments be performed on rods with these alternative cladding concepts during LOCA conditions to compare their response to that of fuel rods with traditional zirconium-based cladding. Consider the work of Massey et al. [66], who performed separate effects burst testing under LOCA like conditions in the experimental rig at Oak Ridge National Laboratory (ORNL) for Zircaloy-4, FeCrAl, and 304SS cladding tubes. A key observation of this work was the size of the rupture of the different materials as illustrated in Figure 1.3. Given the importance of ballooning and burst behavior on oxidation, flow blockage, and fuel dispersal, a predictive capability for rupture in these alternative materials is necessary.

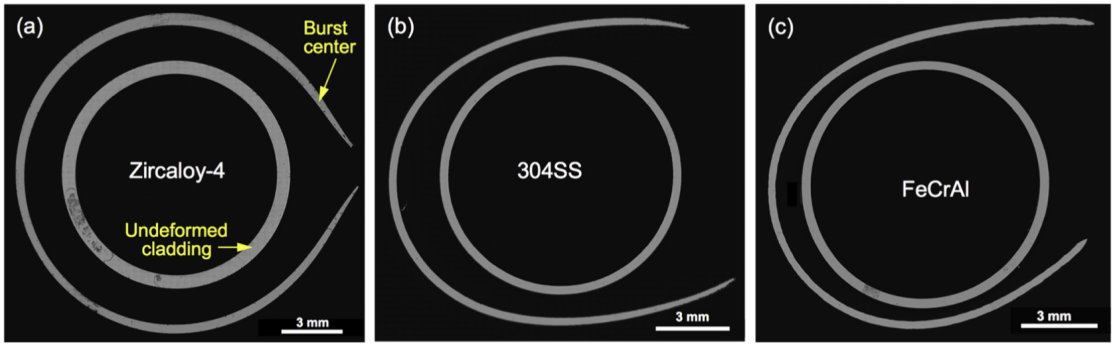

Figure 1.3: Light optical micrographs of the cross-section at the center of the burst and at the undeformed region. Reproduced from [66].

Since existing models for FFRD are conservative and given the importance of predicting

the rupture size on potentially reducing the conservatism, it is proposed to develop a mechanistic model for predicting the rupture size in cladding tubes that can be applied to both zirconium-based and alternative cladding concepts (i.e., FeCrAl and Cr-coated Zircaloy). To achieve this goal, advancements in fuel performance models for fuel fragmentation and pulverization, fuel axial relocation, and oxidation are required. Starting with UO_2 fuel and Zircaloy-4 the models will be developed and compared against a subset of the experimental data available for these materials. The models will then be extended to two select ATF cladding concepts: FeCrAl and Cr-coated Zircaloy. Sensitivity analysis and uncertainty quantification methodologies are employed as appropriate to provide insight into the most influential model parameters on the metrics of interest and to provide an estimation of the uncertainty in the best-estimate simulation predictions. In some cases parametric studies are used to explore the impact of certain model characteristics instead of full sensitivity and uncertainty quantification analyses.

The rest of this dissertation is divided into eight additional chapters. Chapter 2 presents a general overview of the model developed in this work and summarizes the tools and methodologies used throughout the dissertation. Chapter 3 covers fuel fragmentation and pulverization including a comprehensive investigation on the number of fragments formed using discrete fracture techniques coupled with material strength randomization, power ramping rates, mesh sensitivity, and burnup effects. Chapter 4 presents the development of a Layered2D computational framework, verification of the framework implementation, and the modification of an existing fuel axial relocation model to work within the framework. Chapter 5 introduces an improved cladding oxidation model that accounts for mechanical degradation of the cladding and assesses whether it influences rupture behavior. Chapter 6 presents a model to predict rupture size and location in failed cladding tubes and applies to a few existing experiments. Chapter 7 applies the rupture model to advanced cladding materials including Cr-coated Zircaloy and FeCrAl. Chapter 8 summarizes contributions and findings from this work that are of importance to the nuclear research community. Fi-

nally, Chapter 9 identifies areas of future research that could be pursued by building upon the models developed in this dissertation.

CHAPTER 2

METHODOLOGY

2.1 THE DEVELOPED MODEL

The location and size of rupture in failed cladding tubes during a LOCA is influenced by the boundary conditions present on the inner and outer surface of the tube. The inner surface temperature is influenced by the possible redistribution of heat due to axially relocated fuel. The possibility of axial fuel relocation depends upon the size of the fuel fragments that had formed prior to, and during the LOCA. The outer surface is subjected to a degraded heat transfer coefficient that causes distention and accelerated oxidation. The accelerated oxidation leads a reduction in cladding strength as the thickness of the underlying substrate is consumed. The rupture behavior (i.e., location) is also affected by whether or not the boundary conditions vary azimuthally. A comprehensive multiphysics model to predict the location and size of rupture in failed cladding tubes must take into account all of the above influences with some degree of fidelity.

Figure 2.1 provides a schematic of the model developed in this work. Directional arrows indicate whether a parameter influences or is influenced by another parameter. Parameters that have a blue background are those which have no inputs and the parameters that have a red background are those which have no outputs. Some of the parameters listed are tools or methodologies employed in this work while others are developed and created as part of this work. The tools and methodologies not developed as part of this dissertation are detailed in subsequent subsections of this Chapter. Details of why these particular approaches were chosen over others that are available are provided. One parameter is listed

as optional, which is the detailed coupling of systems or thermal-hydraulics codes for the the thermal-hydraulic boundary condition. This is listed as optional because in many cases there is not enough information provided in the experimental database to set up such a thermal-hydraulic analysis. For separate effects experiments the cladding surface temperature is generally prescribed. However, the framework to couple the developed model to these advanced thermal-hydraulics and systems tools exists.

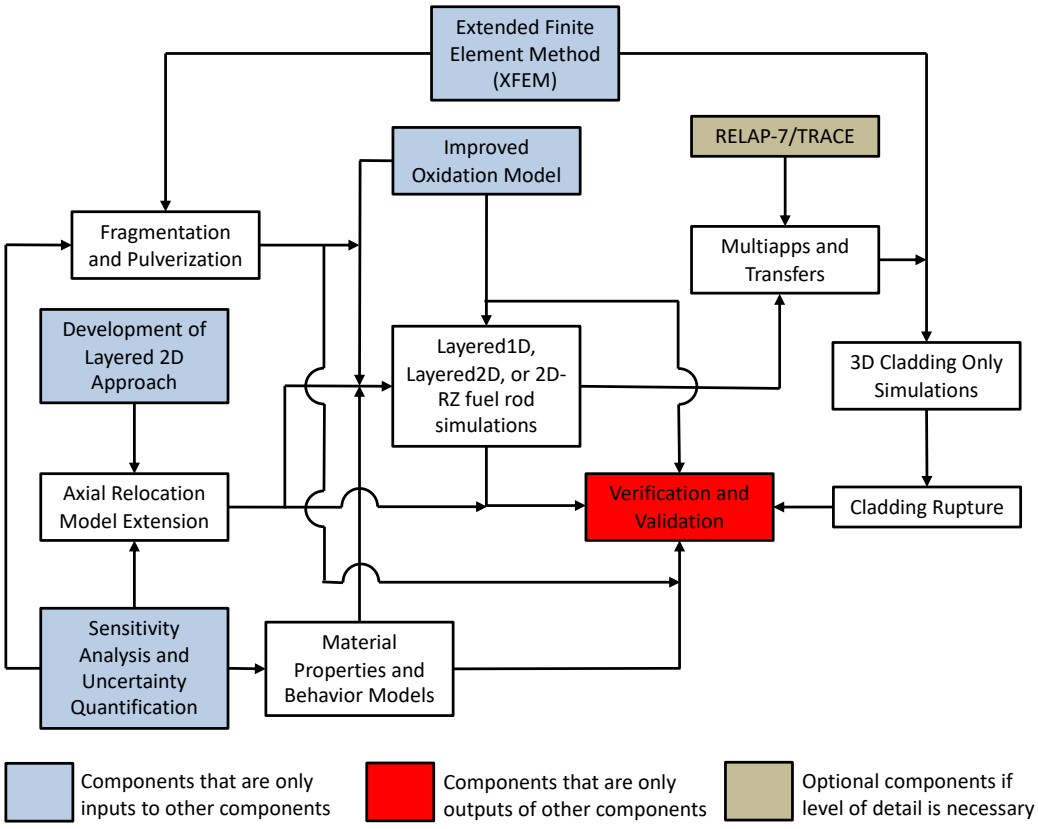

Figure 2.1: Schematic describing the interconnection of different components of the developed model.

2.2 THE MOOSE FRAMEWORK AND BISON FUEL PERFORMANCE CODE

The Multiphysics Object-Oriented Simulation Environment (MOOSE) [82] is a computational framework for solving fully coupled partial differential equations (PDEs) using the Finite Element Method (FEM). The FEM approximates the geometry of interest using a mesh on which the PDEs are solved given appropriate initial and boundary conditions. Optimal convergence requires difficult to compute derivatives of the PDEs with respect to every primary variable (e.g, temperature, displacements, concentration) that are error prone to calculate to construct the Jacobian. To alleviate the need of requiring the exact derivatives to be computed, MOOSE utilizes a computational technique for solving the complex system of PDEs known Jacobian Free Newton Krylov (JFNK) [58].

The JFNK approach allows the Newton method to be used while not having to explicitly form the Jacobian of the system. A preconditioning matrix informed by the Jacobian terms that are known helps guide the initial guess towards the correct solution. The more complete the Jacobian, the less iterations required to achieve convergence. However, the more complex the terms of the Jacobian are to compute the more computationally expensive the simulation. Therefore, the JFNK approach becomes a balance between number of iterations to solve and memory requirements to compute the derivatives in the Jacobian. For complex multiphysics problems that are typically solved by MOOSE and its associated applications, the Jacobian terms (particularly when coupling across different types of physics) are severely nonlinear and non-trivial and JFNK is a good approach to solving such a system. However, with the development of automatic differentiation the difficult and error prone to compute derivatives in the Jacobian can be computed accurately and efficiently. Recent work has begun to transition MOOSE and its associated applications to use automatic differentiation exclusively.

MOOSE itself is open source software and provides a convenient common framework upon which more specific physics modules (or applications) can be developed. The FEM capabilities available in MOOSE are obtained through the third party library called libMesh [57]

and the solvers used are obtained from the third party library PETSc [7]. The more specific physics modules (e.g., heat condition, mechanical contact, solid mechanics, fluid mechanics) are also open source and available in the MOOSE modules packaged along with the framework. Bison on the other hand, is not open source. It is a nuclear fuel performance code developed at INL [133, 132] built upon MOOSE modules and adds capabilities for nuclear materials. RELAP-7, a systems code, is also developed at INL and built upon MOOSE modules for single and two-phase flow behavior in nuclear power plants. It can be coupled to Bison if desired. Both Bison and RELAP-7 depend upon a version of the third party IAPWS-95 library [113] for the computation of water and steam properties.

Figure 2.2 illustrates the inheritance structure of the various codes and libraries. Boxes in the schematic that have a red background correspond to those applications that do not depend on any others whereas those with blue background only depend on others.

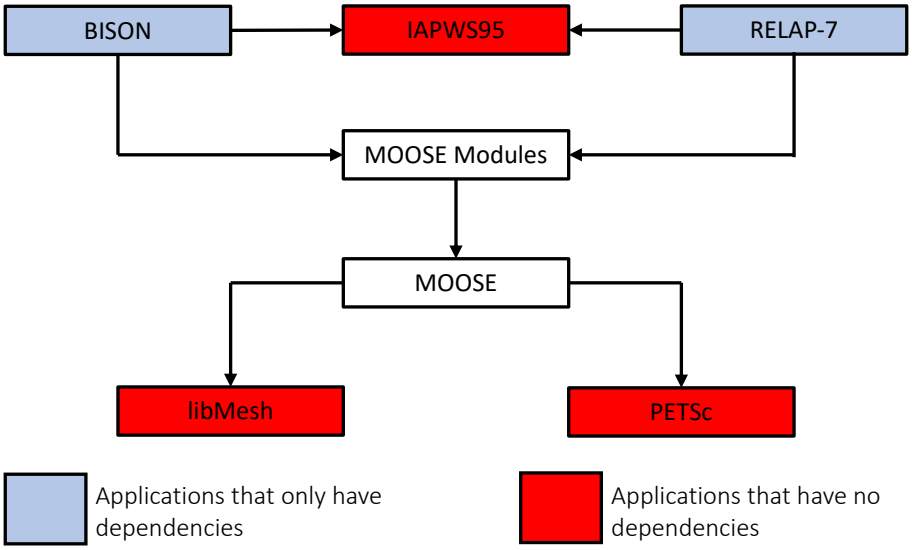

Figure 2.2: Inheritance structure of Bison and RELAP-7 relative to MOOSE, MOOSE modules, and the underlying libraries IAPWS95, libMesh and PETSc.

MOOSE and Bison were chosen as tools in which to develop the model in this work because of their flexibility in geometries that can be analyzed (1D, Layered1D, Layered2D (developed in this work), 2D-RZ, 3D) and the ease at which new models can be added to the code. Bison has been used to investigate a wide range of fuel performance prob-

lems including integral rod behavior [133], discrete fracture [104], missing pellet surface defects [103], and advanced cladding materials [34]. In addition, other codes have been developed based upon the MOOSE framework for investigations of fuel performance at the mesoscale [118], neutronics [127], and thermal-hydraulics [11]. All of these codes build upon a common framework allow coupling and truly multiscale multiphysics problems to be analyzed in detail. Moreover they are free to use and the author of this dissertation is a developer of both MOOSE and Bison. As a developer, the author of this dissertation must conform to the rigorous testing and review processes necessary to submit new code and models. By this way, further confidence can be had in the developed approaches as an independent team member reviews the code for correctness prior to acceptance into the code base.

Other fuel performance codes have been developed over the years in many countries around the world including FRAPCON [40], FRAPTRAN [41] and FALCON [134] in the United States, TRANSURANUS in Germany, ALCYONE in France, ELESTRES and ELOCA in Canada, ENIGMA in the United Kingdom [95], FEMAXI in Japan, and BArra COmbustible (BACO) in Argentina. The majority of these codes utilize a finite different computational technique, only allow a Layered1D representation of the fuel rod, are not free to use, and can be difficult to modify for implementation of new material models and properties. Commercial thermo-mechanics/multiphysics codes such as ABAQUS [130] and COMSOL [87] have also been used for investigating fuel performance, however, these codes are expensive and not efficiently setup to run in parallel for large scale .

2.3 Extended Finite Element Method

The eXtended Finite Element Method (XFEM) is an extension of the traditional FEM approach to allow for explicit modeling of discontinuities within the domain. The mesh in the traditional FEM represents a continuum geometry and is created of elements that are generated by nodes. The number of nodes used to construct the element depends upon the

order of the element (typically linear or quadratic) and the shape of the element (e.g., quad, tri, tet, hex). The higher order and quantity of elements used, the more accurately a complex geometry can be represented. See Figure 2.3 for an illustration of using linear quads to represent a geometry containing a curved boundary. As the number of finite elements increase the geometry is more accurately captured.

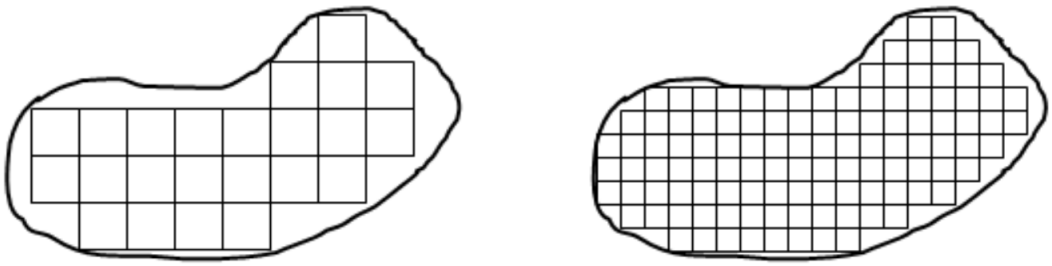

Figure 2.3: Illustration highlighting how a coarser linear finite element mesh (left) captures less of the curved geometry than a finer linear mesh (right). Reproduced from [36].

Values for solution (primary/primal) variables are output at the nodes (e.g., displacements and temperature) whereas derived quantities (e.g., stresses and strains) are typically output on an elemental basis. The value of the solution variables on the interior of the elements is interpolated between nodal values using shape functions which are polynomial functions determined by the order of the element. Material properties, behavior models, and derived quantities are evaluated at interior locations within an element known as quadrature points where weighted averaging is used to determine the elemental value. This interpolation is generally expressed by:

$$\boldsymbol{u}(\boldsymbol{x}, t) = \sum_{I=0}^{n} N_I(\boldsymbol{x})\, \boldsymbol{u_I}(t) \tag{2.1}$$

where $\boldsymbol{u}$ is the solution vector anywhere in the domain, $\boldsymbol{x}$ is the position in space, t is the time, N_I is the shape function for element I, and $\boldsymbol{u_I}$ is the calculated nodal solution. In order to model the discontinuities associated with material interfaces (e.g., metal-oxide interface) or fracture, the original XFEM development uses a Heaviside function [71, 10] to introduce additional degrees of freedom (denoted by $\boldsymbol{e_I}$) to nodes whose element contains

the discontinuity. Therefore, the XFEM interpolation of the solution field is expressed by:

$$\boldsymbol{u}(\boldsymbol{x},t) = \sum_{I=0}^{n} N_I(\boldsymbol{x}) \left(\boldsymbol{u_I}(t) + H(\boldsymbol{x})\, \boldsymbol{e_I}(t) \right) \tag{2.2}$$

For fracture applications, additional degrees of freedom are added to the elements in which the crack tip is located to more accurately capture the singularities associated with the crack tip while avoiding the requirement of mesh refinement [104]. An alternative to introducing discrete discontinuities in the mesh using the Heaviside function was proposed by Hanbso and Hanbso [46] called the phantom-node method. This method models the discontinuity by creating two copies of the original elements that are traversed by the discontinuity that overlap. Each of the copies are made of two parts, physical (part of the solution) and non-physical (excluded from the solution). The nodes in the physical portion of these elements are connected to the the original nodes of neighboring elements whereas the nodes in the non-physical section are called phantom nodes. Because the element copies represent the original mesh topology, the standard interpolation scheme given by Equation 2.1 can be used. Figure 2.4 illustrates the decomposition of a triangle element using the phantom-node algorithm. The active part of the copied elements are denoted by Ω and phantom nodes are show with a ~ above the number.

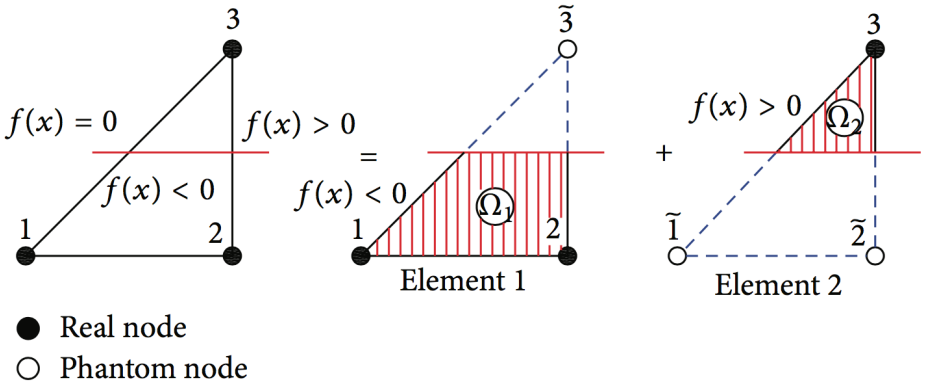

Figure 2.4: Decomposition of a cracked element using the phantom-node algorithm. Reproduced from [5].

The XFEM is chosen in this work over other methods of introducing discontinuities in the analysis such as Peridynamics or the Discrete Element Method (DEM) because it more

naturally fits in the underlying FEM framework that MOOSE and Bison are built upon. Peridynamics and the DEM on the other hand are bond based algorithms that represent the geometry of interest as a network of one dimensional bonds between nodal locations. These bonds have an associated material property to quantify their strength (e.g., critical stretch). If this strength parameter is exceeded in a particular bond it is deemed broken for the rest of the analysis. The bond base formulations are good at modeling discontinuities in a domain but until recently [44, 49, 70, 77, 126] have had difficulty coupling to other physics for truly multiphysics analyses. While continued investigation of the use of Peridynamics and the DEM may be of interest to the fuel performance modeling community it is beyond the scope of this work.

2.4 Multiapps and Transfers

Multiapps and transfers are systems available in the MOOSE framework to enable the simulation of complex multiphysics systems. Multiapps have multiple uses, such as decoupling physics into two separate simulations (e.g., across different length or time scales), coupling a MOOSE based application to an external application, or to spawn multiple simulations from a single master analysis [111]. Transfers define what information and how it is passed between different simulations. Multiple options are available on the MOOSE transfer documentation page [112].

2.5 Sensitivity Analysis and Uncertainty Quantification

Sensitivity Analysis (SA) and Uncertainty Quantification (UQ) have only recently began to be used in conjunction with fuel performance modeling [50, 81]. The purpose of SA is to identify the inputs parameters or models that have the strongest correlation with the output parameters of interest. A simple example would be determining how the uncertainty in the fuel thermal conductivity affects the predictions of fuel centerline temperature or fission gas release. Throughout this work many models have associated uncertainty and their cor-

relation with specific outputs of interest (depends on the case studied) is included. Here, two simple SA correlation coefficients are employed that identify linear and monotonic relationships between inputs and outputs. First, the Pearson (simple) correlation coefficient measures linear relationships between an input and output and is calculated by:

$$\tau_{xy} = \frac{\sum_{i=1}^{n} x_i y_i - n\bar{x}\bar{y}}{(n-1)\, s_x s_y} \tag{2.3}$$

where x_i are the values of the input, y_i are the values of the output, n is the number of samples, $\bar{x}$ is the mean value of the input, $\bar{y}$ is the mean value of the output, s_x is the standard deviation of the input, and s_y is the standard deviation of the output. The mean and standard deviation of the input is calculated by Equation 2.4. Similarly for the output.

$$\bar{x} = \frac{1}{n} \sum_{i=1}^{n} x_i \tag{2.4a}$$

$$s_x = \sqrt{\frac{1}{n-1} \sum_{i=1}^{n} \left(x_i - \bar{x}\right)^2} \tag{2.4b}$$

The value of of the Pearson correlation coefficient is always between -1.0 and 1.0, with -1.0 and 1.0 representing a perfectly negative and positive linear relationship between the input and output parameters, respectively. The Spearman (rank) correlation coefficient determines monotonic nonlinear relationships between the input and output and is performed on the ranks of the data. Rank correlation coefficients are also useful when the magnitude between the input and output parameters are large as it allows one to determine if the smallest ranked input is correlated to the smallest ranked output. To compute the rank, the input and output values are ranked from the their highest to lowest values. For duplicate values their corresponding ranks are averaged. Once ranked, the Spearman correlation coefficient is calculated by:

$$r_s = 1 - \frac{6 \sum_{i=1}^{n} d_i^2}{n\left(n^2 - 1\right)} \tag{2.5}$$

where d_i is the difference in the paired ranks and n is the number of samples. If the ranks are equal (i.e., rank 1 in put equals rank 1 in output) the Spearman correlation coefficient is

instead calculated by:

$$r_s = 1 - \frac{\sum_{i=1}^{n} \left(x_i - \bar{x}\right)\left(y_i - \bar{y}\right)}{\sqrt{\sum_{i=1}^{n} \left(x_i - \bar{x}\right)^2 \sum_{i=1}^{n} \left(y_i - \bar{y}\right)^2}} \tag{2.6}$$

The value of the Spearman correlation coefficient is also between -1.0 and 1.0. The simple and rank correlation coefficients have been widely used in the statistics community, but as mentioned previously vary rarely applied to fuel performance analysis. Throughout the development of the cladding rupture model, these correlation coefficients are used to identify the relationship between the input parameters and output parameters of interest. In particular, the Spearman coefficient is used when a number of the input parameters have orders of magnitude variation. As seen by the equations, multiple simulations (or samples) are required to generate enough statistics to calculate the coefficients. The MOOSE framework upon which Bison is built has a stochastic tools module that is in its infancy that provides some of these statistical features. An advantage of this model includes the ability to have the sensitivity analysis, uncertainty quantification, and Bison calculations completed all in a single input file. However, there are currently some limitations with the module making it not yet ready for use in this work. Thus, in this work, Bison is coupled to the Dakota software [2] developed at Sandia National Laboratories (SNL), which provides a simplistic interface for spawning multiple simulations at once through statistical sampling techniques (e.g., Monte Carlo, Latin Hypercube) and calculates the correlation coefficients and uncertainty automatically. Figure 2.5 shows how information is passed between Dakota and Bison to perform the analyses. The dotted box around all the boxes pertaining to Bison are to illustrate that Dakota treats the application it is interfaced with as a black box. Any code could be coupled Dakota to perform statistical analyses in this way.

2.6 Verification and Validation

Computational or numerical models must be verified and validated. Verification comes in two flavors, code and solution. Code verification ensures that the model is properly input

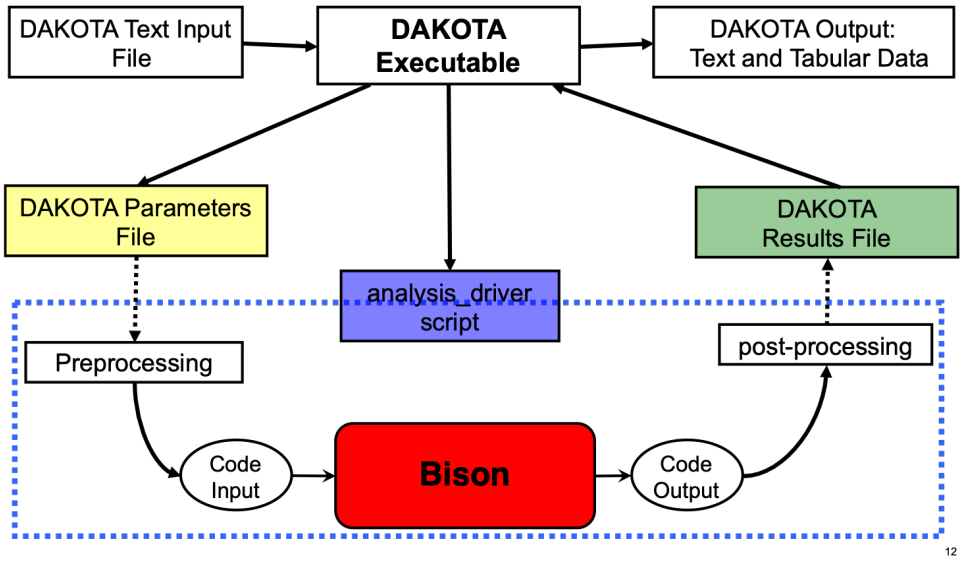

Figure 2.5: Schematic illustrating the information flow between Bison and Dakota for the sensitivity and uncertainty quantification studies.

into the code and results in a known analytical solution. These simulations are typical small in size and run quickly. Development in the Bison fuel performance code requires all existing code verification tests to pass when new code changes are made. In addition, at least one verification test must accompany any code changes. Solution verification is where both spatial and temporal convergence studies are completed to ensure the calculated solution is indeed converged. In FEA simulations spatial convergence is verified through mesh sensitivity studies and temporal convergence is achieved by varying the maximum timestep size.

Validation on the other hand ensures that the code is able to adequately predict reality. This is achieved by comparison of the code output to measured experimental data. Experimental data either comes from separate effect or integral tests. Separate effects tests are designed to isolate one particular phenomenon of interest whereas integral tests are designed to investigate complex fuel rod behavior. An example of a separate effects experiment is a simple tension experiment to determine the elastic properties of a material. Integral tests are typically highly instrumented experiments irradiated in test reactors such as the Advanced Test Reactor (ATR) at Idaho National Laboratory or the Halden Reactor

in Norway to look at complex integrated fuel rod phenomena. The validation cases used in the remaining chapters are introduced and described at their first use. Some are utilized in multiple subsequent chapters.

CHAPTER 3

FUEL FRAGMENTATION AND PULVERIZATION

A large portion of the content presented in this chapter has been published in the Journal of Nuclear Materials [35]. This chapter reproduces the content from the journal publication and adds additional paragraphs and studies to properly fit into the dissertation document as a whole.

3.1 LITERATURE REVIEW

Fragmentation of the UO_2 fuel pellets in nuclear fuel rods begins with fracture early in their life, with finer fragmentation occurring as the length of irradiation exposure increases. Under normal operating conditions, fuel fracture is caused by the large thermal gradient induced in the fuel due to the low thermal conductivity of the fuel. As irradiation progresses the quantity of fragments increases due to the degradation of the thermal conductivity with burnup causing an increase in the temperature gradient. While fragmentation occurs during the life of the fuel, quantification of its severity prior to a LOCA event is of great importance. In addition to the fragments formed during normal operation, small fragments may form during the LOCA by a process known as pulverization (also known as fine fragmentation) [120]. This phenomenon typically occurs at the pellet periphery associated with the HBS [42, 84]. This region is highly porous in which the voided regions are typically populated with bubbles filled with fission gases. As the cladding and fuel temperatures increase during the LOCA the bubbles become overpressurized and rupture, resulting in a disintegration of the HBS in the form of very small (< 100 μm) fragments [60]. While the sizes of fuel fragments can follow a wide distribution, one may simplify the sizes into a

binary system of large and small fragments, where large fuel fragments are formed through the fragmentation process and small fuel fragments are formed through pulverization [53]. The extent of fuel fragmentation and pulverization plays two critical roles in understanding the fuel rod behavior during a LOCA. First, the fragmented fuel may relocate as the cladding distends causing a redistribution of the heat load within rod and second once the cladding has failed the amount of fuel dispersed from the rod is directly a function of the size of the fuel particles to that of the rupture opening.

The study of fuel fracture as a function of irradiation has been investigated through both experiments and modeling. Experiments have been conducted with two distinct goals in mind: (1) determining the fracture properties (e.g., fracture stress, strain, or toughness) [28, 39, 61, 76, 75, 88] of UO_2 for use in modeling or (2) providing insight into the number or size of the fragments that form and the mechanisms of their formation [12, 102, 75, 120, 121]. Modeling approaches can be identified as either empirical [9, 23, 120, 125] or discrete [49, 54, 70, 77, 97, 104, 126, 131]. Empirical approaches determine the number of fragments or cracks that form through an algebraic fit to experimental data and affect the bulk material behavior by modifying the elastic constants of UO_2whereas Discrete approaches on the other hand explicitly model the localized fracture within the simulation domain using advanced modeling techniques such as the eXtended Finite Element Method (XFEM), Discrete Element Method (DEM), cohesive zones, or peridynamics. Previous studies using these mechanistic approaches included unrealistically fast ramping rates for normal operation and limited irradiation effects. Friction between the fuel and cladding during pellet-cladding mechanical interaction has also been found to influence the fracture behavior within the fuel [97].

3.1.1 Empirical Approaches to Fragmentation

The binary system described earlier to identify the mechanism upon which fuel particles have formed was originally proposed by Jernkvist and Massih [53]. This classification is

used extensively throughout this work. Therefore, the terms ‘fragments’ and ‘pulvers’ are used to differentiate between the particles formed through the normal operational processes and the pulverization process, respectively, throughout this work. The normal operation processes include thermal gradients, fuel swelling, and creep.

Several empirically based correlations have been developed to determine the size of the fragments formed due to the thermal gradients within the fuel pellets. In these empirical correlations the fragment sizes are only a function of the number of radial cracks that form during operation. In reality, axial and circumferential cracks can also form under certain operational conditions (e.g., power downs). Axial and circumferential crack formation is not included in this work.

Due to the low thermal conductivity of UO_2 the radial temperature gradient within the fuel increases with increasing linear heat rate of the fuel. As the power increases the number of radial cracks that form increases to reduce the stresses within the fuel. Oguma [75] found that radial cracks began to form at a linear power of approximately 6 kW/m and reached a saturation of 16 cracks at a power of about 40 kW/m. The cracks are assumed to occur at radial locations that result in equal sized fragments as illustrated in Figure 3.1.

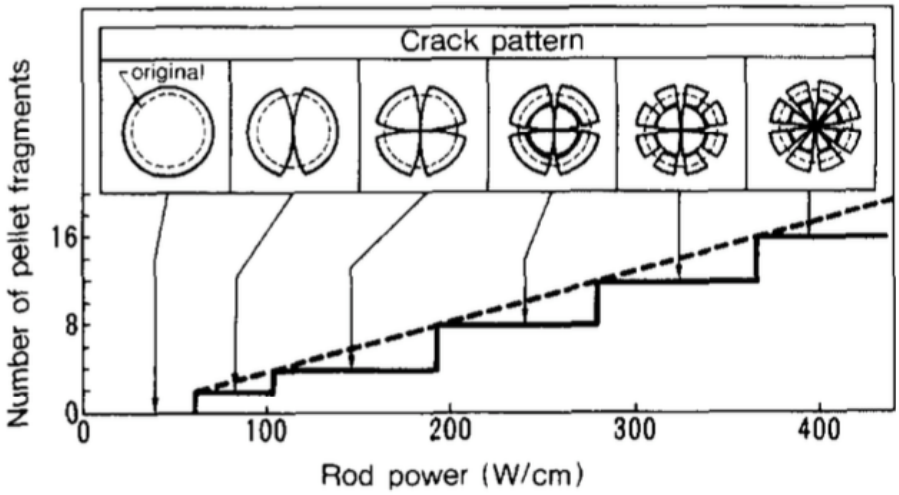

Figure 3.1: Changes in the radial crack pattern during the first rise to power. Reproduced from [75].

To predict the size of the fragments that form, three empirical correlations have been proposed. All of the correlations report a non-integer number for the number of cracks. The simplest correlation is the most recent proposed by Barani et al. [9]:

$$n_f = \begin{cases} 0, & q'_{max} < 5.0 \\ 1.0 + 11.0\left(1.0 - \exp\left(-\frac{q'_{max}-5.0}{21.0}\right)\right), & q'_{max} \geq 5.0 \end{cases} \tag{3.1}$$

where n_f (-) is the number of radial fragments formed and q'_{max} (kW/m) is the maximum linear heat rate experienced by the fuel. One of the earliest models proposed was that of Walton and Matheson [125]:

$$n_f = 0.8\left(\sqrt{Bu_{av}} + \sqrt{3.3\{x\}}\right) \tag{3.2}$$

where Bu_{av} (MWd/kgHM) is the average fuel burnup. The $\{x\}$ notation in Equation 3.2 is the Macaulay brackets, which define the following discontinuous function:

$$\{x\} = \begin{cases} 0, & q'_{max} - 6.0 < 0 \\ q'_{max} - 6.0, & q'_{max} - 6.0 \geq 0 \end{cases} \tag{3.3}$$

where the units for q'_{max} are the same as in the Barani et al. model. The last model is that of Coindreau et al. [23], which first calculates the number of radial fragments in fresh fuel subjected to the maximum linear heat rate:

$$n_f^\circ = \max\left(1, \min\left(\frac{7.0q'_{max} - 8.0}{17.0}, 16.0\right)\right) \tag{3.4}$$

before including irradiation (burnup) effects through:

$$n_f = \min\left(n_f^\circ + \frac{\left(16.0 - n_f^\circ\right) Bu_{av}}{50.0}, 16.0\right) \tag{3.5}$$

where the units for Bu_{av} and q'_{max} are the same as in the Walton and Matheson model. Once the number of fuel fragments is known, taking an assumption that they are equally

distributed around the pellet circumference, the characteristic length of the fragments can be calculated:

$$l_f = D_P \min\left(1.0, \frac{\pi}{n_f}\right) \tag{3.6}$$

where D_P is the pellet diameter (m).

Figure 3.2 plots the three correlations as a function of linear heat rate for fresh fuel (i.e., $Bu_{av} = 0$). None of the correlations approach the saturation condition ($n_f = 16.0$) presented by Oguma [75] at 40 kW/m (see Figure 3.1. Experimental data has been included from Oguma [75] and Walton and Husser [124]. It is observed that the Barani et al. and Walton and Matheson correlations have a stronger fit to the plotted data due to being based upon this dataset. The dataset used for the creation of the Coindreau et al. correlation is not available and therefore not included in Figure 3.2.

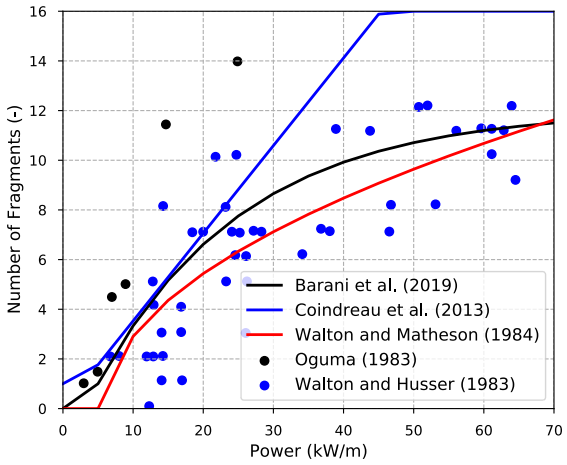

Figure 3.2: Comparisons between the three empirical correlations for predicting the number of radial fuel fragments for fresh fuel including experimental data from Walton and Husser [124].

Of the three empirical correlations, only two have a burnup dependence. This burnup dependence attempts to capture the effect of irradiation (change in material properties, swelling, etc.) on fragment formation. Figure 3.3 illustrates the increase in the number of fragments formed by the Coindreau et al. and Walton and Matheson correlations alongside the experimental data of Walton and Husser [124]. The linear and square root dependence

on burnup, seen in Equations 3.2 and 3.5, is readily observable. Curves for different maximum power levels are shown. It is observed that only at low burnups does the Coindreau et al. match with the experimental data. This is consistent with the low burnup cluster of data points corresponding to a wider range of powers. The higher burnup data points correspond to experimental powers <15 kW/m. As before, the data underlying the Coindreau et al. correlation is not available and is not included in the figure leading to the over estimation at higher burnups. On the other hand, the Walton and Matheson correlation matches reasonably well for the lower power high burnup data points. Especially since this correlation is based upon the plotted data.

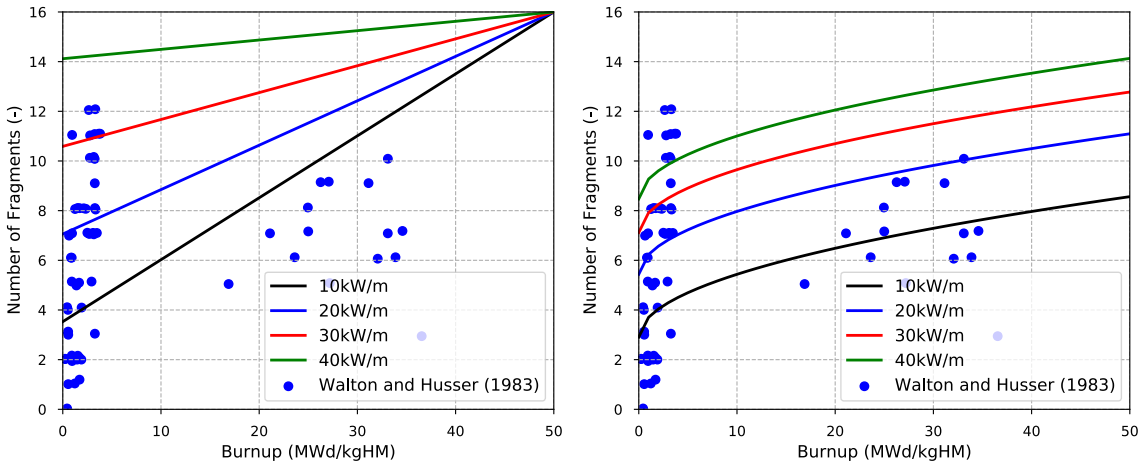

Figure 3.3: Increase in the number of radial fragments formed as a function of burnup for different maximum power levels for (a) the Coindreau et al. and (b) the Walton and Matheson models including experimental data from Walton and Husser [124].

The empirical correlations provide an estimate of the number and, consequently, the size of radial fragments that form as a function of burnup and maximum linear power supplied to the fuel. However, the dependence on power and burnup are not based upon any physical description but rather fit to experiments in which the number of fragments were observed on micrographs. The models do not take into account the mechanism in which the fragments form (i.e., fracture toughness or tensile strength being exceeded) or other effects,

such as ramping rates to the maximum power and at what time during the irradiation the maximum power is achieved. Recently, many research groups have begun using mechanistic fracture techniques to investigate these phenomena and to gain insight into the effects of the discontinuities (cracks) on the mechanical and temperature behavior of the pellet.

Williamson and Knoll [131] utilized the ABAQUS finite element code with a cohesive zone fracture technique coupled to the FEM to evaluate when and where cracks form, how they interact with each other, and how the stress field is affected by the presence of the cracks. Their model was able to capture axial (transverse) and radial cracks and focused on the initial rise to power. However, the issue with the cohesive zone approach employed is that the potential crack paths have to be known *a priori* and only eight radial crack paths were included in the model, contrary to the observations of Oguma [75]. The results obtained by the authors illustrated that the stress state of the pellet is strongly effected by the inclusion of mechanistic cracks.

Huang et al. [49] investigated fuel cracking during the rise to power and under cyclic loading using the DEM. A finite element simulation was used to develop the temperature boundary condition on the exterior of the pellet. The benefit of DEM over cohesive zone models is that the crack initiation locations are not required to be known *a priori*. The investigation of a maximum power level on the number of macroscopic cracks that form was consistent with Oguma's observations up to 25 kW/m, after which the DEM predicted very little increase in the number of predicted cracks as the power level increased. Cyclic power loading resulted in the formation of circumferential cracks.

Spencer et al. [104] investigated the formation of radial cracks during the initial rise to power to 25 kW/m over 10000 s using the XFEM with a crack initiation and extension criterion defined as when the hoop stress exceeds the tensile strength of UO_2 (taken as 130 MPa in their study). A small variation from the 130 MPa tensile strength value was randomly distributed across the pellet to permit crack and fragment formation. Using this approach, about 6 radial cracks or fragments were predicted to form, which is consistent

with the correlation proposed by Walton and Matheson if the average burnup is set to zero to represent fresh fuel. Later efforts by Jiang et al. [54] used XFEM with a fracture mechanics-based growth criterion, using nominal values of 2 and 4 MPa$\sqrt{m}$ for the critical stress intensity factor. Although the crack patterns differed somewhat in those two cases, both cases predicted the formation of about 6 radial cracks at a power of 25 kW/m.

Mella and Wenman [70] demonstrated the use of peridynamics for modeling the mechanistic fracture of advanced gas-cooled reactor (AGR) fuel. While the reactor type is different than the one of interest in this work (i.e., light-water reactor), the approach demonstrates that peridynamics is able to predict radial and axial cracks. At a high-level, peridynamics is a non-local mesh-free methodology that uses an integral rather than a differential formulation of mechanics. It represents the material using a set of points connected by bonds, and models fracture by removing individual bonds when a critical criterion (e.g., critical stretch) is reached. Once a bond is broken, it remains broken for the rest of the simulation and does not permit crack healing.

Oterkus and Madenci [77] applied the peridynamics approach to light-water reactor fuel. The authors investigated extremely short simulation times (9 s) to demonstrate the capability for a single power level. Wang et al. [126] have also utilized peridynamics for light-water reactor fuel analysis. Building on Oterkus and Madenci's initial demonstration, Wang et al. investigated different power levels. The boundary conditions used by Williamson and Knoll [131] were used by these authors. Hu et al. [48] demonstrated a 3D simulation of fracture of fresh fuel with peridynamics. These studies all predicted the formation of a number of cracks that was somewhat consistent with Oguma's observations for fresh fuel.

3.1.2 PULVERIZATION

Pulverization is believed to be caused by the overpressurization of gas bubbles in the HBS. This postulation is due to the observation by Une et al. [121] of significant fission gas release accompanying the generation of finely fragmented fuel. Based upon limited experimental

data, Turnbull et al. [120] developed a threshold for pulverization that depends on the local burnup and temperature within the fuel. The pulverization threshold proposed by Turnbull et al. is presented in Figure 3.4. The dependence of the threshold on local burnup highlights the fact that the periphery of the fuel pellet will likely pulverize first due to its higher local burnup and the formation of the HBS.

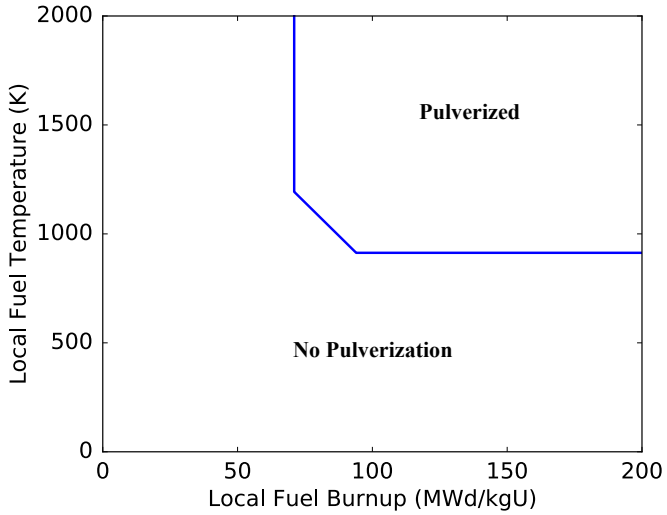

Figure 3.4: Burnup dependent temperature threshold for pulverization of UO_2 fuel.

Ongoing research activities by the mesoscale modeling team at INL is exploring improvements to the empirical threshold that incorporates microstructural insights into the mechanisms driving fine fragmentation [33]. Application of these preliminary lower-length scale informed models is beyond the scope of this work.

3.2 Mechanistic Verification of Empirical Models

The empirical correlations for fuel fragmentation take into account irradiation effects but do not take into account power ramping rates or the random distribution of fracture strength. The existing mechanistic modeling approaches also have their limitations, as thus far the irradiation times have been limited or in some cases the ramping rates unrealistically fast (e.g., < 10,000 s) for normal operation. All of the studies with mechanistic models surveyed here have either focused on rise to power conditions or short cyclic loading and only con-

sidered the fuel, rather than the full fuel/cladding system. None have considered the effect of burnup on the quantity of fragments or fracture patterns. Moreover, when randomness in material strength was considered, only a single random realization of the material strength was evaluated. The fracture pattern predicted for a given random realization is one potential outcome, but it is important to understand the statistical distribution of the fracture behavior that could occur because every fuel pellet will have its own random distribution of strength. To characterize the statistical distribution of the predicted fracture patterns and numbers of fragments, fracture simulations should be performed using many realizations of the spatially varying strength in the pellet.

3.2.1 Model Description

A mechanistic modeling approach is utilized that investigates the sensitivity of the number of fragments formed due to material strength randomization, criteria for strength randomization, mesh density, power ramping rate, and irradiation effects. The goal is to determine whether or not predictions of the empirical correlations fall within the uncertainty of the mechanistic modeling approaches that use detailed representations of the physics. If they do, increased confidence can be had in using the empirical correlations in more computationally intensive studies because, despite not explicitly taking into account ramping effects or the distribution of strength, the calculated values fall within the uncertainty of the mechanistic model, which does take into account the underlying physics associated with fracture.

The mechanistic modeling technique chosen in this work is the XFEM. XFEM incurs minimal additional computational overhead costs, and is a natural extension of the FEM, so if it is added to an existing FEM-based fuel performance code such as Bison, which is used in this study, the full set of models for burnup-dependent behavior can readily be used. The XFEM approach employed here uses the same basic crack initiation and growth criteria used by Spencer et al. [104]. Crack initiation is permitted at the outside radial surface of the fuel once the hoop stress exceeds the tensile strength of UO_2. Cracks are allowed to

extend into the next element ahead of the crack tip if the hoop stress in that element exceeds the tensile strength. It is important to note that this approach is sensitive to the mesh size because the ability of the model to capture the stress singularity that occurs at a crack tip depends on the mesh. The dependency of the solution on the mesh size is addressed by a parameter study in the present work.

This crack propagation method requires two inputs to define the evolution of cracks as a function of time: the crack initiation threshold and the crack propagation criterion. The material's tensile strength is used for both of these here, and is spatially randomized to represent the effects of local defects. To generate this randomized spatial distribution of the tensile strength in the fuel, two methods are compared in this work. The first is a uniform $\pm 2.5\%$ randomization about the mean tensile strength value. A uniform distribution indicates that any value in the range of $\pm 2.5\%$ of the mean is equally probable. This is easy to implement, but is expected to introduce mesh size dependencies. Physically, larger finite elements should be weaker as they represent is more material within the domain, meaning that the chance of microstructural defects (flaws) being present to decrease the tensile strength is higher than for smaller elements. Contrarily, smaller finite elements are stronger. Therefore, three mesh densities (coarse, medium, fine, see Figure 3.5) are investigated to assess the influence of the mesh on the predicted fragmentation results.

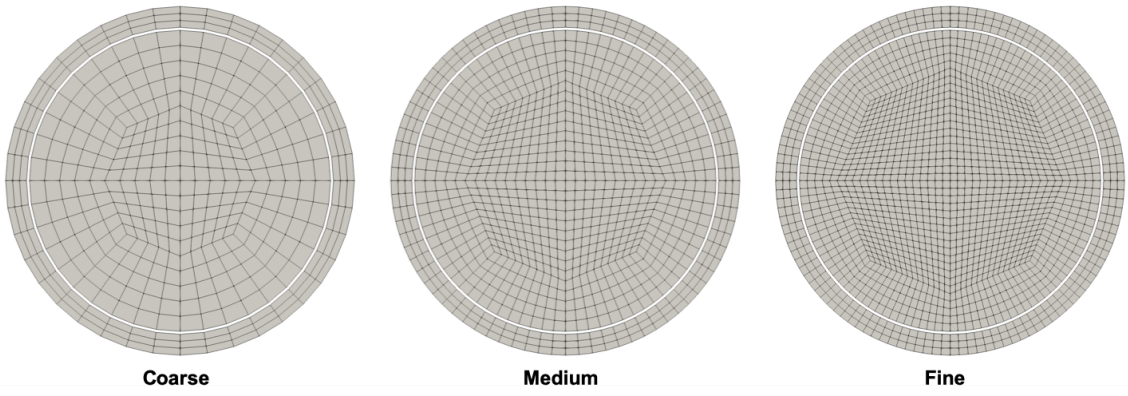

Figure 3.5: Mesh densities used in the fragmentation analyses.

The second randomization criterion is expected to address the mesh density dependence

by using a weakest link Weibull model [137] that adjusts a Weibull distribution with a weighting factor to account for the element volume (V) using the following form [108]:

$$\eta = \bar{\eta}\left[\frac{\bar{V}\ln(R)}{V\ln(0.5)}\right]^{1/k} \tag{3.7}$$

where $\bar{\eta}$ is the median value of the strength variable; $\bar{V}$ is the reference volume, which is the volume of a test specimen that has a median strength equal to $\bar{\eta}$; R is a uniform random number on the interval from 0 to 1; and k is the Weibull modulus. In this analysis, $\bar{\eta}$ corresponds to the mean tensile strength value.

As can be seen from the preceding discussion, the most important material property for mechanistically investigating fuel fracture is the tensile strength of UO_2. For the Weibull criterion, the volume of the specimen used in the experiments is also important. The earliest experiments of the fracture strength of UO_2 were completed by Evans and Davidge [28] through three-point bending tests on $24 \times 6 \times 5$ mm bar specimens. Two different grain size samples (8 μm and 25 μm) were investigated as a function of temperature. In general, the larger grain specimens had a lower fracture strength ranging from ~130 to ~170 MPa compared to ~160 to ~220 MPa for the small grain specimens.

Radford [88] performed biaxial loading experiments on 1–2 mm-thick cylindrical specimens that were 15 mm in diameter. Grain sizes ranged from 5 to 25 μm and densities (directly correlated with porosity) ranged from ~91 to 98.5%. After normalizing the measured data to 95% theoretical density, the range of reported tensile strengths were ~70 to 136 MPa. An empirical correlation for the tensile strength (TS) was developed as a function of porosity (P), grain size (GS), and pore size (PS):

$$TS = 403.21\exp(-6.17P)(GS + 3PS)^{-0.29} \tag{3.8}$$

where P is in volume fraction (i.e., between 0 and 1.0), and GS and PS are in μm. Oguma [76] performed a similar study on the microstructural effects on the tensile strength of UO_2 using biaxial flexure tests on 1.5–2 mm thick cylindrical specimens that were 15 mm in diameter. Here, two regions with different grain size (small and large) were analyzed. Small grained

samples were in the range of 7 to 30 μm, whereas large grained samples were in the 60 to 90 μm range. The measured tensile strengths ranged from ∼50 to ∼120 MPa. A different empirical correlation was created as a function of porosity (P), grain size (GS), and pore size (PS).

$$TS = 626.0 \exp(-0.057P)(0.5 \cdot GS + PS)^{-0.5} \tag{3.9}$$

where P is a percent, and GS and PS are in μm. More recently, Gatt et al. [39] performed bending tests on two different sized bar samples: $10 \times 1.5 \times 1.5$ mm and $28 \times 4 \times 4$ mm. Multiple samples were created for each size, with varying grain sizes denoted as small or large but the actual sizes of the grains were not reported. The average reported values of the tensile (rupture) strength of UO_2 was ∼112 MPa.

In the fragmentation analyses completed here, the initial porosity of the fuel is 5% and the grain size is 10 μm. According to [110], the typical pore size in fresh fuel is distributed over the range of 0.1–10 μm. Substituting the porosity, grain size, and pore size into Equations 3.8 and 3.9 gives estimated values of 105.50 MPa and 121.35 MPa, respectively. Given the uncertainty in the ranges of measurements by all of the research groups, a mean tensile strength value of 110 MPa was used in this work. For the volume-weighted Weibull case, the reference volume and Weibull modulus were 3.53×10^{-7} m^3 and 10.0, respectively.

3.2.2 Initial Rise to Power

The sensitivity of the number of fragments formed due to material strength randomization, power ramping rate, and irradiation effects is studied here in two steps. First, the effect of material strength randomization and power ramping rate on the number of fragments during the initial rise to power of the fuel is studied. Then, burnup and irradiation effects are incorporated through the material and behavior models of the UO_2 fuel and Zircaloy-4 cladding, as described in Section 3.2.3.

According to Capps et al. [19], a typical PWR ramping rate for the first cycle of fresh fuel is given by a ramp rate of 30% of the maximum linear heat generation rate (L_{max})

per hour up to 20% of L_{max}, followed by a ramp at 3% of L_{max} per hour up to L_{max}. Three different ramping rates were used and are plotted in terms of normalized power as a function of time in Figure 3.6. The fastest ramping rate used in this study (5%/h after the initial rise to 20% power) is significantly slower than those used in previous studies [49, 77, 104]. In the simulations, after the maximum power is achieved, the power is held for 5,000 s to ensure thermal equilibrium is attained. To account for material strength randomization, 200 simulations were completed using different random seeds for each combination of mesh density, ramp rate, and maximum linear heat generation rate (see Table 3.1) for both the uniform and volume-weighted Weibull randomizations of strength. This gives a total of 28,800 analyses.

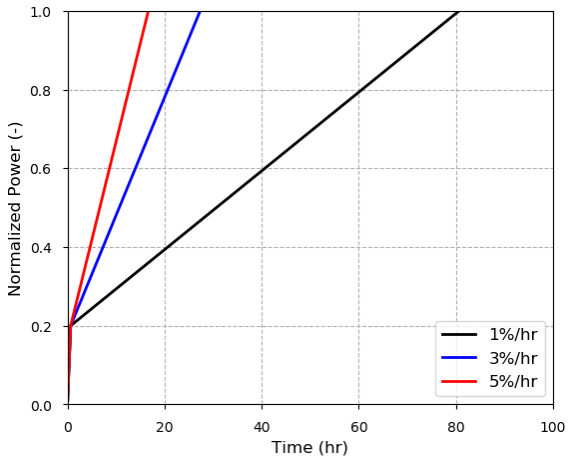

Figure 3.6: Ramping rates investigated in the fragmentation studies. 3%/hr is typical for the normal operation of PWRs.

Table 3.1: Combinations of inputs used in the rise to power fragmentation study.

Mesh Density	Ramp Rate to $0.2L_{max}$ (hr^{-1})	Ramp Rate to L_{max} (hr^{-1})	Maximum LHGR (kW/m)[†]
Coarse	$0.3L_{max}$	$0.01L_{max}$, $0.03L_{max}$, $0.05L_{max}$	5 – 40
Medium	$0.3L_{max}$	$0.01L_{max}$, $0.03L_{max}$, $0.05L_{max}$	5 – 40
Fine	$0.3L_{max}$	$0.01L_{max}$, $0.03L_{max}$, $0.05L_{max}$	5 – 40

[†] 5 kW/m increments inclusive.

The domain used in the fuel fragmentation study consists of a 2D cross-sectional slice

containing fuel, a gas gap, and cladding. Figure 3.7 illustrates the tensile strength distribution throughout the fuel pellet cross-section for two of the 200 random seeds for the uniform and volume-weighted Weibull criteria.

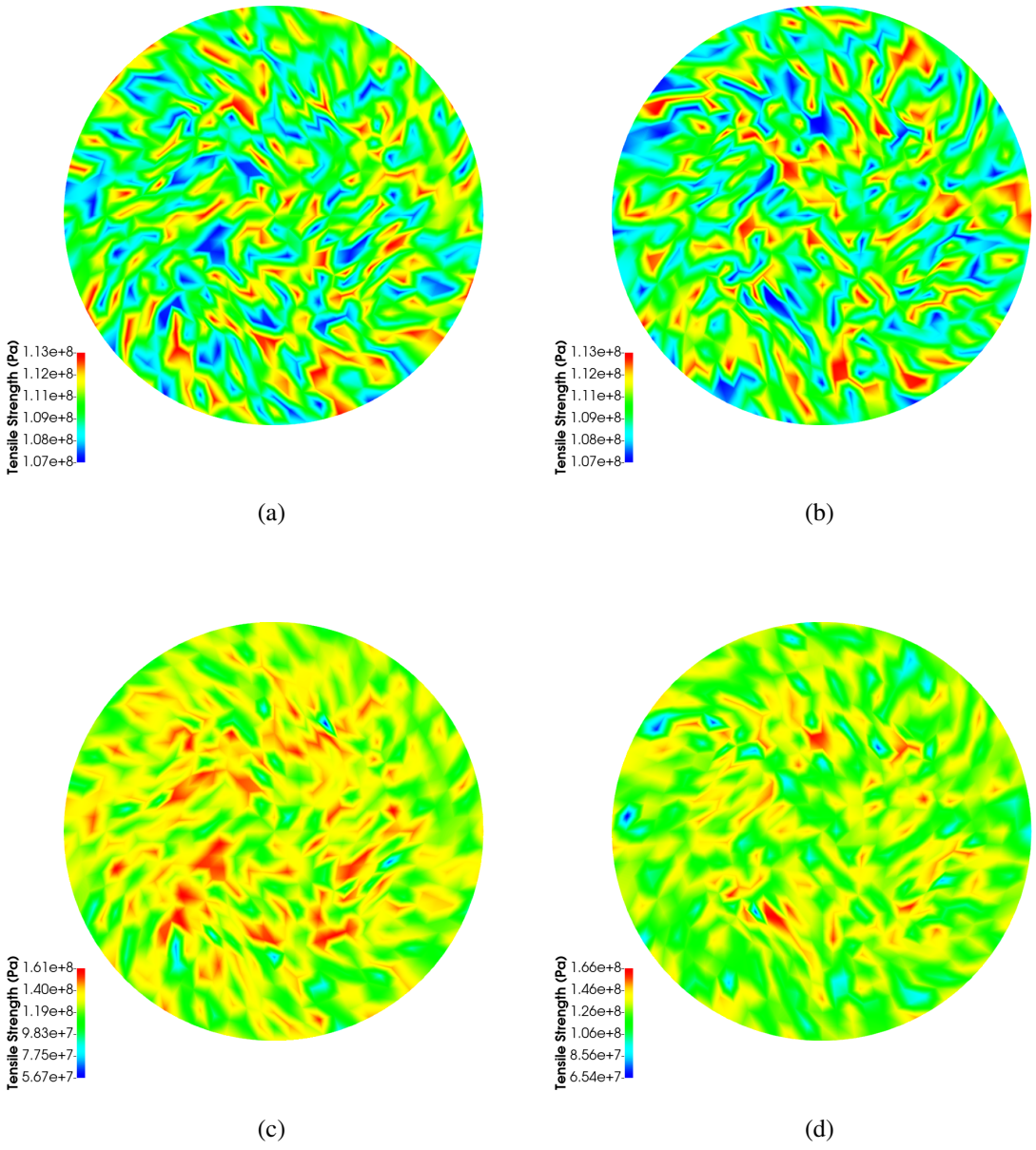

Figure 3.7: The randomization of tensile strength throughout the fuel pellet for 2 of the 200 random seeds for the medium mesh. The cladding is not shown. The top row is for the uniform criterion and the bottom row is for the volume-weighted Weibull criterion.

A generalized plane strain approach is used, where a finite out-of-plane strain is per-

mitted, to account for the affect of creep, axial growth, swelling, and thermal expansion on the in-plane behavior of the materials. In standard plane strain analyses, the out-of-plane strain is exactly zero. The generalized plane strain condition assumes that the out-of-plane strain is uniform over a component, but has a nonzero value that is computed such that the area integral of the out-of-plane stress is zero. This permits axial expansion of the fuel, but assumes that the fuel pellets behave as infinite cylinders. The models that compute plenum gas volume and pressure in Bison account for out-of-plane expansion of the rod, and compute a gas volume per unit thickness using a user-supplied amount of plenum height per axial unit of rod length. The ratio of plenum height to fuel height assumed here is 0.03854, which is consistent with the plenum to fuel ratio in a typical full length fuel rod. The end caps are not explicitly modeled in the generalized plane strain model, so the pressure applied in the axial direction of the rod is imposed in the out-of-plane direction of the planar model as a boundary condition to the cladding. This axial pressure is calculated by:

$$P_{axial} = \frac{P_{coolant} D_{co}^2 - P_{plenum} D_{ci}^2}{D_{co}^2 - D_{ci}^2} \tag{3.10}$$

where P_{axial} is the axial pressure (Pa), $P_{coolant}$ is the coolant pressure (Pa), P_{plenum} is the plenum pressure (Pa), D_{co} is the cladding outer diameter (m), and D_{ci} is the cladding inner diameter (m).

Because the hoop stress imposed by thermal gradients is fairly uniform around the periphery of the fuel, this can lead to the formation of a large number of cracks around the outer surface of the pellet at roughly the same time. This is mitigated somewhat by the use of a randomized strength, which causes a more limited number of cracks to initiate. Once the cracks propagate, they relieve the stress in the surrounding area, leading to localization in a smaller number of cracks.

Due to this localization process, only a few of the cracks that initiate around the periphery will propagate deep enough into the pellet to form fragments. To track the number of cracks that propagate to various depths, and in turn track the number of fragments formed, a code object called `RadialCrackCounter` was developed for Bison that keeps track of

the number of cracks that are of certain lengths at each time in the simulation. The as-fabricated fuel radius and the number of bins to group crack lengths into are specified. An illustration of how the `RadialCrackCounter` works is provided in Figure 3.8. The dashed circles indicate the bin boundaries, and 10 bins are assumed in this illustration. The bin width is described as the as-fabricated fuel radius divided by the number of bins. The tally in a particular bin captures all cracks whose tip falls within the bin width. The number of bins cannot be greater than the number of radial finite elements in the mesh. In this study, the coarse mesh has 10 radial elements to equal the number of bins.

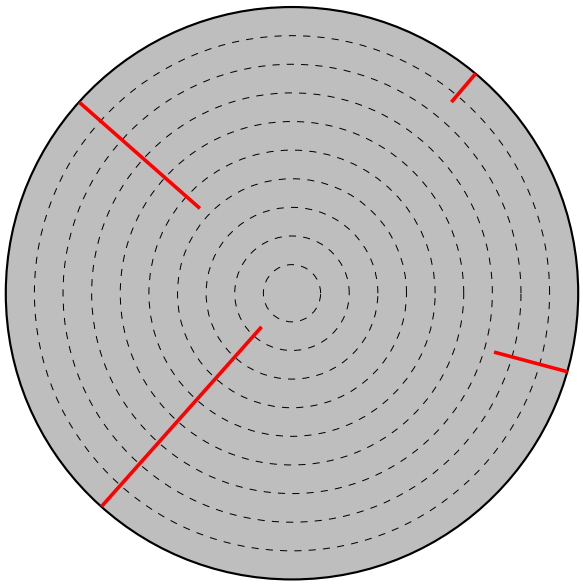

Figure 3.8: Illustration on the function of the radial crack counter. The lines represent different cracks extending to different bins. In this example, there would be one crack each in Bins 2, 3, 6, and 9.

Figure 3.9 presents the results from the radial crack counter for the initial rise to power up to 20 kW/m for the three mesh densities using the (a) uniform and (b) volume-weighted Weibull strength randomization criteria. Each point on the plot corresponds to the mean value obtained from the 200 realizations of the spatially randomized tensile strength field. It can be seen that the second bin in the case of the coarse mesh and the first bin in the case of the medium and fine meshes do not have data points shown on the plot. This is due to the previously mentioned formation of many small cracks at the pellet periphery, of which only

a small subset propagates further into the pellet. These small cracks are not deep enough to result in large fragment formation, so in subsequent plots showing the total number of cracks at a given power level and ramp rate, only the deeper cracks are considered, and the number of cracks reported corresponds to the sum of the number of cracks in Bins 3 through 10 for the coarse mesh and 2 through 10 in the medium and fine cases. It is observed that the number of cracks that initiate at the pellet periphery when using the volume-weighted Weibull distribution is reduced relative to the uniform distribution case.

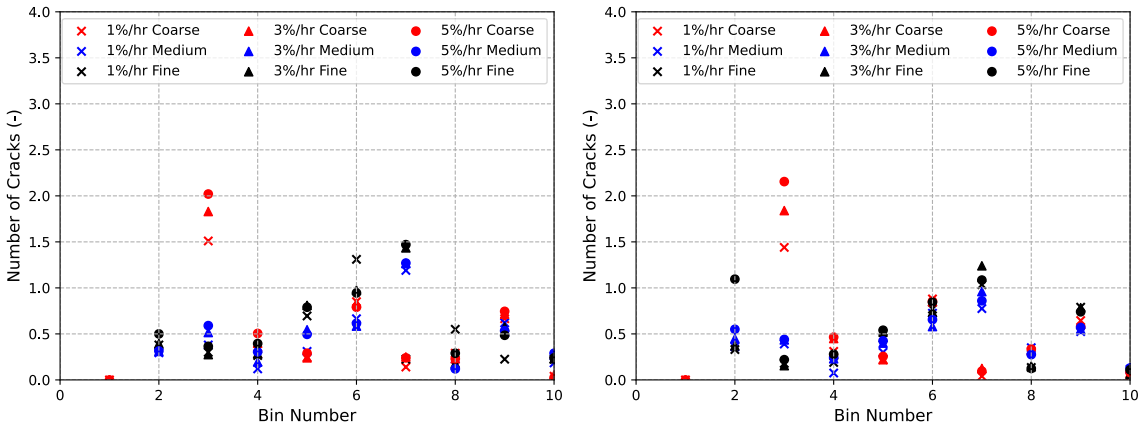

Figure 3.9: The number of cracks per bin for the initial rise to power to 20 kW/m using (a) uniform and (b) volume-weighted Weibull randomization of strength.

Figure 3.10 shows the calculated number of cracks at each power level during a rise to power event for the three different ramp rates (denoted by different symbols) and mesh densities (different colors). Figure 3.10a is for the uniform strength randomization, and Figure 3.10b is for the volume-weighted Weibull strength randomization. Each point corresponds to the mean value predicted from the 200 different realizations of tensile strength randomization. In general, the number of calculated cracks increases with an increasing mesh density and ramping rate. For example, for the uniform strength randomization, there is a noticeable difference between cracks that form in the fine mesh compared to the coarse and medium meshes. This effect is significantly reduced for the volume-weighted Weibull strength randomization, which indicates that the element volume correction employed in

the weakest-link Weibull theory is quite effective at minimizing mesh size effects. There is still some mesh size dependency even when accounting for the element volume, which is due to the use of a stress-based fracture growth criterion. It is expected that using a fracture mechanics-based criterion (e.g., critical energy release rate) would minimize this effect, but this was not done in the present effort because it introduces considerable additional complexity to the study.

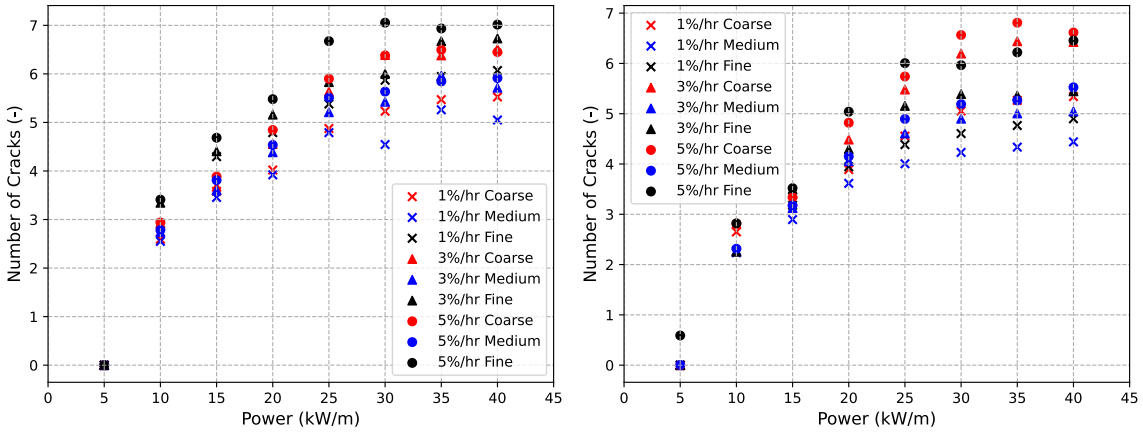

Figure 3.10: Calculated number of cracks during the rise to power for different powers for the (a) uniform and (b) volume-weighted Weibull strength randomization criteria. The points correspond to the mean value of all simulations for the respective mesh density and ramp rate.

3.2.3 Base Load Burnup Accumulation

Under base load operating conditions the linear heat generation rate is held constant after reaching its maximum value. To include irradiation effects, the steady-state power is held until a maximum burnup of 40 MWd/kgU is achieved for all of the combinations listed in the initial rise to power table (see Table 3.1). Data is extracted from each case at 10 MWd/kgU increments (i.e., 10, 20, 30, and 40). Burnup or irradiation effects are incorporated into the analyses through the material models used for the UO_2 fuel and Zircaloy-4 cladding. For the fuel, this includes models such as thermal conductivity degradation, irradiation dependent

elastic constants, solid fission product swelling, gaseous swelling and fission gas release, and thermal and irradiation creep. In the cladding, models that are affected by irradiation that influence the time at which fuel-to-cladding contact may occur (resulting in an alteration of the fuel stress state driving fracture) are irradiation dependent elastic constants, thermal and irradiation creep, and irradiation growth. Details of the correlations used for these material behaviors can be found in the Bison theory manual [69]. The cracks per bin as a function of the burnup are shown in Figures 3.11 and 3.13 the total number of cracks as a function of both the power level and burnup are shown in Figures 3.12 and 3.14. Behavior similar to that observed in the rise to power case, is observed here, with negligible increases in the number of cracks predicted as the burnup increased. This behavior is consistent with the Barani et al. [9] correlation, which is not dependent on burnup.

It should be noted that, with an increasing burnup, the average number of cracks predicted appears to be decreasing slightly. This is attributed to the fact that, of the 200 tensile strength realizations at each power and burnup level combination, a number of the cases did not successfully run all of the way to the target burnup because they reached a state where a finite element was cut on more than two edges, which is not currently permitted by Bison's XFEM algorithm. This condition typically indicates the coalescence of two cracks into a single crack. For the power levels of 35 kW/m and 40 kW/m, none of the 200 simulations achieved a burnup of 40 MWd/kgU and 30 MWd/kgU, respectively. While these burnup levels are low for normal LWR operation, it should be noted that typical reactor operation reduces the power in later fuel cycles. A study exploring the effects of load follow operations (many power changes during operation) is the subject of future work. Section 3.2.4 illustrates that the exclusion of simulations that do not achieve the desired burnup thresholds does not affect the comparisons of the mechanistic modeling approach to that of the empirical correlations.

All of the preceding plots have presented the mean values of all the simulations as data points for particular ramping rates and mesh densities for the two different strength ran-

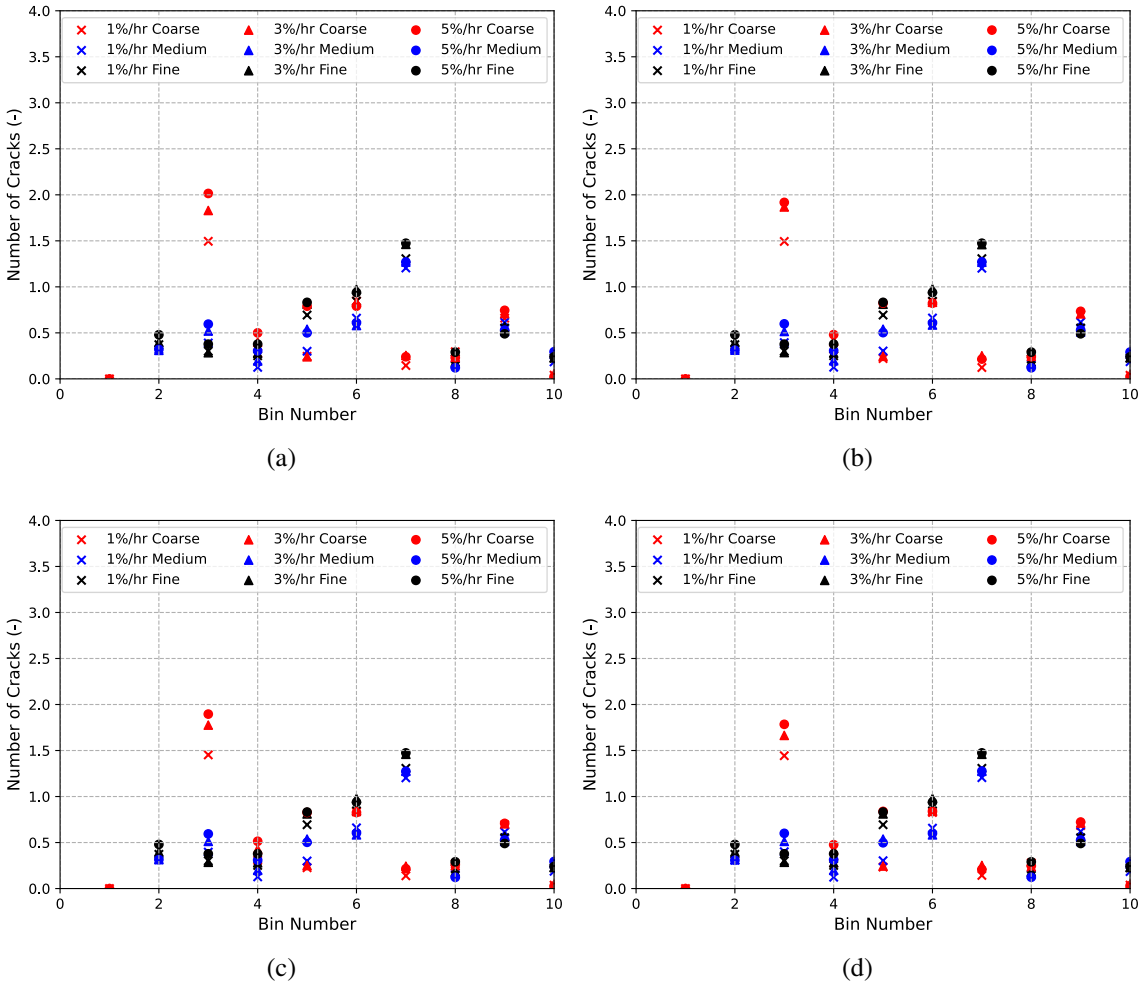

Figure 3.11: The number of cracks per bin at the various burnup levels when the maximum power is 20 kW/m for the uniform strength randomization criterion. (a) 10 MWd/kgU, (b) 20 MWd/kgU, (c) 30 MWd/kgU, and (d) 40 MWd/kgU.

domization criteria analyzed. Since the average standard deviation also plays a role in determining whether the mechanistic approaches are able to predict the calculated values from the empirical correlations (see Section 3.2.4, it is important to visualize the distribution of predicted cracks for a representative case. Figure 3.15 shows distributions of the number of simulations that predicted a certain number of cracks for the case where the maximum power was 20 kW/m,and the ramping rate was 3%/hr. The x-axis of the histogram plots are set to range from 0 to 16 to correspond with the crack range observed by Oguma [76]. Figures 3.15(a), (c), and (e) correspond the histograms for the uniform strength randomization

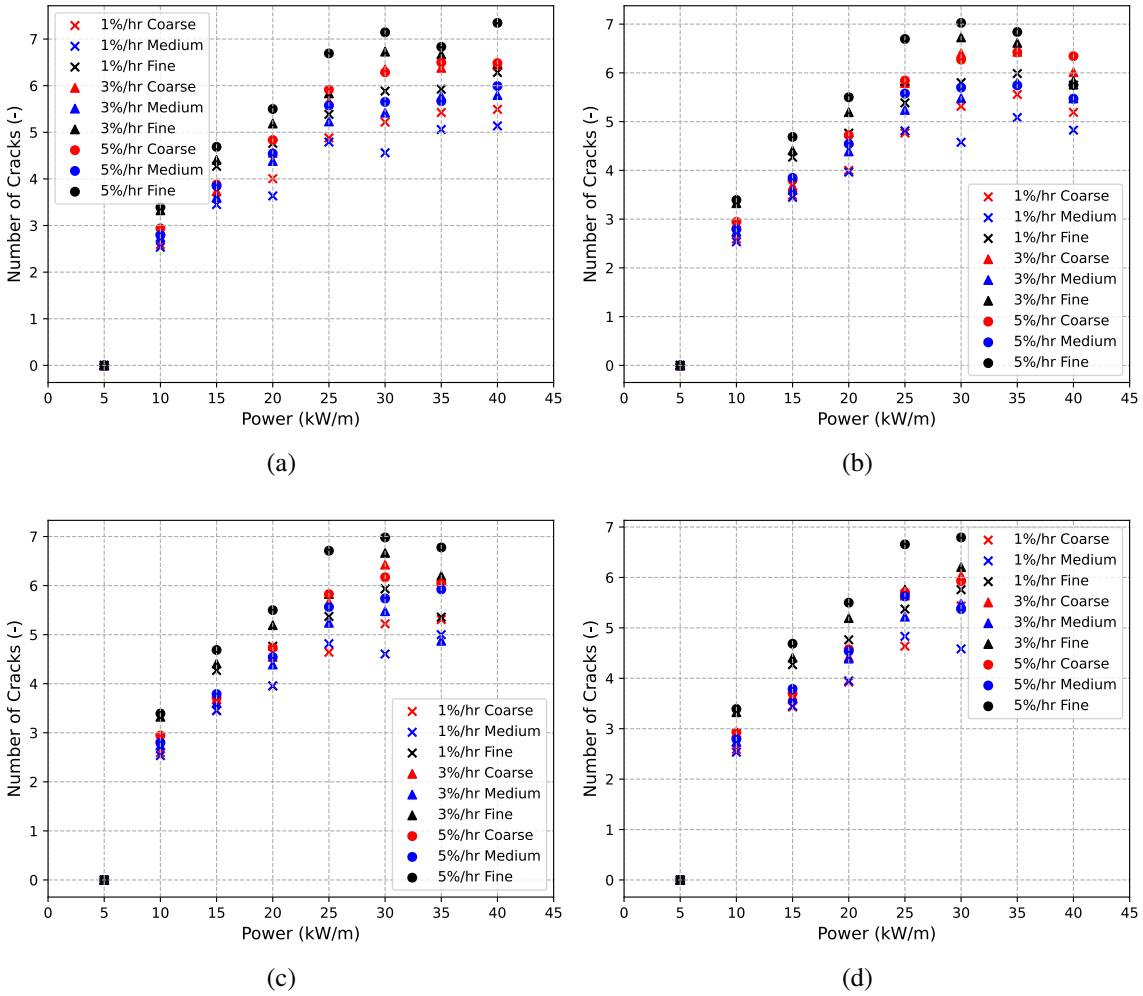

Figure 3.12: Calculated number of cracks as a function of burnup for different powers for the uniform strength randomization criterion. (a) 10 MWd/kgU, (b) 20 MWd/kgU, (c) 30 MWd/kgU, and (d) 40 MWd/kgU. The points correspond to the mean value of all simulations for the respective mesh density and ramp rate.

during rise to power for the coarse, medium, and fine mesh densities, respectively. Similarly, Figures 3.15(b), (d), and (f), correspond to coarse, medium, and fine mesh densities for the volume-weighted Weibull strength randomization during rise to power. It is observed that as the mesh density increases, the spread of the histograms becomes narrower for both the strength randomization criteria. Examining peak of the histograms indicates that a small mesh dependence is observed for the uniform strength randomization as the peak number of cracks shifts from 4 to 5 as the mesh becomes finer. This shift is not observed in the

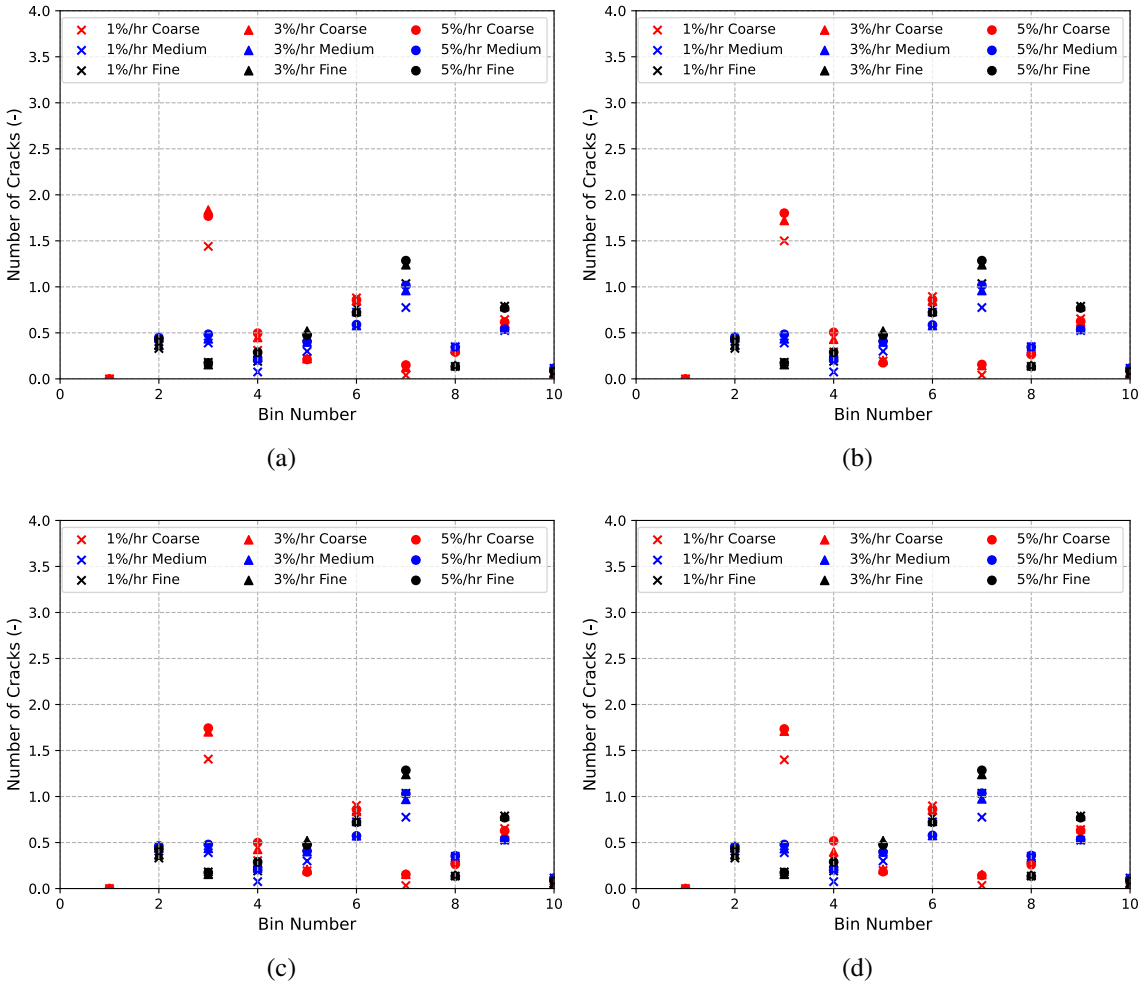

Figure 3.13: The number of cracks per bin at the various burnup levels when the maximum power is 20 kW/m for the volume-weighted Weibull strength randomization criterion. (a) 10 MWd/kgU, (b) 20 MWd/kgU, (c) 30 MWd/kgU, and (d) 40 MWd/kgU. The points correspond to the mean value of all simulations for the respective mesh density and ramp rate.

volume-weighted Weibull case.

When the strength distribution is randomized, it is expected that the locations of the cracks will vary between realizations, but macroscopic measures of the overall extent of cracking should ideally remain relatively constant. To study whether this is the case, distributions of the numbers of cracks in the 10 bins reported by `RadialCrackCounter` are plotted in Figure 3.16 for five randomly-selected realizations from the 200 that were evaluated. These distributions are shown for both the uniform and volume-weighted Weibull

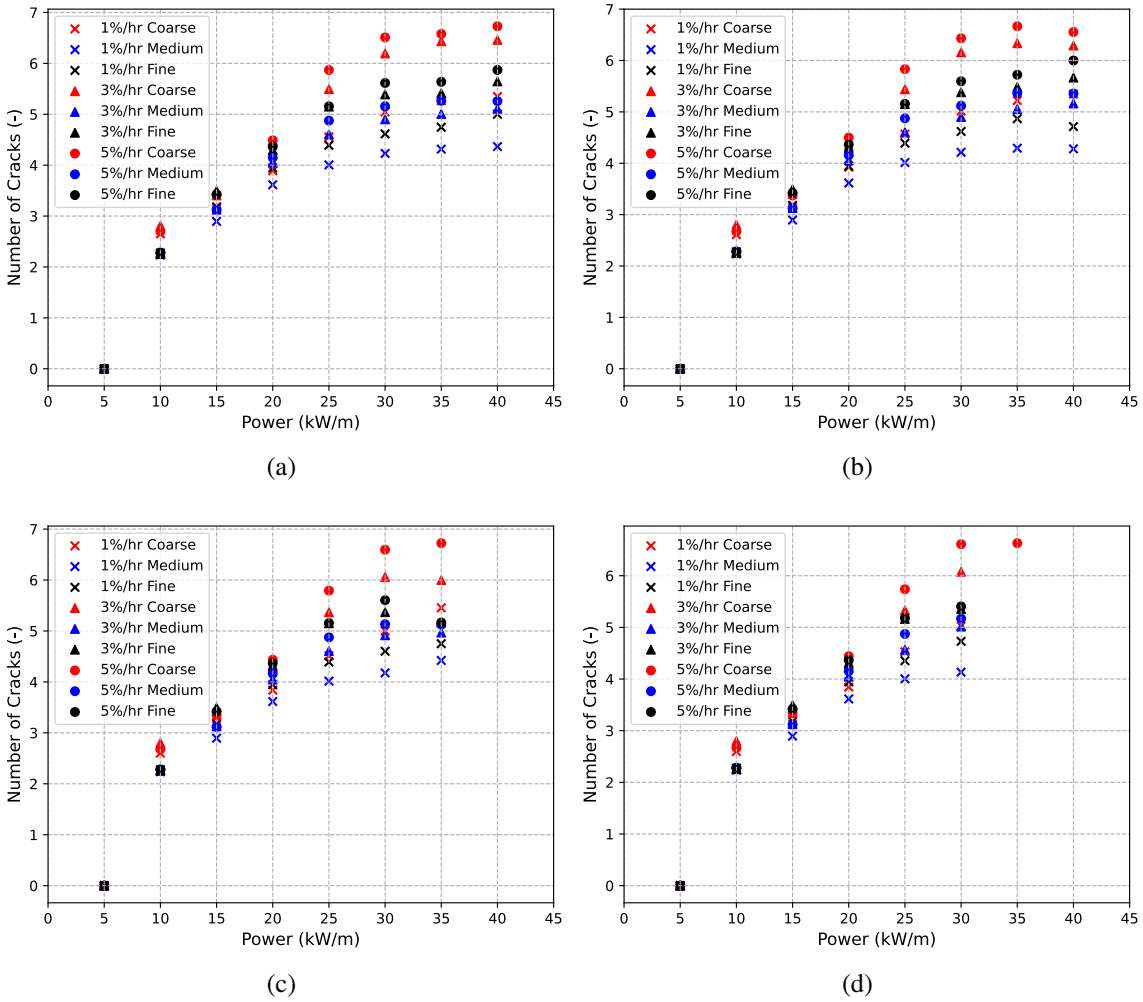

Figure 3.14: Calculated number of cracks as a function burnup for different powers for the volume-weighted Weibull strength randomization criterion. (a) 10 MWd/kgU, (b) 20 MWd/kgU, (c) 30 MWd/kgU, and (d) 40 MWd/kgU. The points correspond to the mean value of all simulations for the respective mesh density and ramp rate.

cases. For these cases, the mesh density was medium with a ramping rate of 3%/hr to a maximum power of 20 kW/m at a burnup of 40 MWd/kgU. As before, it is observed that in the uniform realizations there are a larger concentration of small cracks formed at the pellet periphery when compared to the volume-weighted Weibull results. While there are certainly differences between the individual realizations, the general trends on the total number and sizes of major cracks are fairly consistent across the realizations.

The XFEM used in this work allows for discrete representation of the cracks that form,

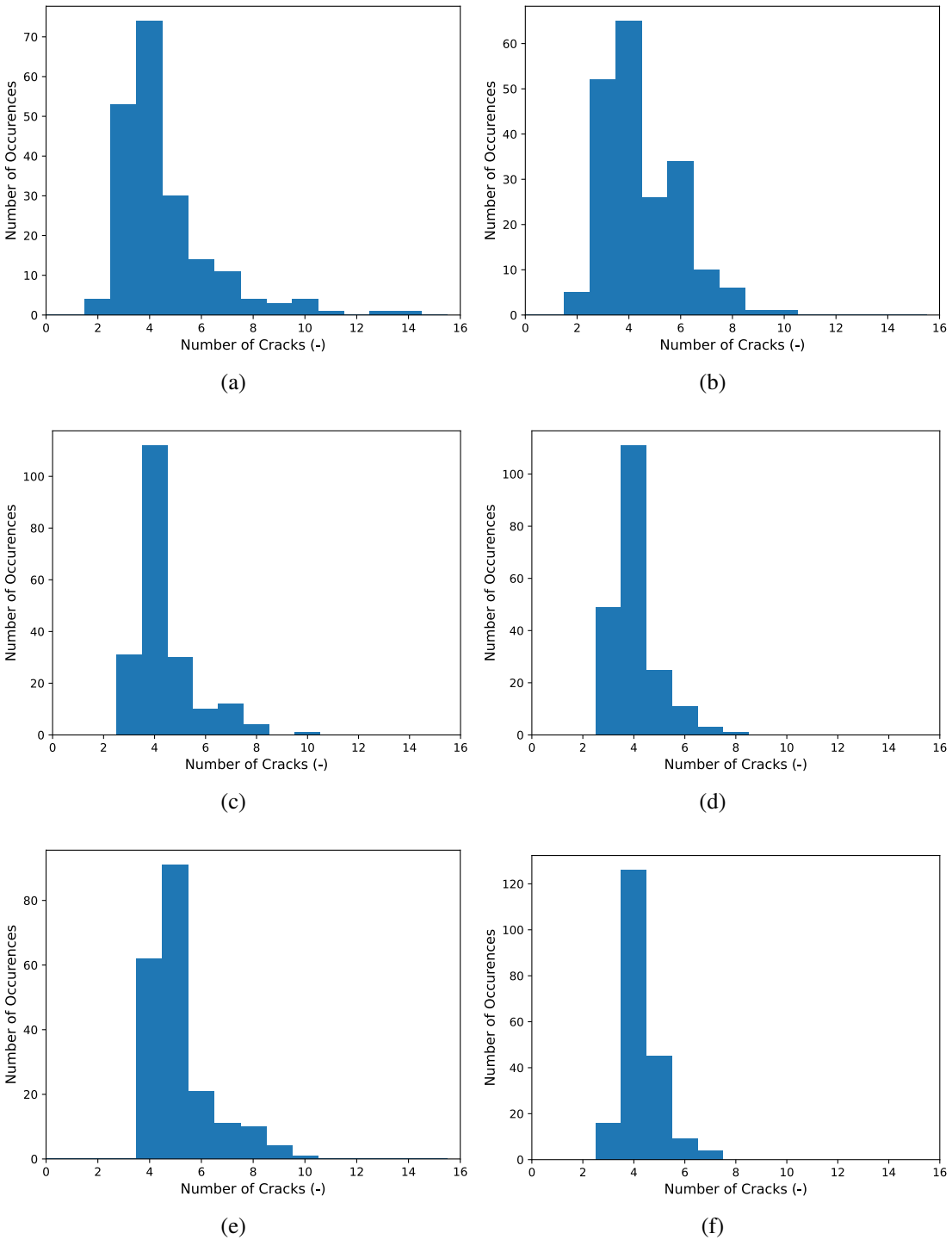

Figure 3.15: Histograms of the number of simulations that calculated a certain number of cracks for (a) uniform coarse, (b) volume-weighted Weibull coarse, (c) uniform medium, (d) volume-weighted Weibull medium, (e) uniform fine, and (f) volume-weighted Weibull fine during rise to power for a maximum power level of 20 kW/m and a 3%/hr ramping rate.

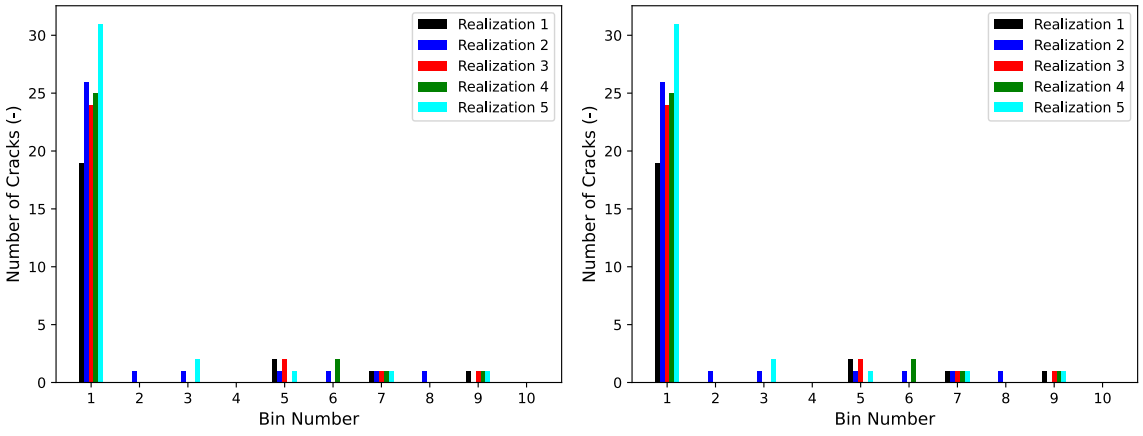

Figure 3.16: Distributions of the crack length output by `RadialCrackCounter` for five selected realizations using the (a) uniform and (b) volume-weighted Weibull strength randomization criteria.

including their location. To further illustrate the consistencies in behavior between random realizations, contour plots of temperature at the rise to power, 20 MWd/kgU, and 40 MWd/kgU burnups using the uniform randomization criterion are presented for the two random realizations presented in Figure 3.7 are provided in Figure 3.17. The plots correspond to the case where maximum power was 20 kW/m, the mesh density was medium, and the ramping rate was 3%/hr. Similar contours are shown for the volume-weighted Weibull distribution in Figure 3.18. The subplots on the left of these figures correspond to the first random realization whereas the right subplots correspond to the second random realization. After rise to power the cracks are readily visible and change location based upon the random seed, although the numbers and lengths of these cracks are consistent between simulations. As irradiation progresses some of the cracks become more difficult to see as gap closure (fuel-to-cladding contact) begins to close the cracks at 20 MWd/kgU. The fuel-to-cladding gap is completely closed at a burnup of 40 MWd/kgU. Crack healing is not included in the analyses completed in this work.

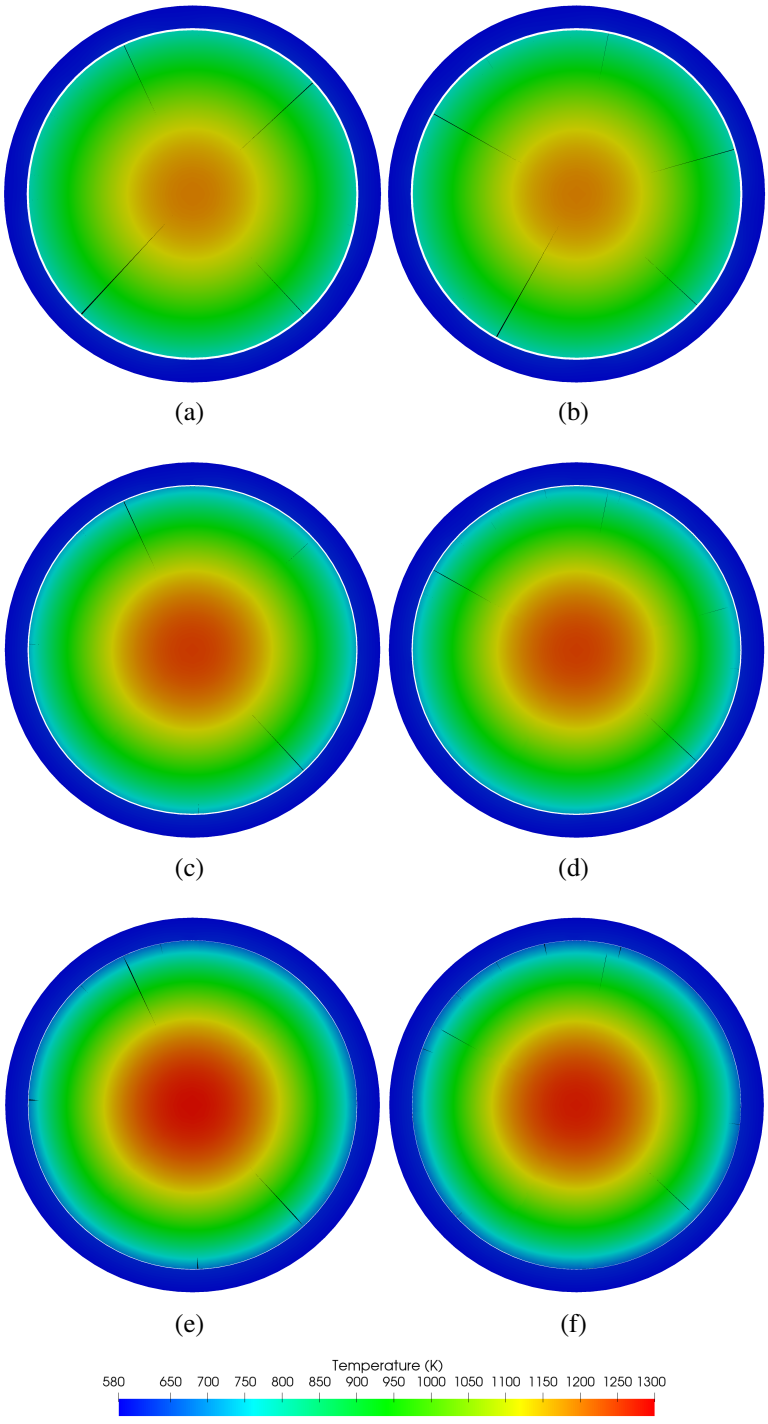

Figure 3.17: Temperature contours illustrating crack locations for two different random realizations (left and right) of strength using the uniform criterion. The top to bottom rows shows at rise to power, 20 MWd/kgU, and 40 MWd/kgU. The mesh density is medium with a maximum power of 20 kW/m and a ramping rate of 3%/hr.

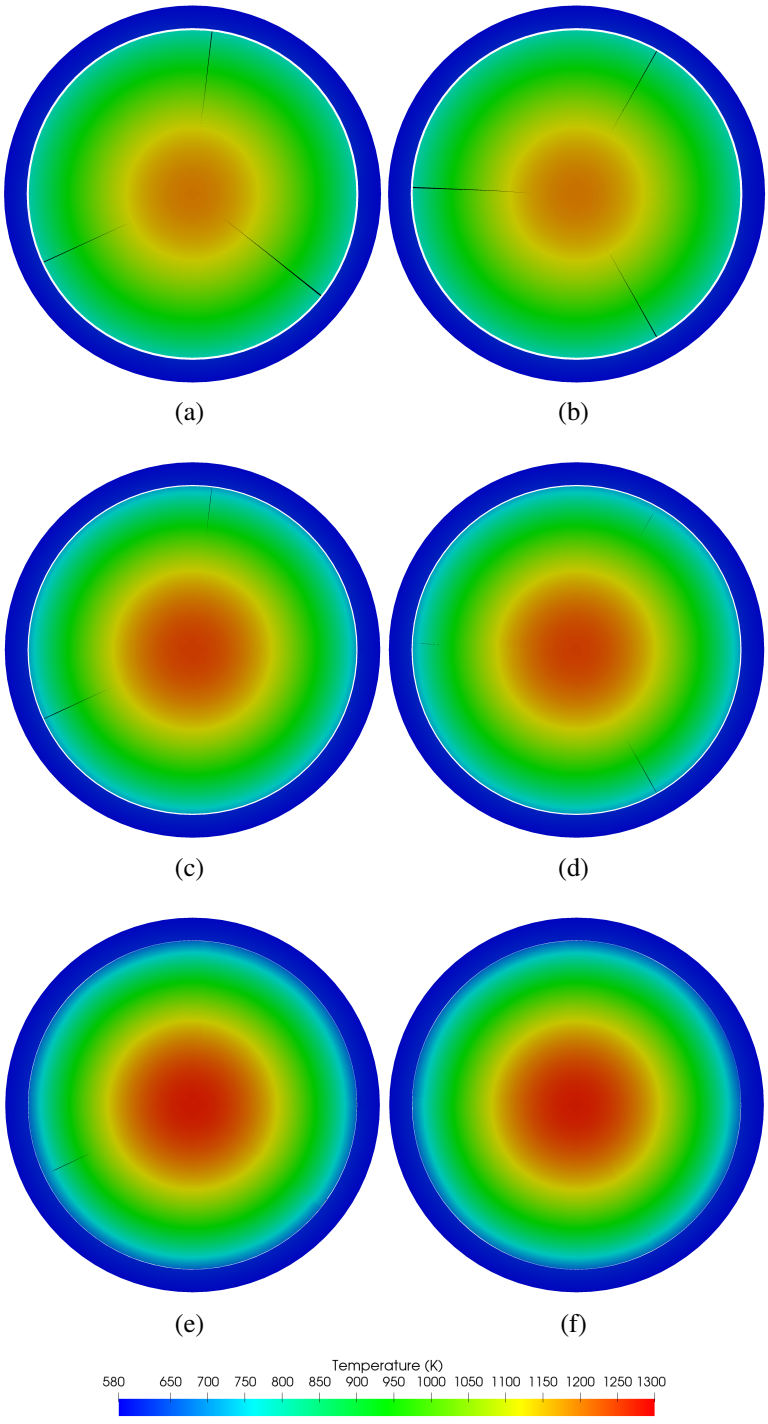

Figure 3.18: Temperature contours illustrating crack locations for two different random realizations (left and right) of strength using the volume-weighted Weibull criterion. The top to bottom rows shows at rise to power, 20 MWd/kgU, and 40 MWd/kgU. The mesh density is medium with a maximum power of 20 kW/m and a ramping rate of 3%/hr.

3.2.4 Comparisons to Empirical Correlations

To determine whether or not the mechanistic approach taken in this study sufficiently matches the empirical correlations presented in Figures 3.2 and 3.3, the correlations are taken to be exact (i.e., no associated uncertainty). This allows the use of a statistical measure known as the normalized Euclidean distance [68]. At each data point, the Euclidean distance is given by:

$$d_i^2 = \frac{\left(P_i - D_i\right)^2}{\sigma_i^2} \tag{3.11}$$

where, in this application, P_i represents the model prediction (mean of the all of the simulations) at a given burnup and power level for a given mesh density, ramp rate, and initial strength randomization criteria; D_i is the value of the respective empirical correlation at that same power level and burnup; and σ_i represents the standard deviation of all the simulations at the given burnup and power level for a particular mesh density, ramp rate, and initial strength randomization criteria. The total normalized Euclidean distance is then calculated via:

$$d_{ne} = \sqrt{\Sigma_{i=1}^{N} d_i^2} \tag{3.12}$$

Finally, the average total normalized Euclidean distance can be determined from:

$$\bar{d}_{ne} = \frac{d_{ne}}{N} \tag{3.13}$$

where N correspond to the total number of power and burnup combinations. In this case, there are 8 power levels and 5 burnup intervals selected, however, there is no standard deviation for all of the 5 kW/m power levels, and the 35 kW/m and 40 kW/m power levels did not reach all 5 of the desired burnup levels, resulting in a total of 32 data points. In this study, the average total normalized Euclidean distance is reported for each mesh density and ramping rate in Tables 3.2 through 3.4 for the Barani, Coindreau et al., and Walton empirical correlations, respectively. In comparisons with the Barani correlation, any D_i values corresponding to a burnup value are taken as the rise to power value since the correlation does not have a burnup dependence. If $\bar{d}_{ne} < 2$, a good agreement between the mechanistic

approach and empirical correlations is achieved. This corresponds to a 95% confidence that the empirical correlation would fall within the uncertainty of the mechanistic calculations. By examining the tables, one sees that, for all three empirical correlations for both uniform and volume-weighted Weibull tensile strength randomization and almost all ramp rates and mesh densities, $\bar{d}_{ne} < 2$. The only exception is the 1%/hr ramping rate with the fine mesh for the Coindreau et al. correlation. It is also observed $\bar{d}_{ne}$ decreases with increasing mesh density for the uniform case whereas $\bar{d}_{ne}$ increases with increasing mesh density for the volume-weighted Weibull case. The raw data used to generate Tables 3.2 through 3.4 are provided in Chapter A. Based upon the findings here, improved confidence can be had on using the empirical correlations for large scale fuel fracture in subsequent calculations of axial relocation.

Table 3.2: The normalized Euclidean distance between the fragmentation study calculations and the Barani et al. [9] empirical correlation.

	Uniform			Weibull		
	1%/hr	3%/hr	5%/hr	1%/hr	3%/hr	5%/hr
Coarse	0.276	1.048	0.189	0.358	0.253	0.223
Medium	0.457	0.364	0.341	0.782	0.601	0.503
Fine	0.318	0.283	0.320	0.797	0.697	0.567

Table 3.3: The normalized Euclidean distance between the fragmentation study calculations and the Coindreau et al. [23] empirical correlation.

	Uniform			Weibull		
	1%/hr	3%/hr	5%/hr	1%/hr	3%/hr	5%/hr
Coarse	0.949	1.325	0.696	1.020	0.876	0.846
Medium	1.199	1.054	0.984	1.881	1.721	1.557
Fine	0.998	0.923	0.940	2.043	1.944	1.896

3.3 Summary

Ceramic nuclear fuels undergo cracking and fragmentation throughout their life in the reactor. Large fragments are formed by thermal gradients within the fuel and fine pulvers may form during a LOCA transient. The focus of this chapter was to examine the large scale

Table 3.4: The normalized Euclidean distance between the fragmentation study calculations and the Walton et al. [125] empirical correlation.

	Uniform			Weibull		
	1%/hr	3%/hr	5%/hr	1%/hr	3%/hr	5%/hr
Coarse	0.679	0.978	0.476	0.716	0.609	0.588
Medium	0.834	0.728	0.662	1.325	1.222	1.112
Fine	0.674	0.598	0.582	1.428	1.344	1.351

radial cracking in nuclear fuels during normal operation. These large fragments correspond to a large amount of the fuel present for subsequent fuel movement during a transient (see Chapter 4). In the literature, a handful of empirical correlations exist to compute the number of radial cracks that would be expected to form for a given maximum fuel power and burnup. A mechanistic approach using the XFEM was used to include the effects of tensile strength randomization, ramping rates and finite element mesh density to see if the empirical correlations accurately capture these effects despite not directly having terms in the equations to account for them. It was found through the mechanistic analysis that given all of the effects that influence large scale cracking in UO_2 that the empirical correlations are within the uncertainty of the mechanistic model predictions. This gives confidence that when the number of large scale cracks (fragments) are needed when computing how the fuel will relocate during a LOCA the empirical correlations are sufficient at this time. It is recommended that the volume-weighted Weibull distribution be used when randomizing the material strength. In order to reduce the uncertainty in the fracture predictions, manufacturers have to figure out ways to more reliably create fuels with consistent tensile strengths. Unfortunately, ceramics have inherent local flaws that form during manufacture that will likely give rise to local cracking. No two pellets will crack identically as the process is thereby stochastic. On average, however, the number of cracks can be estimated.

CHAPTER 4

FUEL AXIAL RELOCATION

A subset of this chapter is under review for publication in the Nuclear Engineering and Design. Some other details in this chapter have also been briefly summarized in a published Journal of Nuclear Materials [80] article. The author of this dissertation is also a co-author on the Journal of Nuclear Materials publication and relevant details are reproduced here.

4.1 LITERATURE REVIEW

Once the fuel pellets have fragmented or pulverized, there is the possibility that the fuel particles will axially relocate into the distended (ballooned) regions of the rod resulting in a redistribution of the heat load. This axial movement has been observed experimentally as shown Figure 1.2c. A key point is that the extent of axial relocation of the fuel depends upon the size of the fragments that form as well as the extent of cladding distention that occurs. It should be noted that at the top of a fuel rod(let) many times there remains a fuel plug above the the voided region due to being sufficiently restrained by the cladding at this location.

Limited models have been proposed in the literature to predict this phenomenon of axial fuel relocation. An early model proposed by Siefken [99] examined two experimental LOCA test series completed at the Power Burst Facility (PBF) at INL and the FR2 reactor at the German research center Kernforchungszentrum Karlsruhe. Based upon the results of the experiments it was proposed that relocation of fuel into a crumbled state occurs if the void fraction at a particular axial elevation exceeded a critical value of 0.30 where the void

fraction at an axial elevation z is calculated by:

$$\alpha_z = 1 - \frac{V_{fz}}{V_{cz}} \tag{4.1}$$

where α_z is the void fraction, V_{fz} is the volume of the fuel per unit length (m^3/m), and V_{cz} is the internal volume of the rod per unit length (m^3/m) given by:

$$V_{cz} = \frac{\pi D_{ciz}^2}{4} \tag{4.2}$$

where D_{ciz} is the inner cladding diameter at an elevation z (m). If the fuel has crumbled in a particular region, the volume of fuel is determined by analysis of the experimental data. If the fuel has not crumbled, the volume is simply $V_{fz} = \pi R_p^2$, where R_p is the as-fabricated fuel radius (m). Then by solving a one-dimensional representation (in the radial direction) of the heat transfer from the fuel rod the effect of fuel relocation on the cladding surface temperature in the crumbled regions is given by:

$$2\pi R_{co}\left(1+\epsilon_{hoop}\right) h \left(T_{surf} - T_{sat}\right) = \pi R_{co}^2 \left(1+\epsilon_{hoop}\right)^2 (1-\alpha)\, q''' \tag{4.3}$$

where R_{co} is the initial outer radius of the cladding (mm), ϵ_{hoop} is the cladding hoop strain, h is the cladding surface heat transfer coefficient (W/m^2-K), T_{surf} is the cladding surface temperature (K), T_{sat} is the saturation temperature of steam (K), α is the void fraction of crumbled fuel (= 0.30), and q''' is the volumetric heat generation in the fuel (W/m^3). Siefken's model provides no quantification of the size of the fuel fragments which is important for fuel dispersal calculations. In addition, the void fraction threshold was based upon the average of all the experiments analyzed where the maximum burnup achieved was only 35 MWd/kgU, which limits the models applicability to the higher burnups of interest for burnup extension by industry (68 to 75 MWd/kgU).

Building upon the knowledge gained over approximately 30 years since the previous axial relocation model Jernkivst and Massih [53] proposed a model to wrap around the fuel performance code FRAPTRAN-1.5. The model tracks the size of fragments and pulvers (i.e., fine fragments) as well as the redistribution of mass and heat load within the rod. Since

FRAPTRAN-1.5 uses a 1.5D (Layered1D) representation of the fuel rod it already contains distinct axial layers to which the axial relocation algorithm can be applied. This model as described below was implemented into Bison before being extended to a Layered2D framework (see Section 4.3).

The amount of fuel relocation strongly depends upon the size of the fuel particles. To address this, Jernkvist and Massih use a binary system that includes larger particles, denoted as fragments, and small particles denoted as pulvers. The amount of fuel in a particular axial layer that is pulverized is calculated first using the pulverization threshold proposed by [120] illustrated in Figure 3.4. Jernkvist and Massih argue that even if the pulverization threshold is exceeded, it will not occur if the contact pressure between the fuel and cladding is > 50 MPa. It is assumed that pulvers are octahedral in shape with a characteristic side length (l_p) of 100 μm (a user input). The number of fragments are calculated using either the Walton and Matheson [125], Coindreau et al. [23], or Barani et al. [9] correlations described in Chapter 3. Once the number of fragments are known their characteristic length is then calculated by:

$$l_f = D_{FP} \min\left(1, \frac{\pi}{n_f}\right) \tag{4.4}$$

where D_{FP} is the as-fabricated diameter (m) of the fuel pellet. Once the volume of pulverized fuel is known in a layer, the mass fraction of pulverized fuel (x_p) can be calculated knowing the total volume of fuel in the layer. The mass fraction of fragments is then simply given by $x_f = 1.0 - x_p$. Once the mass fraction of pulvers and fragments are known, Jernkvist and Massih propose that an effective packing fraction of the binary system can be determined using the methodology proposed by Westman [128]. Using this methodology the effective packing fraction (ϕ) is determined using an internal Newton iteration scheme to solve the following equation:

$$a^2 + 2Gab + b^2 = 1.0 \tag{4.5}$$

where

$$a = \frac{\phi_p \left(\phi_f - x_f \phi\right)}{\phi \phi_f} \tag{4.6a}$$

$$b = \frac{\phi_p \phi_f - \phi \phi_f \left(x_p + x_f \phi_p\right)}{\phi \phi_p \left(1 - \phi_f\right)} \tag{4.6b}$$

and G is a parameter (dimensionless) that depends upon the difference in shape between the fragments and pulvers. In the preceding equations a and b are dimensionless parameters, and ϕ_f and ϕ_p represent the packing fraction (dimensionless) if the crumbled bed of fuel particles was entirely made up of fragments or pulvers respectively. Jernkvist and Massih suggest values of $\phi_f = 0.69$ and $\phi_p = 0.72$. The G parameter is calculated by:

$$G = \begin{cases} 0.738 \left(D_p^p / D_p^f\right)^{-1.566}, & D_p^p / D_p^f \leq 0.824 \\ 1.0, & D_p^p / D_p^f > 0.824 \end{cases} \tag{4.7}$$

where D_p^p and D_p^f are the equivalent packing diameters (m) of the pulvers and fragments, respectively. The equivalent packing diameter is determined via:

$$D_p = \left(3.9431 - \frac{4.5684}{\psi} + \frac{1.8660}{\psi^2}\right) V_p^{1/3} \tag{4.8}$$

where ψ is the sphericity (dimensionless) of the particle and V_p is the volume (m^3) of the particle. In this model fragments are assumed to be prismatic in shape and pulvers octahedral in shape. For a prismatic particle (fragments) whose height is equal to its characteristic side length, $\psi = 0.716$ and $V_p = 0.4330 l_f^3$. For octahedral particles (pulvers), $\psi = 0.846$ and $V_p = 0.4714 l_p^3$ (see Appendix B) for the derivation of the sphericity and volume equations for prismatic and octahedral particles.

Once the effective packing fraction of the crumbled fuel is known, the relocation of the fuel as well as its influence on heat load can be determined. Since the model was initially developed for FRAPTRAN-1.5 the axial slices inherent to the 1.5D assumption provide a convenient way to keep track of mass and heat load redistribution. Assuming the layers are indexed by k (starting from the bottom of the rod) and there are N layers, the condition on

collapse of the fuel in a given layer is:

$$m_k^M > m_k^i \tag{4.9}$$

where m_k^i is the initial as-fabricated fuel mass (kg) in the layer and m_k^M represents the mass (kg) in the layer if it is completely filled with crumbled fuel:

$$m_k^M = \phi_k \rho_f \pi L_k R_{cik}^2 \tag{4.10}$$

where ϕ_k (unitless) is the effective packing fraction in the layer, ρ_f is the density of the fuel (kg/m^3), L_k is the height of the layer (m), and R_{cik} is the cladding inner radius for the layer (m). Two constraints are applied to prevent unrealistic phenomena from occurring. First, relocation can only occur in the downward direction, and second, the amount of fuel that can relocate into a layer is limited by the available mass of fuel existing in all layers above it. These lower (m_k^L) and upper (m_k^U) constraints can be cast into the following equations:

$$m_k^L = \sum_{j=1}^{k} m_j^o - \sum_{j=1}^{k-1} m_j \tag{4.11a}$$

$$m_k^U = m_k^r + \sum_{j=1}^{k} m_j^o - \sum_{j=1}^{k-1} m_j \tag{4.11b}$$

where m_j^o represents the mass (kg) in the j:th layer at the beginning of the timestep (t_o) and m_k^r represents the available mass (kg) to be relocated into the k:th layer. Two additional constraints are placed on the movement of mass in Jernkvist and Massih's model: (1) a residual amount of the initial fuel mass will remain in the layer throughout the simulation (denoted by x^r with a default value of 0.01) and (2) the fuel-to-cladding gap must be large enough to accommodate fuel movement (denoted by g^{th} with a default value of 0.2 mm). The algorithm is divided into two loops with the first beginning at the top layer and moving downwards to determine the amount of available mass to be relocated in each layer followed by a loop from the bottom layer to the top that enforces the upper and lower constraints while relocating the mass to the appropriate layers. The loops are illustrated in Figure 4.1 and Figure 4.2.

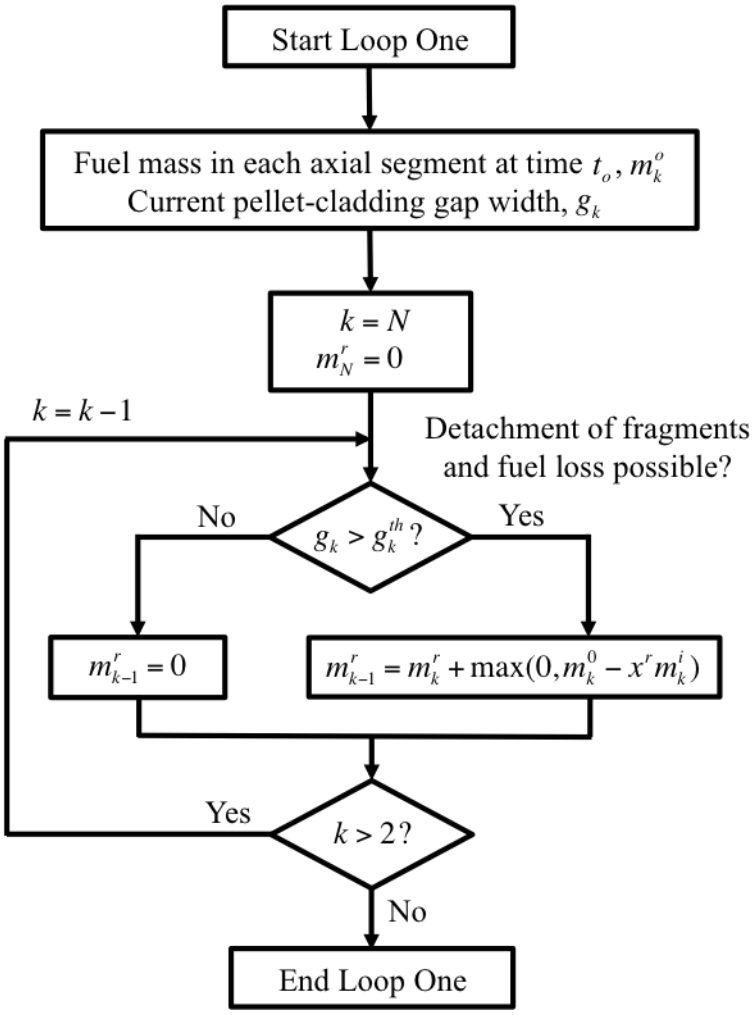

Figure 4.1: The first loop of the axial relocation algorithm which determines the amount of relocatable mass m^r that can be accommodated in each layer. Adapted from [53].

In layers that are crumbled and have accommodated additional fuel the effective thermal conductivity of the fuel and gaseous mixture (i.e., gas from the fuel-to-cladding gap migrates into the voids because the effective packing fraction is < 1.0) needs to be calculated. The model used by Jernkvist and Massih is that of Chiew and Glandt [21]. The correlation is given by:

$$k_{eff} = \frac{(1-\beta)}{(1+2\beta)(1-\beta\phi)} \left(1 + 2\beta\phi + \left(K_2 - 3\beta^2\right)\phi^2\right) k_f \tag{4.12}$$

where β is the reduced thermal polarizability (unitless), k_f is the thermal conductivity of the fuel (W/m-K), ϕ is the effective packing fraction (unitless), and K_2 is a function of β

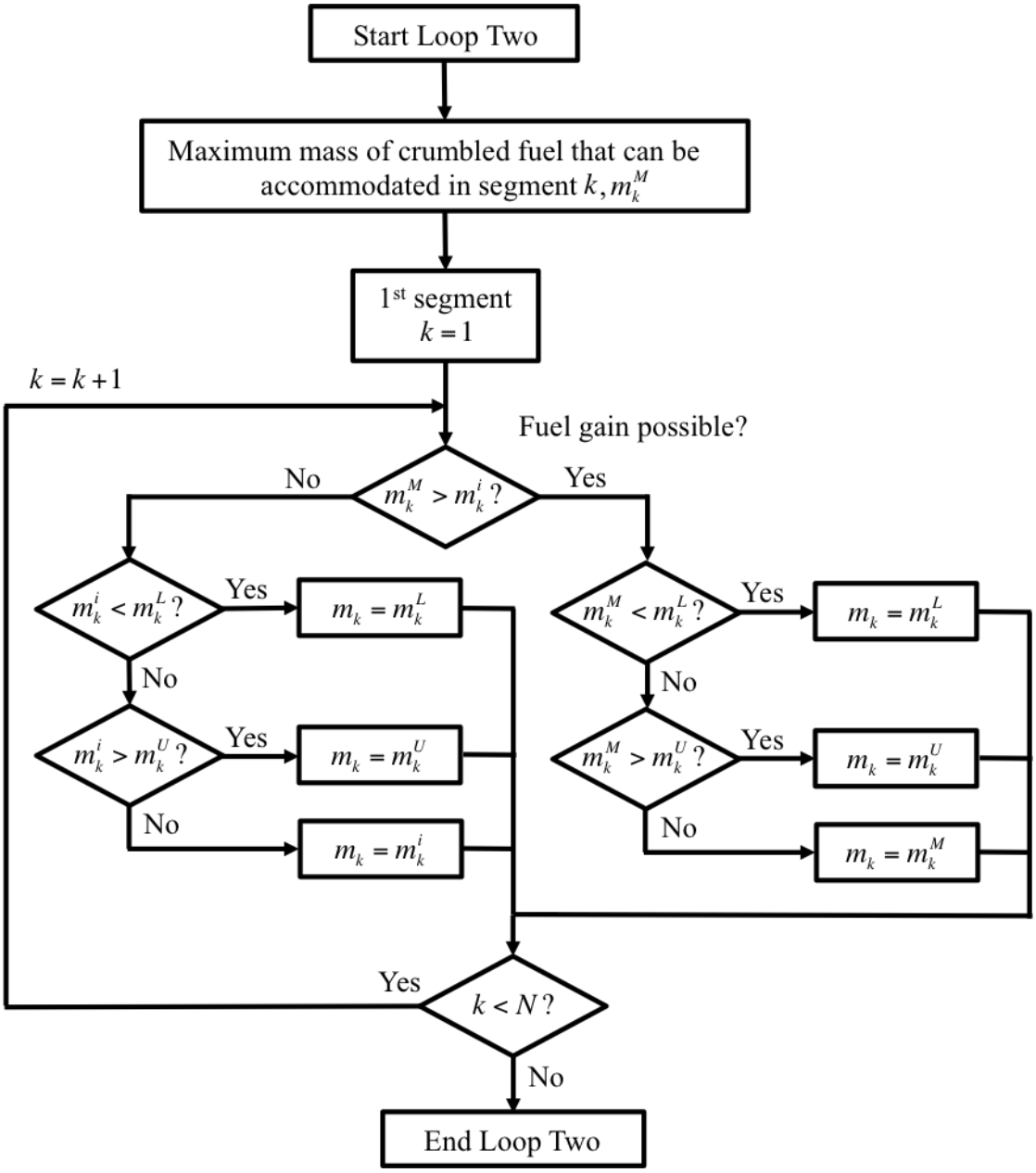

Figure 4.2: The second loop of the axial relocation algorithm that enforces the constraints and moves the mass to the appropriate layers. Adapted from [53].

and ϕ defined later. The reduced thermal polarizability is given by:

$$\beta = \frac{k_f - k_g}{k_f + 2k_g} \tag{4.13}$$

where k_g is the thermal conductivity of the gas (W/m-K) surrounding the crumbled fuel

particles. The K_2 function is approximated by:

$$K_2(\beta, \phi) = K_2^{(0)}(\beta) + K_2^{(1)}(\beta)\,\phi \tag{4.14}$$

where Jernkvist and Massih [53] used best fit approximations to the tabulated values of Chiew and Glandt [21] to obtain:

$$K_2^{(0)}(\beta) = 1.7383\beta^3 + 2.8796\beta^2 - 0.11604\beta \tag{4.15a}$$

$$K_2^{(1)}(\beta) = 2.8341\beta^3 - 0.13455\beta^2 - 0.27858\beta \tag{4.15b}$$

This effective thermal conductivity is used in the modified version of the heat conduction equation described below for layers that have accommodated additional fuel. In layers that are partially or completely void of fuel, the unmodified fuel thermal conductivity is used.

The relocation of fuel throughout the rod during the LOCA transient results in a re-distribution of the energy generation. In a 1.5D representation only the radial direction is of great importance in the heat conduction equation. The modified heat conduction in the radial equation is given by:

$$\phi\rho_f c_{pf}\frac{\partial T}{\partial t} - \frac{1}{r'}\frac{\partial}{\partial r'}\left(k_{eff}\, r'\frac{\partial T}{\partial r'}\right) = \phi q''' \tag{4.16}$$

where c_{pf} is the specific heat of the fuel (J/kg-K). Care must be taken to ensure that in layers where the fuel is crumbled that the outer radius of the fuel is moved outward towards the cladding to take into account the increase in effective diameter of the porous bed of fuel fragments. In the model, Jernkvist and Massih assume that a residual fuel-to-cladding gap (g^r which is a model parameter) remains in the crumbled layers (illustrated in Figure 4.3 adapted from [53]). In layers partially or completely void of fuel the original radial position is used along with k_f instead of k_{eff}.

A recently proposed model by [63] uses the DEM method to model fuel relocation in three-dimensions. This is an interesting approach to be considered in future work when explicitly modeling fuel dispersal outside of the rupture openings that would be predicted by the model proposed in Chapter 6 of this dissertation.

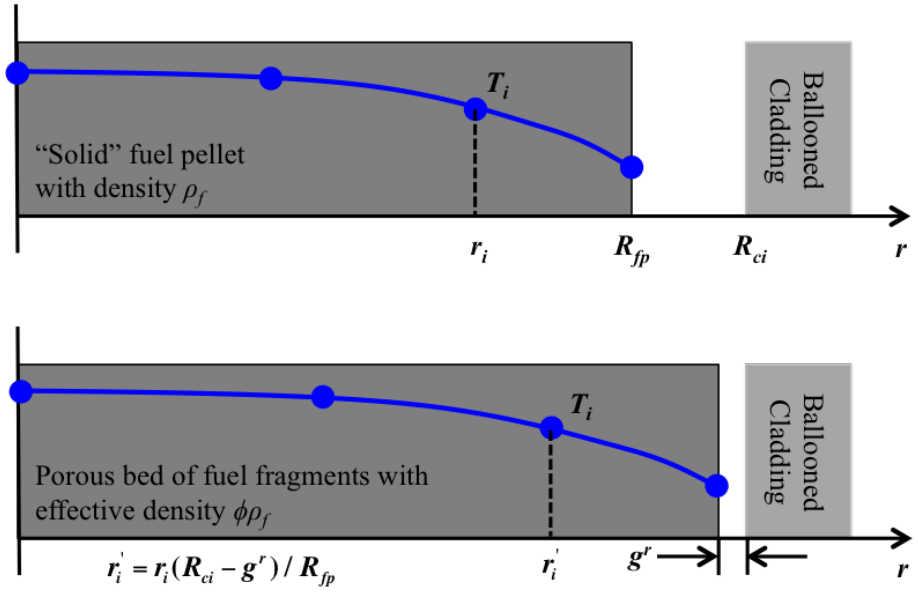

Figure 4.3: Change in fuel geometry and effective fuel density following fuel pellet collapse in the ballooned region of the cladding. A residual gap g^r is assumed to remain.

4.2 THE LAYERED2D FRAMEWORK

The Jernkvist and Massih axial relocation model provides a solid foundation for axial relocation fuel modeling. The original development based upon a Layered1D framework allows for easy tracking of the mass in each of the discrete layers. Unfortunately, during LOCA conditions the thermal degradation on the waterside surface of the cladding is usually non-uniform in the azimuthal direction which the Layered1D formulation formulation cannot capture due to its axisymmetric assumption. Thus, when extending the axial relocation model to two dimensions including azimuthal effects is of great importance. This importance eliminates the possibility of extending the model to 2D axisymmetric simulations due to the inherent symmetry and the lack of discrete layers to account for the mass movement. Moreover, as the number of layers increase in a Layered1D analysis the results approach that of a 2D axisymmetric simulation. To overcome these deficiencies of extending the model to the 2D-RZ formulation a new 2D framework called Layered2D has been developed.

4.2.1 THEORY

This framework, like the Layered1D framework, models the fuel rod with a number of discrete axial slices. The difference being each layer is represented by a 2D slice containing a fuel disc, gas gap ring, and a cladding ring. Figure 4.4 illustrates the 2D formulation. The left figure shows the axial discretization of the rod which is similar to the Layered1D discretization except azimuthally symmetry is not assumed (i.e., symmetry is not assumed at the rod centerline). The right figure provides a top view of a single axial slice (highlighted in red in the left figure). The thermo-mechanics of each axial layer is solved as a separate generalized plane strain calculation with global parameters such as fission gas release, rod internal pressure, and axial (out-of-plane) strain being coupled between the layers to allow predictions of these global rod parameters as well as others including fuel and cladding elongation.

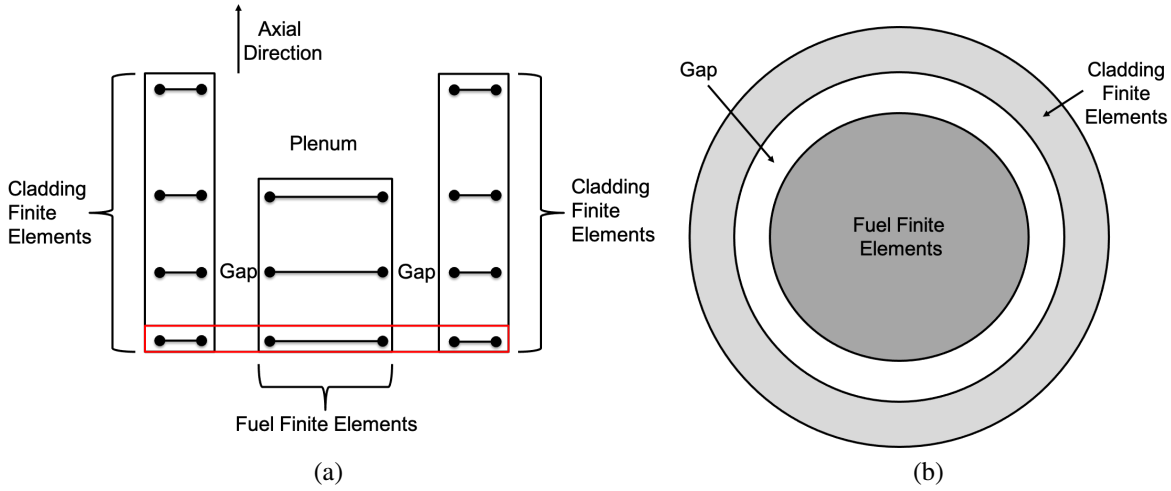

Figure 4.4: Schematic describing the Layered2D formulation. The axial discretization of the fuel rod including fuel gap and cladding elements where azimuthal symmetry is not guaranteed (left). The top view an axial slice with fuel, gap and cladding shown.

4.2.2 GENERALIZED PLANE STRAIN

Since the Layered2D framework uses distinct axial slices to represent the fuel rod, communication between the layers and computation of axial material behaviors (e.g., thermal

expansion, fuel swelling, cladding irradiation growth) is achieved through the use of generalized plane strain equations. Traditional plane strain analyses are used for infinitely thick specimens represented by a single axial slices. It is assumed that the strain in the out-of-plane (normal) direction is zero. In generalized plane strain a non-zero strain is permitted. In each layer the equilibrium conditions for this out-of-plane stress is given by:

$$\int_A \sigma_{zz} dA = \bar{N}_{zz} \tag{4.17}$$

where σ_{zz} is the axial stress, A is the area of the slice, and $\bar{N}_{zz}$ is an applied force or integrated stress. The fuel and cladding have an independent out-of-plane stress in each layer.

4.2.3 Out-of-Plane Pressure

The nature of the Layered2D formulation results in the inability to model end caps of fuel rods. Therefore, since the fuel rod is modeled as an open tube of cladding containing fuel, an out-of-plane pressure must be applied to the fuel and cladding to properly account for the plenum pressure. This out-of-plane pressure is the same as used in the fuel fragmentation models in Chapter 3. For the fuel the out-of-plane pressure is simply given by the plenum pressure. For the cladding an additional axial pressure is given by Equation 3.10.

4.2.4 Mesh Generation

One of the selling points of the MOOSE framework and the therefore Bison is that they are free to use. However, when analyzing complicated geometries and scenarios external meshing tools may be required. To improve the user experience when using the Layered2D framework, an internal meshing capability in Bison was created to avoid the need for a third party meshing tool. When it comes to the Layered2D framework, it is desired that users are able to use it within Bison without the need of an external meshing software. Figure 4.5 provides some examples of the various combinations of features available in the internal Layered2D mesh generator. One can include pellets of different outer radii, missing pellet surfaces, annular pellets, coatings on the cladding, and encapsulate the fuel rod within a

capsule (typically used in experiments). The development of the mesh generator allows geometeric dimensions necessary in some material and behavior models for nuclear fuel performance analysis to be read directly from the mesh.

4.2.5 Implementation Testing

For any capability in Bison, a set of regression test cases are used to ensure that models are correctly implemented and that future modifications to the code do not adversely affect existing functionality. As the Layered2D framework was developed, a set of test cases, described here, were developed to test proper implementation. In particular, these tests are used to confirm that the set of global or layer-specific parameters that are are required when analyzing fuel performance using the Layered2D methodology are computed correctly. These include internal volume, layered internal volume, layered integral, layered side average, and layered side flux integral, layered extreme value, and layered plenum temperature. Details of sample calculations for these specific parameters are shown in the following subsections. An additional analysis evaluates the adequacy of the thermal solution radially through the Layered2D mesh for both a symmetric and an eccentric configuration. This verifies correct connectivity in the meshes created by the internal meshing algorithm described in Section 4.2.4.

Since the Layered2D framework uses the finite element method, the calculation accuracy is subject to the mesh density. In particular, the representation of circular geometries is particularly prone to loss of accuracy if there is an insufficient number of elements along the boundary of the circle. Increasing the finite element order from QUAD4 to QUAD8 can help increase the accuracy without the use of additional elements. The mesh generation tool allows the user to change the number of azimuthal and radial elements along circular boundaries and layer thicknesses, respectively. For ease of implementation, the selection of azimuthal elements is held constant amongst the concentric rings. In the regression testing, several different mesh densities are used for each test case. The number of elements for az-

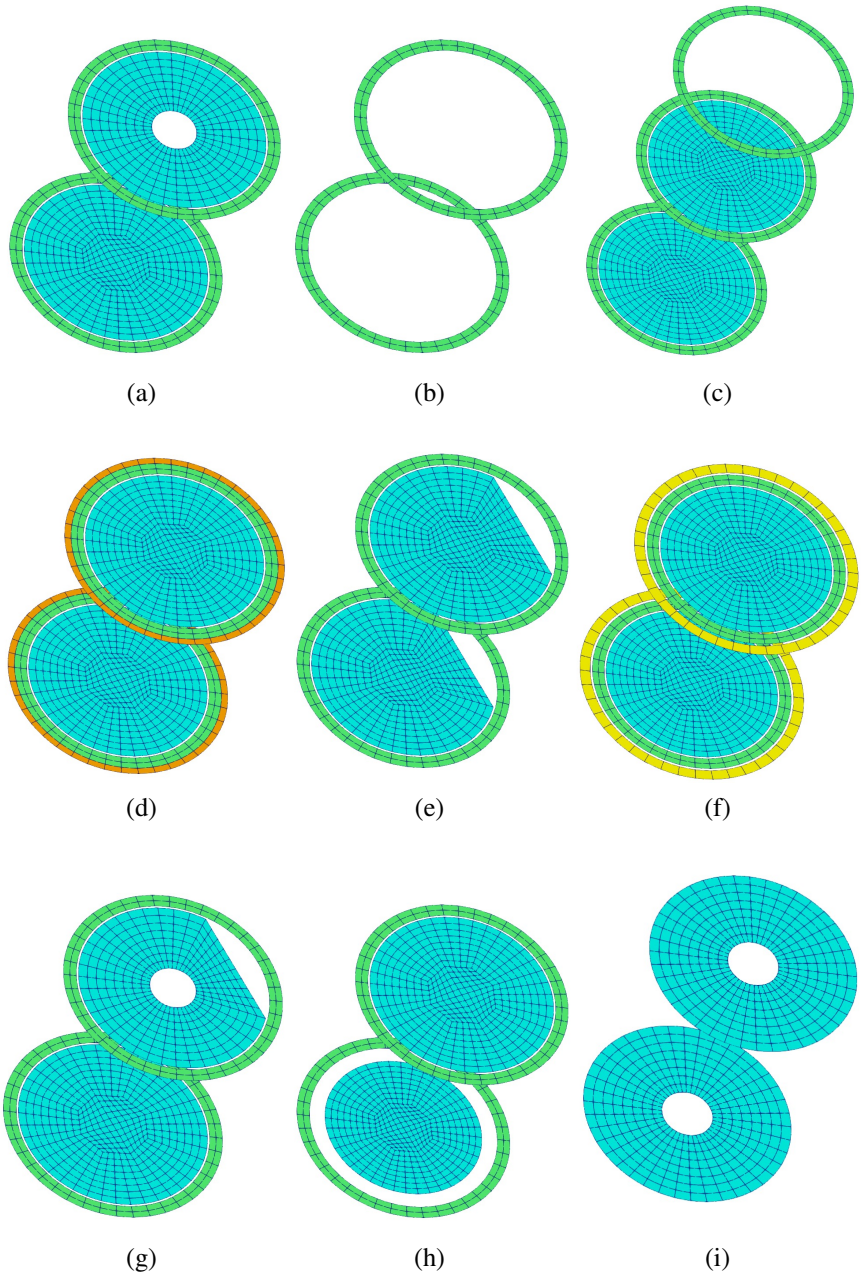

Figure 4.5: Examples of meshes using the Layered2D mesh generator. The different blocks are colored as follows: fuel (cyan), cladding (green), coating (orange), and capsule (yellow). (a) One solid and one annular fuel layer with cladding, (b) cladding only, (c) solid fuel with cladding and a plenum, (d) fuel with a coated cladding, (e) fuel containing a missing pellet surface (MPS) with cladding, (f) fuel with cladding inside of a capsule, (g) one solid fuel layer and one annular fuel layer containing a MPS, with cladding, (h) two solid fuel layers of different diameters with cladding, (i) two annular fuel layers without cladding.

imuthal, radial, fuel, and cladding, in addition to the element type, and the total number of finite elements in the fuel and cladding, are provided in Table 4.1. Each mesh contains one fuel and cladding layer plus a layer representing the plenum containing only a cladding ring. The outer fuel diameter is taken as 8.2 mm with a fuel-to-clad diametrical gap of 160 μm, and a cladding thickness of 0.57 mm. These dimensions are typical radial dimensions of a pressurized-water reactor (PWR) fuel rod. The fuel and cladding layer is assumed to have an out-of-plane thickness of 10 mm and the cladding-only plenum layer has an out-of-plane thickness of 2 mm. These out-of-plane values were arbitrarily chosen for the regression tests.

Table 4.1: Meshes used as part of the mesh sensitivity for the regression tests.

Mesh ID	Element Type	Radial Elements within Fuel	Radial Elements within Cladding	Azimuthal Elements	Total Elements within Fuel	Total Elements within Cladding
1	QUAD4	10	2	16	80	64
2	QUAD4	12	2	32	192	128
3	QUAD4	16	4	64	512	512
4	QUAD4	24	4	128	1536	1024
5	QUAD8	10	2	16	80	64
6	QUAD8	12	2	32	192	128
7	QUAD8	16	4	64	512	512
8	QUAD8	24	4	128	1536	1024

TOTAL INTERNAL VOLUME

Correct computation of the total internal volume between the fuel and cladding, including the plenum region, when using a Layered2D representation of the fuel rod is important to properly determine the rod internal pressure, which impacts other fuel performance metrics of interest. This volume corresponds to the total internal volumes represented by all layers in the mesh. The test case for internal volume simulates a total time of 2 seconds in which the fuel radius is displaced by 45 μm and an axial strain of 0.02 is applied to the fuel and to the upper cladding slice. Based upon the initial dimensions of the fuel, the calculated initial

internal volume is 0.1306 cm^3. After applying the described displacements and strains, the internal volume is analytically determined to be 0.1117 cm^3. The Bison simulation results for the eight different meshes are cataloged in Table 4.2 alongside the analytical solution. With increasing numbers of azimuthal elements for the QUAD4 meshes, the calculated results approach the analytical solution. For the QUAD8 meshes, even the coarsest mesh analyzed results in the correct solution because introducing mid-side nodes on the elements allows for improved capturing of the curvature of the geometry. As would be expected, no mesh dependence is observed with the increasing radial mesh density in the cladding.

INTERNAL VOLUME PER FUELED LAYER

In some analyses (i.e., axial fuel relocation) of nuclear fuel, only the internal volume for layers containing fuel needs to be known. To demonstrate proper implementation of the code object that calculates the layered internal volume in Layered2D, the same regression test scenario as described in Section 4.2.5 can be considered. Since there is only one layer containing fuel and cladding for the meshes used in this section, a single value for the layered internal volume is calculated. The initial internal volume of this layer is based upon the initial dimensions of the mesh which is 0.002081 cm^3. The analytical layered internal volume after applying the described displacements and strains is calculated to be -3.1391×10^{-4} by subtracting the calculated volume of the fuel from the cladding interior volume. A negative value indicates that the fuel for the layer is greater than the volume of the space within cladding inner diameter. This is a valid scenario and typically occurs when the axial strain in the fuel is much larger than that in the cladding. In this situation, within a layer, an axial strain of 0.02 and 0.0 were applied to the fuel and cladding, respectively. The Bison simulation results for the eight different meshes are tabulated in Table 4.2 alongside the analytical solution. Trends identical to those observed in Section 4.2.5 are seen here.

LAYERED INTEGRAL

The layered integral object calculates the volume integral for a variable on specified layers. To illustrate proper implementation of the layered integral calculation inside the Layered2D framework, constant temperatures of 300 K and 600 K are applied to the upper and lower cladding slices, respectively. The fuel present in the meshes analyzed does not play a role in the calculation here. Analytically, the integral ($\int TdV$) is equal to 4.7943×10^{-5} Km^3 and 1.9189×10^{-5} Km^3 for the lower and upper cladding layers, respectively. The results are in agreement with the internal volume scenario in which the Bison simulations achieve the analytical solution due to increasing mesh density and higher order elements. The results are shown in Table 4.2.

LAYERED SIDE AVERAGE VALUE

The layered side average object computes the average value of a variable, while taking into account the original out-of-plane thickness of the layers, on a boundary. The temperature boundary conditions applied in Section 4.2.5 are used in this case as well. The analytical side average value of the temperature over the exterior boundary of the cladding is 350 K. It is observed that no radial or azimuthal dependence on mesh density occurs (see Table 4.2). This is expected when computing averages as the term that is dependent on the mesh (i.e., the surface area) cancels out from the numerator and denominator in the calculation of the average.

LAYERED SIDE FLUX INTEGRAL

The layered side flux integral object computes the total flux through a boundary in a Layered2D analysis by accounting for the out-of-plane thickness of the layers. For this regression test simple radial heat transfer was considered. The heat flux through the exterior of the fuel is equal and opposite to the flux into cladding (due to the normals to the surfaces).

The gap between the surface is assumed to be helium with a thermal conductivity given by:

$$k_{gap}\left(T_{avg}\right) = 0.639T_{avg}^{0.7085} \tag{4.18}$$

where T_{avg} is the average temperature in the gap. This is simply computed as the average temperature of the two surrounding surfaces. In this test the fuel exterior temperature is set to 600 K, and the cladding exterior surface is fixed at 300 K. Both the fuel and cladding are assumed to have a very high thermal conductivity, which results in temperatures of 600 K and 300 K at the fuel exterior and the cladding interior surfaces, respectively. This results in T_{avg}= 450 K. By using this average temperature in Equation 4.18 one obtains a gap conductivity of 0.2 W/m-K. The flux across the gap is computed using cylindrical coordinates through:

$$\phi = \left(T_{fuel} - T_{clad}\right)\frac{k_{gap}}{r\ln\left(\frac{r_f}{r_{ci}}\right)} \tag{4.19}$$

where T_{fuel} and T_{clad} are the fuel and cladding surface temperatures, r is the radial position within the gap, r_f is the fuel radius, and r_{ci} is the cladding inner radius. By substituting the known values and integrating from the fuel exterior surface to the cladding inner surface, which is multiplied by the height of the layer containing the fuel and cladding (10 mm), the analytical solution for the integrated heat flux is found to be 195.18 W. From the results in Table 4.2 it is evident that the heat flux calculation is sensitive to the mesh density, and that with a sufficiently refined mesh, the finite element solution converges to the analytical solution.

Layered Nodal Extreme Value

The layered nodal extreme value is an object that returns the selected extreme value (i.e., maximum or minimum) for each layer in a Layered2D (or Layered1D) simulation. For axial relocation modeling this corresponds to the maximum gap distance for comparison against the gap thickness threshold. The variable of interest in the layered nodal extreme value object is not restricted to displacement. For implementation testing, an axially and

azimuthally varying temperature profile is applied to the exterior surface of the cladding. The local temperature is given by:

$$T(x, y, z) = T(z) + 30.0 \left| \sin\left(\frac{\mathrm{atan2}(y, x)}{2} \right) \right| \tag{4.20}$$

where atan2 defines the angle in the plane that is in the range of $(-\pi < \theta \leq \pi]$, and $T(z)$ is the prescribed temperatures described, previously, for each layer. Assuming a maximum value for the extreme calculation the analytical solution is 330 K in layer 1 and 630 K in layer 2. Since the layered nodal extreme value simply reports a value off of the mesh, which in this case is prescribed directly, the values do not depend upon the mesh as seen in Table 4.2.

Layered Plenum Temperature

The plenum temperature within the fuel rod plays a crucial part in the rod's behavior during irradiation and accidents. In a layered geometry, it is necessary to account for the layer heights in the computation of the temperature. Simply taking the nodal values and performing an average will significantly over estimate the temperature within the plenum leading to unrealistic predictions of rod internal pressure. The plenum temperature algorithm builds off of the existing capability in Bison to utilize a weighted average of the fuel and cladding surface temperature bounding the gas as a function of position. The outer fuel surface and cladding inner surface temperatures of the fuel and cladding layer are prescribed to 800 K and 600 K, respectively. The inner cladding surface in the plenum region is set to 580 K. The calculated plenum temperature is determined to be 590.48 K. Just like the layered side average calculation, there is no radial or azimuthal mesh dependence on the determination of the plenum temperature for layered geometries (see Table 4.2).

Table 4.2: Comparisons of the calculated results for the various implementation tests for each of the eight meshes. The analytical solutions are provided.

Mesh ID	Total Rod Internal Volume (cm^3)	Fueled Layer Internal Volume ($\times 10^{-4} cm^3$)	Layered Integral (Layer 1) ($\times 10^{-5} Km^3$)	Layered Integral (Layer 2) ($\times 10^{-5} Km^3$)	Layered Side Average (K)	Layered Side Flux Integral† (W)	Extreme Value (Layer 1) (K)	Extreme Value (Layer 2) (K)	Layered Plenum Temperature (K)
1	0.10880	-3.0590	4.6750	1.8700	350.0	216.05	330.0	630.0	590.48
2	0.11090	-3.1190	4.7665	1.9066	350.0	209.51	330.0	630.0	590.48
3	0.11150	-3.1340	4.7896	1.9066	350.0	204.70	330.0	630.0	590.48
4	0.11160	-3.1378	4.7954	1.9066	350.0	201.25	330.0	630.0	590.48
5	0.11166	-3.1389	4.7971	1.9066	350.0	194.03	330.0	630.0	590.48
6	0.11166	-3.1391	4.7973	1.9189	350.0	194.52	330.0	630.0	590.48
7	0.11166	-3.1391	4.7973	1.9189	350.0	194.87	330.0	630.0	590.48
8	0.11166	-3.1391	4.7973	1.9189	350.0	195.04	330.0	630.0	590.48
Analytical	0.11166	-3.1391	4.7973	1.9189	350.0	195.18	330.0	630.0	590.48

† corresponds to the calculated flux leaving the fuel.

The previous regression tests focused on global or layered quantities of importance in nuclear fuel analysis. Here, the radial temperature profile in the fuel and cladding layer is computed for all eight meshes, then compared to the analytical solution for cylindrical coordinates with the appropriate dimensions. A 25 kW/m linear heat rate is applied uniformly within the fuel. The thermal conductivity of the fuel and cladding are taken as 2.5 W/m-K and 16 W/m-K, respectively. The unmeshed gap is assumed to have a thermal conductivity of 0.1 W/m-K. The exterior surface of the cladding is fixed at 580 K. Conductance across the gap is captured using available thermal contact algorithms available in Bison. In this case the simplest application of gap conductance is employed, which computes the conductance (h_{gap}) in W/m^2-K in cylindrical coordinates as:

$$h_{gap} = \frac{k_{gap}}{r_f \ln\left(\frac{r_{ci}}{r_f}\right)} \tag{4.21}$$

where k_{gap} is the thermal conductivity within the gap and, r_f is the outer radius of the fuel, and r_{ci} is the cladding inner radius. Thermal expansion is not included because it is desired to have the gap remain constant throughout the analysis. Steady-state heat conduction is assumed.

Figure 4.6a illustrates the radial temperature profile across the fuel, gap, and cladding for each of the eight meshes in Table 4.1 in addition to the analytical solution. For thermal analyses depending only on the number of radial elements within the fuel, it is observed that only Mesh 1 poorly captures the temperature profile. This simple study demonstrates that the internal mesh generator described in Section 4.2.4 is creating meshes with the proper element connectivity. A symmetric profile was analyzed for this situation since there existed an analytical solution. For completeness and to more fully demonstrate the flexibility of the Layered2D framework, a similar case was run with an eccentric pellet moved into initial contact with the cladding on the right side of the fuel rod. This implies that the gap is closed on one side and twice as large (160 μm) on the other. The temperature profile for the

eight meshes in this case is shown in Figure 4.6b. Here, the temperature profile is captured reasonably well beginning with Mesh 3. The effect of the non-symmetric gap is evident when comparing the temperature profiles. The maximum temperature is a few degrees lower in the eccentric case, which is the same behavior observed in [45].

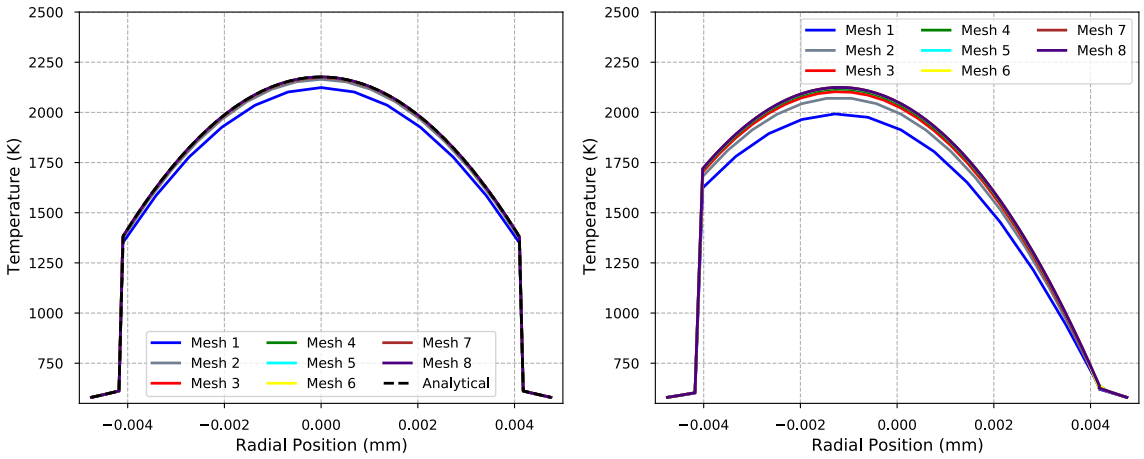

(a) (b)

Figure 4.6: Radial temperature profiles for the thermal verification case for each of the eight meshes for (a) a symmetric fuel slice and (b) an eccentric fuel slice. The analytical solution is included for the symmetric case.

4.3 Extension of the Jernkvist and Massih Model to Layered2D

To make the existing Jernkvist and Massih axial relocation work within the Layered2D framework three modifications are required: (1) the gap calculation in the relocatable mass loop, (2) the calculation of the internal cladding volume, and (3) the mesh movement in crumbled layers.

4.3.1 Fuel-to-cladding Gap Threshold

In the Layered1D formulation the gap in each layer that is compared to the minimum gap threshold (denoted as g_k^{th}) in Figure 4.1 is simply calculated as the difference between inner cladding radius at time t and the as-fabricated fuel radius. If the calculated gap exceeds

the minimum gap threshold mass is deemed relocatable from the layer. In the Layered2D formulation the possibility of azimuthally varying gap thicknesses required the development of a new UserObject in Bison that calculates the maximum inner cladding radius in each layer. Subtracting the as-fabricated fuel radius from this maximum inner cladding radius determines the gap size compared to g_k^{th}. Therefore, in the extended axial relocation model if any azimuthal location has a fuel-to-cladding gap greater than the threshold gap (default is 0.2 mm) mass is deemed relocatable in that layer.

4.3.2 Cladding Internal Volume

Similarly to the gap calculation described above the layered internal cladding volume in each layer is easily calculated in the Layered1D formulation due to the azimuthal symmetry. In that case the current cladding volume used in the calculation of crumbled mass m_k^M (see Equation 4.10) is simply given by $\pi L_k R_{cik}^2$. In the Layered2D formulation azimuthal variation in cladding distention can lead to a non-circular cross section of the inner area of the cladding. Therefore, a new Bison UserObject was developed to compute the cladding internal volume on a layered basis. The volume of the enclosed space in each layer is calculated as the integral over the cladding inner surface in that layer. The integral calculation allows for arbitrary cladding balloons to be represented. It should be noted that due to finite element limitations the accuracy of the integral depends upon the density and order of the finite element mesh as curved domains may not be exactly captured due to faceting.

4.3.3 Mesh Relocation Due to Crumbling

The last portion of the existing axial relocation model that needed to be extended to work in the Layered2D framework is the movement of the fuel mesh towards the cladding in crumbled layers of fuel for thermal feedback and heat generation purposes. In the Layered1D formulation the approach was simply to calculate an eigenstrain that would move the current position of the outer fuel radius to a position that is within the residual gap (g^r) of the

cladding as seen in Figure 4.3. The eigenstrain is calculated as a true strain via:

$$\epsilon = \ln\left(1.0 + \frac{R_{ci} - g^r - R_{po}}{R_{po}}\right) \tag{4.22}$$

In the Layered2D formulation the calculation of the eigenstrain needs to be extended to each azimuthal position such that:

$$\epsilon\left(\theta\right) = \ln\left(1.0 + \frac{R_{ci(\theta)} - g^r - R_{po}\left(\theta\right)}{R_{po}\left(\theta\right)}\right) \tag{4.23}$$

4.4 Verification of the Axial Relocation Model in Layered1D and Layered2D

The axial relocation model was originally developed for use with the 1.5D framework of FRAPTRAN. To ensure proper implementation in Bison a few verification cases from the original model publication [53] were recreated in Bison using the Layered1D approach. By producing the same results for key features of the model as per [53] instills confidence in the implementation in Bison. The features verified here include the mass relocation algorithm, the effective thermal conductivity model, and the adjustment of heat generation due to fuel crumbling. By assuming azimuthal symmetry in the Layered2D case, it can be demonstrated that for symmetric conditions Layered2D produces the same results as Layered1D, giving confirmation of the proper implementation of the model extensions to Layered2D.

4.4.1 Verification of Fuel Mass Relocation in Layered1D and Layered2D

The axial relocation model was originally developed for use with the 1.5D framework of FRAPTRAN. To ensure proper implementation in Bison a couple verification cases from the original model publication [53] were recreated in Bison using the Layered1D approach. The two problems are referred to as the "single balloon" and "twin balloon" cases, respectively. In both test cases, the active length of the fuel is (L_a = 3.6 m), with a fuel pellet diameter of 9.0 mm. The initial fuel-to-cladding gap is assumed to be zero (i.e., the gap is

closed). The effective packing fraction is assumed to be 0.75 after fuel crumbling, and 36 equal length axial segments are used. The duration of the simulation is 100 s. The purpose of the single balloon verification test is to simulate cladding distention which is maximum at the mid-plane of the active length ($z = 1.8$ m). The purpose of the twin balloon verification test is to simulate the effect of having a spacer-grid at the mid-plane of the active length. In the single balloon case, the inner cladding radius varies as:

$$R_{ci}(t, z) = 4.5 \times 10^{-3} + 2.0 \times 10^{-5} t \sin\left(\frac{\pi z}{L_a}\right) \tag{4.24}$$

and in the twin balloon test, the inner cladding radius varies as:

$$R_{ci}(t, z) = 4.5 \times 10^{-3} + 2.0 \times 10^{-5} t \left|\sin\left(\frac{\pi z}{L_a}\right)\right| \tag{4.25}$$

The mass fraction as a function of axial position for these cases is illustrated in Figures 4.7a and 4.7b. Each figure contains three subplots that provide snapshots in time (40, 60, and 100 s) of the fuel mass fraction within the rod. A fuel mass fraction greater than one is understood to mean that the region has gained mass. Mass loss occurs in regions with a value less than one. In the single balloon case, as time progresses the amount of fuel lost at the top of the rod increases and moves into the mid-plane of the rod as expected. As observed in some experiments, and as captured by the model, a fuel plug is predicted at the top of the rod where fuel loss may not occur. This plug is due to the cladding not distending enough at this location to allow the fuel to relocate. In the twin balloon case, mass loss is observed from two locations including the one in the top portion of the rod and another just below the spacer grid at the mid-plane of the rod. It is seen that for the symmetric boundary conditions, both Layered1D and Layered2D approaches give identical results, which follow the trends of the Jernkvist and Massih results from the initial FRAPTRAN implementation [53]. The minor differences in axial positions between Jernkvist and the Bison calculations is due to differences in how the layers are placed in FRAPTRAN and Bison.

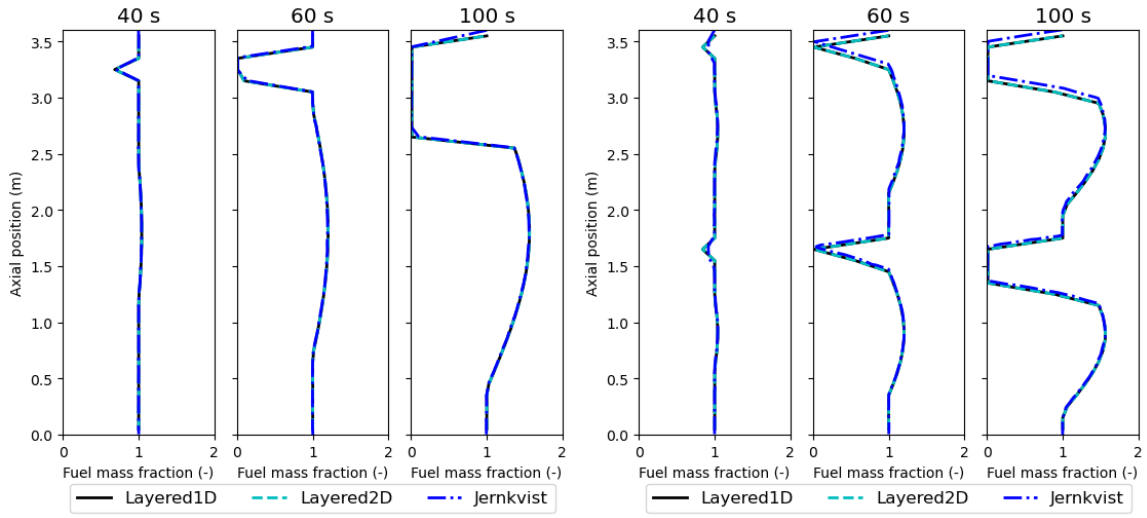

Figure 4.7: Fuel mass fraction as a function of axial position for (a) symmetric single balloon and (b) symmetric twin balloon at selected snapshots in time of 40, 60, and 100 s. Layered1D and Layered2D formulations are compared.

After verifying that the Layered1D and Layered2D models provide the same results for symmetric conditions, asymmetric single and twin balloon cases were completed to show the impact of the assumption that the balloon is azimuthally uniform. Here, the maximum cladding displacement is the same as the symmetric case, but it is shifted to one side. It only applies at the $\theta = \pi$ location, assuming that $\theta = 0$ is at the positive x-axis. At $\theta = 0$ the displacement is zero. In this scenario, the cladding inner radius varies for the single balloon case as:

$$R_{ci}(t, \theta, z) = 4.5 \times 10^{-3} + 2.0 \times 10^{-5} t \sin\left(\frac{\theta}{2}\right) \sin\left(\frac{\pi z}{L_a}\right) \tag{4.26}$$

and in the twin balloon case as:

$$R_{ci}(t, \theta, z) = 4.5 \times 10^{-3} + 2.0 \times 10^{-5} t \sin\left(\frac{\theta}{2}\right) \left|\sin\left(\frac{\pi z}{L_a}\right)\right| \tag{4.27}$$

The results comparing the Layered2D asymmetric balloon to the Layered1D symmetric balloon (because Layered1D is incapable of simulating the asymmetric balloon) are shown in Figure 4.8a and Figure 4.8b. As can be seen, the axial mass fraction is much less in

most axial regions when compared to Layered1D, particularly at the axial heights where the cladding displacement is largest. It is also observed that the fuel in the aysmmetric balloon case begins to relocate later in time. This behavior is expected since the same maximum balloon size is assumed and occurs at only one side of the cladding tube rather than uniformly in the azimuthal direction. Such an assumption results in a reduced volume able to accommodate fuel at any given time, delaying the onset of fuel movement. Consequently less fuel is present in the balloon.

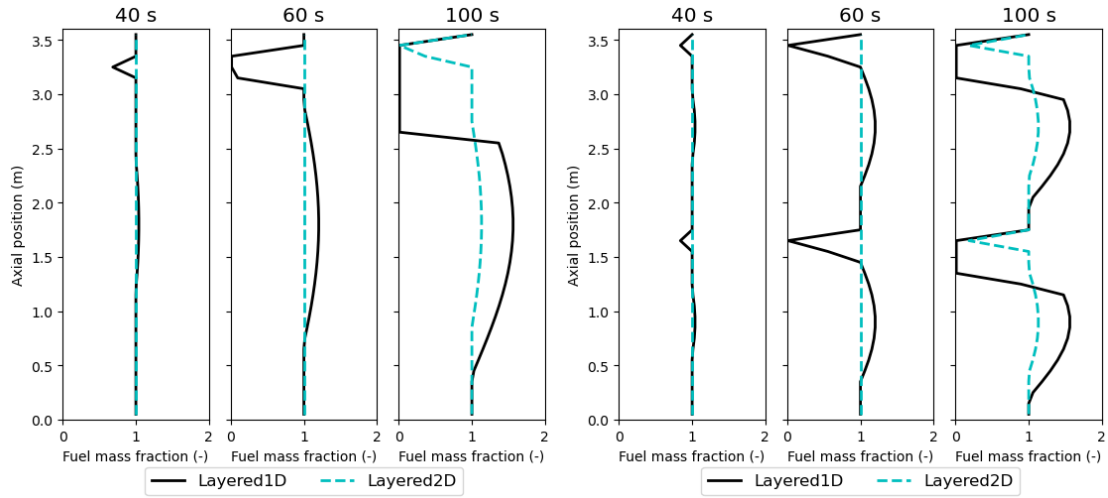

(a) (b)

Figure 4.8: Fuel mass fraction as a function of axial position for (a) asymmetric single balloon and (b) asymmetric twin balloon at selected snapshots in time of 40, 60, and 100 s. Layered1D and Layered2D formulations are compared against the original Jernkvist and Massih calculations [53].

4.5 Validation of the Axial Relocation Model

As mentioned in Chapter 1 numerous experimental programs have been developed to investigate integral rod behavior and thermal-hydraulic consequences during a LOCA for BWRs and PWRs. The experimental programs are covered in great detail in one of two (or both) extensive reviews of the FFRD phenomenon by Raynaud [91] and the OECD NEA CSNI [102]. Early integral experiments that contained data on axial fuel relocation included

the Power Burst Facility tests in Idaho, the FR-2 tests in Germany, the National Reactor Universal (NRU) tests completed in Canada, and the FLASH tests completed in France. More recently the NRC sponsored Studsvik tests conducted in Sweden and the Halden reactor tests series completed in Norway have provided large quantities of integral data. Currently, the US DOE is funding testing at the SATS facility [18] at ORNL and the TREAT reactor at INL. Internationally, LOCA testing continues to be pursued through the Studsvik Cladding Integrity Project SCIP (Studsvik Cladding Integrity Program) that began its first phase in 2004 and has recently begun it's fourth phase set to concluded in 2024 [1]. The older tests series have results documented in Raynaud and the OECD NEA CSNI review documents, but the details of the experiments and operational conditions prior to the experiment being conducted are not well documented. This makes the modeling of these experiments difficult. The more recent tests completed at Studsvik and Halden are more widely available for researchers. As an employee at INL the author of this work has access to the detailed descriptions of the Halden rods in particular. The details of the Studsvik experiments are widely available [30, 47] but the base irradiation used can be difficult to obtain as the fuel was provided to the program by commercial vendors. The more recent SATS studies [18] can also be difficult to simulate due to lack of detailed base irradiation information.

In this chapter a select few of the Halden IFA-650 LOCA tests are used for analysis of the Bison implementation of the axial relocation model and the extension of the model to Layered2D due to the ease of access of the data for both the experiment and base irradiation of the fuel rods.

4.5.1 HALDEN IFA-650 LOCA TEST SERIES

In total, 15 tests have been completed as part of the IFA-650 LOCA test series. Each test was designed for a specific purpose by the varying operational conditions, pre-irradiation history, plenum size, and cladding type to explore the impact of these various phenomena on the behavior of the fuel rod during a LOCA. Of interest in this work is the simulation

of IFA-650.4, IFA-650.9, and IFA-650.14. IFA-650.4 and IFA-650.9 were selected due to the Bison team's participation in the FUMAC project [3]. In particular, IFA-650.4 has been referred to as the experiment whose observations reignited the rapid investigation into FFRD by industry, national laboratories, and universities. IFA-650.14 is of interest due to the lack of cladding failure but significant fuel relocation.

The IFA-650.4 test was the fourth test completed as part of the LOCA test series. The purpose of the test was to repeat the conditions of the IFA-650.3 test on a pre-irradiated fuel rod to assess the validity of existing LOCA safety criteria [55]. In particular, the experiment was designed in such a way to maximize the balloon size to promote fuel relocation and to assess the impacts on cladding temperature and oxidation. The average burnup of the fuel after the base irradiation was ∼92 MWd/kgU. Due to the high burnup of the pre-irradiated fuel, severe fragmentation was observed and axial relocation occurred during the LOCA transient. After the conclusion of the experiment, a large cladding balloon was present. Cladding rupture occurred at 336 seconds after blowdown at a temperature of ∼1058 K and a pressure of ∼5.2 MPa.

The IFA-650.9 test was the ninth test completed as part of the LOCA test series. The purpose of this test was similar to IFA-650.4 and was actually used to clarify and confirm the behavior of significant fuel relocation that was observed in that test. The burnup of the fuel after the base irradiation was ∼89.9 MWd/kgU. Cladding failure occurred ∼133 s after blowdown at a cladding temperature of ∼1083 K and a pressure of ∼6.0 MPa.

The IFA-650.14 test was the fourteenth test completed in the test series. This test focused on BWR irradiated fuel with a similar purpose to the IFA-650.4 and IFA-650.9 tests, to promote cladding ballooning to induce significant fuel relocation. The primary difference in transient characteristics was to have a small plenum to induce large balloons without cladding rupture. The burnup after the base irradiation was ∼72 MWd/kgU. Cladding ballooning began ∼235 seconds after blowdown and the reactor was scrammed after the rod pressure dropped to 74% of its maximum value of 7.73 MPa. The simulation was terminated

350 seconds after blowdown began.

The fabrication characteristics of the three specimens are provided in Table 4.3. The IFA-650.4 and IFA-650.9 rodlets were segmented from PWR mother rods, with the cladding material consisting of a Zry-4 base with a 100 μm niobium-oxide liner to improve oxidation resistance. For both experiments, the refabricated rod was back-filled with a binary mixture of argon (95%) and helium (5%) at 4.0 MPa. Argon was chosen to simulate the effect of a low gap thermal conductivity due to fission gases. The rod plenum volume (i.e., free gas volume) was made relatively large in order to maintain stable pressure conditions until a cladding burst occurred. The total free gas volume was 21.5 cm^3 for IFA-650.4 and 19cm^3 for IFA-650.9 and was practically all located outside the heated region [55, 22].

The IFA-650.14 rodlet was segmented from a BWR mother rod with a Zry-2 cladding with an inner liner. For this experiment, the refabricated rod was back-filled with a binary mixture of argon (95%) and helium (5%) at 2.0 MPa. In this test, the rod plenum (i.e., free gas volume) was made extremely small to promote large cladding balloons without cladding rupture. The majority of the free volume (1.9 cm^3) was within the heated region [119].

Table 4.3: Design data of the IFA-650.4, IFA-650.9, and IFA-650.14 fuel rods.

	IFA-650.4	IFA-650.9	IFA-650.14
Fuel material	UO_2	UO_2	UO_2
Fuel density (%TD)	95.2	95.0	96.0
^{235}U enrichment (wt %)	3.5	3.25	3.71
Active fuel stack length (mm)	480	480	360
Pellet inner diameter (mm)	0	0	0
Pellet outer diameter (mm)	9.13	9.13	8.19
Cladding material	Zry-4	Zry-4	Zry-2
Cladding thickness (incl. liner) (mm)	0.725	0.725	0.63
Cladding outer diameter (mm)	10.75	10.75	9.62
Diametrical gap (μm)	170	170	170
Rod inner free volume (refab.) (cm^3)	21.5	19	1.9
Rod filling gas (refab.) (Ar%/He%)	95/5	95/5	95/5
Initial rod inner pressure (refab.) (MPa)	4.0	4.0	2.0

These rodlets were located inside the IFA-650 test rig and were neutronically heated

from the inside and externally heated using an electrical heater. The purpose of the heater was to simulate the effect of adjacent fuel rods within the core. The IFA-650.4 rodlet was instrumented with three thermocouples on the cladding exterior surface, a pressure transducer to measure the rod internal pressure, and a cladding elongation sensor. Two of the thermocouples were located 8 cm below the top of the fuel stack (at 180° from one another) and one was located in the plenum region 19 cm above the fuel stack. Additional temperature measurements were provided for the coolant at the inlet and outlets of the experimental apparatus. The IFA-650.9 rodlet was also instrumented with three thermocouples on the cladding surface, with one located 10 cm above the fuel bottom and two located 6.5 cm from the top of the fuel stack. A pressure transducer was also included inside the rodlet. The IFA-650.14 rodlet was instrumented with three cladding thermocouples, one 10 cm above the fuel bottom and two 6.0 cm from the top of the fuel stack. One of these upper thermocouples was determined to be faulty during the experiment. This rodlet also included a pressure transducer. As with IFA-650.4, both IFA-650.9 and IFA-650.14 included additional temperature measurements for the coolant at the inlet and outlets of the experimental apparatus.

Details of the Halden IFA-650 tests are well documented in the Halden reports [55, 22, 119]. Each transient consists of five distinct phases: (1) preparatory (forced and natural circulation), (2) blowdown, (3) heat-up and hold at peak cladding temperature, (4) scram, and (5) the conclusion of the experiment. Depending upon the particular experiment, the duration and specific conditions the specimen undergoes during a phase may be different. The reader is encouraged to explore the appropriate documentation for a particular experiment if interested in more specific details.

The base irradiation histories for the three rodlets are provided in Figure 4.9. The IFA-650.4 and IFA-650.9 rods were subjected to seven cycles prior to refabrication. The thermal-hydraulic conditions for the base irradiation were not provided; therefore, typical PWR conditions were used. This includes a coolant pressure of 15.3 MPa, a coolant mass

flux of 3800 kg/m^2-s, and an inlet temperature of 580 K. The IFA-650.14 rod was also subjected to seven cycles prior to refabrication; however, the thermal-hydraulic conditions for the base irradiation were representative of BWR conditions. This included a coolant pressure of 7.14 MPa, a coolant mass flux of 1800 kg/m^2-s, and an inlet temperature of 560 K.

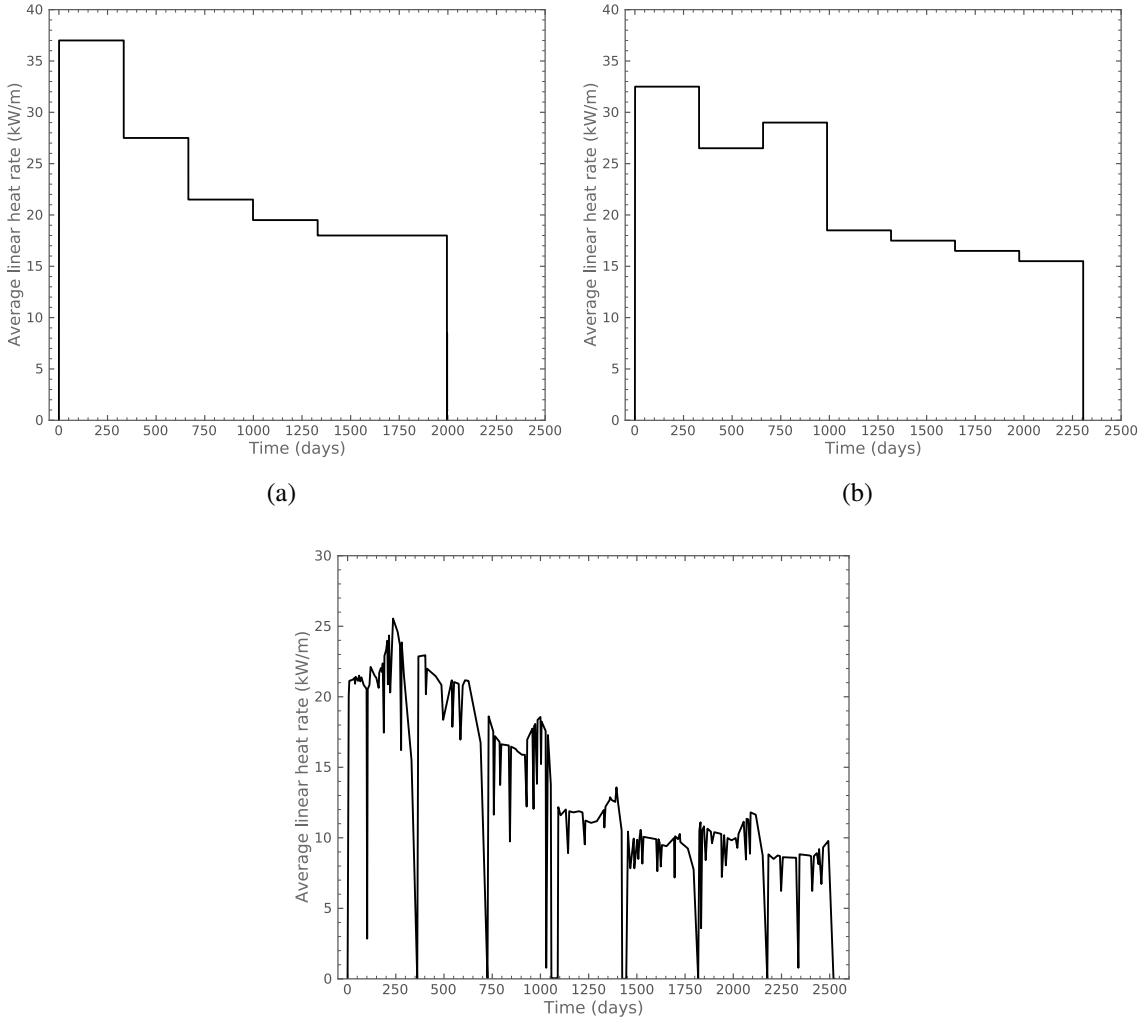

Figure 4.9: Base irradiation power histories for the (a) IFA-650.4, (b) IFA-650.9, and (c) IFA-650.14 rods.

During the experiment, the boundary conditions become extremely complex. There is the neutronic heating internally to the rod, and the external heating from the heater as well as

the complicated coolant conditions due to the LOCA. The axial profile of the neutronic and electrical heater during the transient are prescribed as provided by the experimental measurements. During the preparatory phase, the cladding surface temperature is prescribed based upon measurements from the thermocouples to ensure the proper conditioning of the rods prior to blowdown. After blowdown, the prescribed temperature is removed and the coolant transfer coefficient is significantly degraded. For the IFA-650.4 and IFA-650.14 cases, approximately 30 seconds after blowdown, the convective heat transfer coefficient is set to 50 W/m^2-K and radiation between the outer cladding surface and the heater is activated. For the IFA-650.9 case, the process is similar except an axial profile on the convective heat transfer coefficient after blowdown, as suggested by [52], is employed which linearly varies from 30 W/m^2-K at the bottom of the rod to 70 W/m^2-K near the top.

The radiation heat transfer coefficient (W/m^2-K) between the heater and cladding outer surface is computed by:

$$h_r = \epsilon\sigma(T_c^2 + T_h^2)(T_c + T_h) \tag{4.28}$$

where σ is the Stefan-Boltzmann constant (5.6704×10^{-8} W/m^2 K^4), T_c is the temperature of the outer cladding surface (K), T_h is the temperature of the heater, and ϵ is the effective emissivity between the two surfaces given by:

$$\epsilon = \epsilon_c\epsilon_h R_h(\epsilon_c R_c + \epsilon_h R_h - \epsilon_c\epsilon_h R_c)^{-1} \tag{4.29}$$

where ϵ_c and ϵ_h are the surface emissivities of the cladding and heater (-), respectively, and R_c and R_h the radii of the cladding and heater surfaces (m). In practice ϵ_h is not experimentally known. Estimates have been made for ϵ_c based off of Zircaloy and zirconium-oxide specimens [109]. At lower temperatures the emissivity tends to be low with a peak of approximately 0.75 occurring around 1180 K. The trends are derived using the MATPRO [100] specific heat correlation which also observes a peak in this region associated with the $\alpha \rightarrow \beta$ transition of Zircaloy. Assuming $\epsilon_h = 1.0$ one can approximate that $\epsilon = \epsilon_c$, which is the approach taken in the Bison analyses of the IFA-650 rods presented here.

Simulations of these rods is completed using both Layered1D and Layered2D geometric representations since it is desired to investigate the fuel axial relocation during the LOCA transients including azimuthal effects. However, before incorporating the Layered2D approach for azimuthally varying boundary conditions, it is desired to gain an understanding of the most sensitive inputs on the simulation predictions for the as developed axial relocation model (i.e., a Layered1D geometry). To do this, a sensitivity study is completed that varies some of the axial relocation model inputs in addition to a few other parameters of interest when analyzing a LOCA. Table 4.4 lists the assumed uncertain parameters including their ranges and distributions. The axial relocation parameters assumed to be uncertain here correspond to the gap thickness threshold, the non-relocatable fuel fraction, and the pulver characteristic length. Two additional parameters were assumed to be uncertain, the maximum inelastic increment in the cladding and the effective emissivity during radiation between the cladding and the heater. The maximum inelastic increment is an input parameter into the cladding creep model that determines the maximum creep strain increment that can be taken in a single timestep. If this value is set too high, important features during the ballooning process can be missed, whereas setting it too small can lead to unreasonably long simulation times. For all of these parameters uniform distributions are assumed as it is not clear what the exact value should be and all values in the ranges are assumed to be equally probable. This sensitivity analysis is executed using three different mesh densities (number of layers used to represent the fuel): 15, 30, and 60 using each of the three large fragment models analyzed in detail in Chapter 3: Barani et al. [9], Coindreau et al. [23], and Walton and Matheson [124], and two different cladding failure criteria: plastic instability (PI) and overstrain (OS). For IFA-650.14 the failure criteria does not apply as the rod did not fail. Therefore, only the mesh density and large fragment models are incorporated into the sensitivity analysis of the IFA-650.14 case. For each sensitivity study, 200 simulations are completed, resulting in a total of 5400 analyses.

Bison currently contains six different failure criteria: overstress, plastic instability (also

Table 4.4: Parameters associated with axial fuel relocation modeling assumed to be uncertain for the sensitivity analyses.

Parameter	Uncertainty Range	Distribution
Gap thickness threshold (m)	$[0.1\times10^{-3}:0.5\times10^{-3}]$	Uniform
Non-relocatable fuel fraction (-)	[0.005:0.05]	Uniform
Pulver characteristic length (μm)	[50:500]	Uniform
Maximum inelastic increment (-)	[0.0001:0.01]	Uniform
Effective emissivity during radiation (-)	[0.4:0.75]	Uniform

In addition to the uncertain parameters provided in the table, three large fragment models were analyzed: Barani et al., Coindreau et al., and Walton and Matheseon as well as three different number of layers representing the fuel in the mesh: 15, 30, and 60.

known as strain rate), overstrain, combined overstress and plastic instability, combined overstress and overstrain, and rupture temperature [27, 64, 85]. The PI and OS options were chosen for comparison in this work because the overstress criterion was developed on fresh unirradiated cladding specimens to compute the oxidation effects that when applied to highly irradiated fuel rods predicts premature failure during the base irradiation. The rupture temperature correlation requires the knowledge of the heating rate *apriori* making it more suitable for furnace tests like those completed at Studsvik [47] or the Severe Accident Test Station [101]. The PI criterion determines cladding failure when the inelastic strain rate (creep and plasticity) exceeds a value of 0.027778 s^{-1} and the OS criterion determines cladding failure when the total inelastic strain exceeds a value of 40% engineering strain (33.6% true strain). Appendix C provides a link to the Bison documentation page [69] on the online version of this document that provides additional theory on the failure criteria not used here.

The three large fragment correlations were determined to be valid for use in axial relocation analyses after an extensive investigation in Chapter 3. They are used in the determination of the effective packing fraction for axial relocation based upon the calculated characteristic length of the large fragments given by Equation 4.4. These correlations are also used during the analysis as a means to account for cracking of fuel during normal op-

eration. The approach utilized is an isotropic cracking model based off the work of Barani et al. [9]. In this model the Young's modulus and Poisson's ratio of the fuel is scaled by a factor that is a function of the number of cracks within the fuel:

$$\nu_{damaged} = \frac{\nu}{2^n + (2^n - 1)\,\nu} \tag{4.30a}$$

$$E_{damaged} = \left[\frac{2}{3}\frac{2-\nu}{2+\nu}\frac{1}{1-\nu}\right]^n E \tag{4.30b}$$

where n is the number of cracks, ν is the initial Poisson's ratio (-), and E is the initial Young's modulus (Pa). The number of cracks is computed by Equation 3.1, 3.2, or 3.5 for the Barani et al., Walton and Matheson, and Coindreau et al. models, respectively.

In addition to the axial relocation model, failure criteria, and isotropic damage modeling described above, numerous other Bison models are necessary to simulation the behavior of the fuel and cladding during a LOCA. Appendix C provides a comprehensive list of all Bison models and other MOOSE objects used throughout this dissertation. The rightmost column in that table lists the chapters in which the models were used in at least one analysis presented in the chapter.Appendix D provides the template for the transient portion of the IFA-650.4 analyses for the overstrain criterion using the Barani fragmentation model and a mesh featuring 30 layers.

After analyzing the sensitivity of certain parameters using the Layered1D representation an azimuthal dependence on the heat transfer coefficient after blowdown is applied to introduce asymmetric behavior for IFA-650.4 only. Details are not available on the azimuthal variation in the thermal hydraulics of these experiments and there is insufficient data to create a full TRACE or RELAP-7 input.

Results and Analysis of IFA-650.4

The sensitivity analysis results using the Layered1D formulation for IFA-650.4 are provided in Table 4.5 and Figure 4.10 through Figure 4.20. The table provides the mean value with a 2σ uncertainty of the 200 simulations at the point of cladding failure for rupture time,

the peak cladding temperature, and the rod internal pressure for each mesh density and fragmentation model. The last row in the table provides the experimental measurements at the experimental time of cladding failure. It is observed that the Coindreau fragmentation model predicts a later rupture time, higher cladding temperatures, and lower pressures than the other two fragmentation model. This model is the only one that encompasses the experimental rupture time. Overall, all fragmentation models result in higher than measured cladding temperatures at rupture, which indicates that the thermal hydraulics prescribed through Bison's internal coolant channel model (i.e., the use of a prescribed convective heat transfer coefficient as well as the radiation between the cladding and heater) needs improvement. The thermal-hydraulics could be improved through a TRACE or RELAP-7 analysis. However, for those analyses to be fruitful, enough information about the thermal-hydraulics of the experiment are necessary. All analyses, except the Coindreau calculations predict rod internal pressures that are consistent with the experiment for both failure criteria. One will notice the differences between the two different failure criteria is minimal for each fragmentation model for IFA-650.4. Minor differences are calculated based upon mesh density.

Figure 4.10 through Figure 4.12 presents the Pearson correlation coefficients for every combination of fragmentation models, mesh density, and failure criteria. In each of the three figures, the left-hand and right-hand columns correspond to the plastic instability and overstrain results, respectively. The number of fuel layers increase from 15 to 60 from the top to bottom rows (30 in the middle). As mentioned previously, the Pearson correlation coefficient is a measure of monotonic relationships between the uncertain inputs in Table 4.4 to the outputs of interest: rupture time, peak cladding temperature, and plenum (rod internal) pressure. These Pearson coefficients are always between -1.0 and 1.0. The mathematical details in their computation of the Pearson coefficients from the samples are provided in Section 2.5. In each subfigure, there is a light gray region between -0.3 and 0.3, for which the Pearson correlation coefficients are deemed insignificant (i.e., there is not a

Table 4.5: Comparisons of the mean calculated value of the fuel performance metrics of interest to the experimental values for IFA-650.4. An uncertainty of $\pm 2\sigma$ is included on the simulation results.

Failure Criterion	Frag. Model	# Fuel Layers	Rupture Time (s)	Peak Clad Temp.† (K)	Rod Internal Pressure† (MPa)
PI	Barani	15	306.60 ± 18.69	1078.51 ± 6.18	5.29 ± 0.20
	Coindreau	15	320.08 ± 20.03	1081.36 ± 6.78	5.13 ± 0.14
	Walton	15	310.06 ± 18.80	1079.40 ± 6.16	5.23 ± 0.17
	Barani	30	305.77 ± 18.37	1077.82 ± 6.09	5.36 ± 0.16
	Coindreau	30	319.20 ± 19.89	1083.76 ± 9.10	5.19 ± 0.12
	Walton	30	308.97 ± 18.54	1079.42 ± 5.85	5.31 ± 0.13
	Barani	60	305.67 ± 18.43	1078.38 ± 5.36	5.33 ± 0.15
	Coindreau	60	319.21 ± 19.93	1086.73 ± 5.66	5.17 ± 0.11
	Walton	60	308.84 ± 18.56	1080.31 ± 4.69	5.29 ± 0.12
OS	Barani	15	307.95 ± 18.17	1079.68 ± 6.87	5.19 ± 0.17
	Coindreau	15	321.23 ± 19.61	1081.92 ± 9.20	5.06 ± 0.12
	Walton	15	311.39 ± 18.30	1079.84 ± 6.71	5.14 ± 0.14
	Barani	30	307.20 ± 17.94	1079.37 ± 6.38	5.26 ± 0.13
	Coindreau	30	320.44 ± 19.57	1085.68 ± 9.07	5.12 ± 0.10
	Walton	30	310.35 ± 18.17	1080.51 ± 6.27	5.22 ± 0.10
	Barani	60	307.07 ± 17.95	1079.68 ± 6.07	5.24 ± 0.12
	Coindreau	60	320.41 ± 19.62	1088.55 ± 5.91	5.11 ± 0.08
	Walton	60	310.18 ± 18.15	1081.59 ± 4.99	5.21 ± 0.09
Experiment	N/A	N/A	336	1058	5.2

†at time of rupture

strong positive or negative monotonic relationship between the inputs and outputs). Any bars extended past this gray region are considered significant and provide insight into which uncertain parameters should be investigated further either by modeling or experiments to reduce the uncertainty on the parameter. The same colour scheme is used in each of the three sets of figures, blue representing rupture time, red, peak cladding temperature, and black, plenum pressure.

First, examining Figure 4.10 indicates that for the either of the failure criteria, the number of fuel layers has limited impact on the results. For the plastic instability criterion, which always predicts cladding failure earlier than the overstrain for the same set of sam-

pled input parameters the effective emissivity used in Equation 4.28 has a strong influence on the predicted results of all three metrics of interest. The relationship is negative with plenum pressure and peak cladding temperature, and positive with rupture time. This intuitively makes sense; as the emissivity increases, improved heat transfer occurs between the cladding and the heater, resulting in decreased cladding temperature, which results in less creep, smaller balloons, and decreased plenum temperatures. The decreased plenum temperature results in a lower plenum pressure. On the other hand, due to the reduction in creep the time at which the plastic instability (creep rate) failure criteria is attained is increased. The only other significant correlation, is between the gap thickness threshold of the axial relocation model and the plenum pressure. A higher threshold before allowing fuel to relocate results in a delay in cladding ballooning because the rapid distension, and thus decrease in internal pressure, occurs after fuel is present in the balloon due to the redistribution of the heat load. One may argue that the pulver characteristic length is borderline significant with the cladding temperature. The interaction between this input and output is attributed to the fact that a larger pulver characteristic length using the same large fragment model (in this case Barani) will result in a lower packing fraction in the ballooned region. A small packing fraction indicates that less fuel is present and temperatures will be lower. Limited differences are seen between the PI and OS results, the exception being that the effective emissivity becomes insignificant for the plenum pressure. This is expected for the OS criterion because it is a total inelastic strain threshold for failure, which indicates that in most cases the size of the balloon at failure will be similar for all 200 cases.

The IFA-650.4 Pearson coefficients for the Coindreau large fragment model presented in Figure 4.11 show a slight difference in the relationships than the Barani model. As before, the two most dominant parameters are the effective emissibity and gap thickness threshold, however, the strength of the relationship between effective emissivity and plenum pressure and peak cladding temperature are reduced. In addition, at least for the plastic instability criterion, the pulver characteristic length becomes important for both the plenum pressure

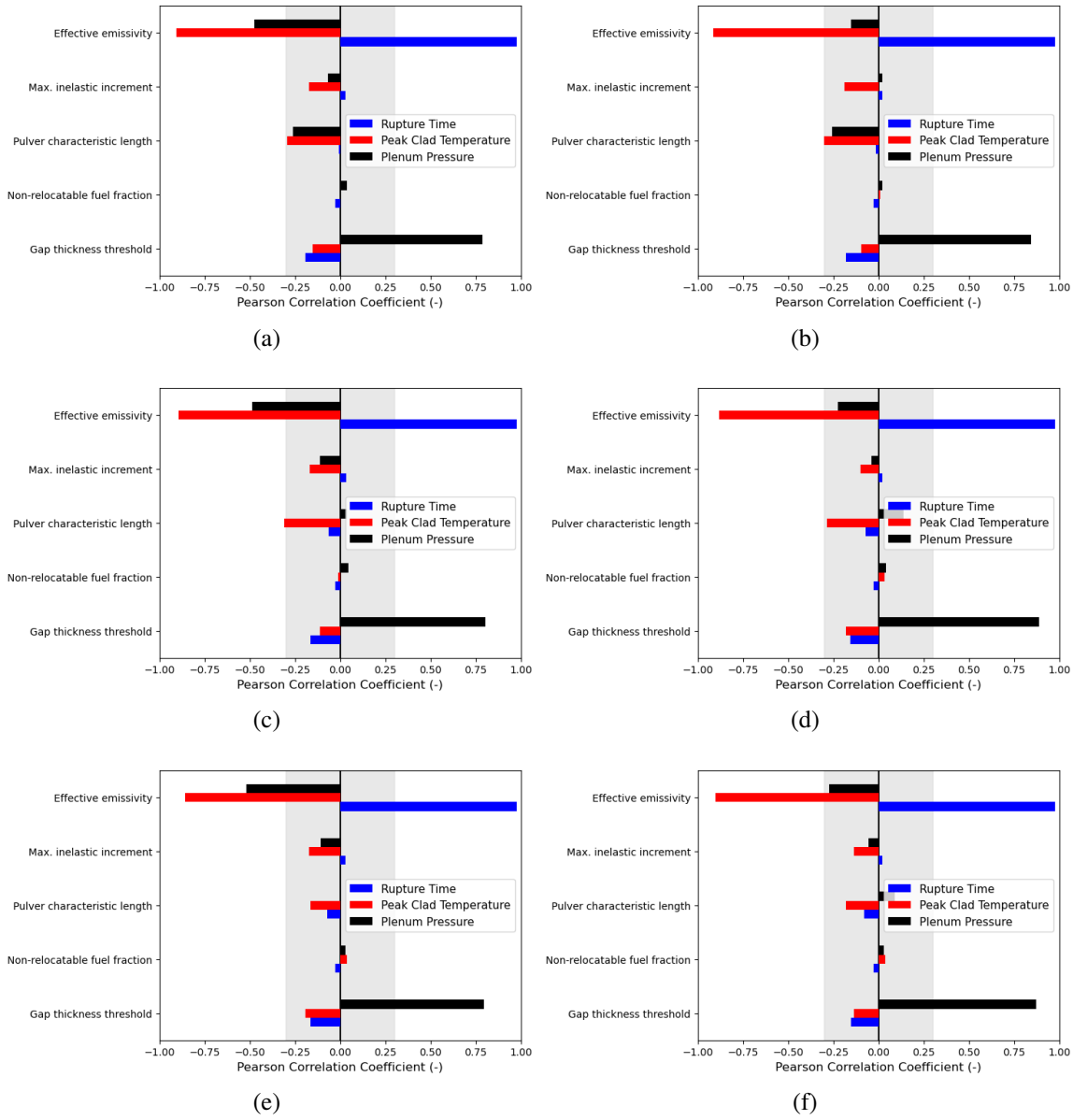

Figure 4.10: Pearson correlation coefficients for IFA-650.4 for the Barani et al. fragmentation correlation. Left and right columns correspond the plastic instability and failure criteria, respectively. The number of fuel layers increases from 15 in the top row to 60 in the bottom.

and peak cladding temperature. This is because the number of large cracks predicted by the Coindreau correlation is higher than that of Barani at the burnups achieved during the base irradiation. Therefore, the packing fraction will be reduced with an increased pulver size due to the fact there are more larger fragments present.

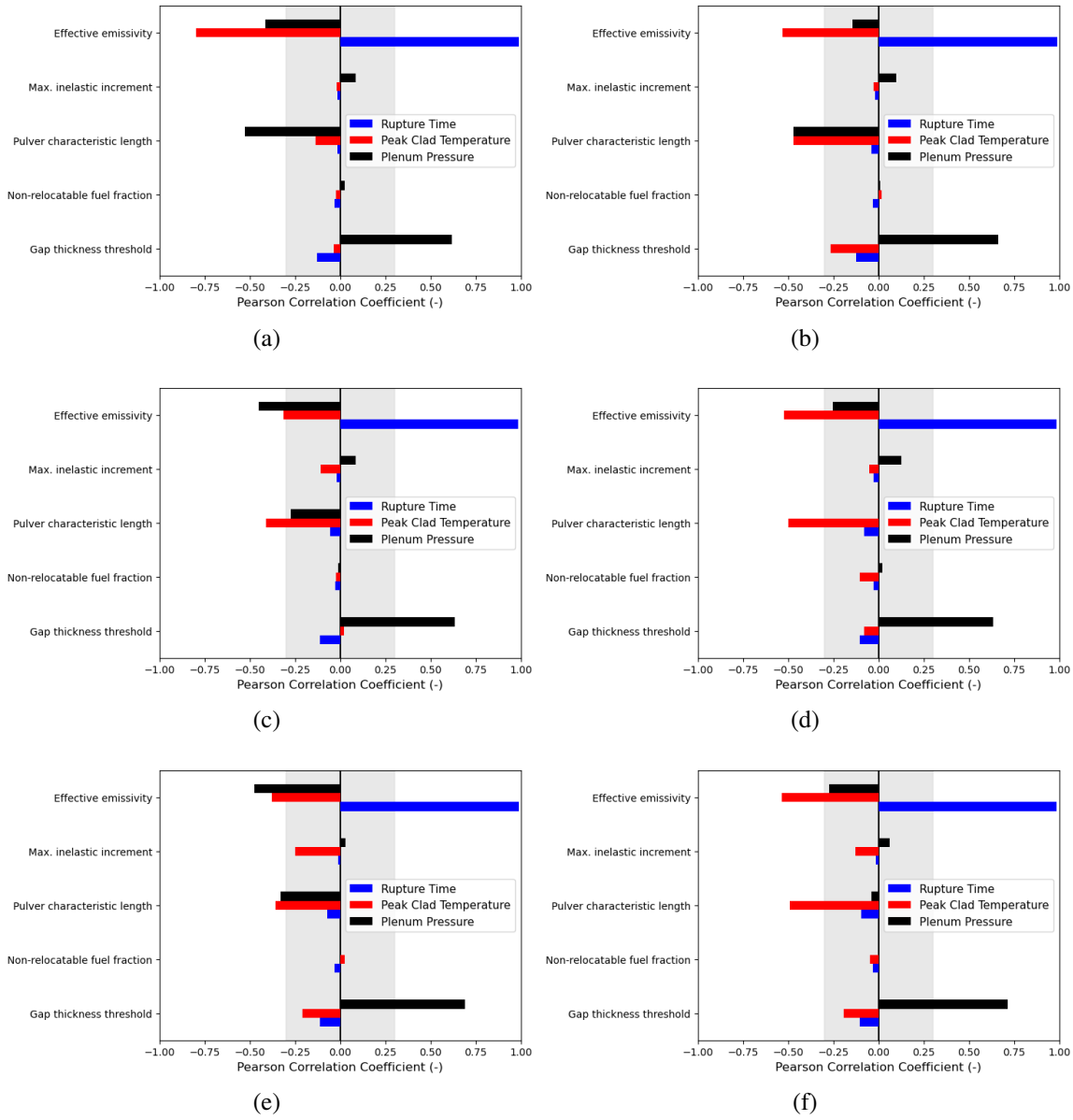

Figure 4.11: Pearson correlation coefficients for IFA-650.4 for the Coindreau et al. fragmentation correlation. Left and right columns correspond the plastic instability and failure criteria, respectively. The number of fuel layers increases from 15 in the top row to 60 in the bottom.

Figure 4.12 presents the Pearson correlation coefficients for IFA-650.4 using the Walton and Matheson large fragment model. The results here are very similar to that of the Barani model.

Another measure of interest when exploring the axial relocation model is the cladding

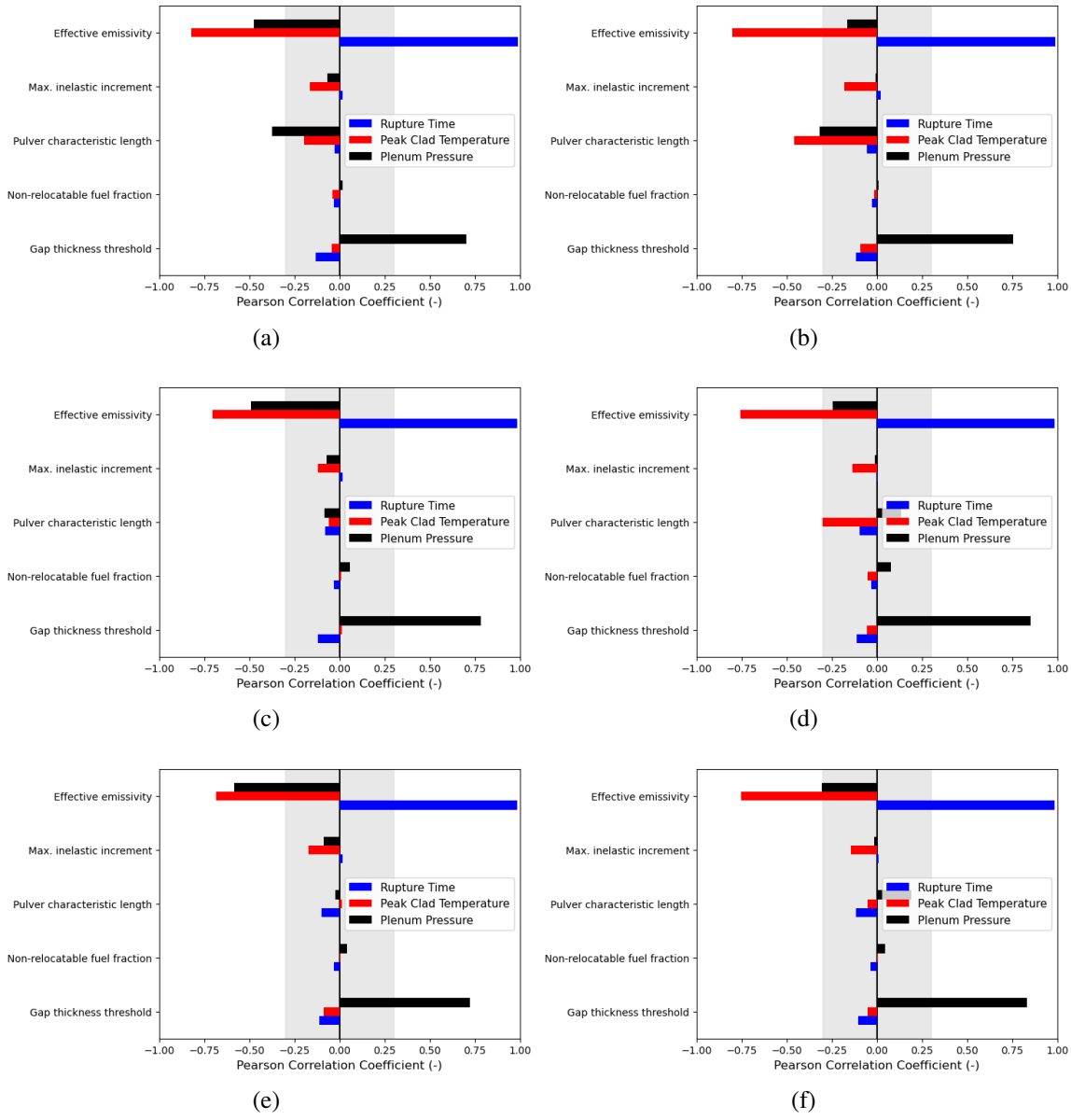

Figure 4.12: Pearson correlation coefficients for IFA-650.4 for the Walton and Matheson fragmentation correlation. Left and right columns correspond the plastic instability and failure criteria, respectively. The number of fuel layers increases from 15 in the top row to 60 in the bottom.

diameter at the time of rupture. The IFA-650.4 experimental measurements do not include a profilometry measurement so all of the results presented in Figure 4.13 through Figure 4.16 do not include an experimental comparison. Figure 4.13 presents the average cladding diameter for the 200 cases for each fragmentation model and failure criteria as listed. The subfig-

ures correspond to the number of fuel layers in the mesh. The dashed-dot line corresponds to the as-fabricated diameter. The axial position of the cladding in the Bison simulations extend past that of the design documents of the IFA-650.4 experiment to enable the correct calculation of the internal volume reported in [55]. It can be seen that a single large balloon is predicted slightly below the rodlet midplane. As expected, in general all fragmentation models and failure criteria combinations follow similar trends with the OS curves extending to a slightly larger diameter. The averages are presented to show that the differences on average are limited between the different fragmentation models. Figure 4.14 through Figure 4.16 illustrate these same averages along with light gray lines of all 200 samples to illustrate the spread on predictions of cladding diameters among the samples for each of the failure criteria and mesh. All of the fragmentation models ahave a larger variation in the peak cladding diameter at the rupture location for the PI criterion vs the OS criterion. As explained when discussion Pearson correlation coefficients, the uncertain inputs will have a larger influence on the creep rate criterion than the total creep strain limit. For the OS criterion, the time at which the total creep strain limit is attained may change, but the same value is reached in all cases, and therefore the balloon size is similar. In the PI case which is creep rate based, the balloon size at the time the limited creep rate is achieved is influenced by quite a few of the uncertain parameters. The Barani and Walton cladding diameters are similar, whereas the cladding diameters predicted when using the Coindreau large fragment model appears to predict a small second balloon forming approximately two-thirds up the rodlet.

Figure 4.17 through Figure 4.20 presents the fuel mass fraction as a function of axial position for IFA-650.4. Figure 4.17 provides the average of all 200 samples for each fragmentation model and failure criterion with each subfigure representing a different mesh density. As with the cladding diameter limited differences are observed amongst the averages. The fuel mass fraction is a measure of the current fuel mass relative to the initial mass at a particular axial location. Therefore, the abscissa axis ranges from 0 to 2, with a

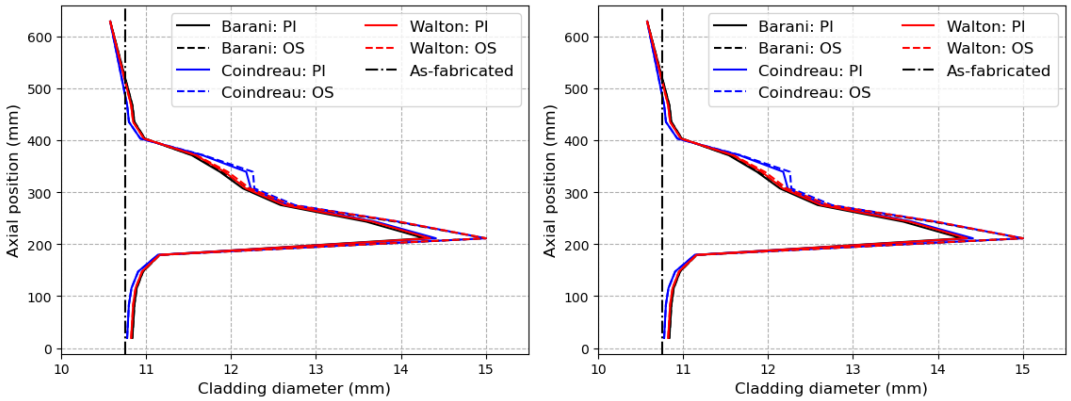

(a) (b)

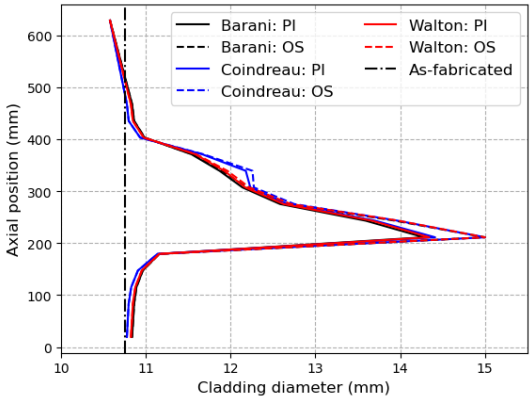

(c)

Figure 4.13: The average cladding diameter of the 200 simulations for the different fragmentation correlations and failure criteria for IFA-650.4. The number of layers used to represent the fuel are (a) 15, (b) 30, and (c) 60. The as-fabricated diameter is also included.

value of 0 representing total fuel loss, which is not possible using the axial relocation model implemented into Bison since there is a non-relocatable fuel fraction (one of the uncertain inputs) for numerical stability reasons. In each row of figures the same Cs-137 gamma scan is provided, highlighting the location of larger quantities of fuel. This gamma scan was taken approximately 6 weeks after the conclusion of the experiment. The gamma scan shows that a single large mass of fuel approxmiately at the midplance of the rodlet with complete fuel loss at the top of the rodlet. The Bison predictions capture the large increase in fuel at the rodlet midplane but a small fuel plug is predicted at the top of the fuel rod. This indicates that in the simulations at the top of the fuel rod, there is insufficient cladding

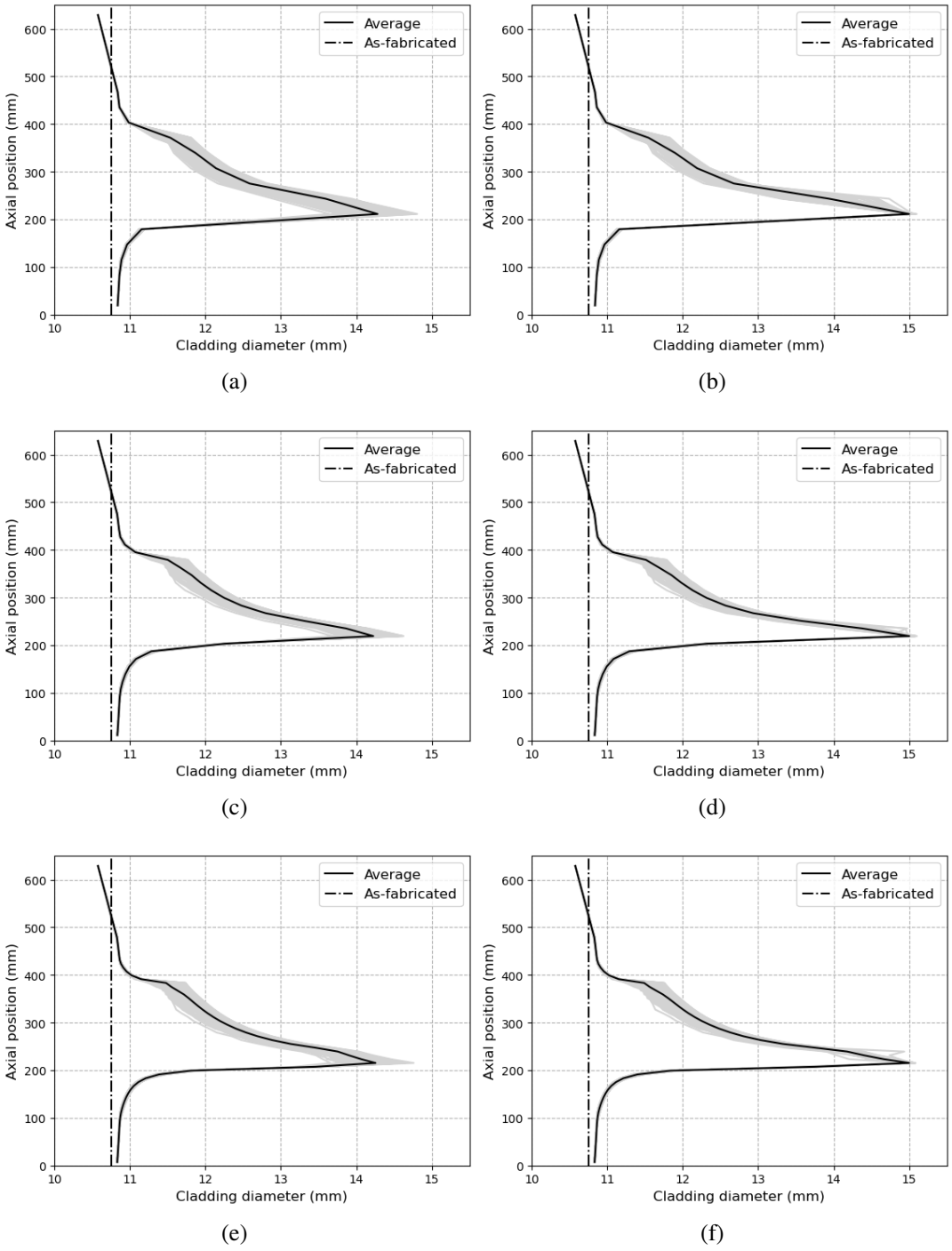

Figure 4.14: The cladding diameter of all 200 simulations for the Barani et al. fragmentation model for IFA-650.4. The left and right columns correspond to the plastic instability and overstrain failure criteria, respectively. The number of layers used to represent the fuel increase from 15 in the top row to 60 in the bottom row. The as-fabricated and average are also included.

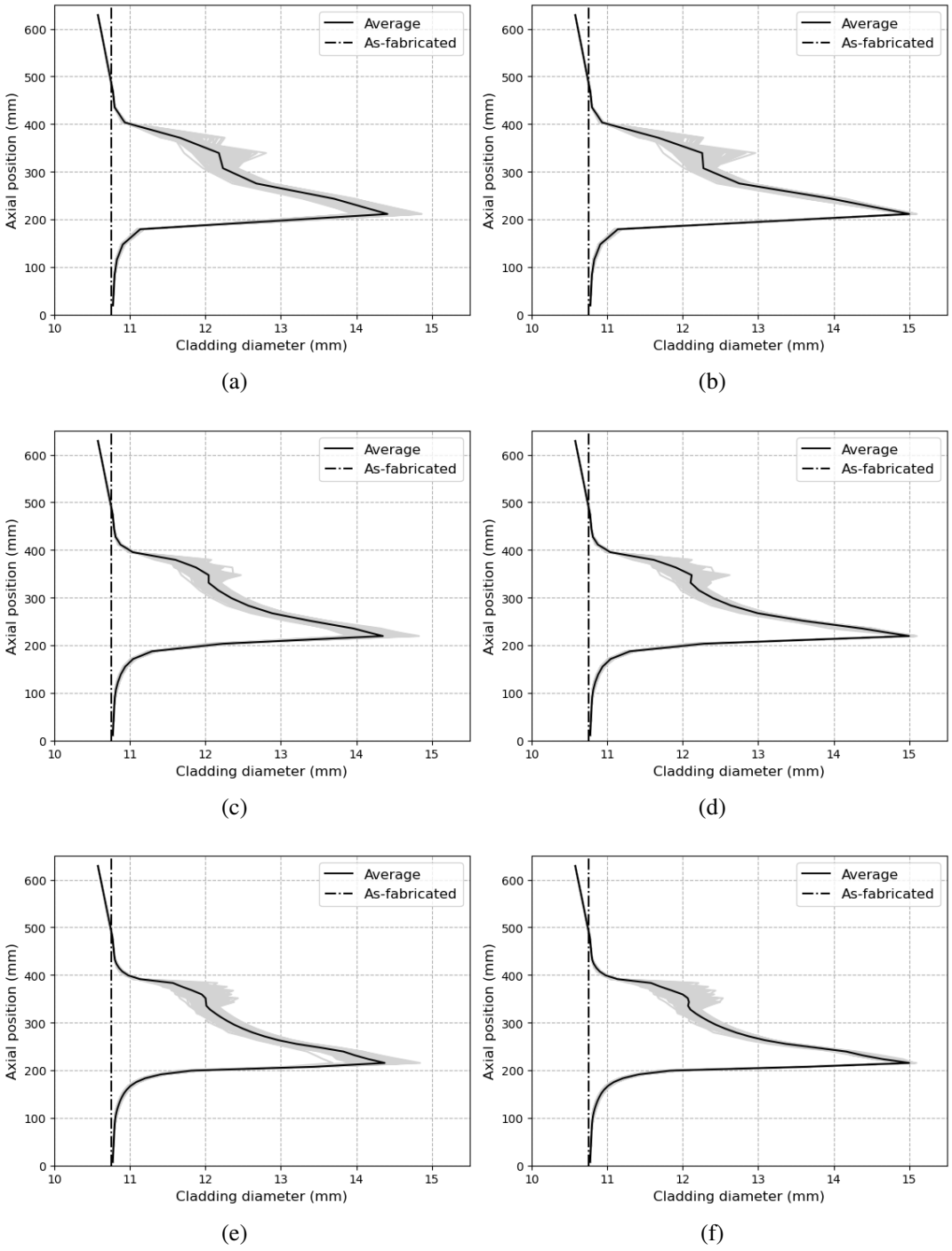

Figure 4.15: The cladding diameter of all 200 simulations for the Coindreau et al. fragmentation model for IFA-650.4. The left and right columns correspond to the plastic instability and overstrain failure criteria, respectively. The number of layers used to represent the fuel increase from 15 in the top row to 60 in the bottom row. The as-fabricated and average are also included.

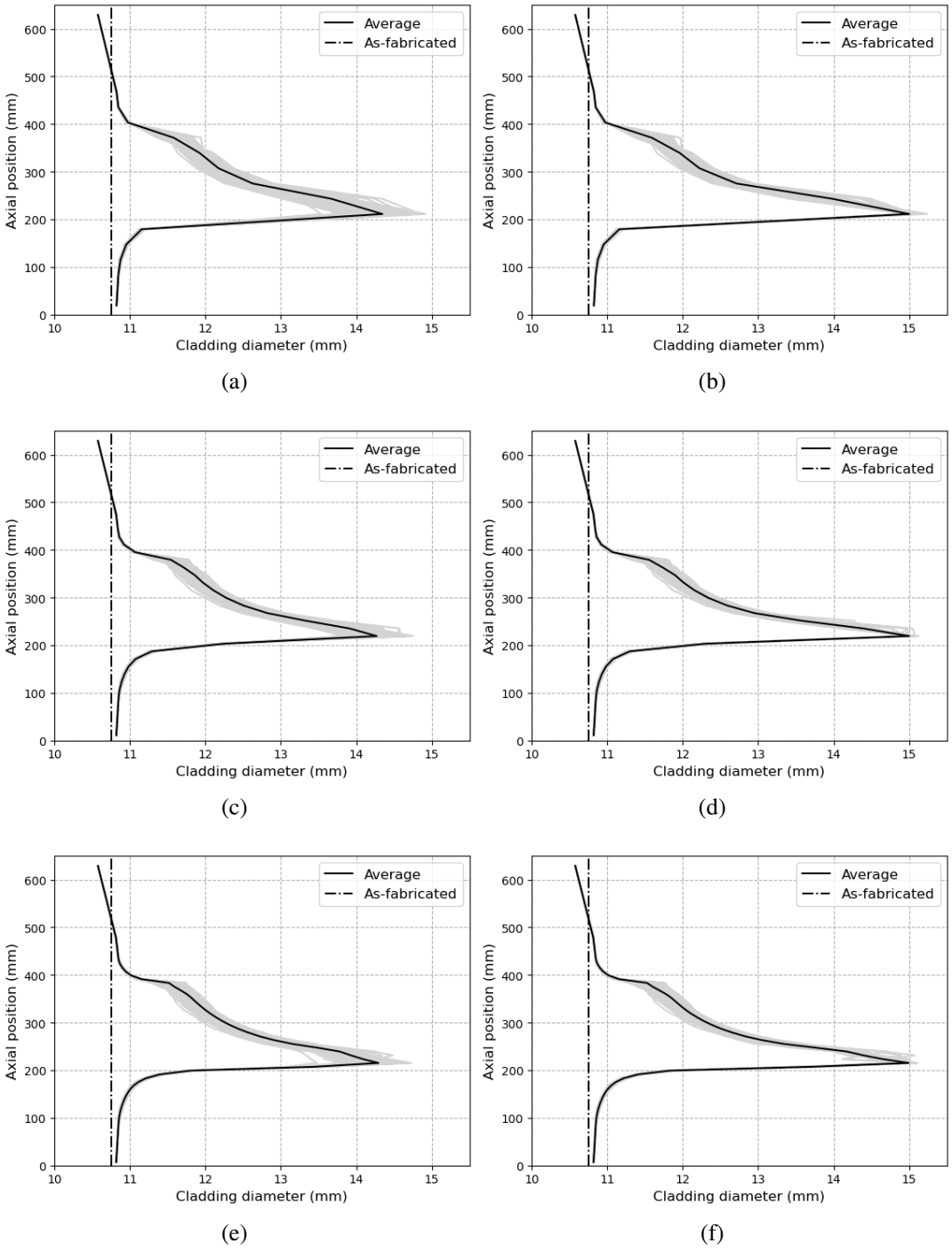

Figure 4.16: The cladding diameter of all 200 simulations for the Walton and Matheson fragmentation model for IFA-650.4. The left and right columns correspond to the plastic instability and overstrain failure criteria, respectively. The number of layers used to represent the fuel increase from 15 in the top row to 60 in the bottom row. The as-fabricated and average are also included.

distention to permit fuel release to axial positions below. In particular for the Coindreau model there is almost zero fuel loss from the top of the rodlet on average. For the other fragmentation models, on average there is at least some fuel loss, albeit small, from the uppermost location of the rodlet.

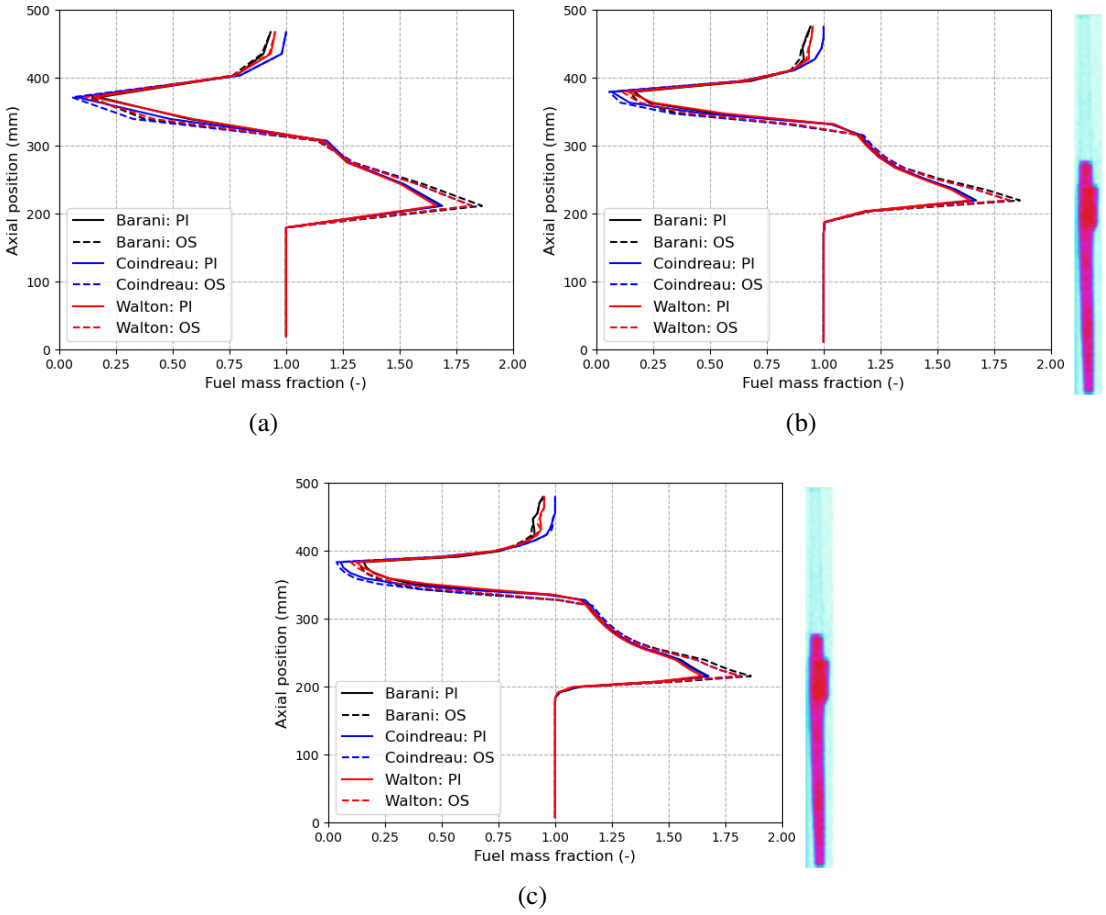

Figure 4.17: The average mass fraction of the 200 simulations for the different fragmentation correlations and failure criteria for IFA-650.4. The number of layers used to represent the fuel are (a) 15, (b) 30, and (c) 60. The as-fabricated diameter is also included.

The 200 samples provided in Figure 4.18 through Figure 4.20 appear to show considerable scatter from the average. Since each line is colored the same, one has to look clustering near the average values. This is particularly difficult in the case where 60 layers are used to model the fuel axially as the points on the plots cluster closer together. The key observation on these plots is the fact that despite the averages predicting limited fuel loss from the top

of the rod, there are a handful of sampled combinations of inputs that do compute complete fuel loss for a large portion of the upper portion of the fuel rodlet consistent with the experimental observations for the Barani and Walton fragmentation models. This highlights that the user could select a combination of inputs within the ranges of study to more accurately predict the experiments. However, in Bison, the goal is not to tune the input parameters for specific experiments but to perform the SA and UQ to identify the spread and input parameters for future computational studies and experiments to help reduce the uncertain and move towards a more predictive capability. This is where the Layered2D approach can play a role as it does not assume the ballooning occurs uniformly along the circumference of the rod.

To exercise the Layered2D framework on a integral fuel performance analysis, the IFA-650.4 case is used. As mentioned previously, not enough information is provided to develop a comprehensive thermal-hydraulics case study on the analysis. However, a multiplicative factor on the time varying heat transfer coefficient that is applied can enable the exploration of azimuthal effects on the cladding deformation and subsequent impact on fuel relocation. This multiplicative factor was chosen such that the azimuthal variation in heat transfer coefficient was from a peak value as provided in the Layered1D analysis, linearly decreasing along the circumference of the rod to a value of 30% less at an angular position of 180 degrees. The values of the uncertain parameters of the axial relocation model correspond to the mean values of the uniform ranges. Only the plastic instability failure criterion was analyzed for Layered2D.

Comparisons of the mass fraction between the Layered1D and Layered2D analysis for IFA-650.4 are presented in Figure 4.21. Because the Layered1D heat transfer coefficients are symmetric and correspond to the higher values at $theta = 0$ in the Layered2D case it is expected in the degraded region, more cladding deformation would happen. Larger deformation would lead to more fuel susceptible to relocation. As can be seen in the mass fraction plot slightly more fuel is released in one of the upper layers into the ballooned

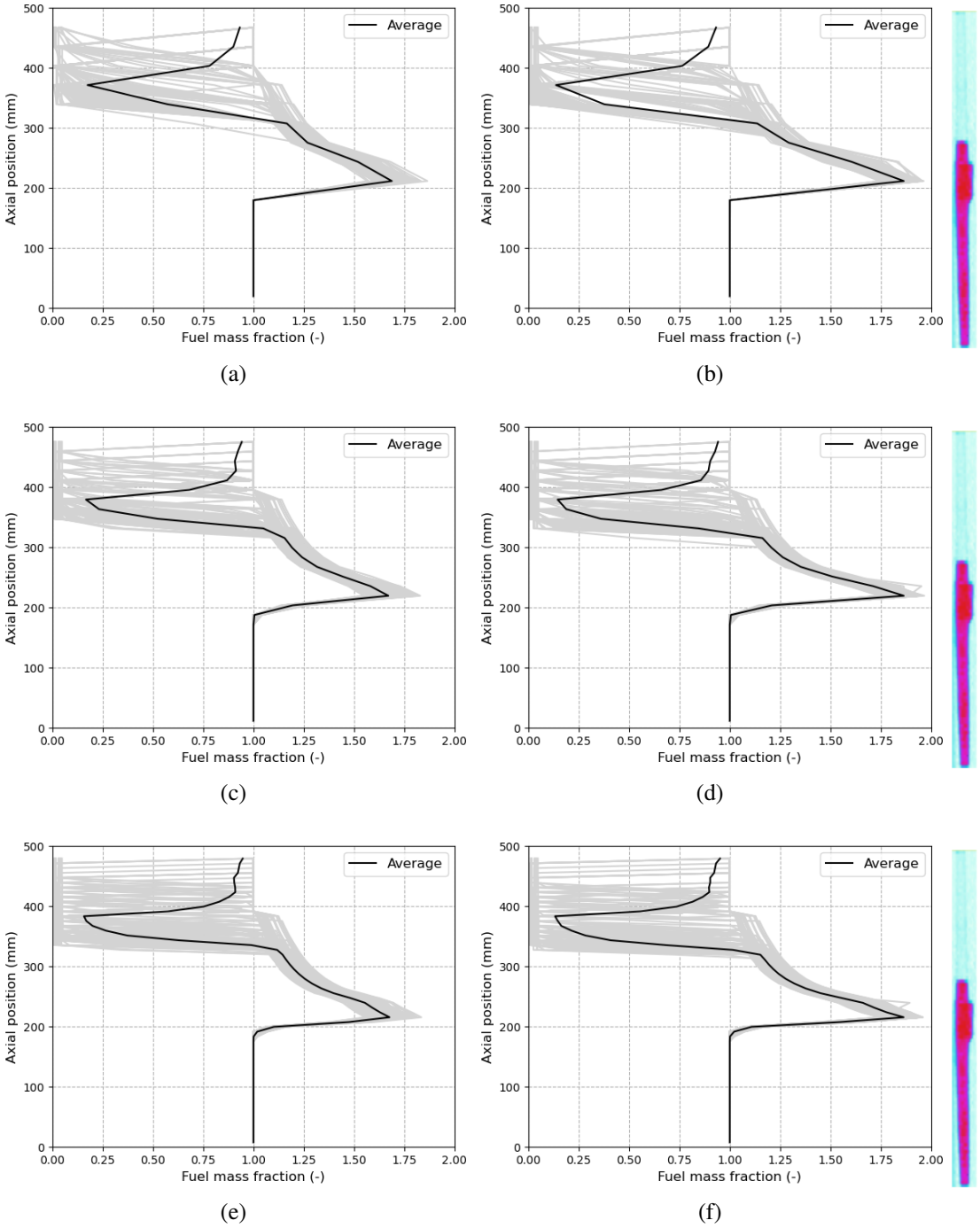

Figure 4.18: The mass fraction of all 200 simulations for the Barani et al. fragmentation model for IFA-650.4. The left and right columns correspond to the plastic instability and overstrain failure criteria, respectively. The number of layers used to represent the fuel increase from 15 in the top row to 60 in the bottom row. The as-fabricated and average are also included.

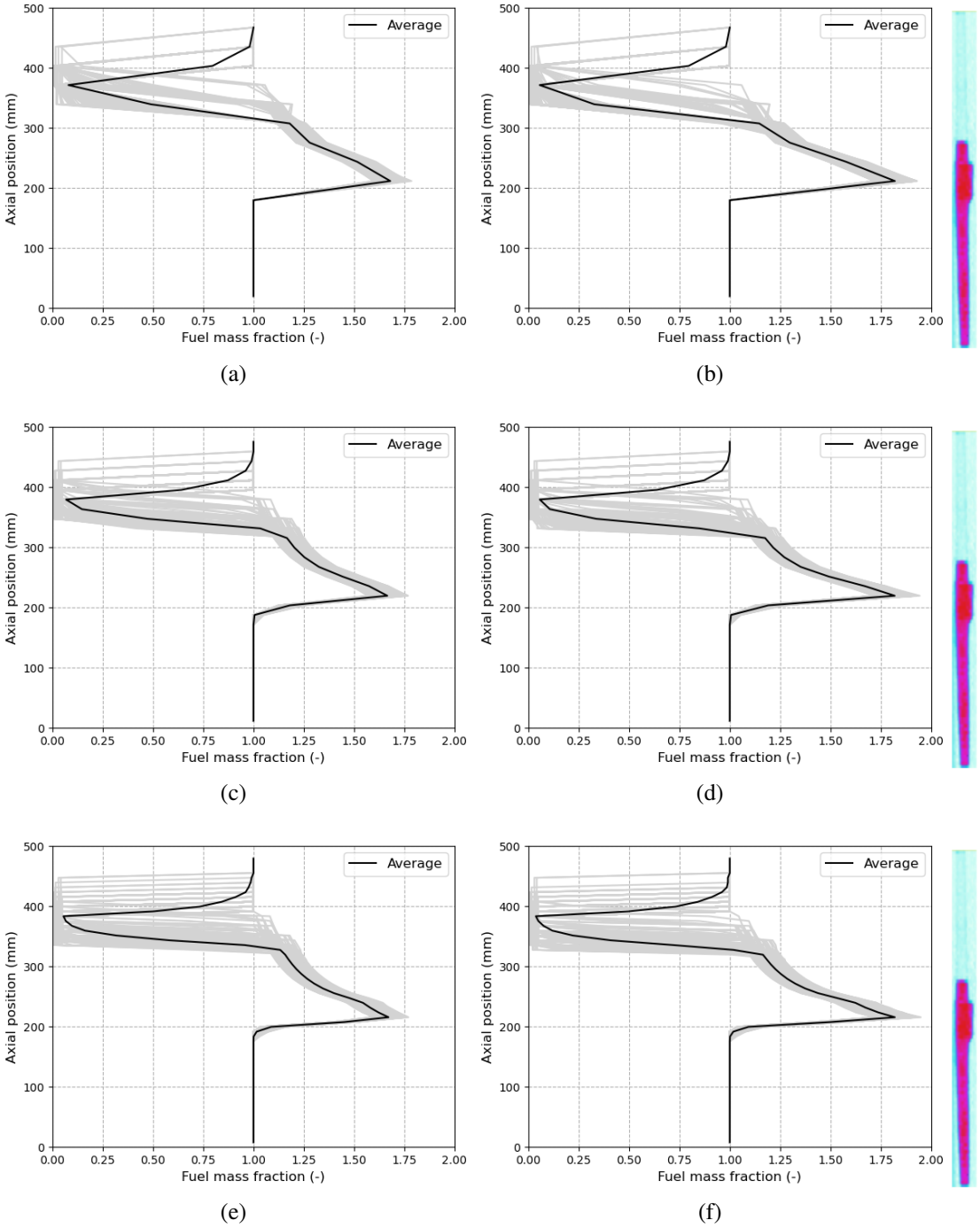

Figure 4.19: The mass fraction of all 200 simulations for the Coindreau et al. fragmentation model for IFA-650.4. The left and right columns correspond to the plastic instability and overstrain failure criteria, respectively. The number of layers used to represent the fuel increase from 15 in the top row to 60 in the bottom row. The as-fabricated and average are also included.

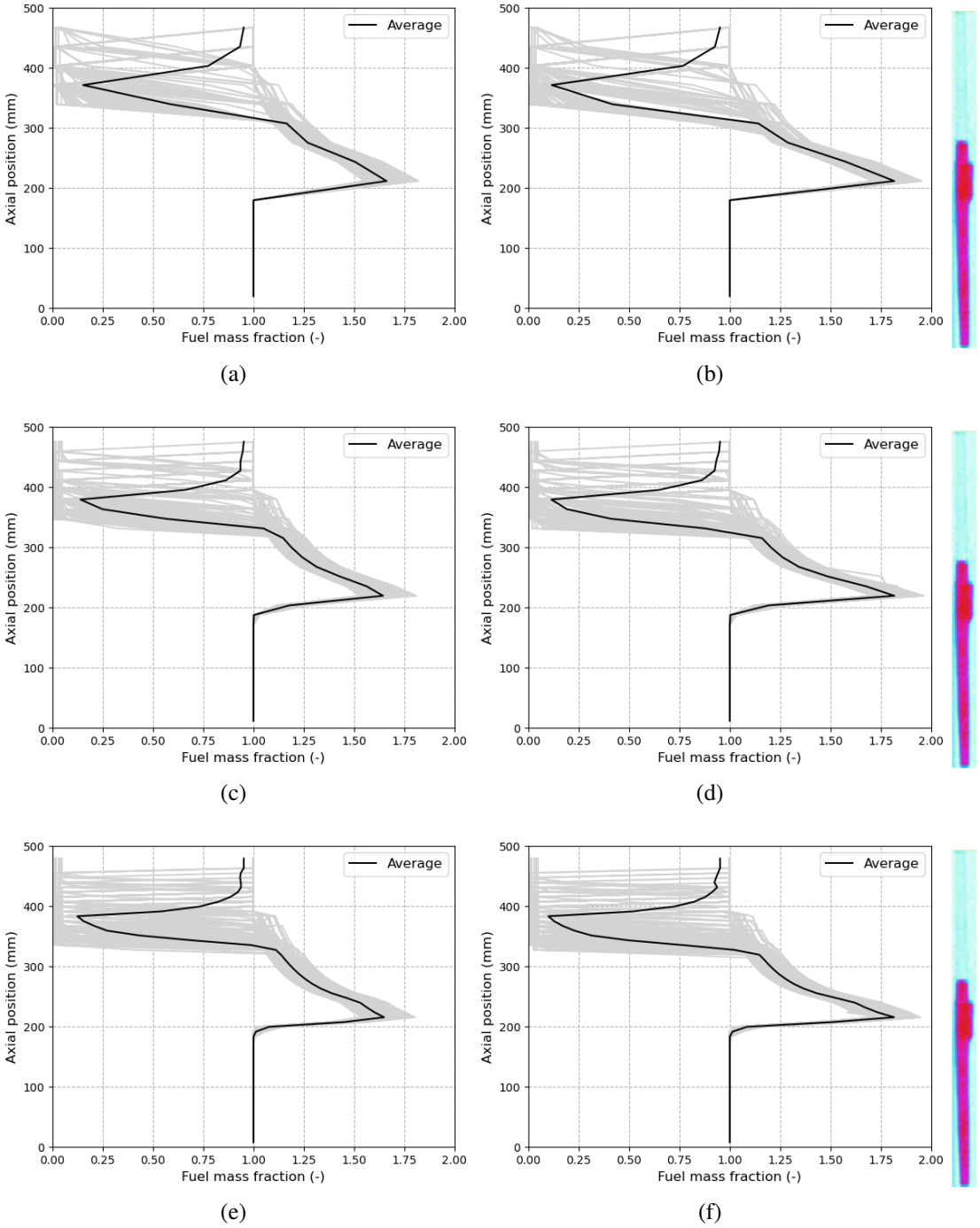

Figure 4.20: The mass fraction of all 200 simulations for the Walton and Matheson fragmentation model for IFA-650.4. The left and right columns correspond to the plastic instability and overstrain failure criteria, respectively. The number of layers used to represent the fuel increase from 15 in the top row to 60 in the bottom row. The as-fabricated and average are also included.

region. Given the lack of data in the experiment for proper developments of the thermal-hydraulic boundary conditions it may not be suitable to pursue a Layered2D version of the IFA-650.4 case. Nevertheless, the development of the capability was completed and it was desired to demonstrate that it is able to capture azimuthal features if they are present.

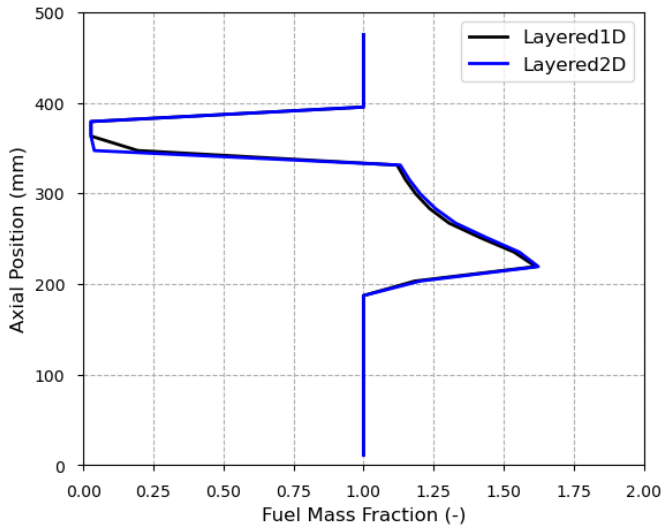

Figure 4.21: Comparisons between Layered1D and Layered2D analyses of IFA-650.4 for the mass fraction.

Results and Analysis of IFA-650.9

All of the same types of of plots presented for IFA-650.4 are provided for IFA-650.9. This experiment was selected for more indepth analysis primarily due to the fact that a unique double balloon was experimentally observed. It is of interest to see if the Bison axial relocation implementation can capture such a phenomenon. The sensitivity analyses results for IFA-650.9 provided in Table 4.6 and Figure 4.22 through Figure 4.32. For this case the rupture time is generally captured with uncertainty with the peak cladding temperature being overpredicted and the rod internal pressure being underpredicted. A higher than expected cladding temperature will drive further creep of the cladding leading to larger distension reducing the pressure. Limited differences as a function of mesh are observed but there are significant differences between the PI and OS failure criteria. In particular, the 2-3 sec-

ond differences in predicted rupture times will reveal that the rodlet undergoes significant change when analyzing the cladding diameter and fuel mass fraction plots.

Table 4.6: Comparisons of the mean calculated value of the fuel performance metrics of interest to the experimental values for IFA-650.9. An uncertainty of $\pm 2\sigma$ is included on the simulation results.

Failure Criterion	Frag. Model	# Fuel Layers	Rupture Time (s)	Peak Clad Temp.† (K)	Rod Internal Pressure† (MPa)
PI	Barani	15	133.63 ± 8.19	1124.43 ± 4.70	5.30 ± 0.2
	Coindreau	15	138.19 ± 10.08	1117.79 ± 3.98	4.99 ± 0.3
	Walton	15	135.71 ± 8.37	1121.16 ± 3.58	5.15 ± 0.16
	Barani	30	133.44 ± 8.67	1124.28 ± 4.26	5.36 ± 0.36
	Coindreau	30	137.78 ± 9.74	1117.44 ± 3.48	5.02 ± 0.26
	Walton	30	135.61 ± 8.45	1121.06 ± 3.79	5.50 ± 0.14
	Barani	60	133.27 ± 8.75	1124.42 ± 3.93	5.38 ± 0.39
	Coindreau	60	137.50 ± 9.57	1116.92 ± 3.61	5.05 ± 0.22
	Walton	60	135.43 ± 8.27	1120.96 ± 4.10	5.20 ± 0.12
OS	Barani	15	135.81 ± 9.03	1132.56 ± 2.29	4.69 ± 0.32
	Coindreau	15	141.34 ± 10.52	1125.12 ± 6.33	4.43 ± 0.34
	Walton	15	138.41 ± 9.53	1127.85 ± 2.75	4.59 ± 0.29
	Barani	30	135.62 ± 9.51	1132.23 ± 1.99	4.76 ± 0.42
	Coindreau	30	140.74 ± 10.29	1123.82 ± 5.49	4.56 ± 0.32
	Walton	30	138.21 ± 9.97	1127.67 ± 2.10	4.64 ± 0.40
	Barani	60	135.40 ± 9.46	1131.84 ± 1.77	4.79 ± 0.43
	Coindreau	60	140.44 ± 10.22	1123.67 ± 5.81	4.61 ± 0.32
	Walton	60	137.93 ± 9.68	1127.10 ± 2.19	4.69 ± 0.34
Experiment	N/A	N/A	133	1083	6.0

†at time of rupture

The Pearson coefficient trends for the double ballooned and higher burnup rod IFA-650.9 are slightly different than that of the single balloon IFA-650.4 case. Here, as seen in Figure 4.22 through Figure 4.24 the relationships between input and output are the same regardless of the large fragmentation model used. The most strongly correlated input is once again the effective emissivity. For this rod however, the second most influence parameter is the maximum inelastic increment, particularly on the peak cladding temperature. For the Coindreau fragmentation model, the maximum inelastic increment also influences the

plenum temperature. The relationships between the outputs and the effective emissivity are the same as for IFA-650.4 and are not further discussed here. The reason for the maximum inelastic increment becoming significant is due to the significant deformation in the two large balloons that form. Since two local areas are deforming rapidly it can be difficult to capture accurately. Thus, a larger inelastic increment will result in a reduction in accuracy of capturing the ballon. The larger inelastic increment will permit larger timesteps that cannot capture the localized deformation in detail. If the deformation is not accurately captured the amount of fuel that relocates into the balloons could be less, which would lead to a reduction in local heat load and a drop in cladding temperatures.

The average cladding diameter of the various fragmentation model, mesh density, and failure criteria combinations are presented in Figure 4.25. The individual realizations along side the averages are presented in Figure 4.26 through Figure 4.28. Contrary to IFA-650.4, there is experimental data for the cladding diameter measured at the 0 degree position of the rodlet. In all of the cladding diameter plots the experimental data is denoted by an x. It can be seen that the Bison simulations do predict the formation of two balloons in all cases. For the PI cases the radial extent of the balloons are much smaller since failure is predicted before the rapid cladding balloon can occur. Even with the overstrain criteria, this strain limit is too small to capture the significantly large balloon at the bottom of the rod. That being said, the OS criterion does a good job at predicting the rodlet midplane balloon. The spread in cladding diameter predictions of the 200 realizations are much more significant for the Coindreau correlation, particularly for the OS failure criteria. In all cases the calculated lower balloon is shifted axially compared to the experimentally measured values. This may be influenced by improved boundary conditions on the cladding outer diameter associated with advanced thermal-hydraulic approaches.

The Cs-137 gamma scan for IFA-650.9 does show the congregation of fuel mass in two distinct regions of the fuel rod. The Bison simulations predict these two regions associated with the larger cladding distance locations as seen in Figure 4.29. Even though the OS

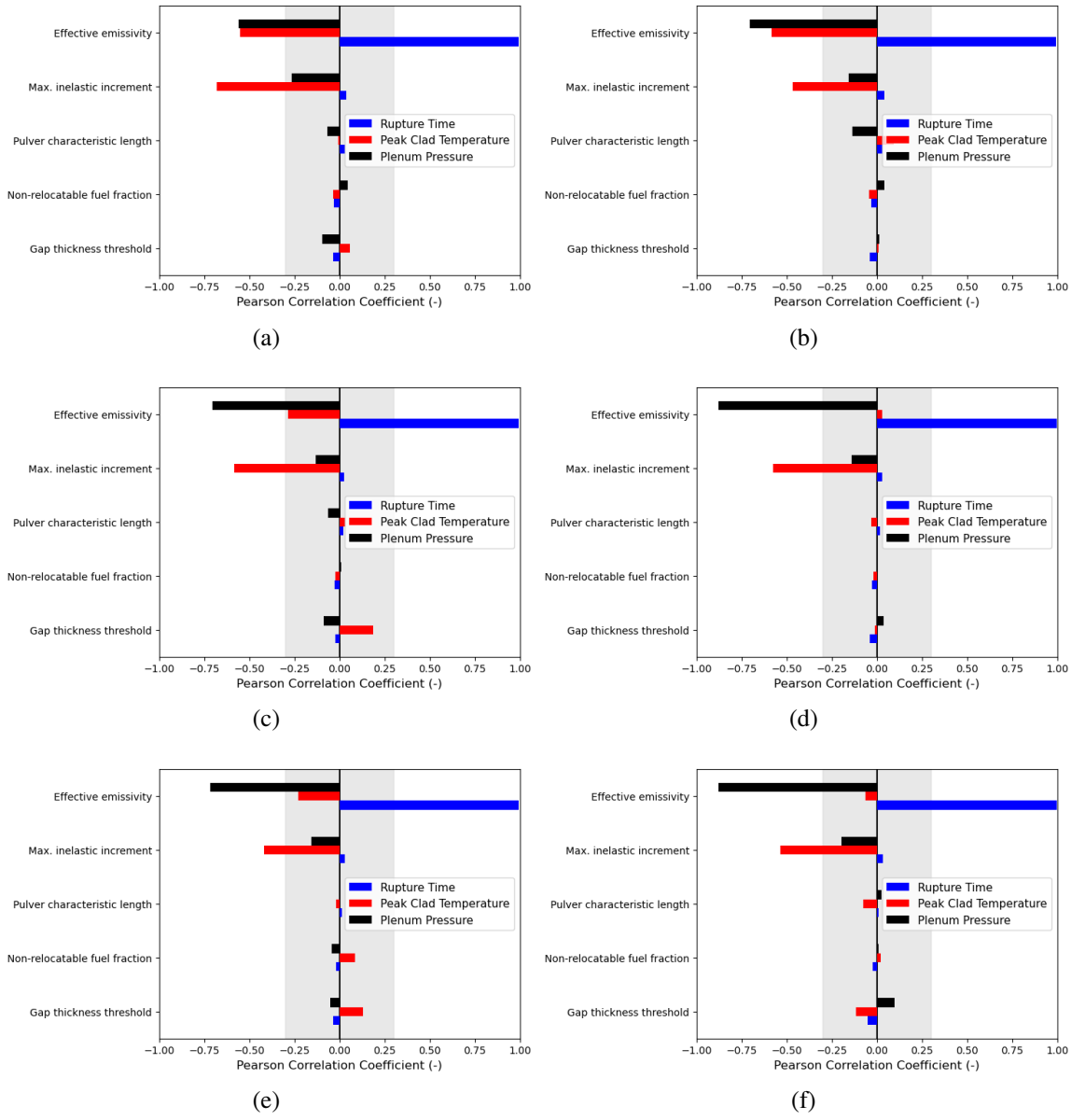

Figure 4.22: Pearson correlation coefficients for IFA-650.9 for the Barani et al. fragmentation correlation. Left and right columns correspond the plastic instability and failure criteria, respectively. The number of fuel layers increases from 15 in the top row to 60 in the bottom.

cases on average are predicted to fail 2-3 seconds after the PI cases it is readily seen that significantly more mass has relocated over that short time period. Similarly to IFA-650.4 the Bison simulations have a difficult time in capturing the behavior at the very top of the fuel rod. In this case there is a fuel plug that is not captured on average. This case, as with

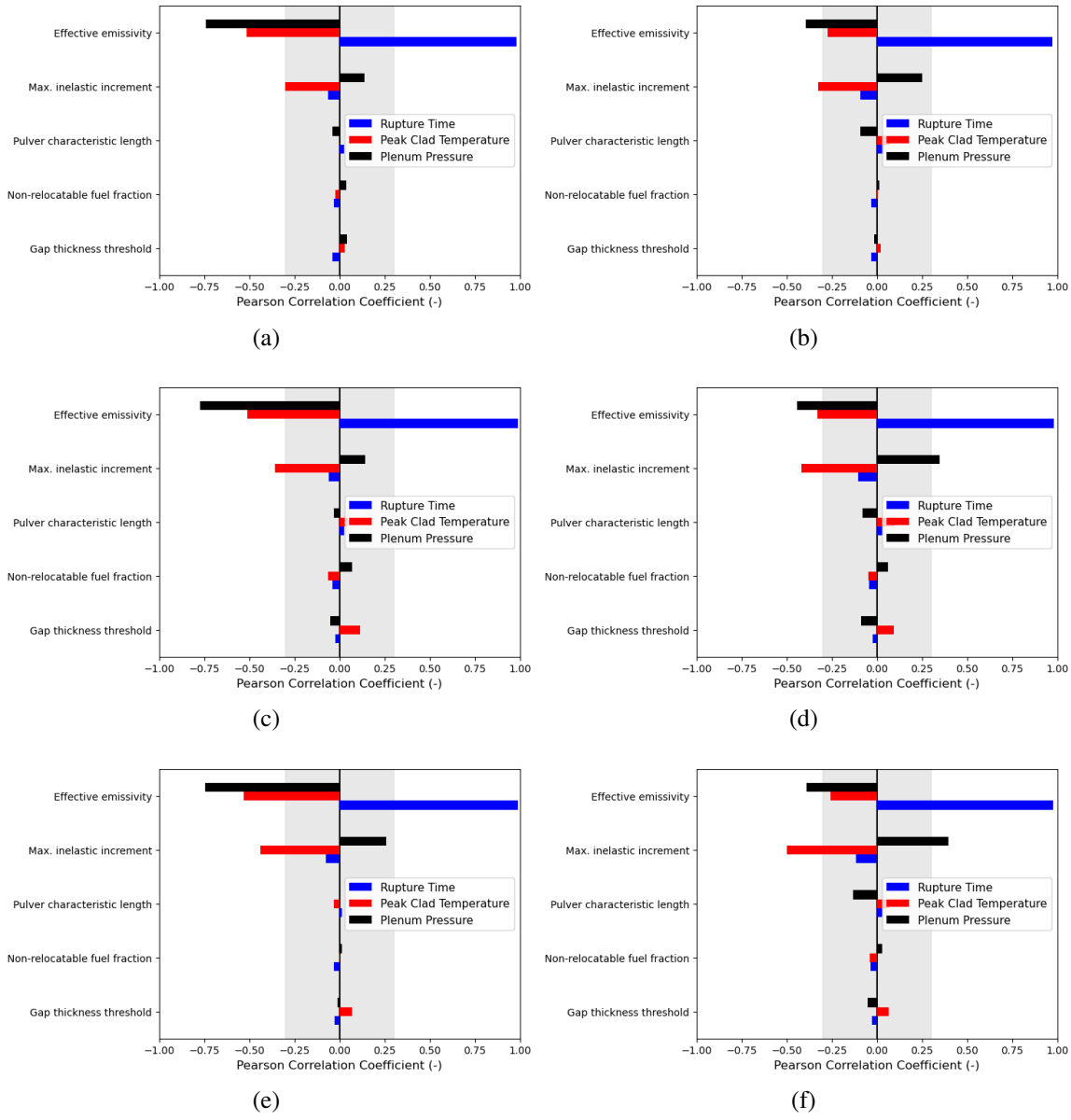

Figure 4.23: Pearson correlation coefficients for IFA-650.9 for the Coindreau et al. fragmentation correlation. Left and right columns correspond the plastic instability and failure criteria, respectively. The number of fuel layers increases from 15 in the top row to 60 in the bottom.

IFA-650.4 both have cladding that is axially longer than experimentally provided to properly account for the internal volume that was reported. This extra length may be influencing the cladding distention and fuel mass movement from the top of the rodlets.

In the plots containing the individual samples (Figure 4.30 through Figure 4.32) it

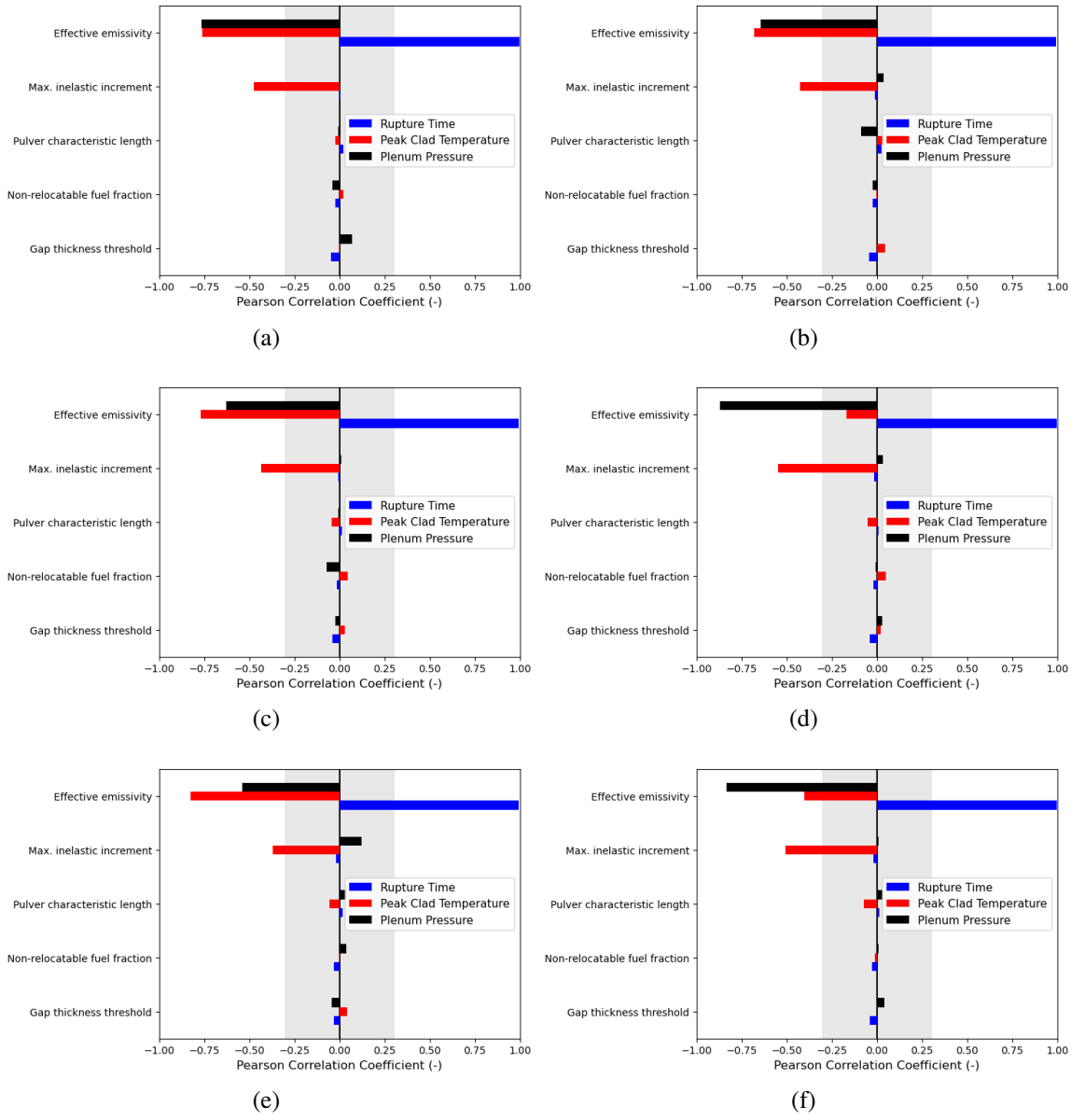

Figure 4.24: Pearson correlation coefficients for IFA-650.9 for the Walton and Matheson fragmentation correlation. Left and right columns correspond the plastic instability and failure criteria, respectively. The number of fuel layers increases from 15 in the top row to 60 in the bottom.

can be seen that some of the realizations do predict the correct rodlet behavior at the top, consistent with IFA-650.4. The amount of fuel loss is directly associated with the fuel mesh axial density. In the Layered1D formulation, since each layer has an associated height, in the 15 layer case, each layer has a larger amount of fuel initially associated with it compared to

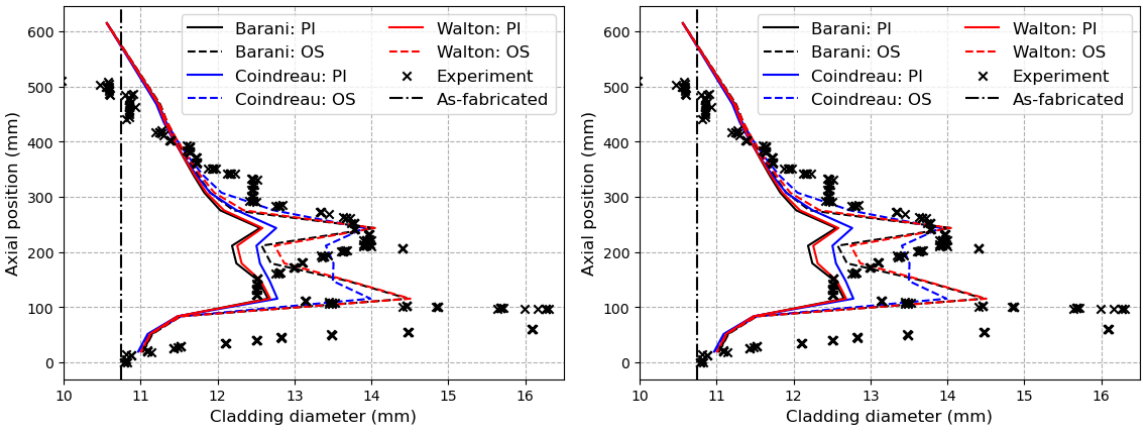

(a) (b)

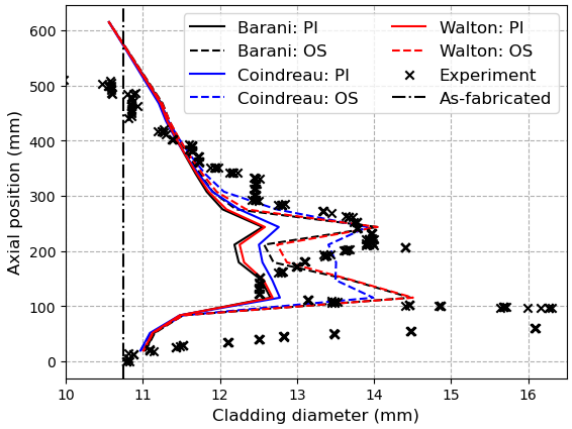

(c)

Figure 4.25: The average cladding diameter of the 200 simulations for the different fragmentation correlations and failure criteria for IFA-650.9. The number of layers used to represent the fuel are (a) 15, (b) 30, and (c) 60. The as-fabricated diameter is also included.

the 60 layer case. Thus, even if the same amount of mass is lost over the same axial distance, this will appear as less mass lost in the top layer in the 15 layer case. This difference in behavior is more pronounced in the the case of the PI failure criterion.

Results and Analysis of IFA-650.14

The sensitivity analyses results for IFA-650.14 provided in Table 4.7 and Figure 4.33 through Figure 4.43. IFA-650.14 was selected due to the unique design of the experiment of having a very small plenum resulting in large cladding ballooning, with no failure. Accordingly,

only a single set of analyses were completed (i.e., no dependence on PI or OS failure criteria). Therefore, comparisons between end time in Table 4.5 are not that meaningful since the simulation was gracefully terminated at 350 seconds. However, of importance is the peak cladding temperature and pressure at this 350 second snapshot in time. As can be seen for this tiny plenum rodlet, Bison severely overpredicts the peak cladding temperature and greatly underpredicts the plenum pressure. This highlights a deficiency in the plenum pressure calculation in Bison for Layered1D geometries when a small plenum is present.

Table 4.7: Comparisons of the mean calculated value of the fuel performance metrics of interest to the experimental values for IFA-650.14. An uncertainty of $\pm 2\sigma$ is included on the simulation results.

Frag. Model	# Fuel Layers	End Time (s)	Peak Clad Temp.† (K)	Rod Internal Pressure† (MPa)
Barani	15	350	1175.61 ± 42.14	1.15 ± 0.45
Coindreau	15	350	1170.29 ± 35.01	1.17 ± 0.60
Walton	15	350	1175.08 ± 40.85	1.13 ± 0.47
Barani	30	350	1182.14 ± 40.59	1.13 ± 0.48
Coindreau	30	350	1172.82 ± 34.50	1.18 ± 0.59
Walton	30	350	1180.98 ± 38.33	1.12 ± 0.50
Barani	60	350	1183.44 ± 42.63	1.18 ± 0.60
Coindreau	60	350	1176.54 ± 34.82	1.20 ± 0.66
Walton	60	350	1183.48 ± 40.16	1.17 ± 0.58
Experiment	N/A	N/A	973	3.5

†at simulation end

The Pearson correlation coefficients for the IFA-650.14 case does not include rupture time as the cladding did not rupture in the experiment or in the simulation calculations. Here, the only parameter with any significant relationship on the outputs of interest is the effective emissivity using in the radiation heat transfer coefficient calculation. Contrary to the results of IFA-650.4 and IFA-650.9, IFA-650.14 shows a different trend in regards to the plenum pressure. In this small plenum case an increasing emissivity results in an increasing internal pressure. This makes sense, since an increasing emissivity would lower the temperatures and subsequently reduce ballooning. In the case of a very small plenum

the pressure is strongly correlated with the volume in the rod as small displacements can yield large changes in volume.

When observing the Bison comparisons to the cladding diameter data for IFA-650.14[1] in Figure 4.36 through Figure 4.39 the location and amount of maximum cladding distention is captured quite well for the Barani and Walton models. The Coindreau model is suppressing the large balloon and predicting two smaller separate balloons.

The smaller plenum size does not require the Bison analysis to have a larger than reported cladding length. Therefore, the mass fraction plots in Figure 4.40 through Figure 4.43 properly calculate the small region of total loss at the top of the fuel rodlet. In addition a larger axial region is calculated to have gained mass, which is the same trend as observed in the Cs-137 gamma scan. Even though the Coindreau fragmentation model computes the beginning formation of a double balloon it is found that a larger portion of that mass moves into the lower balloon. The results between the Barani and Walton correlations are very similar.

4.6 SUMMARY

In this chapter, an overview of existing modeling methods for axial fuel relocation during a LOCA was presented. Full details were provided for the Jernkvist and Massih [53] model as it was used as the basis for further studies in this chapter. A new Layered2D formulation was presented including theory, mesh generation capabilities, and verification were provided. Then, a comprehensive sensitivity study was performed on 3 rodlets from the IFA-650 LOCA test series completed at the Halden reactor in Norway which indicated that the emissivity used for the heat transfer coefficient for radiation between the cladding and heater after blowdown was the most influential parameter. Thus, using this information, a single Layered2D analysis of the IFA-650.4 rodlet was completed using the average values from the sensitivity table for each of the uncertain parameters with an azimuthal variation on

[1]The experimental data is obtained after the experiment and not at the 350 seconds after blowdown

the convective heat transfer coefficient after blowdown. The results illustrated that slightly more fuel is released into the balloon region for Layered2D case when the heat transfer coefficient is degraded by 30% azimuthally from the values used in the Layered1D case. From an industry perspective, the new Layered2D modeling framework provides a tool to analyze the impacts of azimuthal boundary conditions on fuel relocation behavior. However, when conducting experiments care must be taken to better characterize the thermal-hydraulics of the experiment to facilitate proper definition of the complicated azimuthally and axially varying conditions.

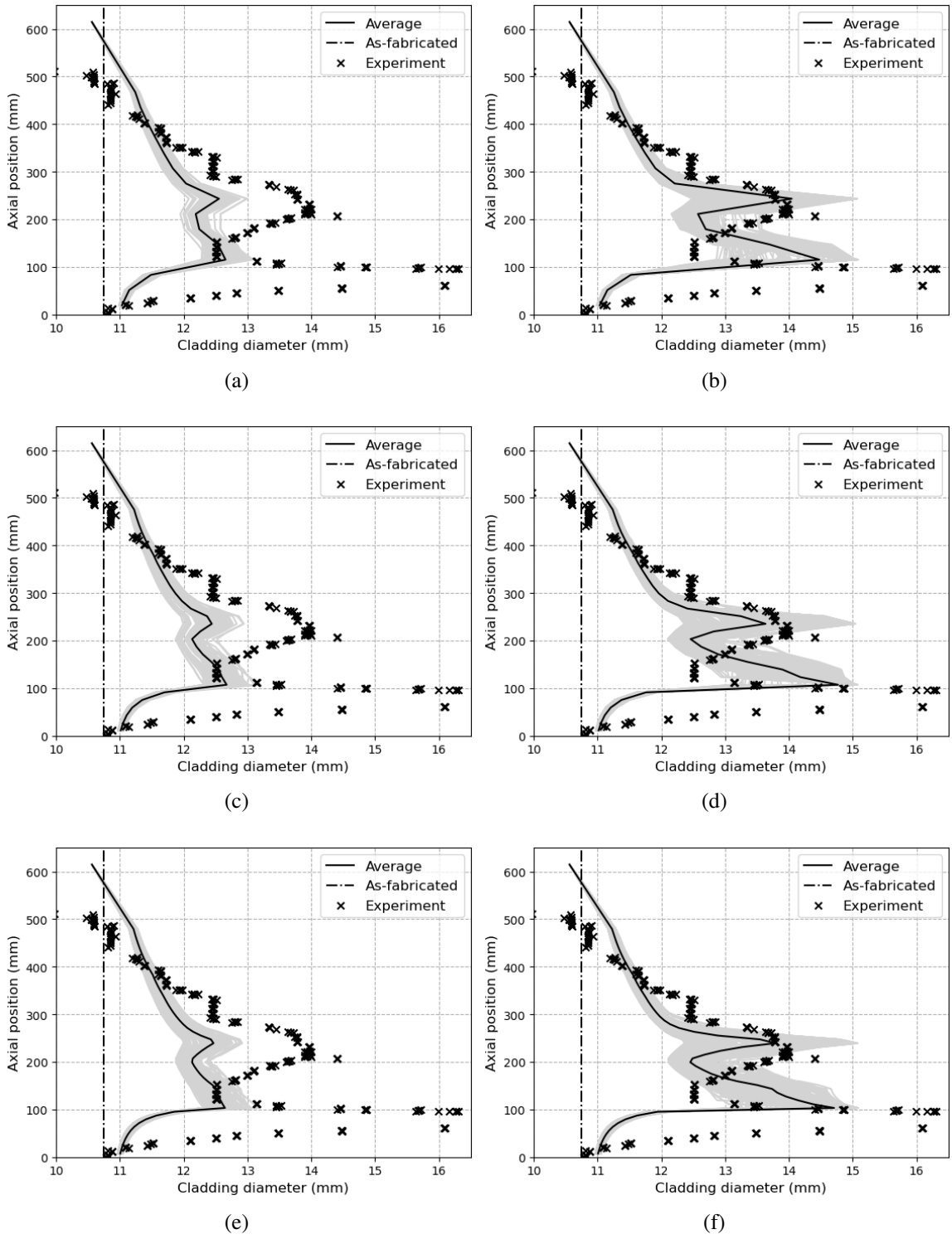

Figure 4.26: The cladding diameter of all 200 simulations for the Barani et al. fragmentation model for IFA-650.9. The left and right columns correspond to the plastic instability and overstrain failure criteria, respectively. The number of layers used to represent the fuel increase from 15 in the top row to 60 in the bottom row. The as-fabricated and average are also included.

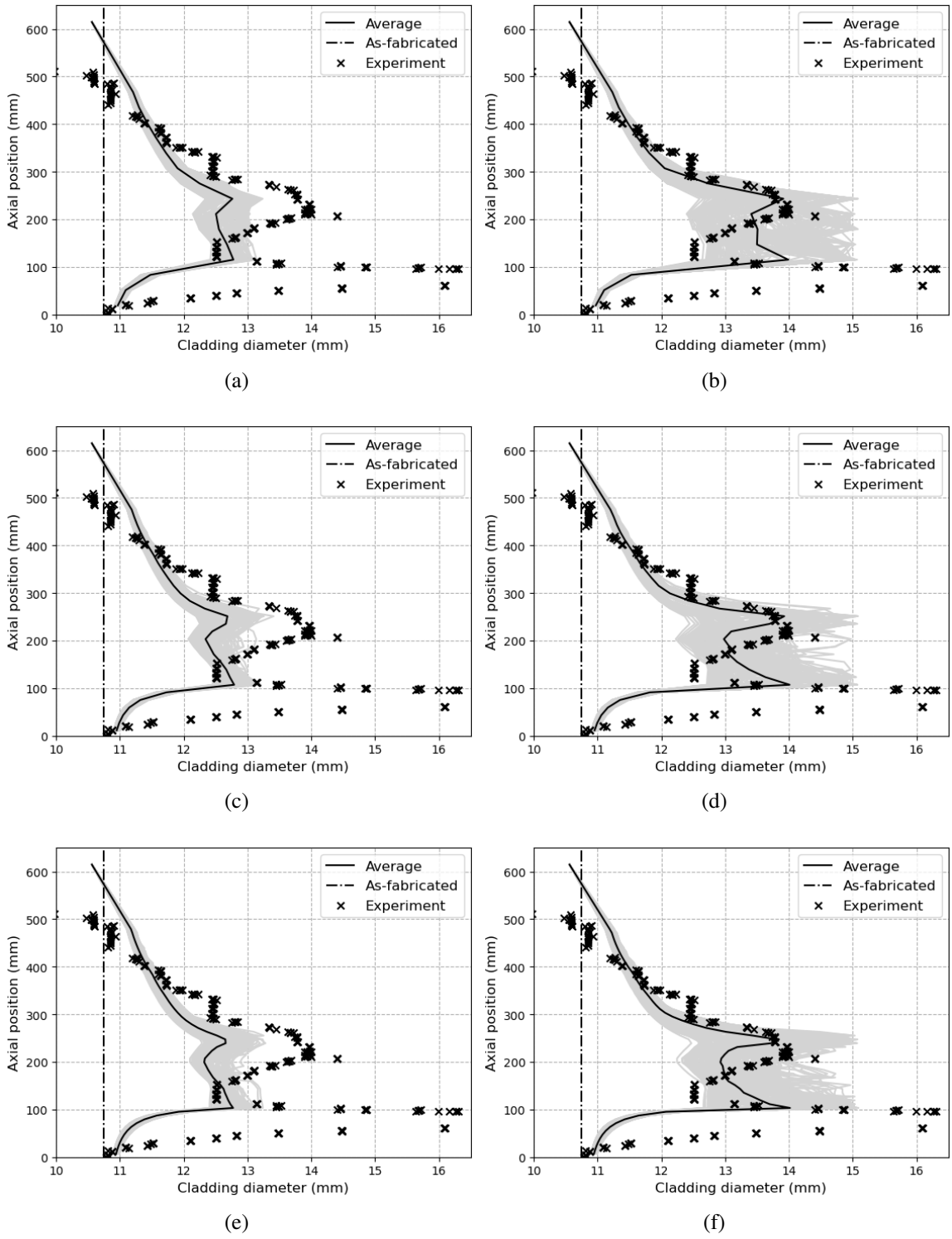

Figure 4.27: The cladding diameter of all 200 simulations for the Coindreau et al. fragmentation model for IFA-650.9. The left and right columns correspond to the plastic instability and overstrain failure criteria, respectively. The number of layers used to represent the fuel increase from 15 in the top row to 60 in the bottom row. The as-fabricated and average are also included.

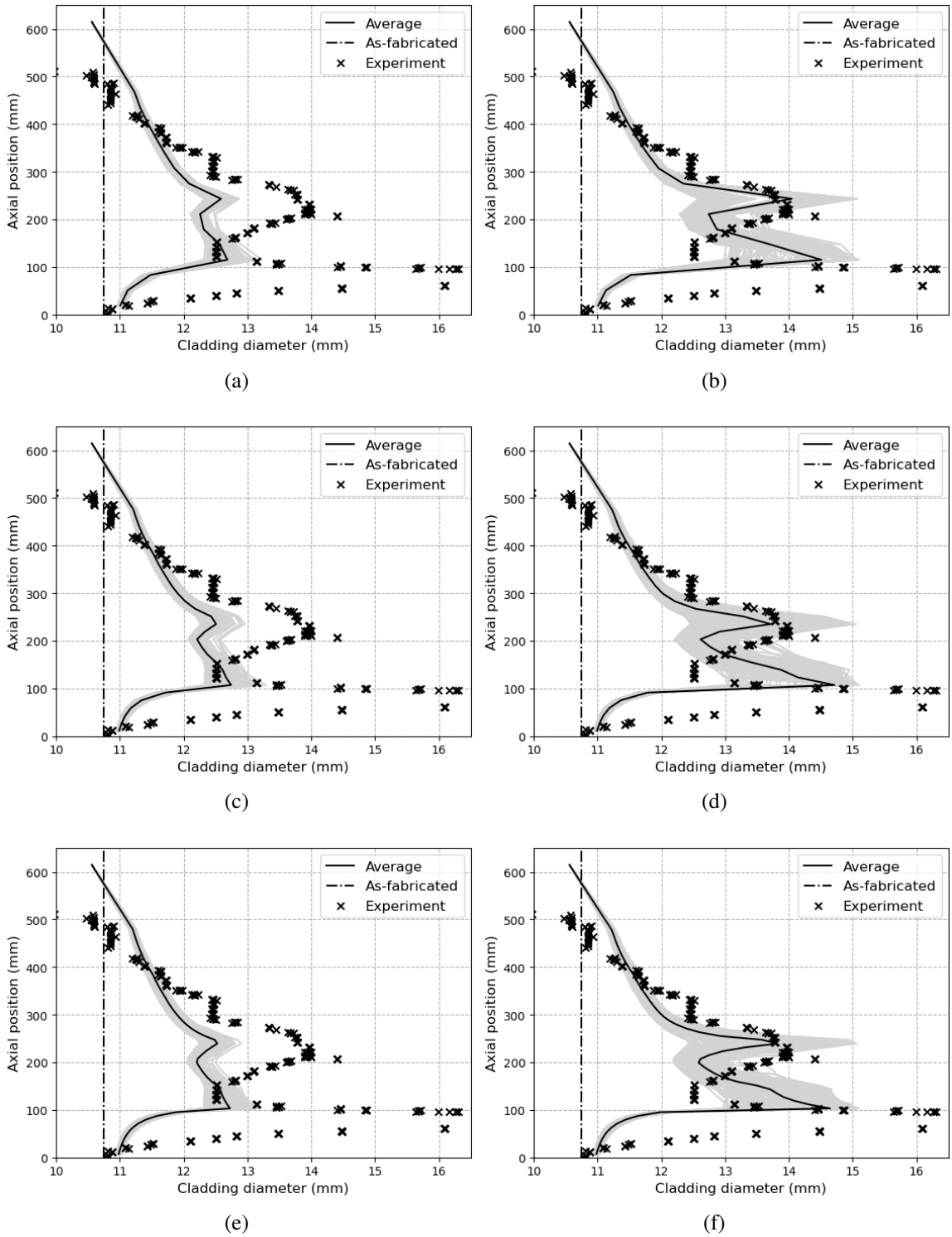

Figure 4.28: The cladding diameter of all 200 simulations for the Walton and Matheson fragmentation model for IFA-650.9. The left and right columns correspond to the plastic instability and overstrain failure criteria, respectively. The number of layers used to represent the fuel increase from 15 in the top row to 60 in the bottom row. The as-fabricated and average are also included.

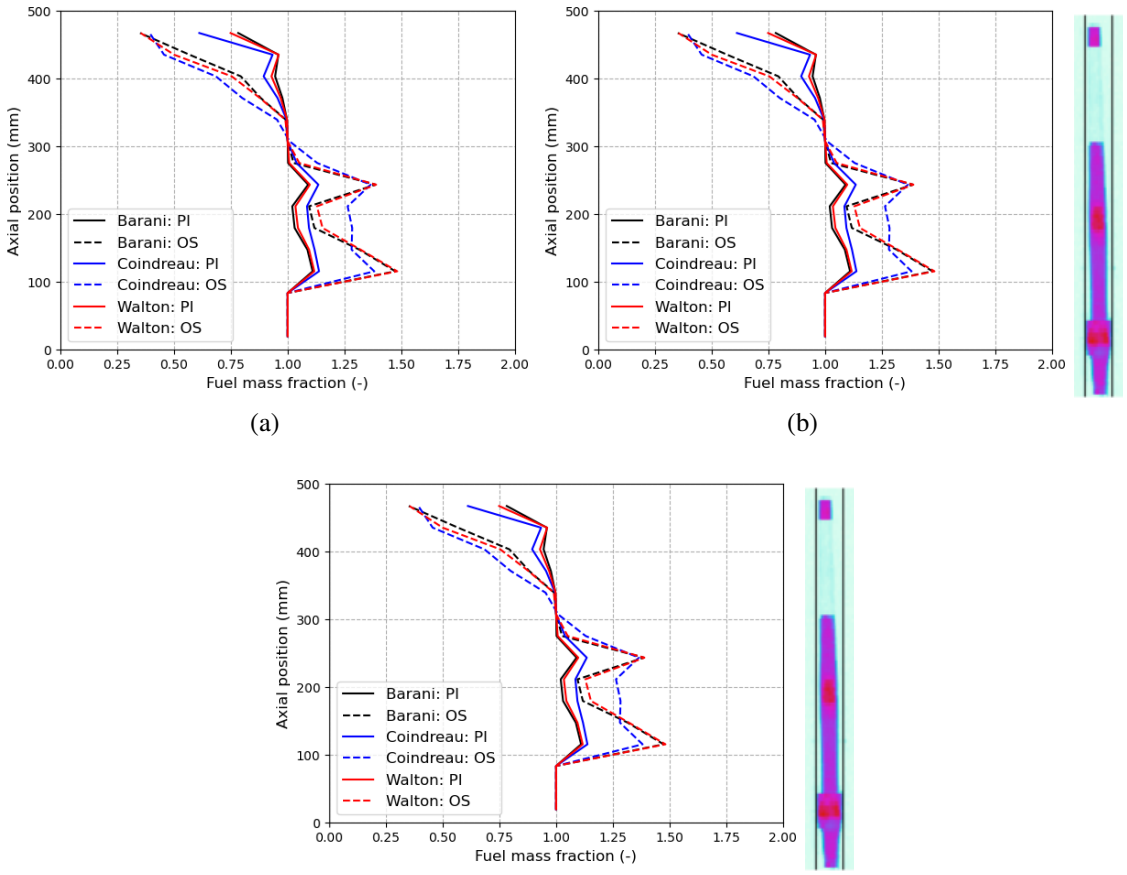

Figure 4.29: The average mass fraction of the 200 simulations for the different fragmentation correlations and failure criteria for IFA-650.9. The number of layers used to represent the fuel are (a) 15, (b) 30, and (c) 60. The as-fabricated diameter is also included.

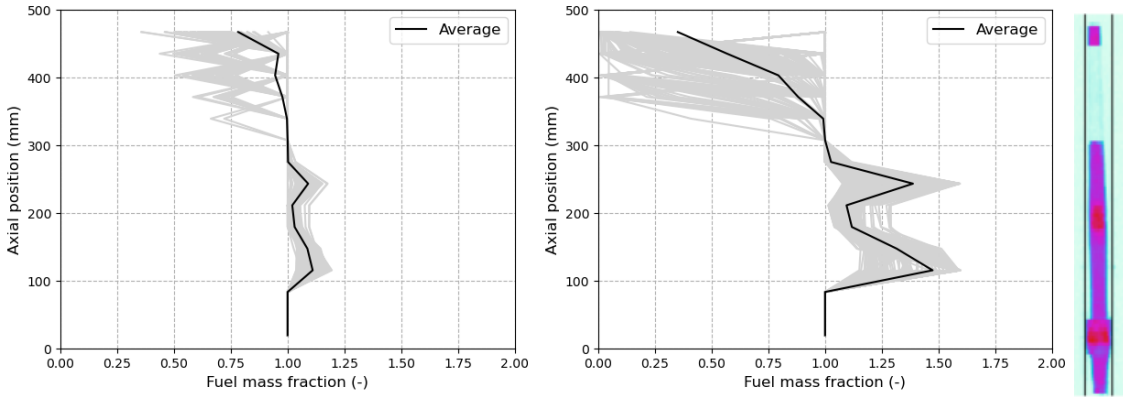

(a) (b)

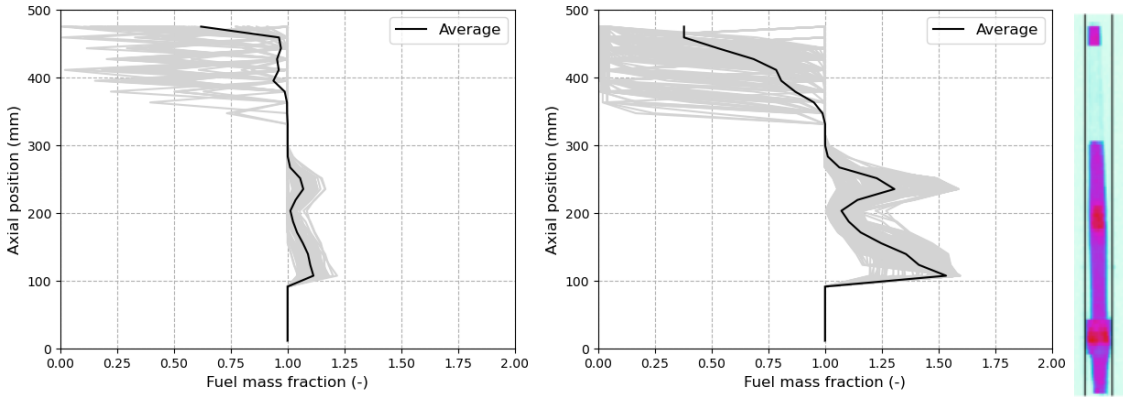

(c) (d)

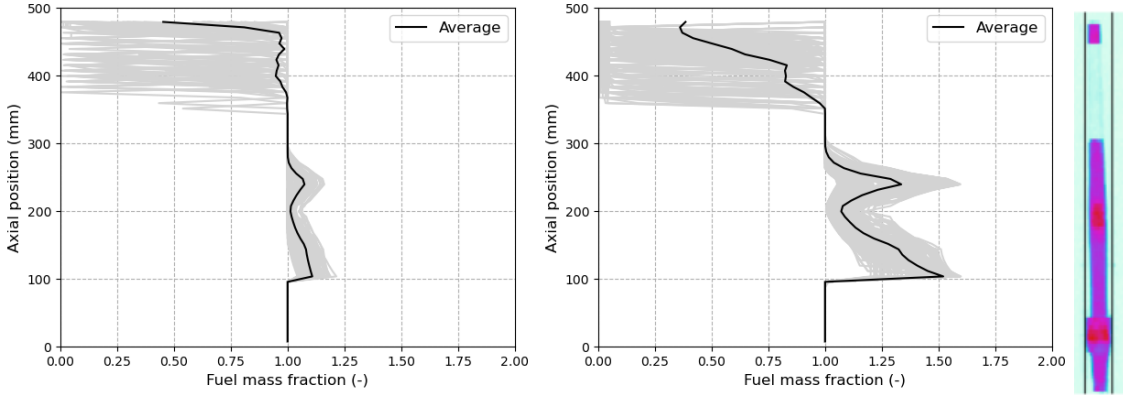

(e) (f)

Figure 4.30: The mass fraction of all 200 simulations for the Barani et al. fragmentation model for IFA-650.9. The left and right columns correspond to the plastic instability and overstrain failure criteria, respectively. The number of layers used to represent the fuel increase from 15 in the top row to 60 in the bottom row. The as-fabricated and average are also included.

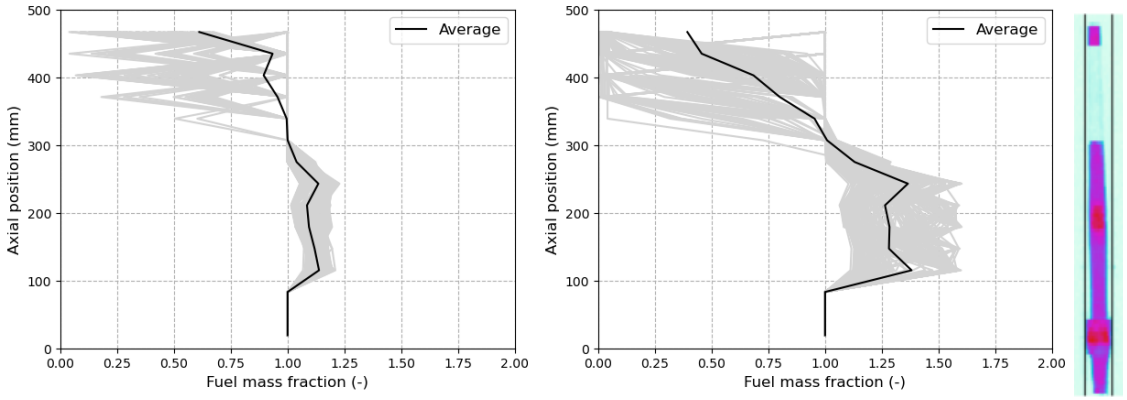

(a) (b)

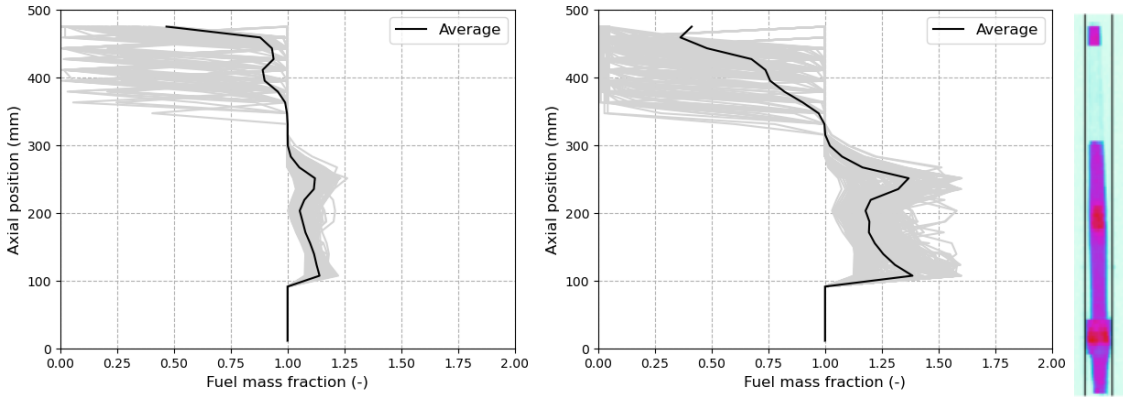

(c) (d)

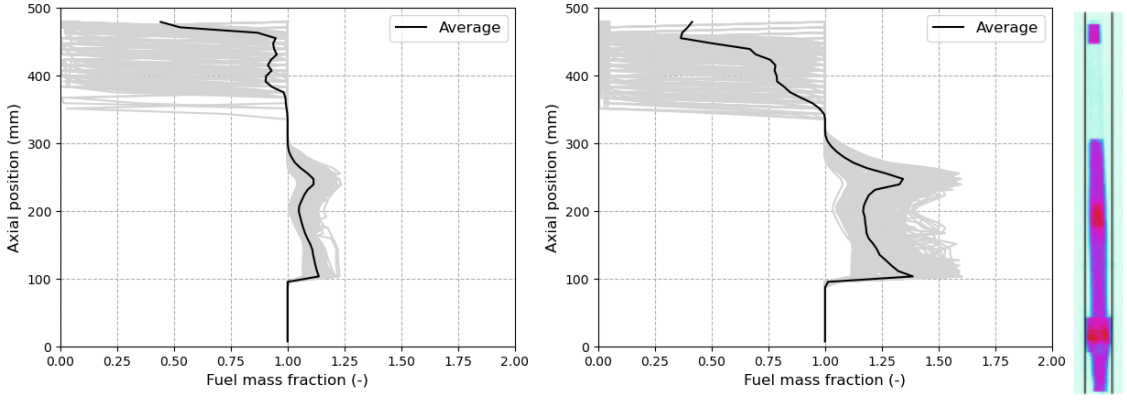

(e) (f)

Figure 4.31: The mass fraction of all 200 simulations for the Coindreau et al. fragmentation model for IFA-650.9. The left and right columns correspond to the plastic instability and overstrain failure criteria, respectively. The number of layers used to represent the fuel increase from 15 in the top row to 60 in the bottom row. The as-fabricated and average are also included.

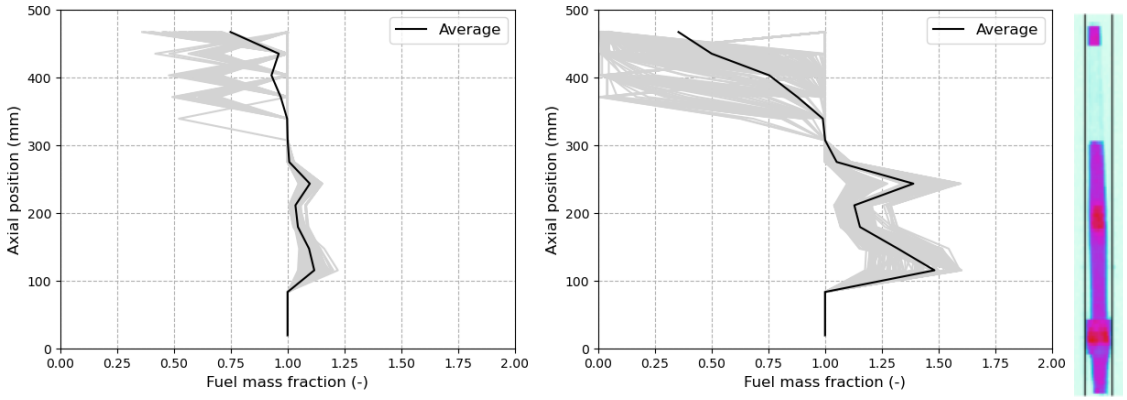

(a) (b)

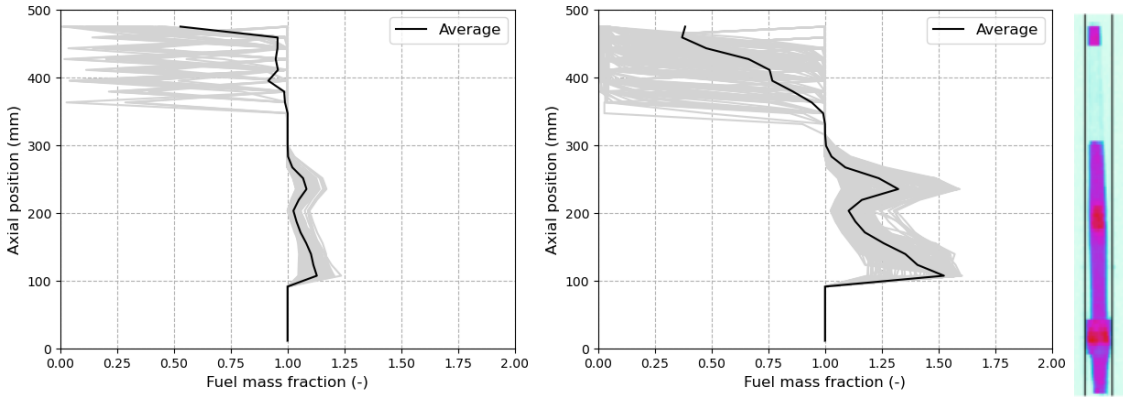

(c) (d)

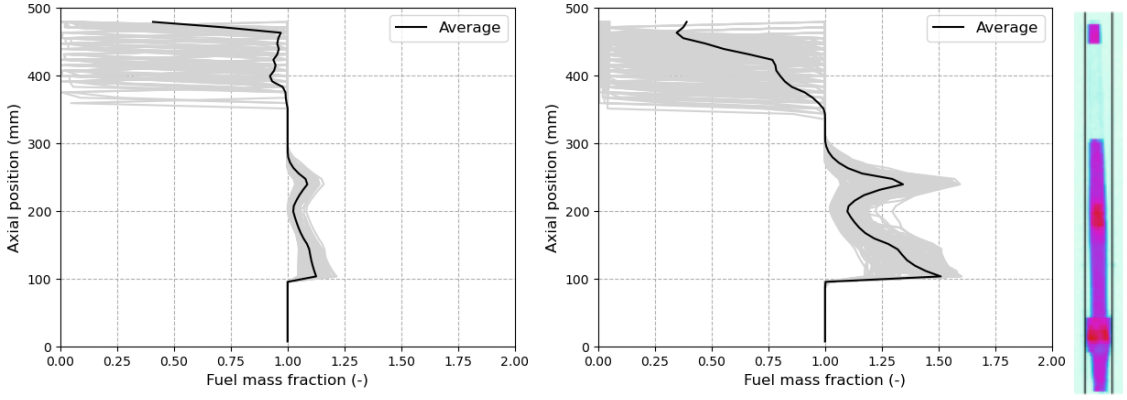

(e) (f)

Figure 4.32: The mass fraction of all 200 simulations for the Walton and Matheson fragmentation model for IFA-650.9. The left and right columns correspond to the plastic instability and overstrain failure criteria, respectively. The number of layers used to represent the fuel increase from 15 in the top row to 60 in the bottom row. The as-fabricated and average are also included.

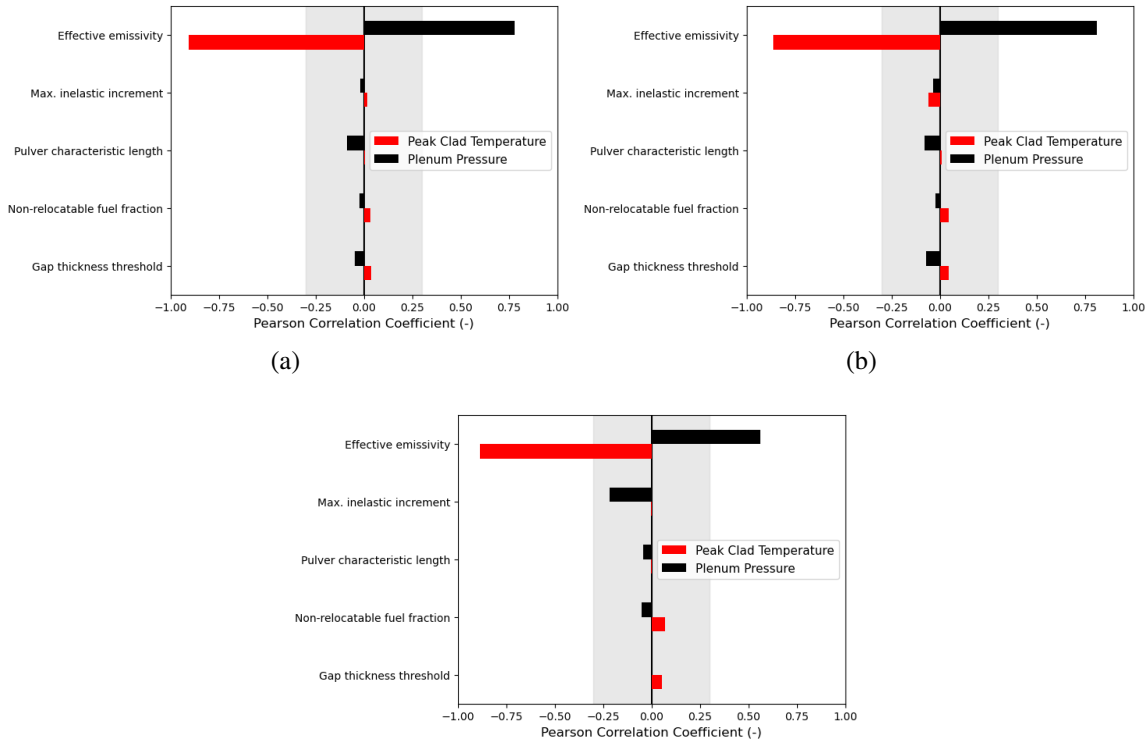

(a)

(b)

(c)

Figure 4.33: Pearson correlation coefficients for IFA-650.14 for the Barani et al. fragmentation correlation. The number of layers used to represent the fuel are (a) 15, (b) 30, and (c) 60.

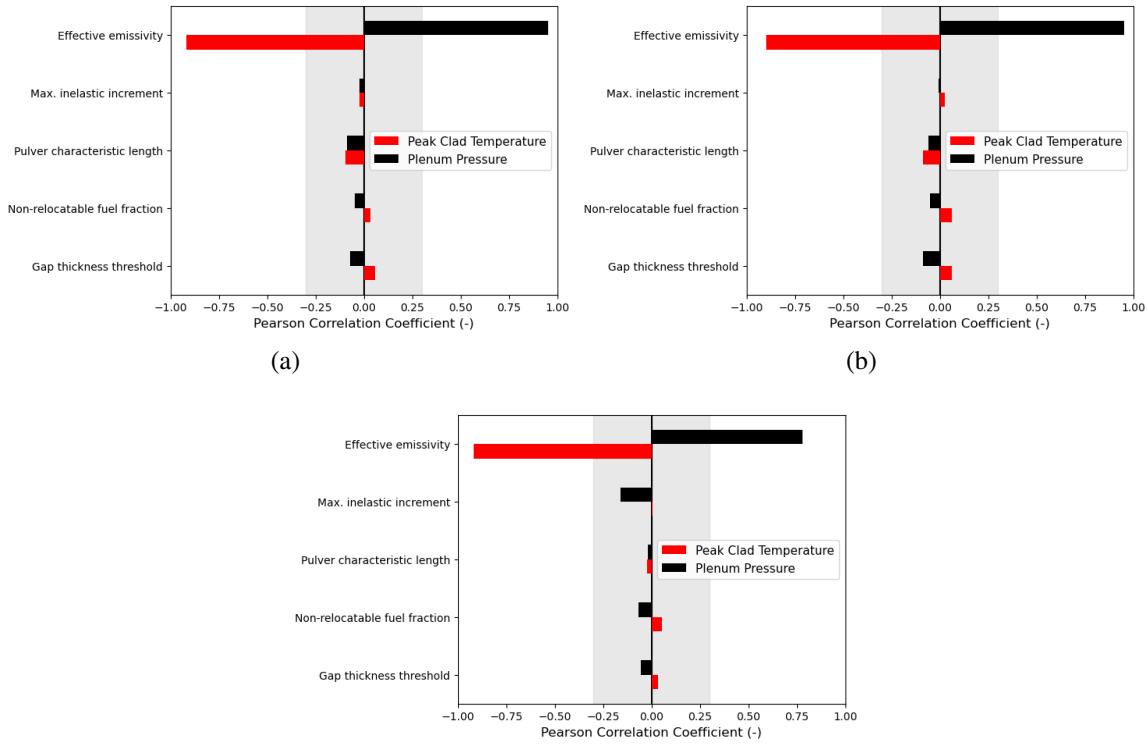

Figure 4.34: Pearson correlation coefficients for IFA-650.14 for the Coindreau et al. fragmentation correlation. The number of layers used to represent the fuel are (a) 15, (b) 30, and (c) 60.

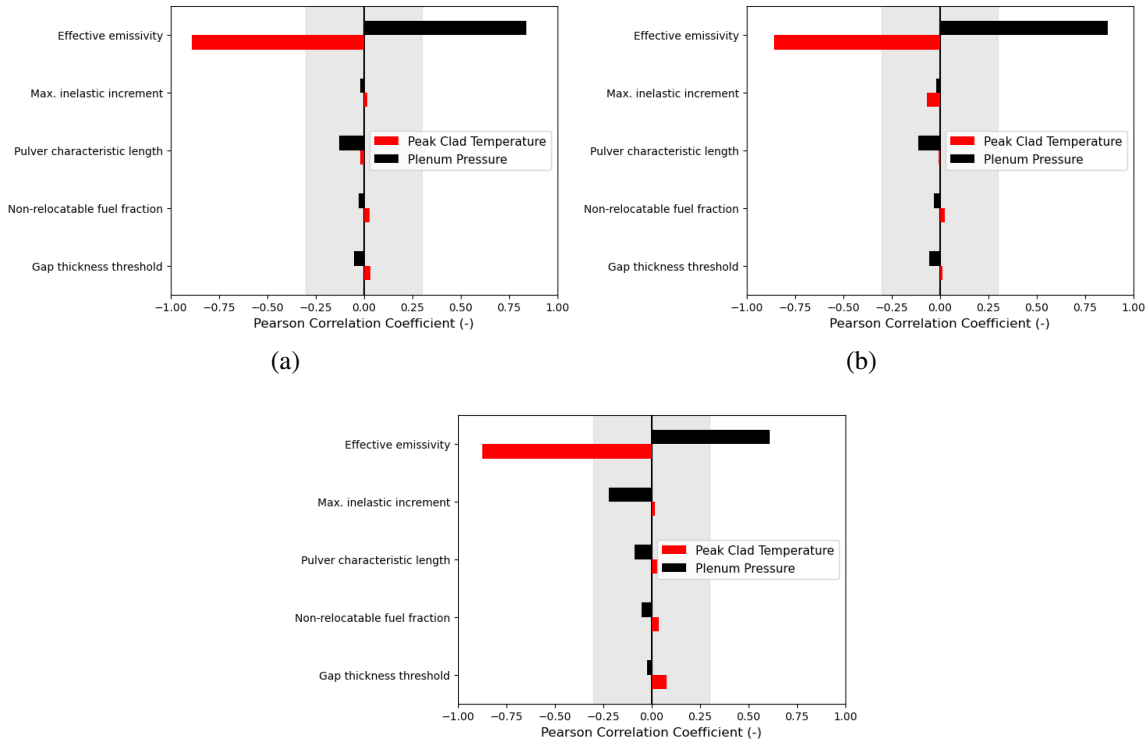

(a)

(b)

(c)

Figure 4.35: Pearson correlation coefficients for IFA-650.14 for the Walton and Matheson fragmentation correlation. The number of layers used to represent the fuel are (a) 15, (b) 30, and (c) 60.

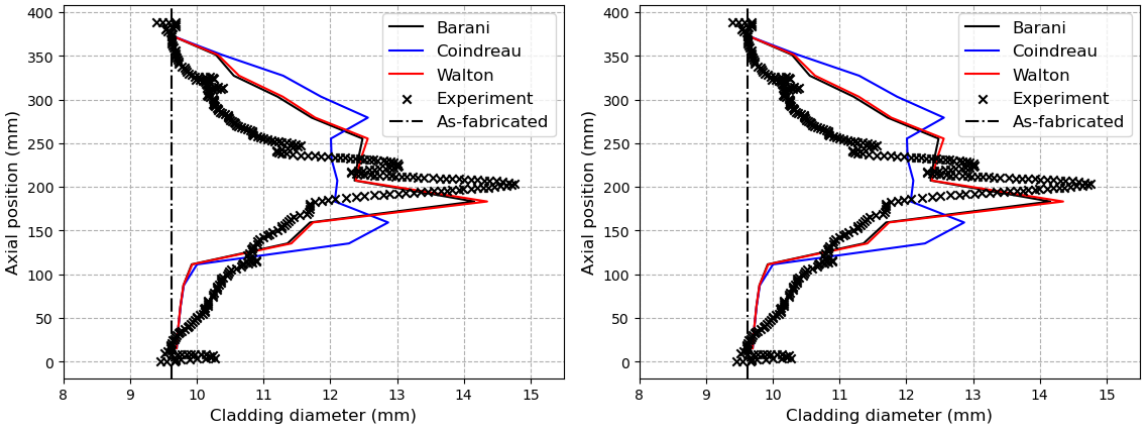

(a)

(b)

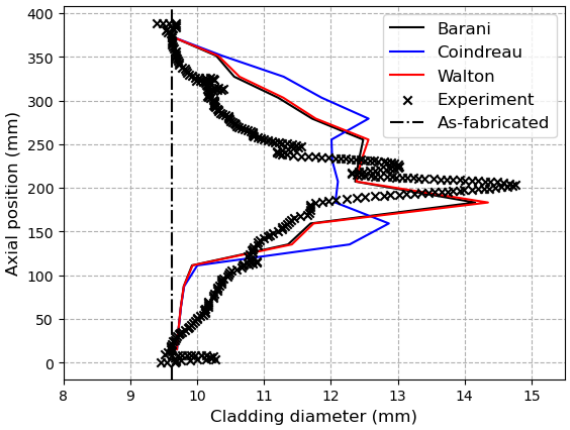

(c)

Figure 4.36: The average cladding diameter of the 200 simulations for the different fragmentation correlations for IFA-650.14. The number of layers used to represent the fuel are (a) 15, (b) 30, and (c) 60. The as-fabricated diameter is also included.

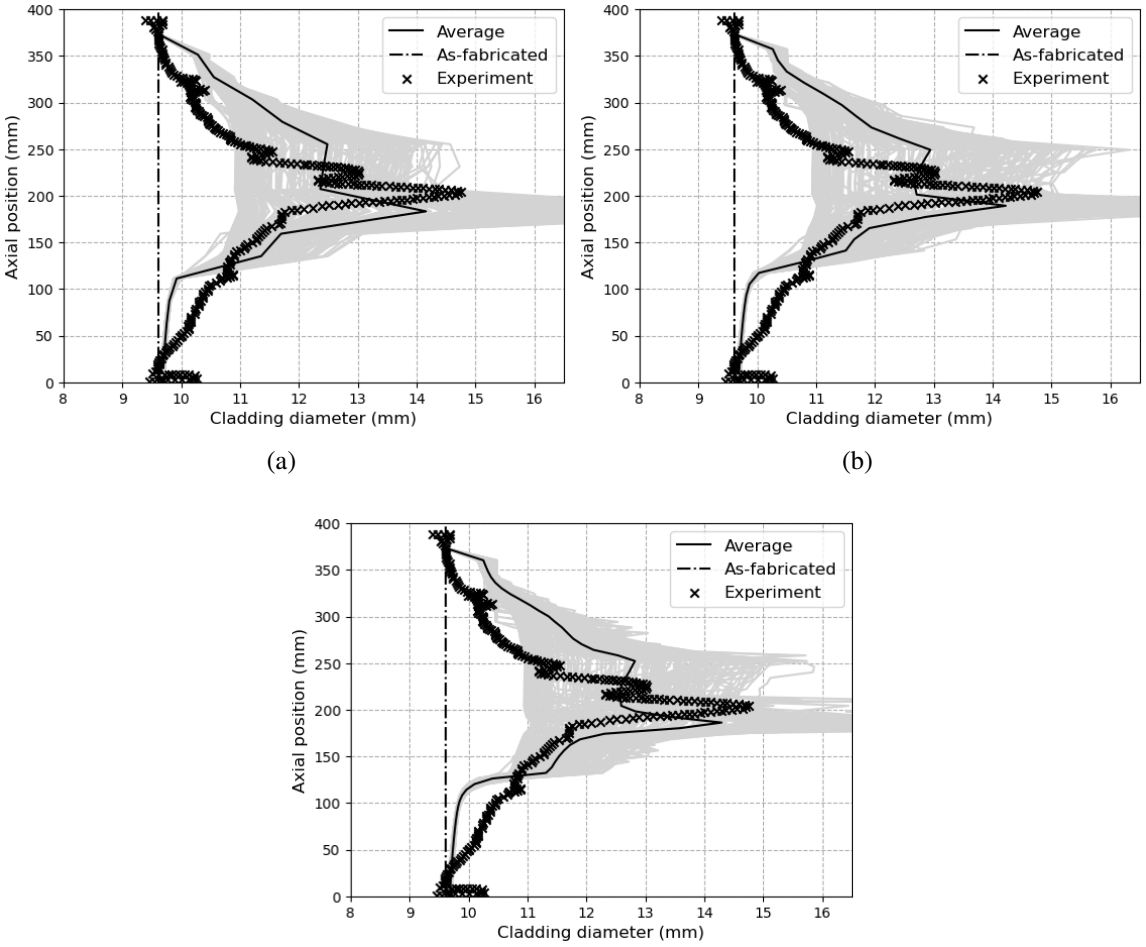

Figure 4.37: The cladding diameter of the 200 simulations for the Barani et al. fragmentation correlation for IFA-650.14. The number of layers used to represent the fuel are (a) 15, (b) 30, and (c) 60. The as-fabricated diameter and average are also included.

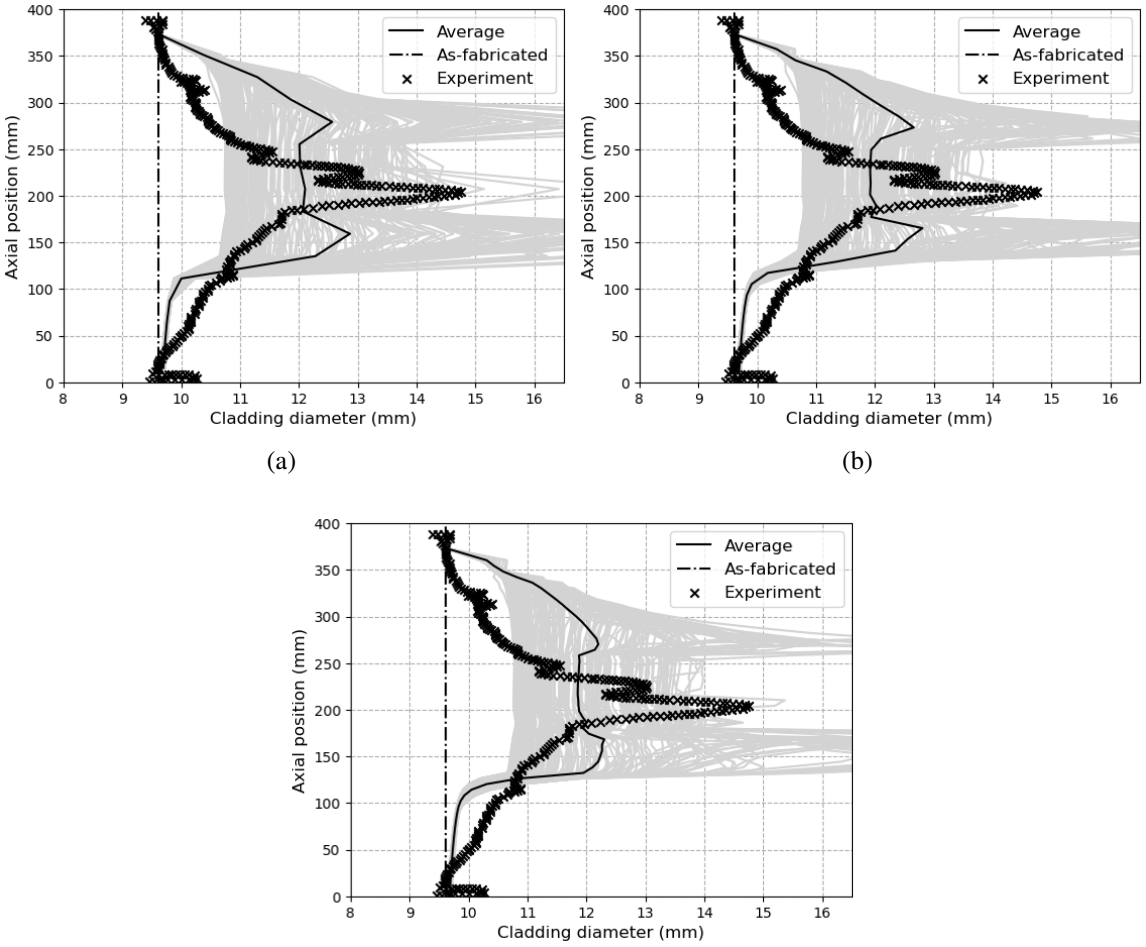

Figure 4.38: The cladding diameter of the 200 simulations for the Coindreau et al. fragmentation correlation for IFA-650.14. The number of layers used to represent the fuel are (a) 15, (b) 30, and (c) 60. The as-fabricated diameter and average are also included.

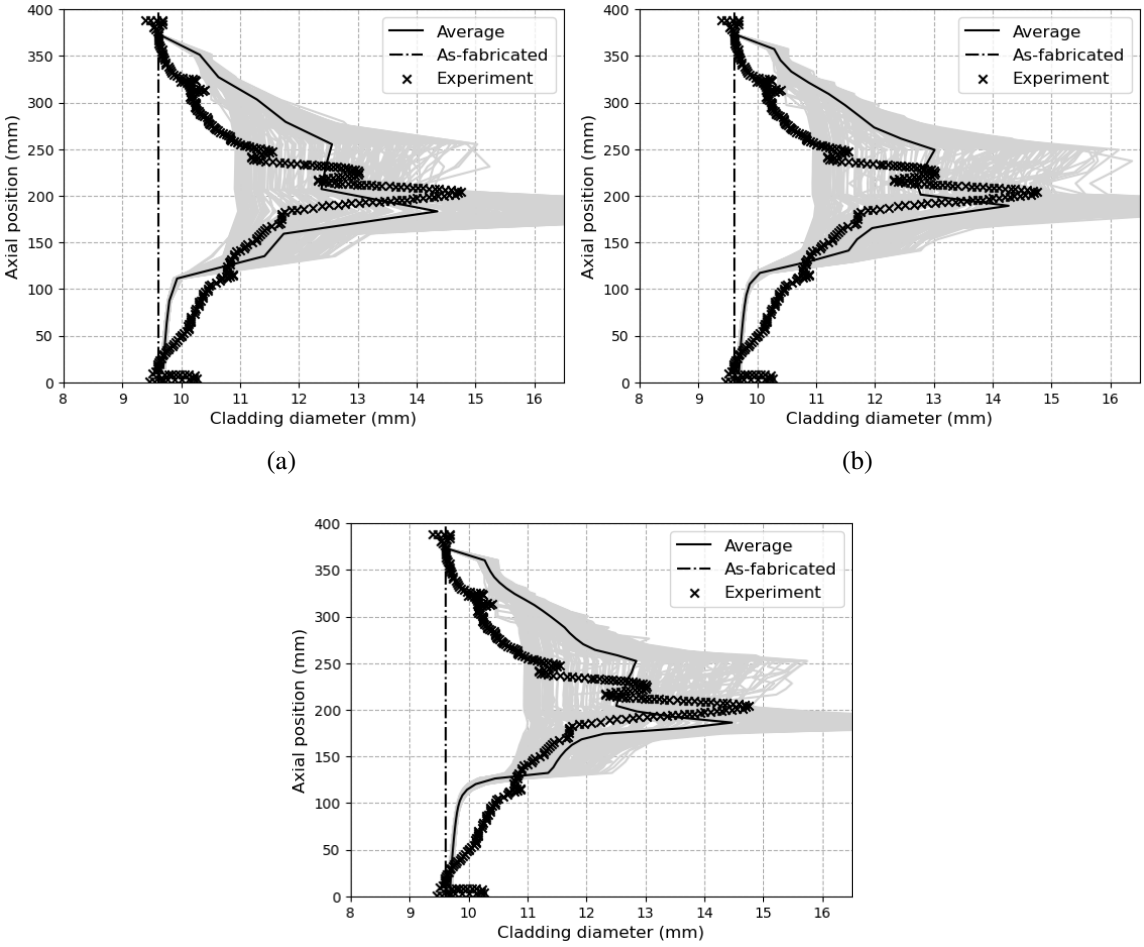

(a)

(b)

(c)

Figure 4.39: The cladding diameter of the 200 simulations for the Walton and Matheson fragmentation correlation for IFA-650.14. The number of layers used to represent the fuel are (a) 15, (b) 30, and (c) 60. The as-fabricated diameter and average are also included.

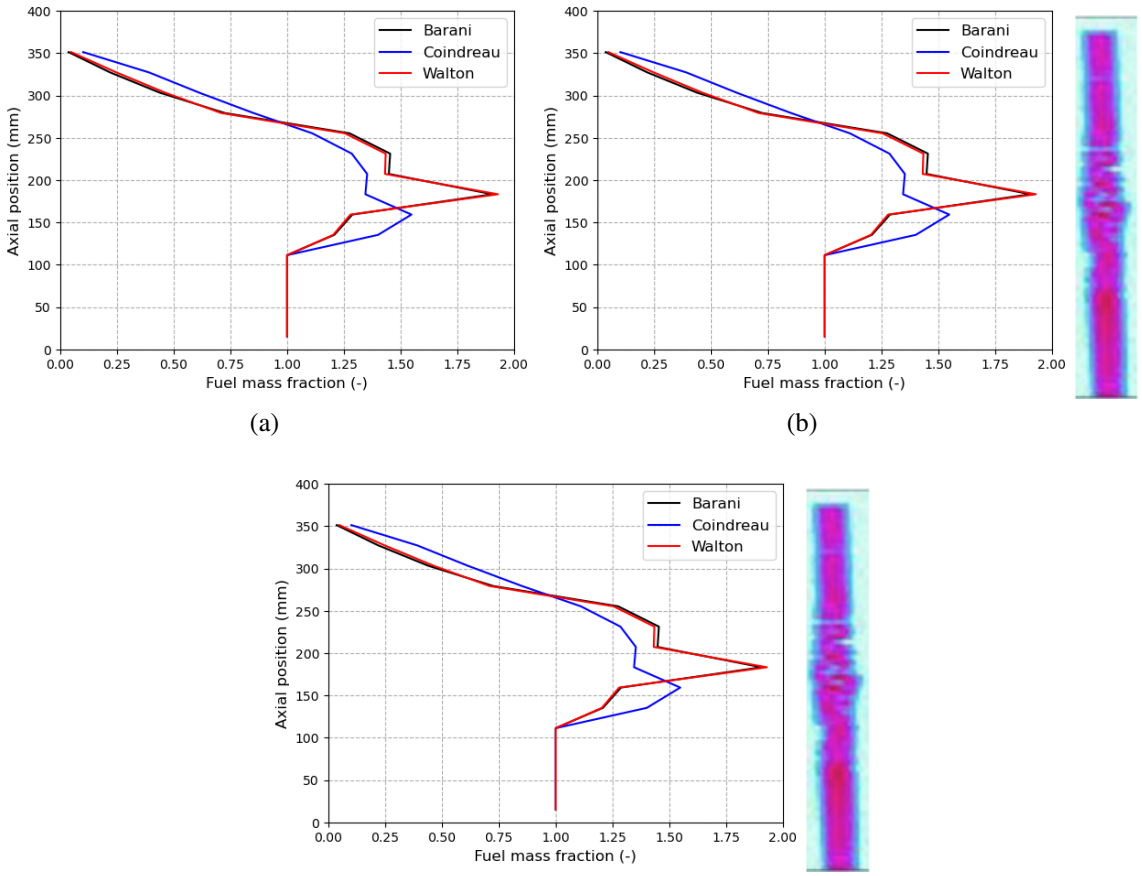

(a) (b)

(c)

Figure 4.40: The average mass fraction of the 200 simulations for the three fragmentation correlations for IFA-650.14. The number of layers used to represent the fuel are (a) 15, (b) 30, and (c) 60. The average is also included.

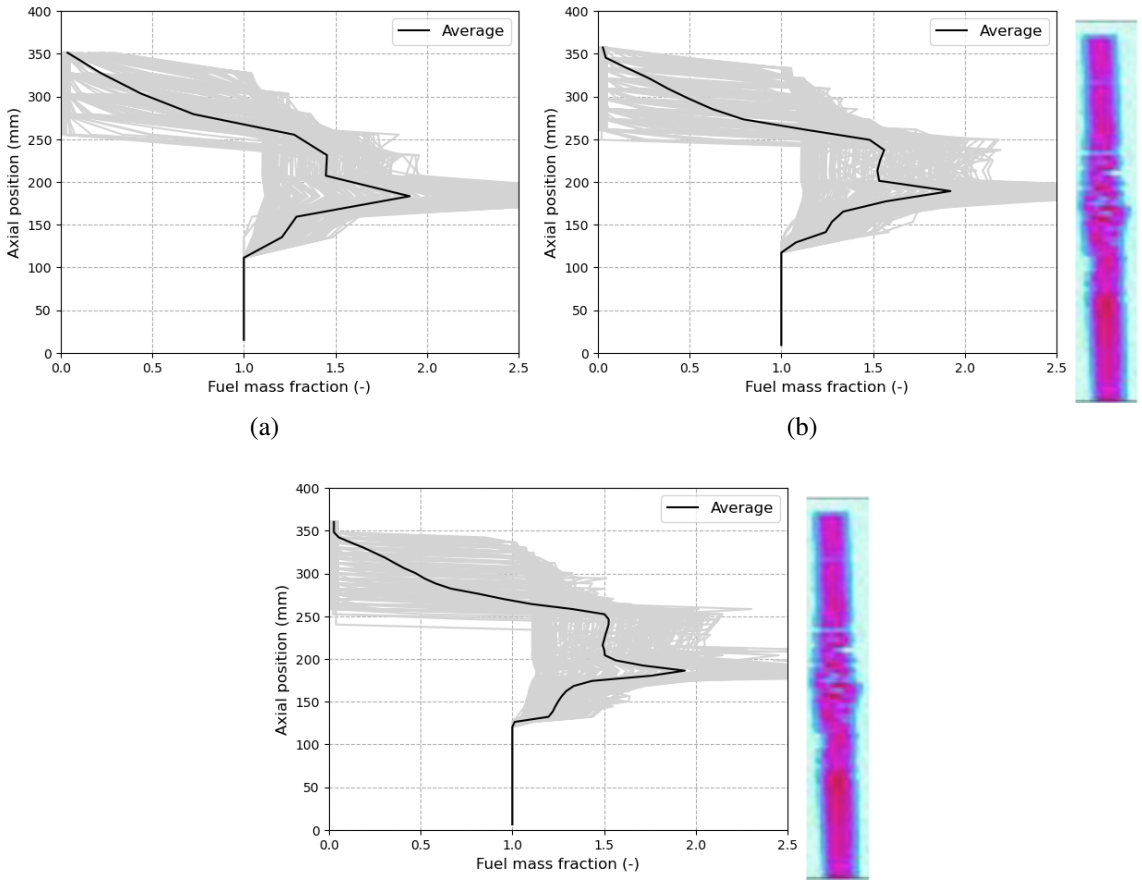

Figure 4.41: The mass fraction of the 200 simulations for the Barani et al. fragmentation correlation for IFA-650.14. The number of layers used to represent the fuel are (a) 15, (b) 30, and (c) 60. The average is also included.

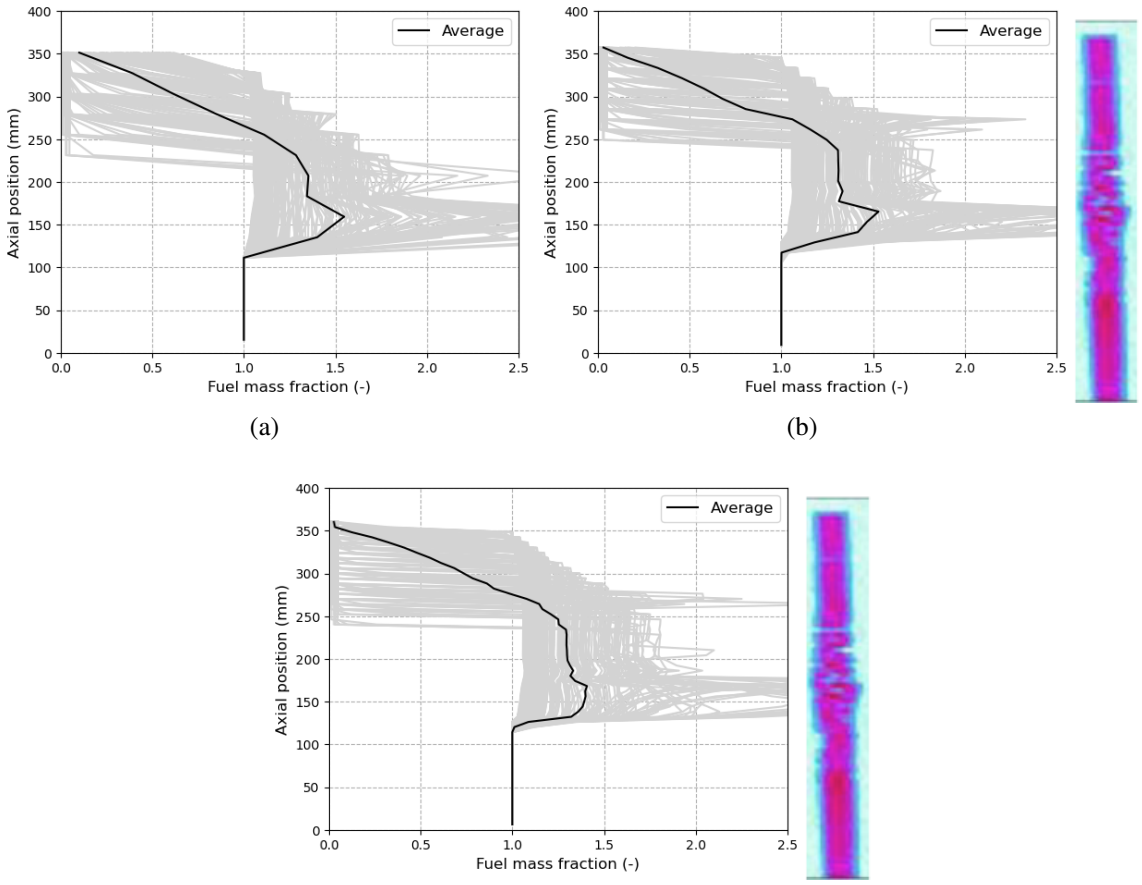

Figure 4.42: The mass fraction of the 200 simulations for the Coindreau et al. fragmentation correlation for IFA-650.14. The number of layers used to represent the fuel are (a) 15, (b) 30, and (c) 60. The average is also included.

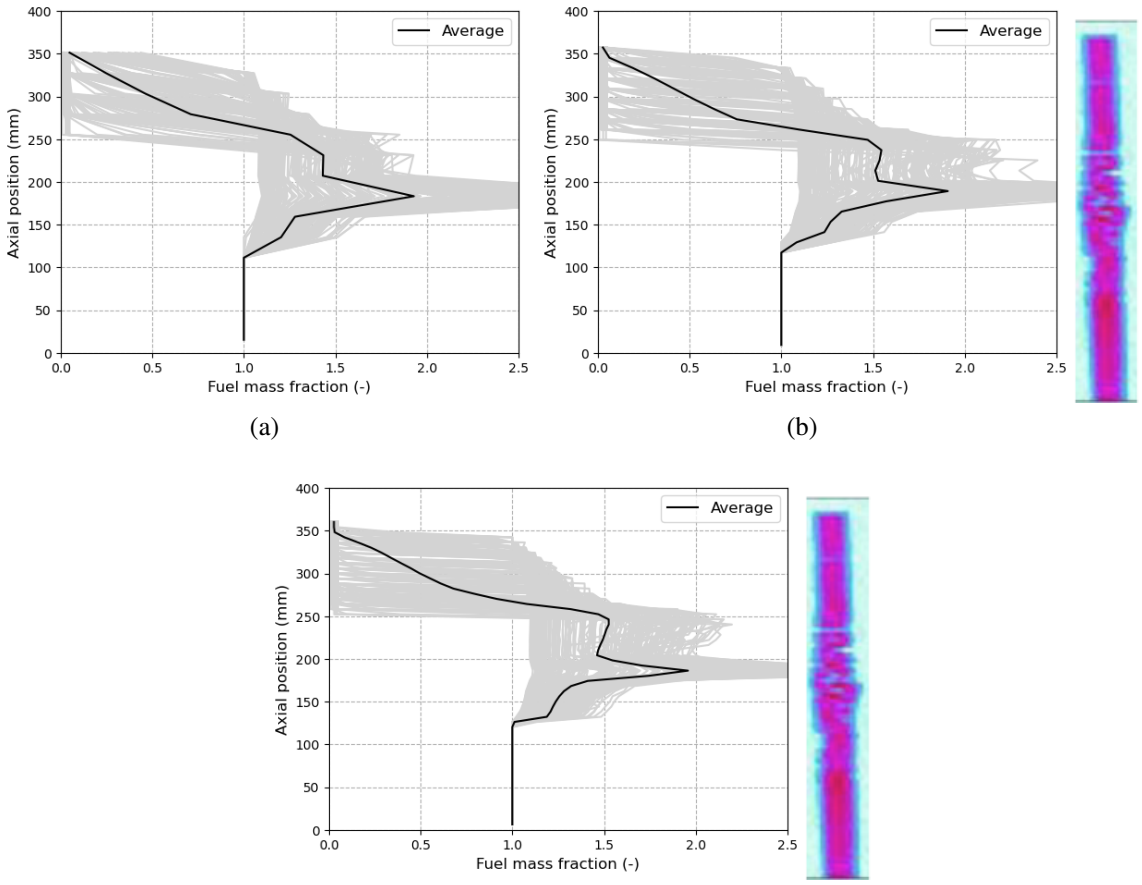

(a) (b)

(c)

Figure 4.43: The mass fraction of the 200 simulations for the Walton and Matheson fragmentation correlation for IFA-650.14. The number of layers used to represent the fuel are (a) 15, (b) 30, and (c) 60. The average is also included.

CHAPTER 5

CLADDING OXIDATION

The preceding chapters primarily focused on model developments related to phenomena that effect fuel rod behavior from the inside of the fuel rod. Another important consideration that needs to be considered during FFRD is the degradation of the cladding due to water-side oxidation. Throughout irradiation the cladding undergoes oxidation that consumes the metallic cladding and forms a brittle oxide on the waterside surface. This oxidation process becomes rapid during a LOCA due to the high temperatures and formation of steam. The reduction in the cladding thickness due to oxidation results in a thinner tube being subjected to the loading conditions experienced during the transient.

5.1 LITERATURE REVIEW

Fuel fragmentation, pulverization, and fuel axial relocation determines the redistribution of the heat load coming from the fuel during a LOCA. The modeling of these phenomena provides a quantification of the heat flux or cladding inner surface temperature as function of axial position being passed to the inner surface of the cladding. The oxidation kinetics of the cladding examines the temperature and mechanical degradation due to exposure to water, steam or air at the outer surface of the cladding. Combining the effects occurring at both surfaces of the cladding allows for an improved prediction of the overall cladding behavior during LOCA conditions and is necessary prior to performing detailed analyses of cladding rupture. An illustration of the oxidation process of zirconium-based alloys is shown in Figure 5.1.

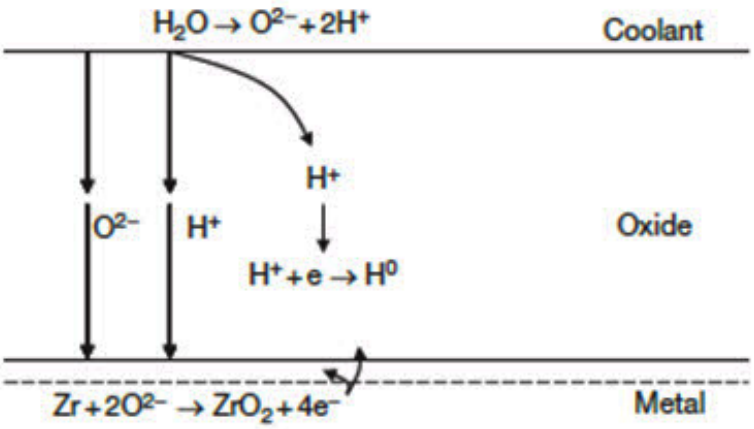

Figure 5.1: Schematic of the oxidation process of a zirconium-based metal. Reproduced from [67].

The balanced chemical equation for this oxidation reaction is given by:

$$Zr + 2H_2O \rightarrow ZrO_2 + 2H_2 + Q \tag{5.1}$$

where Q is the heat produced from the oxidation reaction (6.45×10^6 J/kg). This heat produced from oxidation can become an additional source term in the cladding, particularly at higher temperatures. In the literature, this phenomenon is known as oxide energy deposition (OED). MATPRO library [100] contains an empirical model to take into account the energy deposited within the cladding as a function of the increment weight gain due to oxide formation. The equation is given by:

$$P = 6.45 \times 10^6 \frac{0.74}{0.26} \frac{\Delta W}{\Delta t} 2\pi R_{co} \tag{5.2}$$

where ΔW is the change in weight gain in the timestep (kg/m^2), Δt is the timestep size (s), and R_{co} is the cladding outer radius (m) without oxidation. The $0.74/0.26$ fraction comes from the fact that all of the oxide formed is assumed to be stoichiometric. The weight gain or oxide thickness (the two can be correlated based upon characteristics of the oxide that forms) is calculated based upon the oxidation rate equation. During normal operation (outer cladding temperatures of <673 K) there exists two regimes known as pre-transition and post-transition [93]. In the pre-transition regime where the oxide layer forms a protective

layer the oxide thickness the kinetics follows a cubic rate law (Equation 5.3a) whereas in the post-transition regime the rate law is linear (Equation 5.3b). The linear rate law is due to the cracking of the protective layer allowing oxygen to travel to the metal-oxide interface and oxidize the metal at a rapid rate. The transition oxide thickness is typically taken as 2μm.

$$\frac{d\delta^3}{dt} = K_c \tag{5.3a}$$

$$\frac{d\delta}{dt} = K_l \tag{5.3b}$$

where δ is the oxide thickness, and K_c and K_l are the cubic and linear rate constants, respectively. The rate constant is in the form of an Arrhenius equation of the general form:

$$K = A \exp\left(\frac{-Q}{RT}\right) \tag{5.4}$$

where A is the pre-exponential factor, Q is the activation energy, R is the universal gas constant and T is the temperature. Several empirical correlations have been proposed for the rate constant in the pre- and post- transition regions in fuel performance codes. The underlying data set used to develop the correlations differ. All of the publicly available correlations are generally developed based upon standard Zircaloy-2 and Zircaloy-4 data. The oxidation kinetics of commercial alloys (M5 or Zirlo) are held as proprietary data by the respective vendor who owns the technology. Over the years, correlations have been implemented into Bison as options to compute the oxidation rate constants and subsequently the oxide scale thickness and mass weight gain. Over the decades EPRI proposed two oxidation models known as EPRI/KWU/CE [38] and EPRI/SLI [43]. The first model proposes for the pre-transition region:

$$K_c = 6.3 \times 10^9 \exp\left(-\frac{16266}{T}\right) \tag{5.5}$$

where the units of K_c are μm^3/day and T is in K. In the post transition region the following is proposed:

$$K_l = \left(8.04 \times 10^7 + 2.59 \times 10^8 \left(7.46 \times 10^{-15}\phi\right)^{0.25}\right) \exp\left(-\frac{13775}{T}\right) \tag{5.6}$$

where ϕ is the fast neutron flux in n/cm^2-s to take into account the irradiation enhancement to corrosion in the linear regime. The units of K_l are μm/day. The EPRI/SLI correlation is much more complex such that the pre-exponential factors depend upon the water chemistry (e.g., the concentration of lithium in the water), which for all practical purposes is too detailed as most experimentalists for integral analyses do not provide the attributes of the water chemistry. Once the thickness of the oxide is known the weight gain per unit area can be calculated by (for zirconium based alloys) [105]:

$$\Delta W = 1475 \Delta \delta \tag{5.7}$$

where $\Delta\delta$ is the incremental change in oxide thickness (m) and ΔW is the incremental weight gain per unit area (kg/m^2). In the high temperature regime ($>$ 673 K) the oxidation kinetics is governed by a parabolic rate law: Equation 5.8.

$$\frac{dX^2}{dt} = K_p \tag{5.8}$$

where X can represent either the weight gain or oxide thickness depending on the constants in the Arrhenius law for K_p, the parabolic rate constant. Several correlations for the rate constant during high temperature oxidation have been proposed by Leistikow [62], Prater and Courtright [86], and Cathcart and Pawel [20] to name a few. Depending upon the fuel performance code being used the correlation used in different temperature regimes vary. In Bison, all of the correlations discussed thus far have been implemented as options for use. In general, for Bison analyses it is typically recommended to use the EPRI/KWU/CE model for normal operational conditions, the Leistikow or Cathcart and Pawel rate constant correlations from 673 K to 1800 K with Prater and Courtright being used above 1900 K. In the transition region between 1800 and 1900 K a linear interpolation between the two correlations is used. Table 5.1 lists the pre-exponential factor (both for the mass gain (A_{wg}) and oxide thickness (A_t) formulations), activation energy (for mass gain (Q_{wg}) and oxide thickness (Q_t)) divided by the gas constant, and reference where the correlation was proposed for the Leistikow, Prater and Courtright, and Cathcart and Pawal correlations.

Table 5.1: Parameters for the parabolic rate constant K_p from Leistikow, Prater and Courtright, and Cathcart and Pawel for both mass gain and oxide thickness formulations [96].

Model	A_t (m^2/s)	A_{wg} (kg^2/m^4-s)	Q_t/R (K)	Q_{wg}/R (K)	Ref.
Leistikow	7.82×10^{-6}	52.42	20214	20962	[62]
Cathcart and Pawel	2.25×10^{-6}	36.22	18062	20100	[20]
Prater and Courtright	2.98×10^{-3}	3.3×10^{3}	28420	26440	[86]

Once the mass gain is known the scale thickness can be obtained by inverting Equation 5.7 to solve for thickness. Figure 5.2 plots the oxidation rate constant as a function of temperature. For the linear oxidation rate constant that applies after the transition oxide thickness three different fast neutron fluxes are shown. To enable all rate constants to be plotted together the parabolic and cubic rate constants have the square and cubic roots applied. A logarithmic y-axis is necessary to enable visualization over the orders of magnitude. It is seen that prior to the 2μm transition the oxide is protective and the oxidation rate is orders of magnitude less than the post transition rate constants at identical temperatures. A small observable difference is seen as the fast neutron flux increases. At the transition temperature from normal operating to high temperature oxidation (673 K) there is a several order of magnitude discontinuity in the oxide rate constants. The difference between the Leistikow and Cathcart and Pawel correlations decreases with increasing temperature. Through the high temperature transition region no differences are observed.

Taking the rate constant for the Leistikow model for mass gain over the range of 673 K to 1800 K the OED produced due to oxidation by Equation 5.2 can be plotted as shown in Figure 5.3. The key takeway from the OED plot is the fact that any significant additional source of heat generation in the cladding does not occur until $\geq$1400 K. Many of the experimental test series analyzed in in this work have target peak cladding temperatures near this temperature threshold. However, the ultimate goal of this work is to predict the time of rupture the size and location of that rupture. In all cases rupture tends to occur at temperatures <1200 K for which the additional heat source is minimal. Therefore, for this work, the model for OED is not included in any LOCA analyses. It is highlighted here to show

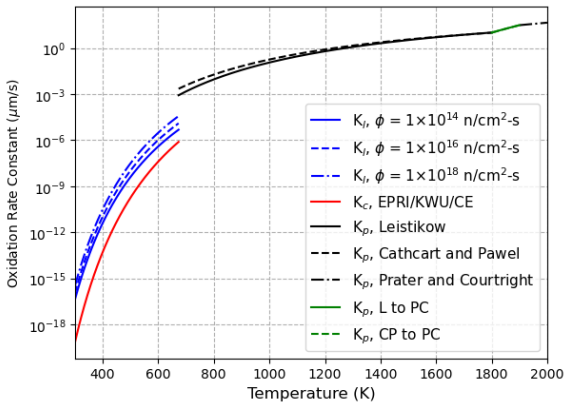

Figure 5.2: Plots of the K_l, K_p, and K_c rate constants available in Bison as a function of temperature. Three different fast neutron fluxes are shown for the linear case in the post-transition regime. K_p and K_c have a square root and cubic root applied to the values obtained from the appropriate equations to make the units consistent amongst the constants. L to PC and CP to PC correspond to the transition rate constants between the Leistikow and Prater and Courtright and the Cathcart and Pawel and Prater and Courtright correlations, respectively.

the importance of including such a model for beyond design basis accidents where double sided oxidation and uncontrollable cladding temperatures are present.

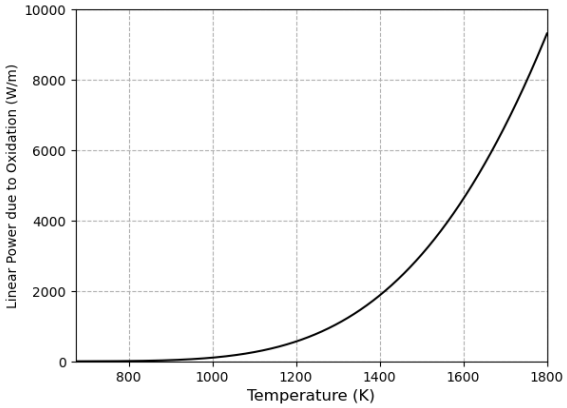

Figure 5.3: The oxide energy deposition when using the Leistikow rate constant correlation.

While the above equations can help quantify the amount of oxide that forms, the addition in weight due to the oxide layer formation, and the additional energy added to the system due to the exothermic reaction at high temperatures, there is a clear deficiency in current fuel performance implementations. As the metal oxidizes the amount of metal left over from the original as-fabricated state decreases. Therefore the thickness of the stronger metallic alloy

decreases over time while the formation of a more brittle oxide consumes the metal and grows. In current fuel performance implementations, the conversion of material properties (e.g., Young's modulus, thermal conductivity) from Zircaloy to ZrO_2 as oxidation occurs, is typically not included. The tracking of the metal-oxide interface can be of great importance when modeling the evolution of the cladding during a LOCA because the stresses leading to nucleation of fractures causing failure will be approached more rapidly as the amount of metal able to withstand the stresses reduces. Thus, failure could potentially be predicted later than observed observed if the degradation in mechanical properties is not accounted for.

Currently, as shown in Table 1.1, one of the thresholds of importance is the ECR. This value is limited at 0.17 or 17% of the total cladding present. Empirical correlations have been developed to quantify the ECR for comparisons to this NRC imposed threshold. For single sided oxidation the ECR is calculated as [73]:

$$ECR_{1s} = 43.9 \left[\frac{w}{t_c} \left(1 - \frac{t_c}{d_{co}} \right) \right] \tag{5.9}$$

and for two sided oxidation:

$$ECR_{2s} = 87.8 \frac{w}{t_c} \tag{5.10}$$

where w is the mass gain due to oxidation (g/cm^2), t_c is the cladding thickness (cm), and d_{co} is the cladding outer diameter (cm). Figure 5.4 plots the single-sided and doubled-sided equivalent cladding reacted as a function of mass gain for two representative Zircaloy-4 cladding thicknesses: 575 *mu*m and 725 *mu*m. In current PWR applications the standard is somewhere close to the 575*mu*m. Some older experiments used the 725 *mu*m thickness tubes. This threshold is attained at relatively low mass gains. Therefore, industry developed proprietary Zircaloy claddings (e.g., M5, Zirlo) to reduce the oxidation rate constants such that there is an improved time (or margin) before the ECR limit is achieved during a LOCA. However, being proprietary, no details of the oxidation rate constants of these commercial alloys are publicly available.

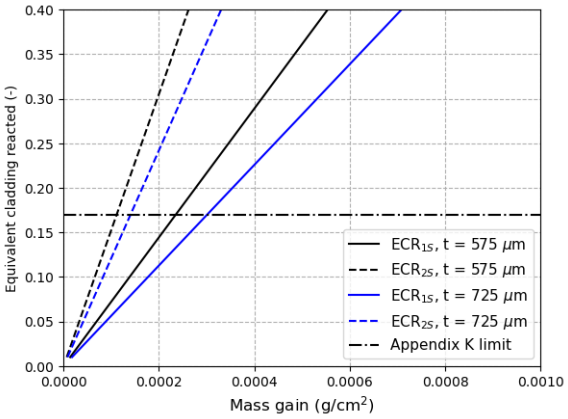

Figure 5.4: The plot of equivalent cladding reacted using the single and doubled sided correlations.

5.2 Mechanical Degradation Model

Advanced techniques have been recently developed in the MOOSE framework for handling moving interfaces using the level-set method [6]. Level-set methods have been around since the late 1980s and were developed to track the evolution of curves and surfaces [98]. The level-set on its own does not track the location of the level set boundary and must be coupled with the XFEM to model the discontinuity. Then, based upon the value of the level-set function being positive or negative on either side of the discontinuity the material properties associated with metal or oxide can be used. The work of Bailly-Salins et al. [6] also explored a more physics-based approach to model oxidation by accounting for the mechanisms that drive the formation of the oxide, rather than using the empirically derived Arrhenius laws presented previously. However, plots presented in [6] illustrate that over the ranges of applicability of interest in this work that the physics-based model is within the uncertainty of the empirical models compared against.

Introduction of the level-set method to account for mechanical degradation of the cladding during oxidation would result in the addition of another primary variable that needs to be solved. In the Layered formulations (1D and 2D) this would be in addition to the temperature, displacements and out-of-plane scalar strains in each fuel and cladding layer. In this

work only the inclusion of degradation is desired, not the explicit modeling of the exact location of the metal-oxide interface. Therefore, a simplistic approach is taken in this work. The approach consists of evaluating correlations for three separate materials for each of the cladding material properties of interest. These models include the thermal conductivity, specific heat, thermal expansion, elasticity tensor, and thermal and irradiation creep. For elasticity, thermal expansion, and the thermal properties an approach as illustrated in Figure 5.5 is used. In the Bison analyses for the cladding two separate materials are solved on the entire domain one using the correlation for Zircaloy and one for ZrO_2. A third material is then used to compute the metal-oxide interface from the oxide thickness computed by the oxidation models and applies the appropriate Zircaloy or ZrO_2 models to each side of the interface. For the creep models, once the material point has transitioned to oxide the creep strain remains the same as at the time of transition for the remainder of the simulation. For elasticity, another option exists to model wall thinning where instead of transitioning to the model for ZrO_2 the elasticity is scaled by a factor of 1×10^{-3} to simulate complete loss of strength of the part of the material that has been oxidized. A non-zero value is necessary for the scaling to ensure numerical stability as a finite element with an elastic modulus of zero would be nonphysical in a mechanics calculation. All of these models can be found in Appendix C which provides a link to the Bison online documentation with detailed theory of the correlations.

Determination of the location of the metal-oxide interface is computed through:

$$x_{moi} = R_{co} - \left(\frac{1.0}{R_{PB}} t_{ox}\right) \tag{5.11}$$

where x_{moi} is the location of the metal oxide interface (m), R_{co} is the cladding outer radius, R_{PB} is the Pilling-Bedworth ratio (value of 1.56 for ZrO_2), and t_{ox} is the oxide thickness. The Pilling-Bedworth ratio accounts for the increase in volume of ZrO_2 compared to the underlying Zircaloy metal. For Layered1D or 2D-RZ geometric representations x_{moi} can vary axially, for Layered2D geomtries x_{moi} can vary both azimuthally and axially depending upon the thermalhydraulic conditions.

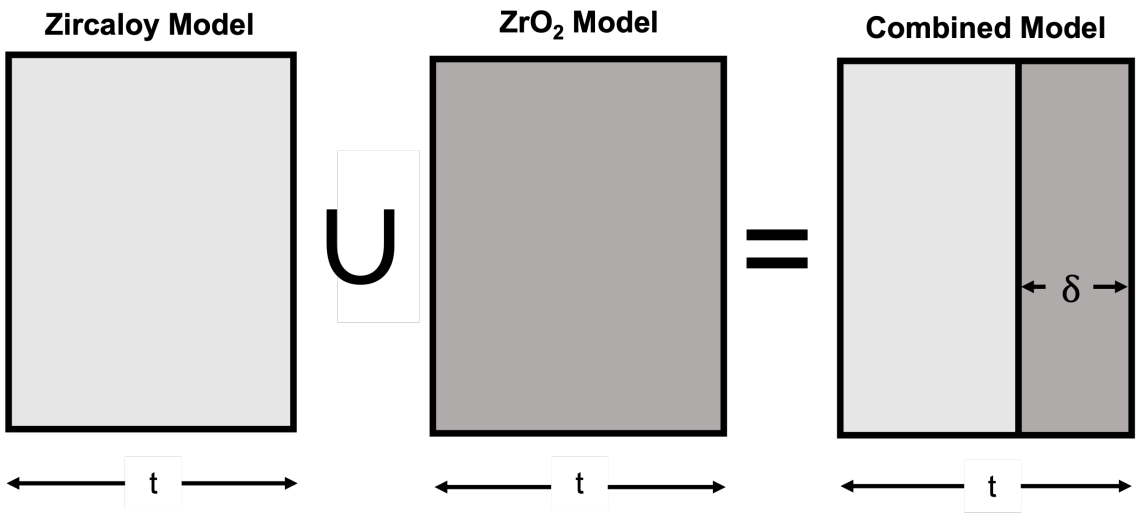

Figure 5.5: Schematic illustrating how the model for mechanical degradation due to oxidation is formulated. δ represents the amount of cladding consumed due to oxidation and t corresponds to the as-fabricated cladding thickness.

5.3 VERIFICATION

To verify that the approach illustrated in Figure 5.5 has been properly implemented into Bison simple verification cases are analyzed for elasticity, thermal expansion, and thermal properties.

5.3.1 ELASTICITY

Test cases for both the wall thinning and oxide transition approaches are provided. A representative piece of cladding is modeled in a 2D-RZ axisymmetric geometry with an inner radius of 5 mm and a total thickness of 500 μm. An prescribed oxide thickness of 156 μm is assumed, which when used with the Pilling-Bedworth ratio for Zircaloy of 1.56 results in a total thickness of cladding substrate consumed of 100 μm. The tube is loaded in tension with a 100 MPa pressure applied on the top. On the bottom of the tube the cladding is fixed axially but free to move radially which essentially creates a symmetric plane at this location (i.e., half the geometry is modeled). The load is linearly increased from 0 over 10 seconds and held for 2 seconds to ensure equilibrium is achieved. Five finite elements are

used radially. A schematic of this setup is provided in Figure 5.6.

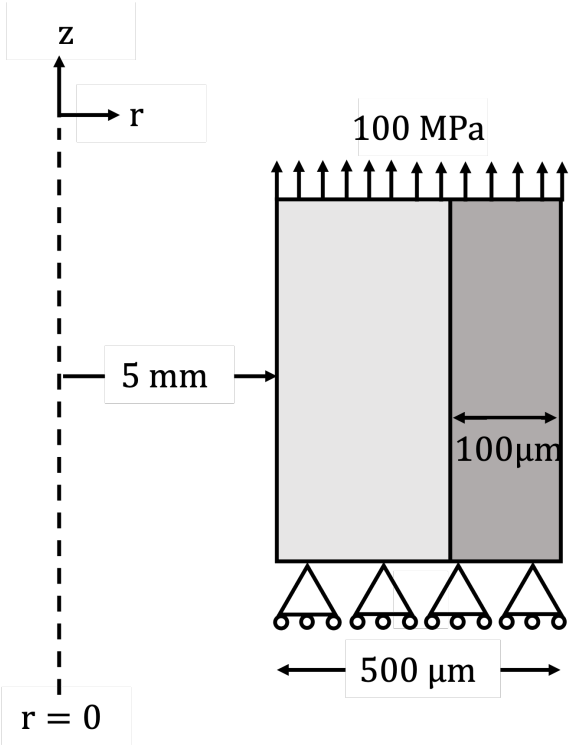

Figure 5.6: Schematic describing the loading conditions for the verification problem used for mechanics.

For both the wall thinning and transitioning cases verification of correct implementation is achieved by comparing the stress results of the newly developed models for degradation to geometries that are meshed such that there are two distinct blocks of appropriate thickness bonded together. In the multi-block meshed case the Zircaloy properties are applied on the left-hand block with the ZrO_2 properties applied to the right-hand block. Figure 5.7 presents the radial profile of the hoop stress at 3 times (4, 8, and 12 seconds) during the simulation for the loading condition described in Figure 5.6. Cases with 5 radial elements are shown in the top row and those with 10 radial elements are in the bottom row. In MOOSE/Bison stresses (and strains) are output as constant monomial variables, which means that there is a single value for any given finite element. Therefore, a staircase like behavior of the plots can expected when such quantities are plotted over a line. It can be seen that the stress state varies over time as the loading is increased to the 100 MPa value. Actually modeling

the oxide that forms with ZrO_2 material properties causes a transition from a tensile to compressive stress within the material. The simulation that modeled both blocks and the one that used the degradation model provide the exact same answers. Surprisingly, the use of wall-thinning causes a significant drop in the stress throughout the cladding thickness. The mesh density has a particularly large impact on the results of the wall-thinning model.

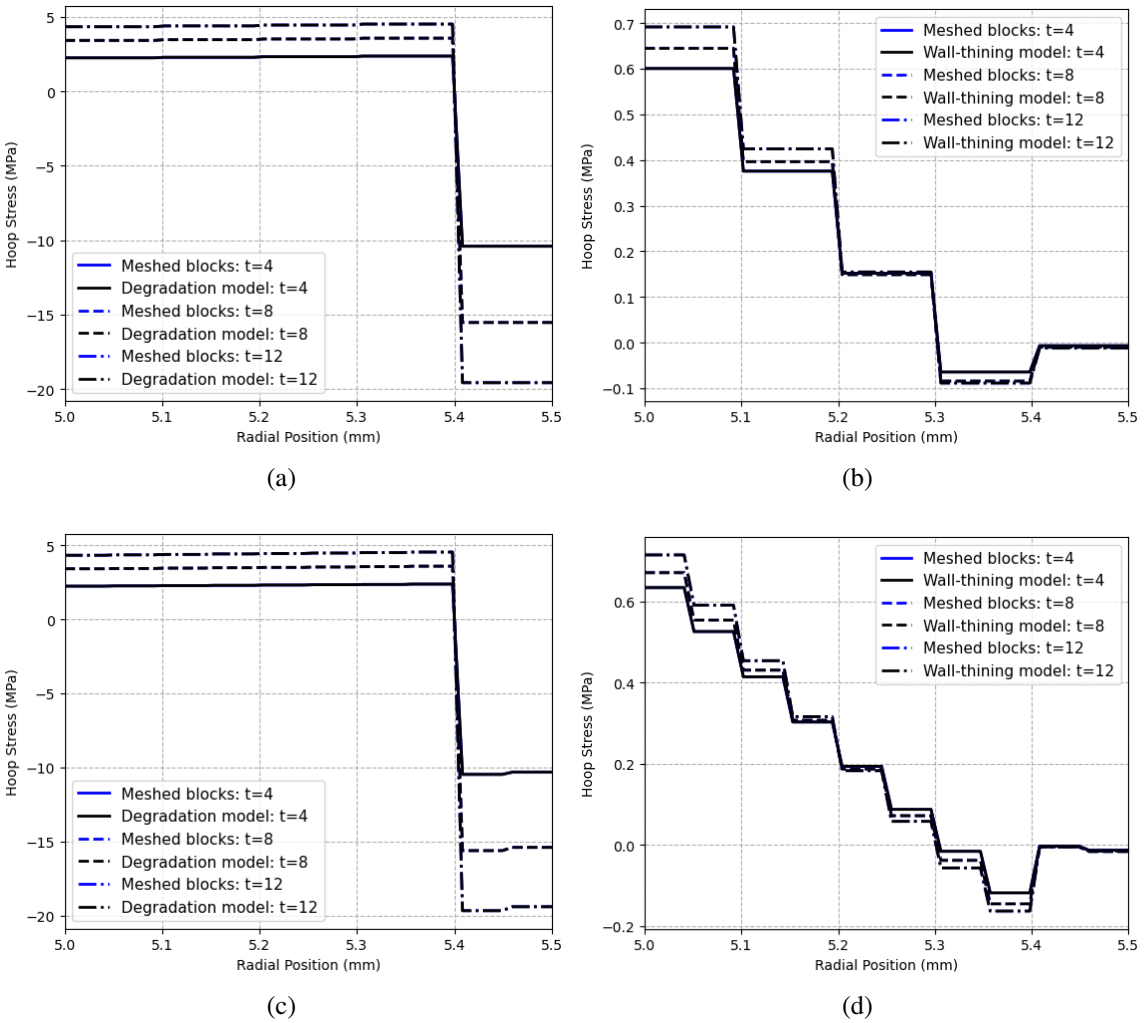

Figure 5.7: Verification of the mechanical degradation model for the elasticity tensor when using (a) the ZrO_2 model and (b) wall-thinning with 5 radial elements and (c) the ZrO_2 model and (d) wall-thinning with 10 radial elements.

5.3.2 Thermal Expansion

The verification problem for thermal expansion is the same as for the elasticity case described previously with the addition of thermal expansion to both the Zircaloy and ZrO_2 blocks. The results of both approaches are shown in Figure 5.8. As with the elasticity case the results using 5 and 10 radial elements are shown in the top and bottom rows, respectively. The trends are the same as the elasticity case, however, one can see in the analysis that explicitly models the oxide that the stresses are higher in the cladding than the case without thermal expansion.

5.3.3 Thermal Properties

The geometry for the thermal property, particularly thermal conductivity, verification is the same as Figure 5.6. However, no mechanics are included in this analysis. Therefore the roller loading on the bottom and the pressure load on the top are removed. Instead, prescribed temperatures are supplied on the interior and exterior surfaces of the tube. For this simple demonstration the inner and outer surfaces of the tube are set to 800 K and 580 K, respectively. The results presented in Figure 5.9 shows that the degradation model is working correctly and that mesh density is not important for the thermal solution through the cladding radius.

5.4 Oxidation in Layered2D

5.4.1 Azimuthal effects of temperature

The Layered2D framework naturally allows for both axial and circumferential variation. The varying temperature profile also induces differential oxidation. A study presented here demonstrates the ability to simulate axially and circumferentially varying oxide thickness under representative surface temperatures of a Zircaloy cladding tube held at normal reactor operation, followed by a LOCA transient similar to what would be observed in a furnace

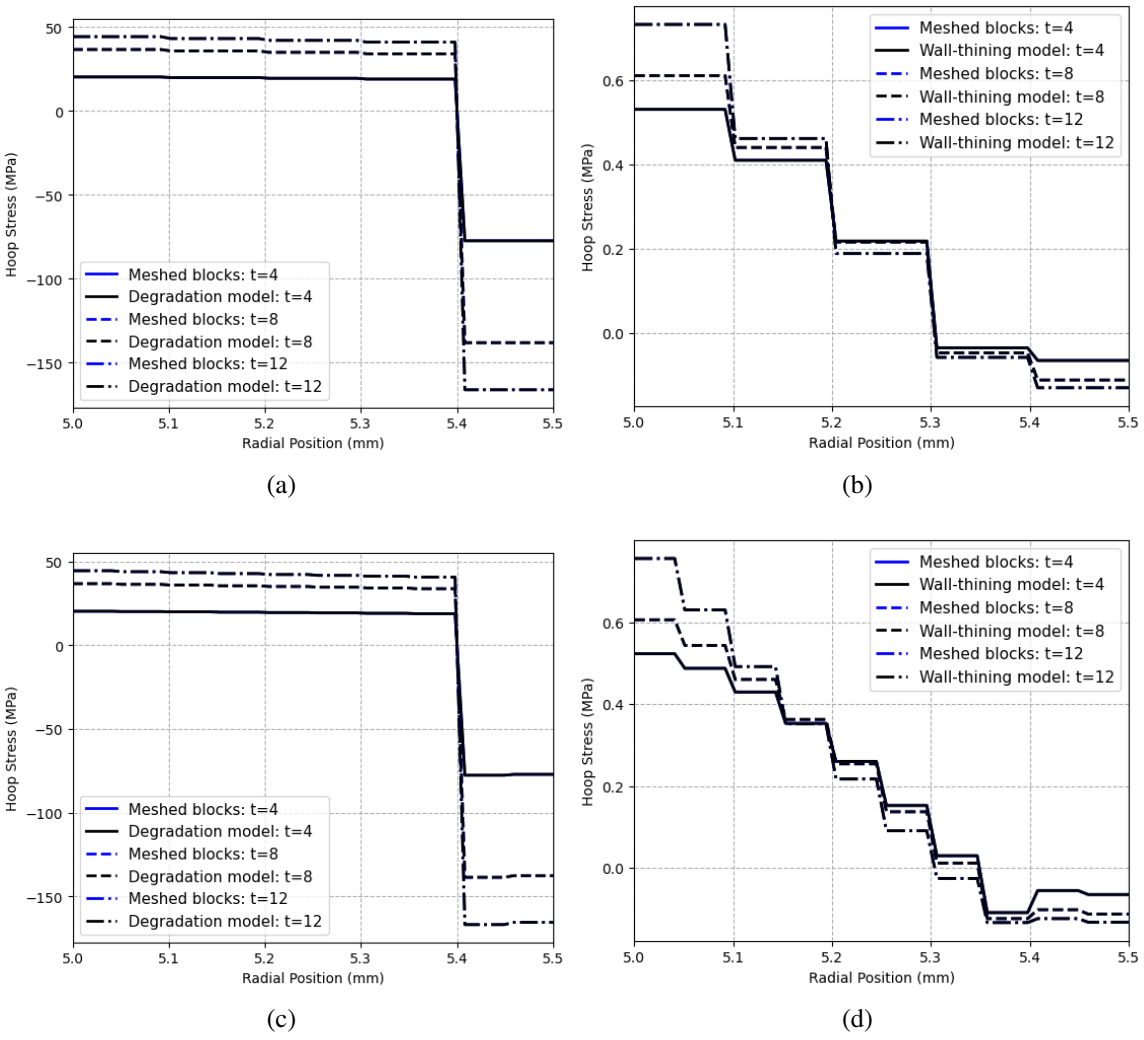

Figure 5.8: Verification of the mechanical degradation model when including thermal expansion using (a) the ZrO_2 model and (b) wall-thinning with 5 radial elements and (c) the ZrO_2 model and (d) wall-thinning with 10 radial elements.

test [101, 47] to replicate a LOCA in a laboratory environment. The cladding tube is 30-cm long with an inner diameter of 8.36 mm and a thickness of 0.57 mm. Each layer is assumed to be 3 cm thick for a total of 10 layers in the analysis. Two cases are assumed for what is termed the normal operation phase where the temperature is azimuthally uniform. The first is more representative of typical operation with an with an inlet (bottom of the tube) value of 580 K. The second case is a high temperature coolant case to induce a larger amount of oxidation with an inlet temperature of 630 K. Due to the relatively short length of the

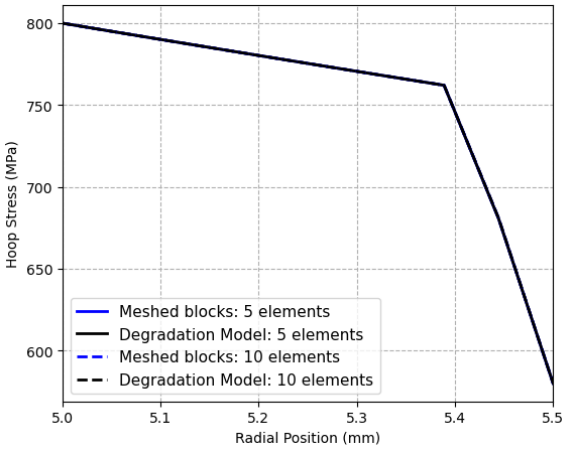

Figure 5.9: Schematic describing the loading conditions for the verification problem used for mechanics.

tube (representative of lengths put into furnace tests), the axial variation in temperature is assumed to linearly increase by 10 K from inlet to outlet in both the low and high inlet temperature cases. This temperature condition is held for 3 years, after which the temperature profile transitions to a product of sinusoidal functions to account for an axial profile with a maximum temperature at the midplane and values of 20 K less at the tube-ends, as well as a 30 K maximum circumferential variation. The time evolution of the maximum cladding surface temperature during the transient is representative of a SATS [101] or Studsvik [47] test as shown in Figure 5.10. The target peak cladding temperature is 1100 K and the temperature increase occurs at a rate of 5 K/s. The typical quench portion associated with these experiments is not included in Figure 5.10 because the simulation terminates well before the time of the quench. The time-dependent cladding surface temperature is given by:

$$T_{surf} = \begin{cases} T_{inlet} + \frac{10z}{0.3}, & \text{for } t \leq (x - 550) \\ T_{inlet}, & \text{for } (x - 550) < t \leq x \\ T_{inlet} + A, & \text{for } t > x \end{cases} \tag{5.12}$$

where T_{inlet} is the inlet temperature (K), and A is an equation that varies depending upon if the case is the normal operation (A_{norm}) or high temperature coolant (A_{high}) case.

$$A_{norm} = \frac{20\,(t-x)\left(25+\sin\left(\frac{\pi z}{0.3}\right)\right)}{104} - 30\sin\left(\frac{\theta}{2}\right) \tag{5.13a}$$

$$A_{high} = \frac{20\,(t-x)\left(22.5+\sin\left(\frac{\pi z}{0.3}\right)\right)}{90} - 30\sin\left(\frac{\theta}{2}\right), \tag{5.13b}$$

$x = 94608550$ s, t is the time (s), z is the axial position (m), and θ is the azimuthal position (rad).

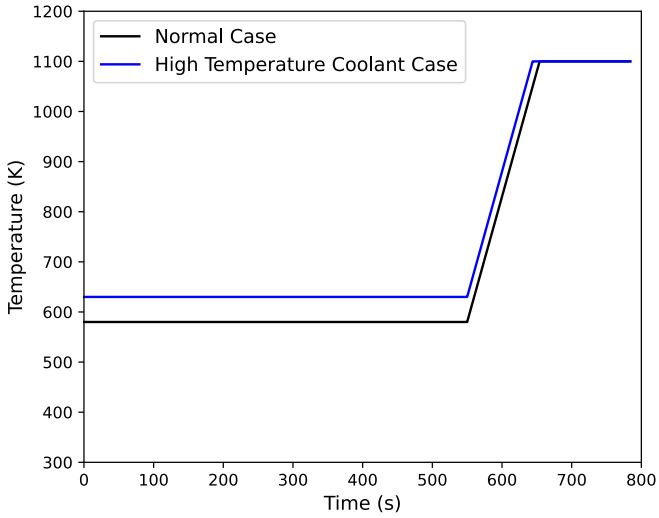

Figure 5.10: The evolution of the maximum cladding temperature as a function of time during the transient portion of the analysis.

A mechanical load is necessary to induce ballooning. During the normal operation phase, the internal pressure is linearly ramped from an initial pressure of 2 MPa to 8 MPa to simulate the increase in pressure due to fission gas release. During this ramp-up, the external pressure is held at 15.5 MPa. Upon beginning the transient, the external pressure is dropped to atmospheric (101.325 kPa), while the internal pressure remains constant at 8 MPa. The simulation is terminated when the plastic instability criterion is exceeded, denoted when the cladding creep rate exceeds 0.02777 s^{-1} [64, 79].

Calculation of the oxide thickness is shown at the end of the base irradiation (t = 9460800 s) for the normal operation case in Figure 5.11a. The difference between the oxide

thickness at the time of cladding failure (t = 94608643.7s or 643.7 s after the start of the transient) and at the end of normal operation is shown in Figure 5.11b for the normal operation case. This incremental accumulation of oxide during the transient is plotted instead of the total oxide thickness at cladding failure to highlight the asymmetry in the relatively small accumulation of oxide thickness during the transient. Ten lines, representing each layer in the mesh, with the oxide thickness (or oxide thickness difference) plotted as a function of azimuthal position, θ, are shown. The legend indicates the axial position of the layer. Note that the axial positions are associated with the thickness of the layers (i.e., Layer 1 is at 0.015 m, and Layer 10 is at 0.285 m). As expected, at the end of the normal operation period, the oxide thickness is uniform azimuthally in each layer with an increasing oxide thickness at layers at the top of the rodlet. At the time of rupture, there is a small azimuthal dependence on the oxide thickness for the case analyzed here due to the non-symmetric temperature, with a peak oxide thickness at $\theta = 0$.

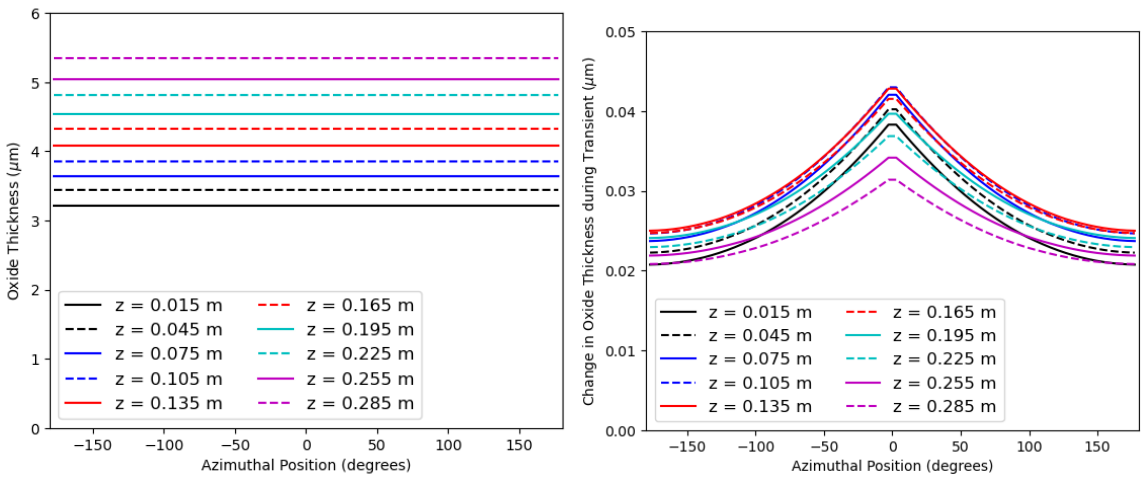

(a) (b)

Figure 5.11: (a) Oxide thickness as a function of axial and azimuthal position at conclusion of normal operation and (b) the accumulation of oxide thickness during the transient as a function of axial and azimuthal position for the normal coolant temperature case.

Figure 5.12a and Figure 5.12b present the oxide thickness at the end of the base irradiation and differential oxidation during the transient at the time of burst (633.7 s after transient initiation) for the high temperature coolant case. As expected, three years at a higher

coolant temperature resulted in a significantly larger oxide thickness at the conclusion of the base irradiation. However, this higher temperature means less of a temperature increase during the transient itself resulting in less change in oxide formation during the transient. This demonstration provides additional evidence that the rapid oxidation that would lead to cladding oxidation levels approaching the Appendix K criterion for ECR occurs after burst.

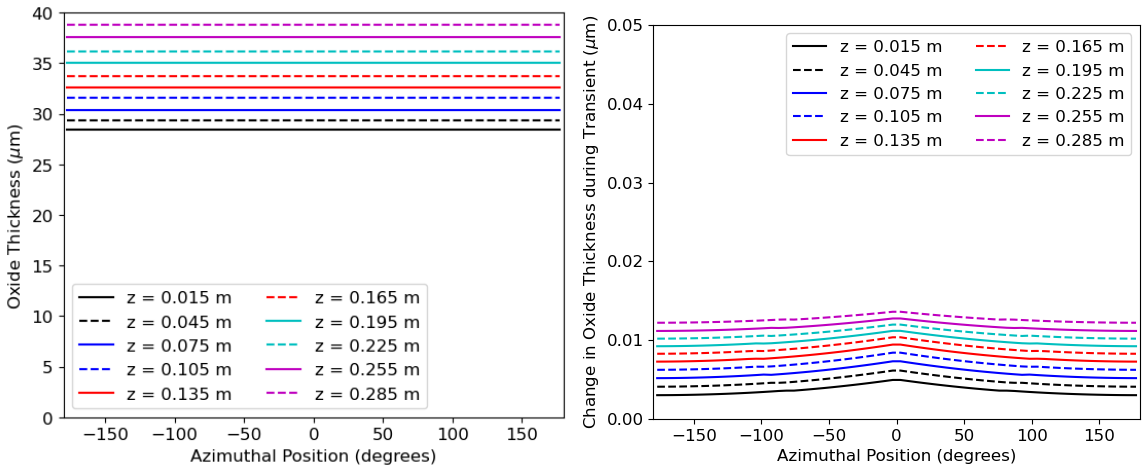

(a) (b)

Figure 5.12: (a) Oxide thickness as a function of axial and azimuthal position at conclusion of normal operation and (b) the accumulation of oxide thickness during the transient as a function of axial and azimuthal position for the high temperature coolant case.

Figure 5.13 shows a contour of the displacement magnitude at the time of burst for both normal operation and the high temperature coolant cases. As can be seen, the azimuthal and axial variations in temperature, albeit small, do cause asymmetric ballooning during the transient. Minimal difference is observed between the low and high temperature cases.

5.5 VALIDATION

To investigate the impact the degradation model may have on Bison predictions to experimental measurements, two experimental series were explored. The first is the REBEKA separate effects tests completed in an oxidizing environment. The second is a revisit of the IFA-650 cases initially simulated in Chapter 4.

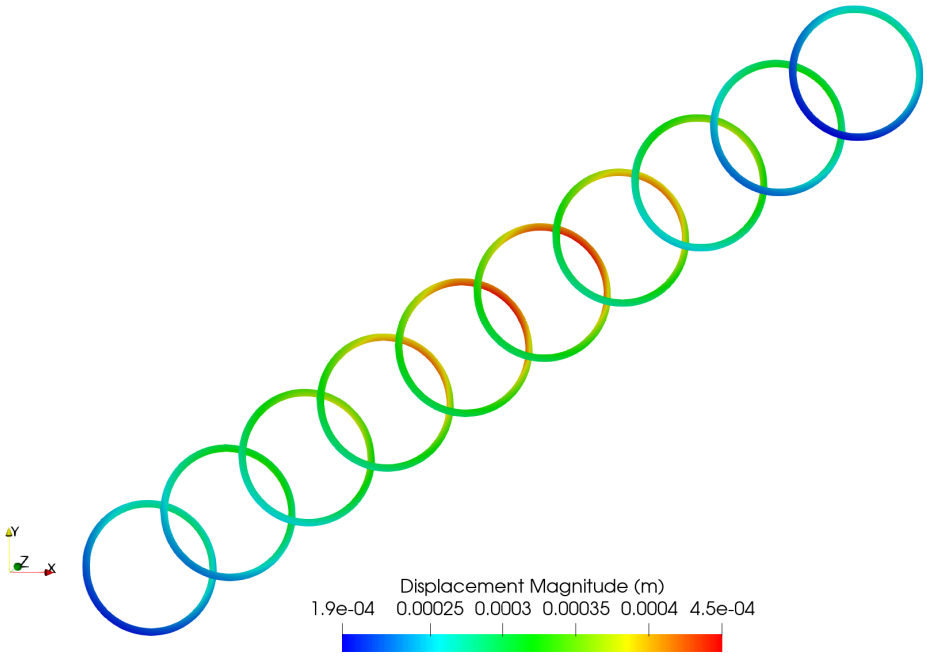

(a)

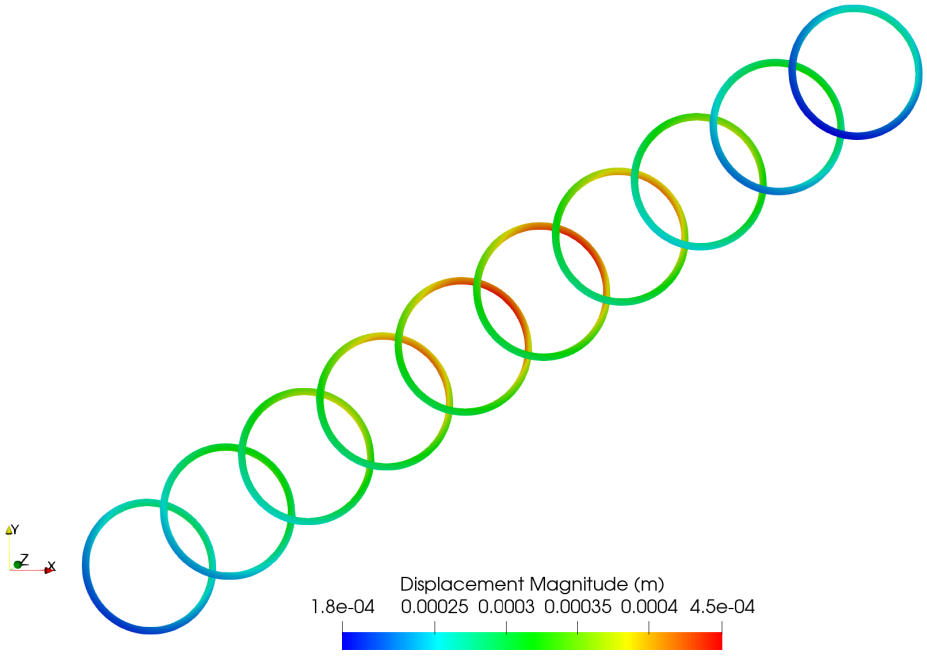

(b)

Figure 5.13: Displacement magnitude at the time of rupture for (a) the normal operation case and (b) the high temperature coolant case.

5.5.1 REBEKA Cladding Burst Experiments

The REBEKA separate effects tests [27, 65] are temperature transient tests in steam performed on single PWR-size Zircaloy-4 tubes. The purpose of the tests was to establish data on cladding ballooning and burst with reference to LOCA-like conditions. The cladding tubes had a fabricated inner and outer diameter of 9.30 and 10.75 mm, respectively, with a 325-mm heated length. The cladding was heated indirectly by conduction heating from the inside using an electrically insulated heater rod. The test parameters covered a range of 1 to 14 MPa for the internal rod pressure and 1 to 30 K/s for the heating rate. The test atmosphere was almost stagnant steam at atmospheric pressure and 473 K. The cladding temperatures were measured by thermocouples attached to the outer surface of the cladding. More details on the experimental apparatus and conditions are given in Erbacher et al. [27] and Markiewicz and Erbacher [65].

For these cases, the Bison calculations utilize a 2D-RZ axisymmetric representation for these cladding tubes. The Bison internal coolant channel is to have an inlet temperature of 473 K with atmospheric pressure and a nearly zero mass flow rate to simulate stagnant steam. Select rod internal pressures were chosen to study in the 1 to 14 MPa range: 1 MPa, and all even pressures in the range from 2 MPa to 14 MPa. Three different ramping rates were also analyzed: 1 K/s, 10 K/s and 30 K/s. A slight axial profile was applied to the interior surface to induce localized ballooning. Three Bison cases are considered for every combination of rod internal pressure and ramping rate: 1) no mechanical degradation model, 2) explicitly model ZrO_2 formation, and 3) wall-thinning. Two different cladding failure criteria are used here: the combined overstress overstrain and the combined overstress plasticity instability. The overstrain and plasticity instabilities criteria have been described previously. The overstress criteria is a limiting stress that the cladding can withstand before rupture would occur that is based upon temperature and oxygen content via [27]:

$$\sigma_b = a \exp\left(-bT\right) \exp\left(-\left(\frac{100x - 0.12}{0.095}\right)^2\right) \tag{5.14}$$

where x is the oxygen concentration (weight fraction) in the cladding and a and b are experimentally determined constants that vary as a function of Zircaloy phase as shown in Table 5.2.

Table 5.2: Phase dependence of a and b constants in burst stress correlation proposed by Erbacher et al. [27].

Temperature (K)	a (MPa)	b (K^{-1})
$\leq T_\alpha$, α-phase	830	0.001
$T_{\alpha\beta}$, middle of $(\alpha+\beta)$ phase	3000	0.003
$\geq T_\beta$, β-phase	2300	0.003

In Table 5.2, T_α is the transition temperature from α to $(\alpha+\beta)$ phases, $T_{\alpha\beta}$ is the temperature in the middle of $(\alpha+\beta)$ defined as $T_{\alpha\beta} = \frac{1}{2}\left(T_\alpha + T_\beta\right)$, and T_β is the transition temperature from $(\alpha+\beta)$ to β phases. Linear interpolation is used between these temperatures. Bison has a model for the evolution of the phase of Zircaloy called `ZrPhase` that can be found in Appendix C. In this study the oxygen concentration is set to zero in Equation 5.14 and the mechanical degradation model added in this work is activated. The overstress model was considered in these studies because they are fresh cladding tubes. It has been found by Pastore et al. [79] that the overstress correlation does predict premature failure during normal operation for pre-irradiated rods and should not be used in those applications.

The results of the study are shown in Figure 5.14. For these fresh cladding tubes it is observed that despite being in a steam environment and heated internally to high temperature the calculated amount of oxide that forms is <5 μm in almost all cases. Using the Pilling-Bedworth ratio the actual amount of consumed cladding is smaller. This amount of consumption is small compared to the cladding thickness of 0.725 μm used in these experiments. In order to capture this effect at least 73 second order elements would be required through the cladding thickness, which is computationally prohibitive. Given such a small amount of consumption the resulting impact on the stress state of the cladding would be limited. Therefore, all three Bison models for the cladding compute identical results for all ramping rates. The choice of cladding failure model does have an impact. For slower ramp-

ing rates the combined overstress and plastic instability model predicts failure closer to the experiment, particularly at the lower stress conditions. At higher ramping rates the opposite is true, with the combined overstress and overstrain model more closely matching the experiments. This also indicates that at lower pressure conditions the failure criteria is driven by either the overstrain or plastic instability threshold and not the overstress correlation given in Equation 5.14.

5.5.2 HALDEN IFA-650 TEST SERIES

In Chapter 4 the IFA-650 series were analyzed with a focus on predictions of the time to burst and the axial profile of the cladding diameter and fuel mass fraction. Oxidation as described in Section 5.1 was applied during those analyses using the recommended models for lower and high temperature oxidation but mechanical degradation was not assumed. Here, since the impact (if any) of the inclusion of the mechanical degradation model is of interest the Layered1D formulation of the problem is used. The mean values for all of the uncertain parameters in Table 4.4 are used in the simulations here. The Barani [9] large fragmentation model was selected and 30 fuel layers were used with a plastic instability criterion for failure. The fuel performance parameters that could possibly be affected by the mechanical degradation model are the time to rupture, and the cladding temperature and rod internal pressure at rupture. For these settings, cases with and without the degradation model are completed. The results of the study are provided in Table 5.3. Even though the oxide thickness is larger in these pre-irradiated rods that go to high burnup when compared to the fresh cladding tubes of the REBEKA cases, the amount is still insufficient within the mesh resolution assumed to contribute to the calculation.

5.5.3 SUMMARY

A simplistic approach to accounting for mechanical degradation of the cladding due to oxidation was presented. Two options were considered: 1) the material properties were transi-

Table 5.3: Results of the oxidation study for IFA-650.4, IFA-650.9, and IFA-650.14

Experiment	Oxidation Treatment	Rupture Time (s)	Peak Clad Temperature† (K)	Rod Internal Pressure† (MPa)
IFA-650.4	No degradation	319.98	1073.41	5.33
	Degradation	319.98	1073.41	5.33
IFA-650.9	No degradation	140.05	1124.89	5.27
	Degradation	140.05	1124.89	5.27
IFA-650.14	No degradation	350	1169.87	1.59
	Degradation	350	1169.87	1.59

†at time of rupture

tioned to that of ZrO_2 after degradation and 2) wall-thinning was assumed where the elastic properties are simply scaled by a factor of 1×10^{-3}. The number cannot be smaller due to numerical stability issues. Verification of the models were shown for thermal properties, thermal expansion, low and high temperature creep, and elasticity. Demonstration of coupling the oxidation models to the Layered2D framework was also provided. Validation of one separate effects and one integral test series was presented.

Through the Layered2D demonstrations and the 2D-RZ axisymmetric and Layered1D validation exercises it was found that calculated oxidation rates for both irradiated and fresh cladding were much too low prior to rupture to have much of an impact on the time at which rupture occurs. The rapid oxidation that approaches the Appendix K limits set by the NRC occurs after rupture once coolant infiltrates the rod upon reflooding leading to double-sided oxidation. A deficiency in the developed mechanical degradation model is that some mesh dependence exists as it relies on quadrature points where the material properties are calculated to be on either side of the metal-oxide interface. At these small oxide thicknesses even smaller amounts of the metallic substrate is consumed. Typically, for most fuel performance metrics of interest five second order elements through the cladding thickness (as used in the studies presented in this chapter) is sufficient. In order to properly resolve the small oxide thicknesses calculated much finer meshes would be required. This level of fidelity appears

to be unnecessary in determining the time of rupture unless the cladding is subjected to elevated temperatures for a long period of time. For example, the high coolant temperature case presented in the Layered2D demonstration would predict appreciable oxide thickness formation if the irradiation time was doubled from 3 to 6 years. However, most existing LWR reactors would not operate at the coolant temperatures applied in that demonstration case.

From an industry perspective the concern from the oxidation point-of-view is mitigating the rapid oxidation post rupture as temperatures continue to soar towards the Appendix K limit of just under 1480 K and beyond and not the impact on the mechanical response prior to rupture as originally postulated.

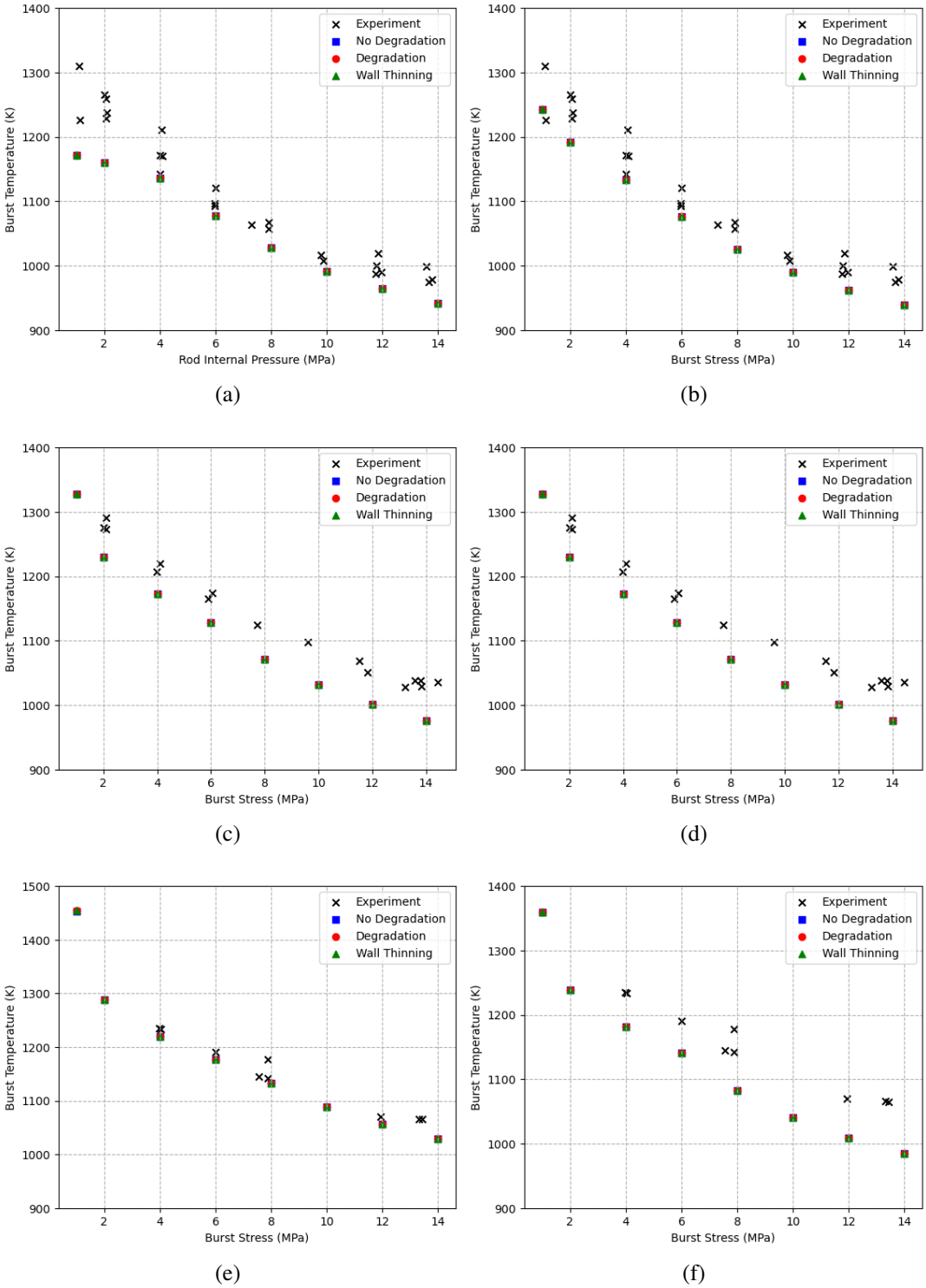

Figure 5.14: Comparisons of the Bison predictions to the experimental measurements for the burst temperature are shown for 1 K/s, 10 K/s, and 30 K/s from top to bottom. The combined overstress overstrain failure criterion is shown on the left and the combined overstress and plastic instability criterion shown on the right. The no degradation, degradation, and wall thinning model predictions are included.

CHAPTER 6

CLADDING RUPTURE

6.1 LITERATURE REVIEW

The cladding provides the final barrier to release of radioactivity into the primary coolant system. During a LOCA, this radioactivity can make its way into the containment building of the nuclear power plant. At high burnups fuel fragments may be dispersed into the coolant system if their size relative to the rupture opening is small enough. Throughout the preceding chapters cladding failure has been determined by a variety of different criteria, including plastic instability, overstress, overstrain, and a variety of combinations of the three. These criteria as has been shown in previous chapters are reasonable at predicting the time and location of rupture, but are unable to provide a prediction of the opening size. Thus, as it stands no model exists to estimate the opening size in Bison. Recall that the extensive literature review on FFRD [102] suggests that predictions of rupture opening size are necessary to estimate the amount of fuel dispersal from the cladding.

6.2 QUANTIFICATION OF RUPTURE AREA

Experiments throughout the decades as summarized in [91, 102] and more recently by [16] measured the ruptured area for both integral and separate effects (non-fueled rodlet) experiments. Fuel conditions ranged from fresh fuel rods up to highly burned fuel at $>$ 90 MWd/kgU rod average burnup. Cladding specimens in furnace tests ranged from virgin samples to highly irradiated rodlets. Figure 6.1 present a variety of experimentally observed rupture opening sizes and shapes for Zircaloy cladding from the Studsvik and Halden test

series. In general the rupture openings for Zircaloy claddings tend to be longer than they are wide and typically are approximated as elliptical in shape despite being lenticular in shape. The width and length of the rupture are measured by post experiment using lines on photographic images as in Figure 6.2.

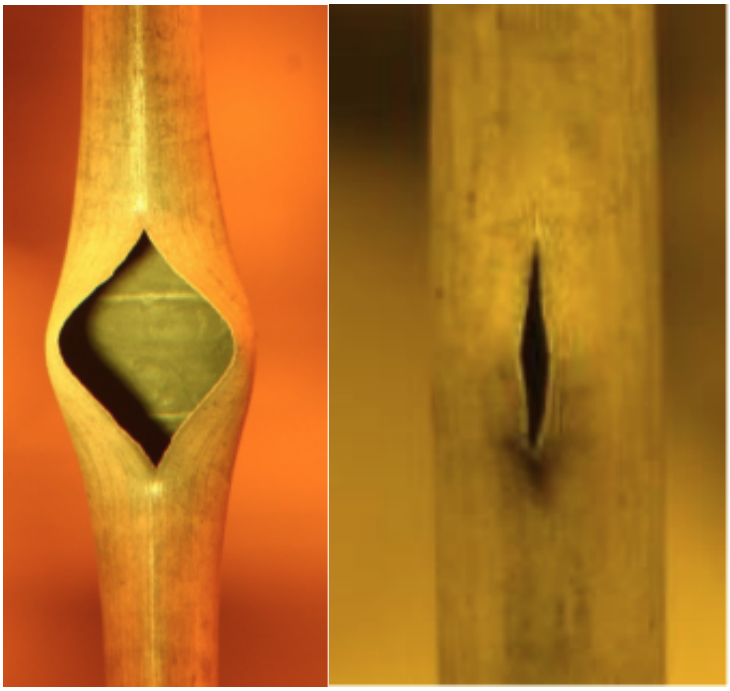

(a) Studsvik Rod 191 (b) Studsvik Rod 198

(c) Halden IFA-650.2

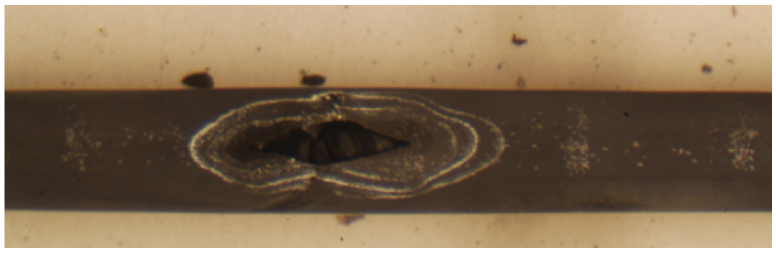

(d) Halden IFA-650.10

Figure 6.1: Photographs of Zircaloy burst shapes and sizes selected from the available experimental database summarized in [91].

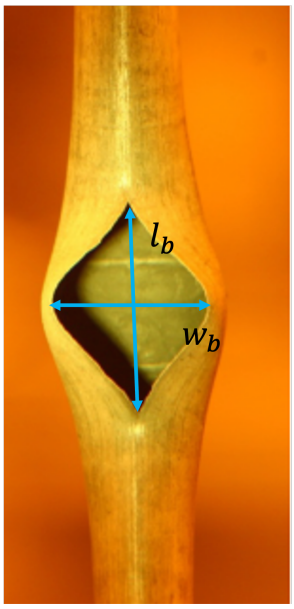

Figure 6.2: Definition of rupture width (w_b) and rupture length (l_b).

Over the last few years a couple empirical models have been proposed to estimate the size of the rupture in failed cladding tubes based upon quantities measured after the conclusion of experiments. Jernkvist [51] provided a comprehensive review of rupture opening measurements and developed a model based upon 235 tests. The report discusses potential effects of hydrogen content on burst times through the modification of the α to $\alpha + \beta$ and β to $\alpha + \beta$ transition temperatures. In Bison, the Zircaloy phase is calculated by the `ZrPhase` model (see Appendix C for details). According to Jernkvist, for fuel dispersal calculations, only the rupture opening width is of importance and not the rupture length. Thus, a model of the following form was proposed for the rupture width:

$$w_b\left(\sigma_b\right) = \alpha D_o\left(1 - \exp\left(-\beta\left(\sigma_b - \sigma_{th}\right)\right)\right) \tag{6.1}$$

where w_b is the rupture width (mm), D_o is the as-fabricated cladding diameter (mm), σ_b is the hoop stress at burst, and α, β, and σ_{th} are fitting constants. Best-estimate values of these constants were found to be $\alpha = 0.5848$, $\beta = 3.35 \times 10^{-8}$ Pa^{-1}, and $\sigma_{th} = 5$MPa. This best-estimate correlation is plotted against the supporting database in Figure 6.3. In the figure, the open circles correspond to experiments where the opening width was directly

measured, whereas the crosses correspond to experiments where the opening width had to be estimated from the measured rupture area. The correlation used to relate rupture opening area and rupture opening width is given by:

$$A_b = 0.619 w_b^2 \left(\frac{11.4}{w_b + 0.81} + 0.95 \right) \tag{6.2}$$

where A_b is the rupture opening area (mm^2). This best-estimated model is said to bound 56.8% of the 285 supporting database. A more conservative model can be captured by increasing the value of the constant α.

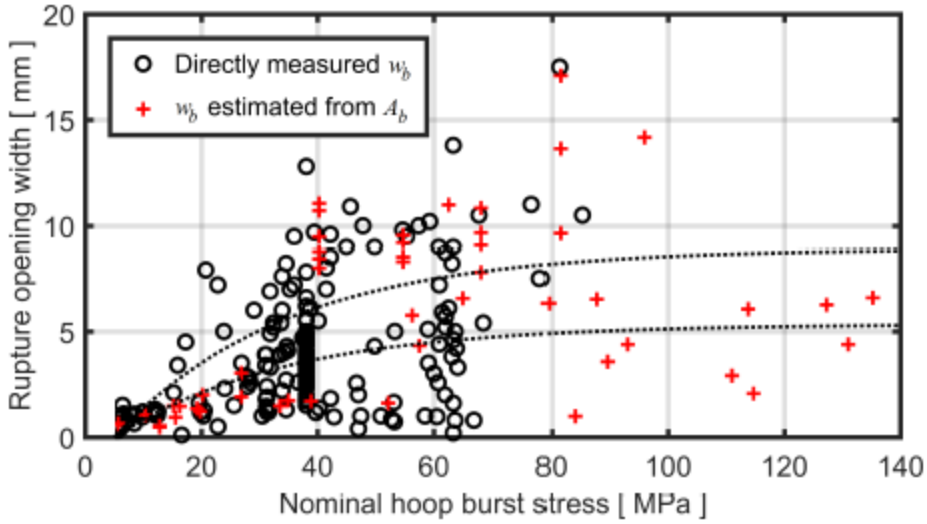

Figure 6.3: Range of the best-estimate rupture opening widths in comparison with the supporting database. The dotted lines corresponded to Equation 6.1 with cladding outer diameters of 9.13 and 15.20 mm, respectively, which are the lower and upper bounds on cladding diameter used in the supporting database. Reproduced from [51].

Once the rupture width has been determined, the area can be calculated by Equation 6.2 and the rupture length can be obtained by:

$$l_b = \frac{11.4 w_b}{w_b + 0.81} + 0.95 \tag{6.3}$$

The second empirical model for rupture area is based upon research conducted by a group at the ORNL [17]. The authors present two models that are denoted as the average and limiting models. The ORNL formulation is based upon the peak cladding hoop strain

at burst (%), which occurs at the burst location. The rupture length (mm) is estimated by:

$$l_b = C_1 \left(\epsilon_{hoop} - C_2\right)^{C_3} - C_4 \tag{6.4}$$

where ϵ_{hoop} is the peak cladding hoop strain (%) and C_1 (mm/%), C_2 (%), C_3(-), and C_4 (mm) are fitted constants. Depending upon whether the model is assumed to be average or limiting. The determined coefficients for the two models are summarized in Table 6.1.

Table 6.1: Coefficients for the limiting and average models for rupture length by ORNL [17].

Model	C_1 (mm/%)	C_2 (%)	C_3 (-)	C_4 (mm)
Limiting	20	8	0.22	18
Average	55	8	0.09	60

Once the rupture length is estimated the proposed correlations for the rupture width is given by:

$$w_b = \begin{cases} D_o \left(C_5 l_b^{C_6} + C_7\right), & l_b < l_{th} \\ D_o, & l_b \geq l_{th} \end{cases} \tag{6.5}$$

where D_o is the as-fabricated cladding outer diameter (mm), l_b is the rupture width, and C_5 (-), C_6 (-), C_7 (mm), and l_{th} are constants. The coefficients for the limiting and average cases for the rupture width are provided in Table 6.2.

Table 6.2: Coefficients for the limiting and average models for rupture width by ORNL [17].

Model	C_5 (-)	C_6 (-)	C_7 (mm)	l_{th} (mm)
Limiting	0.055	0.92	-0.01	24
Average	0.032	0.92	0	43

After defining the equations for the rupture length and width Capps et al. [17] explored the rupture area calculated by assuming different rupture shapes: rectangle, rhombus, and

ellipse (oval). The standard area equations for these primitive shapes are used:

$$\text{Rectangle: } A_b = w_b l_b \tag{6.6a}$$

$$\text{Rhombus: } A_b = \frac{w_b l_b}{2} \tag{6.6b}$$

$$\text{Ellipse: } A_b = \frac{\pi w_b l_b}{4} \tag{6.6c}$$

The area equations are plotted as a function of peak hoop stress in Figure 6.4 for both the average and limiting cases. The underyling experimental data supporting the development of the ORNL model is not shown. The authors suggest that the rectangle approximation would capture the majority of the available experimental data including many outlier data points. For the best representation of the totality of the underlying dataset the authors suggest the rhombus be used as the rupture area shape for the model.

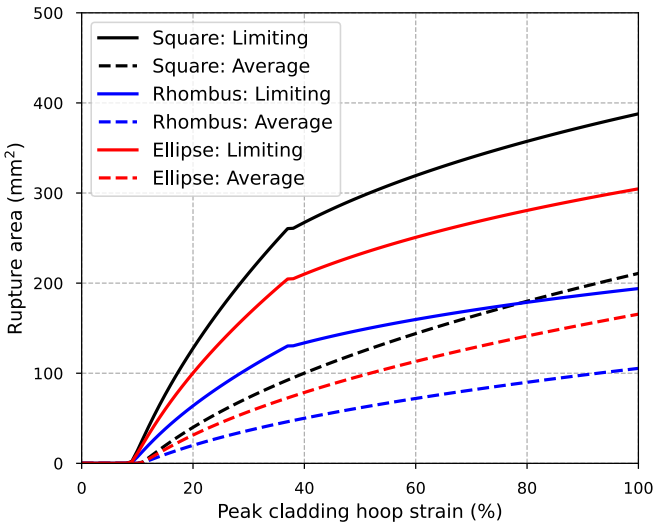

Figure 6.4: Plots of the rectangular, ellipse, and rhombus rupture shape assumptions for the average and limited cases for the ORNL model. A cladding outer diameter of 10.75 mm is assumed in the creation of the plot. Adapted from [17].

It should be noted that Jerkvist [51] in the development of their model indicate that the hoop strain at burst (equivalent to the peak cladding hoop strain) is not a suitable parameter for the rupture width. Two reasons were given for this statement, first, the rupture width does not correlate well with the peaking cladding hoop strain, and two, fuel performance

codes are notoriously poor at predicting this value accurately. A comprehensive international benchmark on fuel performance modeling under LOCA conditions [3] illustrated this fact, with numerous international organizations with their codes having a difficult time predicting the magnitude of the cladding diameter and consequently the strains within the cladding.

6.3 Susceptibility of Fuel Dispersal

One of the earliest models for fuel dispersal estimates was to assume that all fuel <1 mm in size anywhere within the fuel rod may be dispersed [90]. A recent Research Information Letter (RIL) published by the NRC proposed six additional models for determining the amount of fuel dispersed in a fuel performance analysis. It should be mentioned that RIL is not regulatory guidance, but may be used to determine whether any regulatory actions are necessary. The six proposed models are outlined below:

1. All fuel smaller than 1 mm in the length of the rod with greater than 3% strain
2. All fuel smaller than 2 mm in the length of the rod with greater than 3% strain
3. All fuel in the length of the rod with greater than 3% strain
4. All fuel smaller than 1 mm in the length of the rod with greater than 2% strain
5. All fuel smaller than 2 mm in the length of the rod with greater than 2% strain
6. All fuel in the length of the rod with greater than 2% strain

where these models only apply to regions of the fuel with an average burnup >55 MWd/kgU.

The authors presented comparisons to data from Studsvik Cladding Integrity Program (SCIP) test series. The program began in 2004 and is currently in its forth iteration (i.e., SCIP-IV). At present, neither the author of this work, INL, or the University of South Carolina are participants in SCIP and therefore any data from these experiments is not avail-

able beyond what is presented in the RIL. The RIL only shows comparisons of the 6 proposed models for fuel dispersal against the experimental measurements for dispersal, but not enough detail is provided to enable simulations of these experiments. The authors of the RIL [8] also make a clear distinction between dispersed and mobile fuel. The definitions are as follows:

> **Dispersed fuel:** Fuel that was dispersed during the experiment.
>
> **Mobile fuel:** Fuel that could relocate even if relocation did not occur during the experiment. Often determined by measuring the amount of additional fuel dispersed after shaking of the experimental apparatus. Therefore, mobile fuel encompasses that dispersed during the transient and after shaking.

The authors of the RIL suggest when selecting a dispersal model that comparisons to experiment be maded against the mobile fuel measurements. This is because the models do not account for rupture opening size or the volume and pressure evolution of the fill gas during the transient. They state that it is reasonable to assume that above 55 MWd/kgU that any fuel within the length of the rod greater than 3% cladding strain could disperse. This suggests that the third proposed model is considered to be reasonably conservative.

6.4 Axial Gas Communication

A topic that has not yet be discussed in this work that may play a role in fuel dispersal and the final shape of the balloon of the cladding is axial gas communication. Traditionally, fuel performance codes have treated axial gas communication to be instantaneous such that any fission gas release or volume changes immediately equalizes the pressure throughout the rod. In addition, after cladding rupture, if the simulation is continued the rod internal pressure is instantly set to the external pressure on the rod. By making this assumption even as the temperature increases post rupture there is no driving force to induce further creep and ballooning.

Experimental evidence [25, 129] has indicated that in some cases after cladding rupture there can be delay up to a couple minutes (~120 seconds for the pressure to decay to atmospheric. Other experiments have been conducted to estimate the permeability of the fill gas through fragmented nuclear fuel at different burnups [72, 94]. For a specific fuel rod this can be determined by conducting many experiments with a differential pressure across the fuel and measuring the time it takes for the pressure on both sides to equalize. Two approaches can be done here: 1) pressurizing one side to a known pressure and holding until the other side of the rod (initially at atmospheric pressure) comes up to the same pressure, 2) pressurizing one side to a known pressure and allowing to decay to atmospheric pressure.

The pressure decay delay observed in some experiments may effect ballooning behavior and the resulting final geometry that must be cooled due as a pressure differential remains post rupture for up to several minutes. During this time, the cladding temperature typically continues to rise to target peak cladding temperature and is held for a duration set in the experiment.

A model exists in the literature proposed by Khovstov et al. [56] that computes the depressurization as a function of cladding hydraulic diameter and the fractured state of the fuel (i.e., flow bypass when an annulus exists between the fuel and cladding and through a crumbled fuel column). The model has been applied to a few of the Halden IFA-650 tests elsewhere. Any gas flow blockage by fragmented fuel is subject to dispersal as the pressure equalizes.

6.5 Rupture Model

While the empirical models presented in the literature review section of this chapter provide reasonable correlations for predicting the rupture area relative to the underlying experimental data base they do not provide a means of explicitly modeling the rupture opening. Discretely modeling the burst opening in ruptured cladding tubes provides a framework for follow-on analyses to mechanistically model dispersal and the distribution of the dis-

persed fragments throughout the primary coolant system. Such a framework will in the future enable advanced calculations of LOCA behavior that can move towards an explicit best-estimate model for fuel dispersal.

The developed model presented in Figure 2.1 highlights that global data is passed from a Layered2D simulation to a cladding only 3D simulation to model the rupture opening. This statement is true for cladding burst experiments containing fuel. For cladding only experiments Layered1D, Layered2D, or 2D-RZ models can be used to obtain the global quantities as necessary depending upon the experimental conditions. Three-dimensional simulations are necessary for the rupture opening modeling regardless if there is no azimuthal temperature variation as the presence of the rupture introduces local non-linearities that cannot be captured by axisymmetric models. Modeling the axial extent (length) of the rupture cannot be captured by the Layered1D or Layered2D frameworks since the associated thicknesses of the layers are not explicitly modeled. Discrete modeling of discontinuities such as cracks has been completed previously in this work in Chapter 3. Since the cladding rupture is essentially the opening of a crack the XFEM (see Section 2.3) is also used here. As mentioned the approach is to run the experiment in a 2D-RZ, Layered1D or Layered2D formulation as required to generate global quantities of interest to be applied to the cladding only experiment including cladding inner and outer surface temperatures as a function of time and location, the time and location of rupture (using one of the many empirical criteria available in Bison), and the calculated rod internal pressure evolution inside the tube. Note that the evolution of mechanical properties due to oxidation is not required as the extensive study in Chapter 5 determined that pre-rupture during representative LOCA conditions it is not of concern.

At this time, 3D propagation of XFEM cracks in MOOSE is limited to predefined growth directions and prescribed crack velocities. The velocity of crack growth under LOCA conditions in Zircaloy-tubes is not known. Thus, to overcome these challenges and enable preliminary predictions of cladding rupture opening using the computational approach de-

veloped here, XFEM is used to prescribe a crack that has a length that corresponds to the experimentally measured value for l_b at the time of rupture. Axial gas communication is not included here but could be added by appending a longer pressure evolution post-rupture. Instead, a few seconds are appended post rupture for the rapid depressurization case. The simulations are then used to determine w_b, and consequently A_b.

6.6 Demonstration of the Rupture Model

To illustrate the methodology used in simulating the rupture opening in cladding tubes a cladding only geometry is used. The setup is similar to that of the REBEKA [27, 65] or Studsvik [47] experiments where the pressure is held relatively constant and the temperature is linearly increased until burst. Here, a 5 K/s ramping rate is assumed to a target peak cladding temperature of 1400 K. A sinusoidal axial profile to induce localized ballooning is given by:

$$T(z) = 300 + \frac{1080}{220}t + \frac{20}{220}t \sin\left(\frac{\pi z}{0.3}\right) \tag{6.7}$$

where t is the time (s), and z is the axial position. The tubes are 300 mm long. Tubes of two different radial dimensions were analyzed: 1) inner/outer diameter of 9.30/10.75 mm with a thickness of 725 μm and 2) inner/outer diameter of 8.36/9.5 mm with a thickness of 570 μm. The first set of dimensions are representative of older cladding designs that some of the existing experimental data is based upon. The second is more representative of the currently employed cladding dimensions. Four rod internal pressures (2, 4, 6, and 8 MPa) and four crack lengths (5, 10, 15, and 20 mm) are simulated.

In order to determine at which time to terminate the full 3D simulations, 2D-RZ axisymmetric analyses were completed to determine the time of rupture using the combined overstress plastic instability burst criterion, which is a combination of the overstress discussed in Section 5.5.1 and plastic instability used in Section 4.5.

The calculated results of rupture width, length, and area are tabulated in Table 6.3 for all the combinations of pressure, crack length, and tube dimensions. This corresponds to

32 different analyses. The results show that increasing rod internal pressures lead to predict rupture earlier in the temperature transient. For a given internal pressure the rupture width and consequently area increases with increasing rupture length. Larger rupture lengths at lower internal pressures results in larger rupture areas than small length cracks at the higher internal pressures. Larger diameter (i.e., thicker) cladding tubes generally led to smaller rupture areas. This is because a higher pressure is required to displace the cladding the same distance. The demonstration study focuses on relatively lower rod internal pressure consistent with some cladding tube experiments. If one examines the experimental data used to develop the ORNL empirical rupture model [17] one will see that the calculations are reasonable even if the data here is not correlated against peak hoop strain.

Select examples of what the rupture opening looks like are presented in Figure 6.5. The 15 and 20 mm long cracks for the 8 MPa loading are shown for both the small and large diameter tubes as they have large opening areas that are easy to visualize. As is tabulated in Table 6.3 smaller rupture areas are observed for small length cracks under the same pressure condition. Significant deformation is observed as one increases the rupture length.

6.7 VALIDATION

While the authors developing the empirical correlations [17, 51] present a lot of data on the plots for the derivation of their correlations, much underlying conditions for those experiments is not readily available for fuel performance analyses. To demonstrate the use of the discrete modeling of rupture model developed in this work, a select few cases for details of the experiments are publicly available are analyzed. The 3 cases studied include the SATS North Anna Rod #1 [89] experiment and Studsvik Rods 191 and 196 [47, 30].

6.7.1 SATS NORTH ANNA ROD #1

The SATS North Anna Rod #1 was the initial demonstration experiment in the hot-cell version of the ORNL SATS facility. The installation in the hot-cell has enabled furnace

Table 6.3: Results of parametric analysis to demonstrate the rupture model on Zircaloy cladding only tubes.

Clad ID/ Clad OD (mm)	Rupture Length (mm)	Rod Internal Pressure (MPa)	Rupture Time (s)	Rupture Width (mm)	Rhombus Rupture Area (mm^2)	Ellipse Rupture Area (mm^2)
8.36/9.5	5	2	181.058	6.38×10^{-3}	0.016	0.025
	10	2	181.058	0.0448	0.224	0.352
	15	2	181.058	0.242	1.815	2.851
	20	2	181.058	0.541	5.410	8.498
	5	4	169.352	0.0228	0.057	0.090
	10	4	169.352	0.103	0.515	0.809
	15	4	169.352	0.947	7.103	11.157
	20	4	169.352	2.62	26.200	41.155
	5	6	157.325	0.0318	0.080	0.125
	10	6	157.325	0.138	0.690	1.084
	15	6	157.325	1.69	12.675	19.910
	20	6	157.325	8.24	82.400	129.434
	5	8	146.870	0.0213	0.053	0.084
	10	8	146.870	0.091	0.455	0.715
	15	8	146.870	3.85	28.875	45.357
	20	8	146.870	8.89[†]	88.900	139.644
9.30/10.75	5	2	183.722	0.0259	0.065	0.102
	10	2	183.722	0.0874	4.370	6.864
	15	2	183.722	0.392	2.940	4.618
	20	2	183.722	0.693	6.930	10.886
	5	4	172.199	0.024	0.060	0.094
	10	4	172.199	0.0963	0.482	0.756
	15	4	172.199	0.848	6.360	9.990
	20	4	172.199	2.1	21.000	32.987
	5	6	162.215	0.0409	0.102	0.161
	10	6	162.215	0.173	0.865	1.359
	15	6	162.215	1.43	10.725	16.847
	20	6	162.215	6.24	62.400	98.018
	5	8	151.306	0.0332	0.083	0.130
	10	8	151.306	0.171	0.855	1.343
	15	8	151.306	2.96	22.200	34.872
	20	8	151.306	7.86[†]	78.600	123.465

[†] These cases failed to make it to the target time due to severe deformation and numerical instability

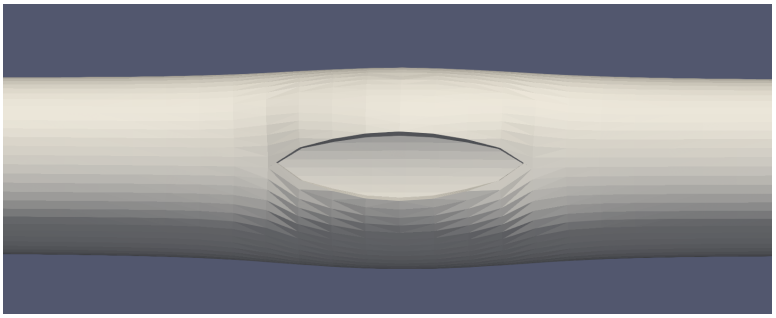

(a)

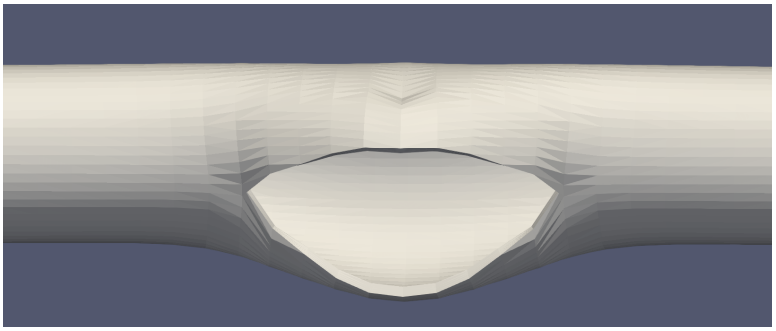

(b)

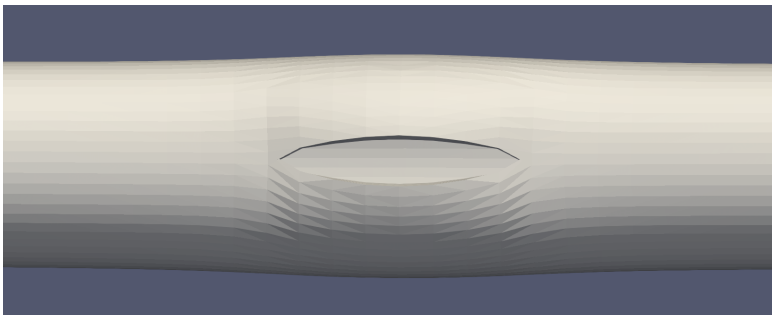

(c)

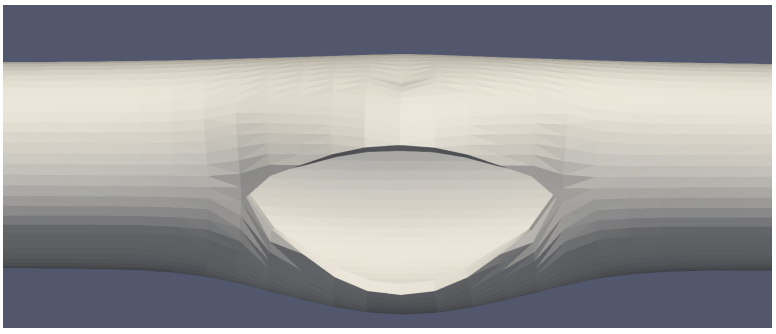

(d)

Figure 6.5: Visualizations of the rupture opening for the Zircaloy demonstration cases with 8 MPa loading for (a) small diameter $l_b = 15$mm, (b) small diameter $l_b = 20$mm, (c) large diameter $l_b = 15$mm, (d) large diameter $l_b = 20$mm.

testing under LOCA-like conditions on spent nuclear fuel. The North Anna rod selected for testing was identified as rod P16 that was characterized prior to re-fabrication [89]. The average burnup of the rod was 67.3 MWd/kgU prior to the transient experiment. The axial location of the segment was selected from a region of the mother rod where there would be no spacer grid effects. The ends of the rodlets were sealed by Swagelok. Details of the refabrication procedure utilized by the ORNL experimentalists can be found in [89]. In addition to cladding rupture area, additional parameters of interest were measured during the experiment including, burst pressure (MPa), and burst temperature (K). The experimentally measured rupture length for inclusion in the 3D analysis is 16 mm.

Dimensions of the refabricated rodlet are presented in Table 6.4. The Swagelok thicknesses, fuel diameter, and fuel-to-clad gaps were assumed to ensure the total rodlet length and clad outer diameter were equal to the experiment specifications. Since no experimental evidence is provided of the azimuthal variation in the furnace test a 2D-RZ axisymmetric analysis is used first to develop the appropriate time history boundary conditions and determine the time of rupture. Studies using both the PI and OS failure criteria were completed.

Table 6.4: Rodlet specifications for the Bison model of the North Anna #1 SATS test.

Parameter	Value
Rodlet height (mm)	289.96
Fuel stack height (mm)	264.16
Bottom and top plenum height (mm)	12.7
Endcap (Swagelok) thickness† (mm)	6.35
Fuel outer diameter† (mm)	8.2
Fuel-to-cladding gap thickness† (mm)	0.08
Cladding thickness (mm)	0.57
Cladding outer diameter (mm)	9.5
Initial enrichment (wt% U-235)	4.2
Cladding type	M5
Initial fuel density (kg/m^3)	10431

†Assumed dimensions such that the cladding dimensions matched the experiment

The phases of the transient supplied in the SATS facility are similar to that of the

Studsvik experiments (see Section 6.7.2). For the North Anna experiment 5 primary stages occurred:

1. Heat specimen to 573.15 K and ~8.27 MPa
2. Increase temperature at 5 K/s from 573.15 K to 1473.15 K
3. Hold temperature for 90 s at 1473.15 K
4. Decrease temperature at 3 K/s from 14713.15 K to 1073.15 K
5. Quench once temperature reaches 1073.15 K

It should be mentioned, that the temperature hold and decrease, and quench phases are not modeled in the Bison analysis as post-rupture behavior is not of interest in this work. Figure 6.6 presents the exterior temperature and interior pressure evolution applied to the irradiated segment of cladding from the North Anna P16 mother rod. The external pressure is assumed to atmospheric.

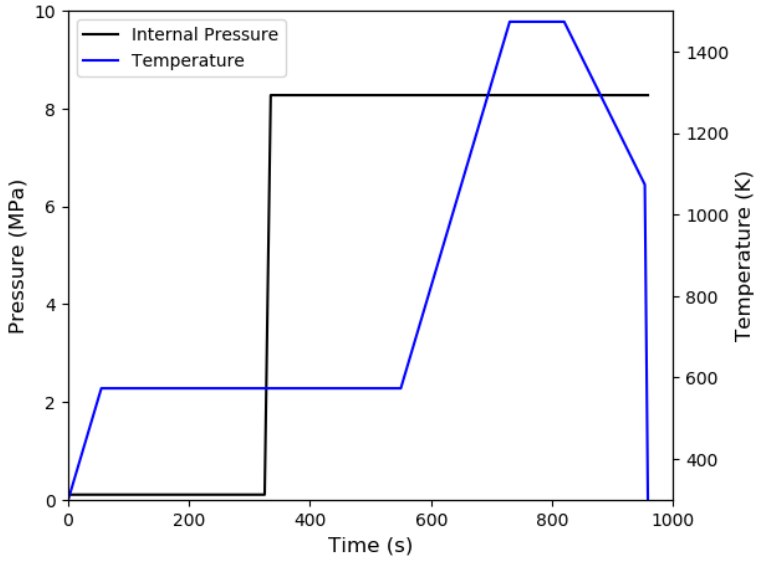

Figure 6.6: Internal pressure and temperature supplied to the interior and exterior surfaces of the cladding, respectively, for the North Anna Rod #1 simulations.

While the North Anna rodlet contained fuel, it is not included in the LOCA analysis completed here. This is due to the fact that the commercial base irradiation to condition the

fuel is unknown. The only information regarding the fuel is the initial enrichment, density, and discharge burnup. A simplistic approach is used to account for the irradiation induced creep and growth of the cladding for such a discharge burnup using an estimation of the fast neutron fluence that the cladding would experience assuming a constant power up to that burnup. The derivation of this initial fluence starts with the average burnup which can be approximated by:

$$Bu_{avg} = \frac{\dot{F} t M}{\rho N_A} \tag{6.8}$$

where Bu_{avg} is the average burnup (FIMA), $\dot{F}$ is the fission rate (fissions/m^3-s), t is the time (s), M is the molar mass of UO_2 (0.270 kg/mol), ρ is the initial fuel density (kg/m^3), and N_A is Avogadro's number. The volumetric heat generation can be calculated from the fission rate as:

$$Q''' = \dot{F} \epsilon_f \tag{6.9}$$

where Q''' is the volumetric heat generation rate in W/m^3, and ϵ_f is the energy per fission (taken as 3.2×10^{-11} J/fission). Alternatively, the volumetric heat generation can be calculated through the linear heat generation rate supplied to the fuel:

$$Q''' = \frac{4 P_{lin}}{\pi D_f^2} \tag{6.10}$$

where P_{lin} is the linear heat generation rate (W/m), and D_f is the fuel pellet diameter (m). By equating the two equations for volumetric heat generation, an expression for the fission rate can be obtained:

$$\dot{F} = \frac{4 P_{lin}}{\pi D_f^2 \epsilon_f} \tag{6.11}$$

Then, by substituting the fission rate equation into the average burnup equation and rearranging, an expression for the time required at a constant linear power to achieve the known discharge burnup is obtained:

$$t = \frac{Bu_{avg} \rho N_A \pi D_f^2 \epsilon_f}{4 P_{lin} M} \tag{6.12}$$

For some reactors a multiplication factor can be multiplied by the linear heat generation rate to obtain the fast neutron flux. In the absence of other data for the North Anna plant,

the default value in Bison is assumed (3×10^{13} neutrons/m^2-s/(W/m)). Since the power is assumed constant one can multiply the fast neutron flux by the time to obtain the fast neutron fluence used in the analysis:

$$\Phi = 3 \times 10^{13} P_{lin} t = 3 \times 10^{13} \frac{Bu_{avg} \rho N_A \pi D_f^2 \epsilon_f}{4M} \tag{6.13}$$

By substituting all the known values for the North Anna plant an approximate value of 8.356×10^{25} neutrons/m^2 is determined for the fast neutron fluence used in the analysis. In the 3D cladding analysis the prescribed rupture length is 16, as reported in the experimental post-irradiation examination [89].

Comparisons of the Bison simulations to the SATS experimental measurements are provided in Table 6.5. Two different depressurization rates were analyzed in the Bison simulations denoted as fast and slow. The fast depressurization rate corresponds to equilibrium of the internal pressure to the external pressure over 2 seconds post-rupture. The low depressurization rate corresponds to 7 seconds. The experimental measurements determined that the shape of the burst was oval so only an elliptical area calculation has been completed from the measured or calculated lengths and widths. The predicted rupture temperatures are within 10 K for both the OS and PI failure criteria. This is a very good comparison as it indicates that the time of failure is within 4 seconds of the experiment as the ramping rate is 5 K/s for both failure criteria. It is found that the PI study for both slow and fast depressurization rates post rupture predict smaller than experimentally observed rupture areas. In fact the width of the fast depressurization case is extremely narrow. On the other hand the fast and slow depressurization rates using the overstrain criteria, which only predicted failure approximately 3 seconds later than the PI case, bound the experimentally determined rupture area. This observation identifies that the choice of failure criteria, which impacts the rupture temperature, has a strong influence on the opening behavior of the rupture.

Figure 6.7 shows a close-up of the predicted rupture area for the PI and OS criteria simulations. The fast PI case computed a rupture width that is too small to visualize and is therefore excluded. The rupture areas are readily observable for the slow PI study and both

Table 6.5: Bison comparisons to the SATS North Anna experiment #1.

	Rupture Temperature (K)	Rupture Width (mm)	Rupture Area (mm^2)
Bison OS Fast	1057.1	1.48	18.60
Bison OS Slow	1057.1	5.68	71.38
Bison PI Fast	1043.5	7.62×10^{-4}	9.58×10^{-3}
Bison PI Slow	1043.5	0.665	8.36
Experiment	1064	3	37.70

slow and fast OS studies. Comparing the rupture opening shape to that observed in the post experiment picture shown in Figure 6.8 indicates a similar shape is predicted.

6.7.2 Studsvik Rods 191 and 196

The NRC sponsored LOCA tests conducted at the Studsvik reactor in Sweden were designed to explore the fragmentation and dispersal behavior of nuclear fuel. Flanagan et al. [30] tabulated important details of the Studsvik tests for use in the modeling. Models for two of the experiments, Rods 191 and 196 are already a part of the Bison validation suite and were added in support of a previous project [33]. These two rods were chosen as part of the previous project because Rod 191 experienced severe fine fragmentation and relocation, while Rod 196 did not. The details of these rods are presented in [33] but are reproduced here for completeness.

Information regarding the experimental conditions and pre-irradiation histories of Rods 191 and 196 have been obtained through publicly available documents [30, 47] and informed estimation when data is not available. Figure 6.9a illustrates the power history used to achieve the desired burnups prior to refabrication for the experiments. For Rod 191, this information was provided by EPRI and was said to be publicly known, featuring irradiation cycles. For Rod 196, it is known that two cycles were used to achieve the discharge burnup ($\sim$55 MWd/kgU) but that the detailed history is not available. Therefore, a representative two cycle irradiation was assumed as shown in the figure.

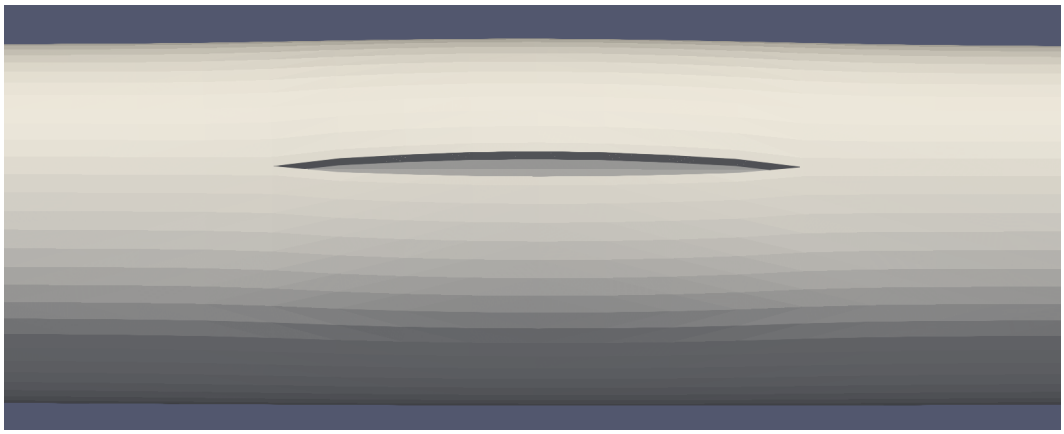

(a)

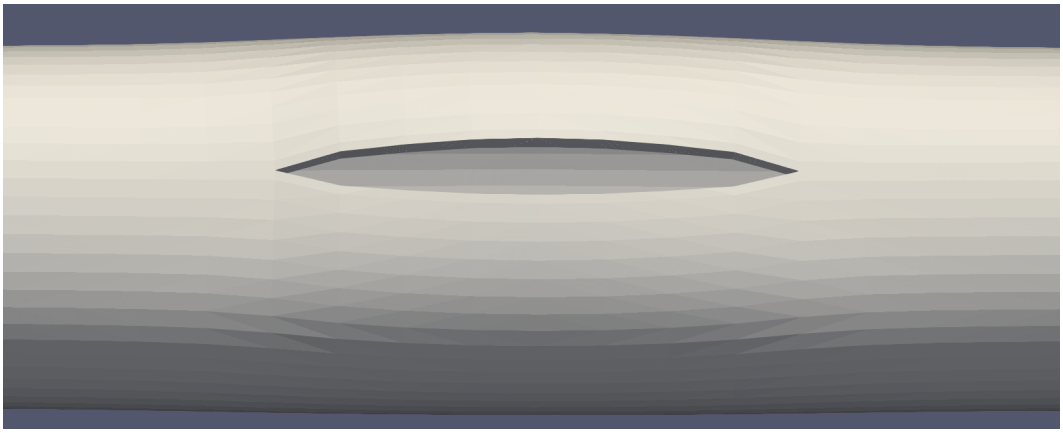

(b)

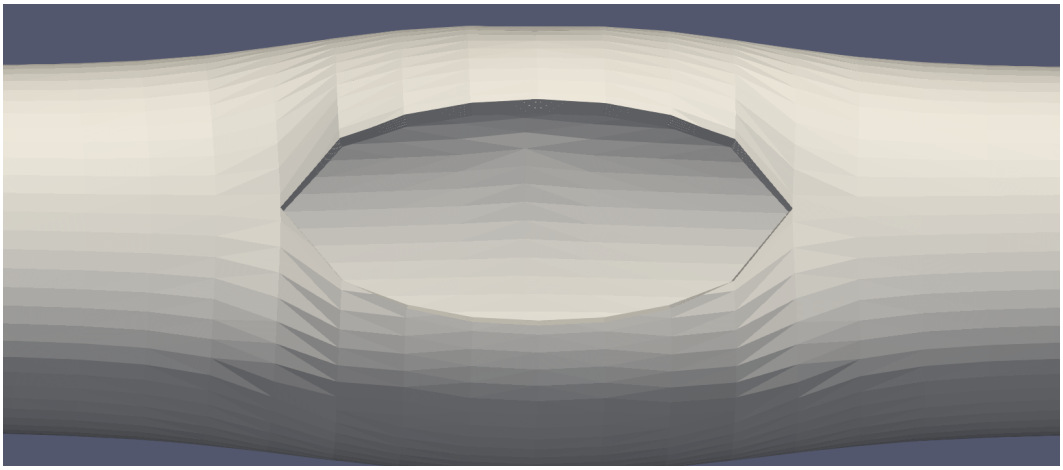

(c)

Figure 6.7: Visualization of the rupture opening for the North Anna experiment #1 study using the (a) PI criterion and slow depressurization rate, (b) OS criterion and fast depressurization rate, and (c) OS criterion and slow depressurization rate.

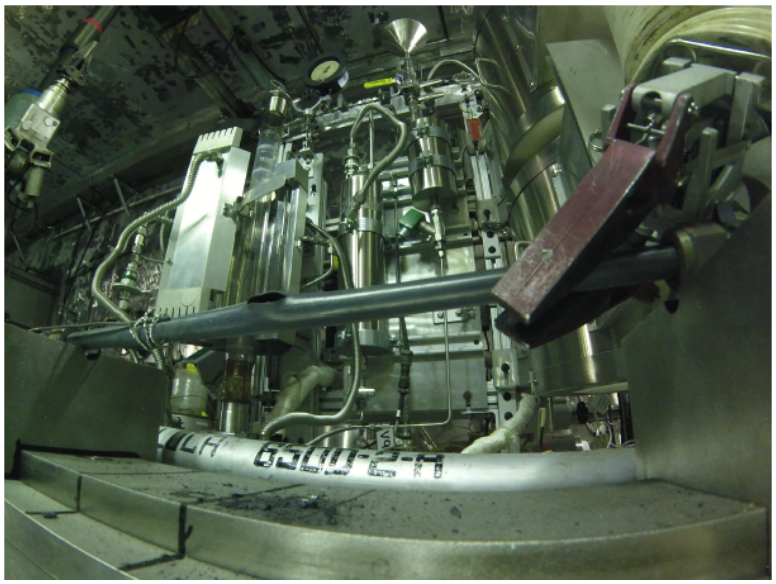

Figure 6.8: Picture of the North Anna #1 tube post experiment in SATS. Reproduced from [89].

After the base irradiation, the rodlets were refabricated and inserted into the Studsvik test train inside a hot cell. The experimental specimens are subjected to external heating at a rate of 5 K/s to the target peak cladding temperature. The target temperature was 1433 K and 1233 K for Rods 191 and 196, respectively. Figure 6.9b illustrates the time history of the maximum temperature supplied to the cladding outer surface. This maximum occurs at the rod axial midplane. A slight axial profile on the temperature (20 K less at the ends) is assumed to induce localized ballooning. Table 6.6 provides additional information related to the two rods that is necessary for analysis. The additional free volume corresponds to the volume outside of the rod but able to communicate directly with the plenum (i.e., the pressure lines). IFBA (Integral Fuel Burnable Absorber) is a burnable poison, Zirconium diboride (ZrB_2) placed on the exterior surface of the fuel to control reactivity and prolong cycle length [74].

A Layered1D representation was used to simulate the rods using information provided in Table 6.6 due to the lack of any azimuthal variation data provided in the experiments and the necessity of including the axial relocation model. For the thermal-hydraulic boundary condition during the base irradiation, the internal coolant channel model is used with an

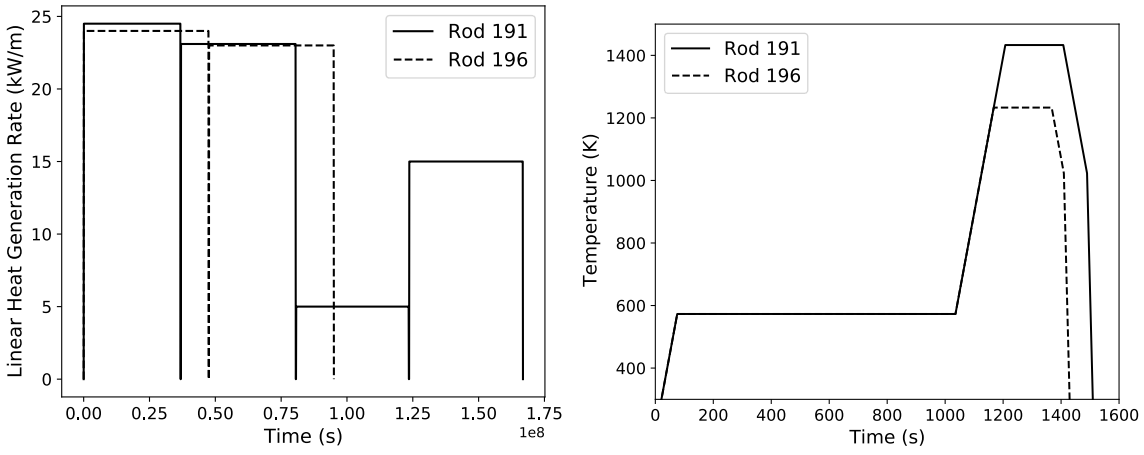

(a) (b)

Figure 6.9: (a) The linear heat generation rate supplied to the rods during base irradiation and (b) the temperature applied to the cladding outer surface during the experiment.

Table 6.6: Manufacturing and operational characteristics of Studsvik Rods 191 and 196 [30, 47].

	Rod 191	Rod 196
Rod height (mm)	300	300
Pellet stack height (mm)	265.4	260.6
Pellet radius (mm)	4.1	3.92
Gap thickness (mm)	0.08	0.08
Cladding thickness (mm)	0.57	0.57
Cladding material	ZIRLO	ZIRLO
Upper plenum height (mm)	22.9	24.86
Lower plenum height (mm)	12.75	14.5
Fill gas (mm)	He	He
Fill gas pressure (MPa)	2 MPa	2 MPa
Refabrication pressure (MPa)	11 MPa	8.2 MPa
IFBA coating	NO	YES

inlet pressure of 15.5 MPa, mass flow rate of 3800 kg/m^2-s, and an inlet temperature of 580 K. The prescribed crack lengths in the 3D cladding only portion of the calculations are 21.6 and 1.5 mm for Rods 191 and 196, respectively. Table 6.7 provides a comparison between the Bison simulations and the experimental data tabulated in Flanagan et al. [30]. In reporting the area, an elliptical shape is assumed. Cases for both the plastic instability and the overstrain are included for both rods. A depressurization rate over 2 seconds is assumed. It is observed for both rods that the Bison predictions overpredict the rupture temperature.

In the case of Rod 196 this discrepancy is significant at 67-80 K above the experimentally measured value. Despite this, the maximum burst strain bounds the experimental value for 196. For Rod 191 Bison predicts more fuel being released than experimentally observed. This is because all fuel that would be anywhere in the rod that has a particle size less than rupture width is dispersed even if it is below the rupture opening location. The Bison calculations underpredict the rupture area opening for Rod 191, which according to Jernkvist [51] is one of the larger rupture openings observed in any of the LOCA experiments analyzed. The Studsvik series in particular had significant rupture opening sizes for the high burnup rods subjected to the temperature transient (Rods 189, 191, 192, and 193 in [30]). Figure 6.10 presents the rupture contours for the PI and OS cases of Rod 191. One of the reasons for convergence issues at these higher rod internal pressures and large crack lengths could be attributed to the mesh density used in the vicinity of the crack. It is desired to use the same mesh density as the underlying 2D-RZ axisymmetric mesh in the axial and radial directions to ensure the transferred boundary conditions from the lower dimensional analysis result in the same behavior. Both the PI and OS cases for Rod 191 failed to make it completely down the depressurization ramp. Nevertheless, the model is able to predict rupture and the shapes appear similar to the that Figure 6.1a.

Table 6.7: Bison comparisons to Studsvik rods 191 and 196. Both plastic instability (PI) and overstrain (OS) failure criteria are included.

	Rupture Temperature (K)	Rupture Width (mm)	Rupture Area (mm^2)	Max. Burst Strain (%)	Fuel Mass Dispersed† (g)
Rod 191 OS	986.8	8.70*	147.59	39.1	82.6
Rod 191 PI	971.5	6.39*	108.40	14.1	82.6
Rod 191 Exp.	953	17.5	292.76	50	52
Rod 196 OS	1049.6	0	0	39.3	0
Rod 196 PI	1026.3	0	0	13.1	0
Rod 196 Exp.	959	0.2	0.47	25	0

† assumed to be all fuel determined to have a particle size less than the rupture opening width.; * severe convergences issues upon rupture. Full depressurization curve not achieved.

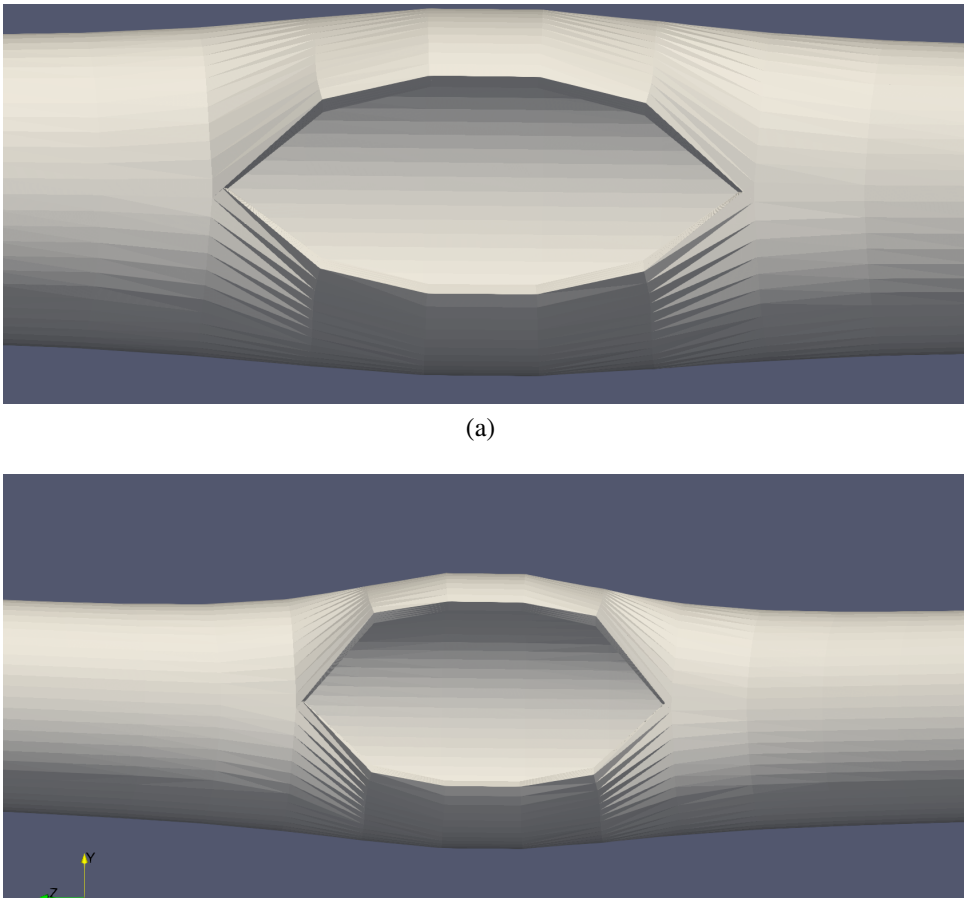

(a)

(b)

Figure 6.10: Visualizations of the rupture opening for Studsvik Rod 191 for (a) the plastic instability and (b) the overstrain failure criteria.

6.8 SUMMARY

The cladding is the final barrier to radioactive release to the primary coolant system in a nuclear reactor. Upon rupture, fission gases will be released and fragmented fuel particles may be ejected. A literature review has outlined two empirical models for predicting rupture area as well as six suggested approaches for fuel dispersal. Here, a model for discretely calculating the rupture width and subsequently the area was presented. The reason the rupture lengths were prescribed based is because fuel cannot be released if the rupture width is small enough compared to the characteristic length of the fuel fragments. A demonstration case was performed that varied the loading pressure, crack length, and cladding thickness

to evaluate the impact on the calculated rupture area. These tubes were only subjected to a temperature transient and had no base irradiation effects included. Next, 3 validation cases were analyzed, one was a cladding only experiment pre-irradated in the North Anna commercial plant before being burst tested in the SATS at ORNL. The calculated rupture areas bounded the experimentally measured value. The next two validation cases were part of the same Studsvik test series, with one rod pre-irradiated to high burnup and the second pre-irradiated to a moderate burnup. These cases utilized the fully developed model (minus a Layered2D geometry and oxidation degradation) created in this work and the results were reasonable for both rupture area and fuel dispersed for both rods analyzed. However, the rupture temperature was overpredicted.

From the industry or regulatory perspective, this work develops and demonstrates a modeling tool for predicting the location and area of ruptures in cladding tubes. While all the cases analyzed assumed azimuthal symmetry, this was because most of the publicly available experimental database does not have details on the azimuthal behavior, even if it is known to be present.

CHAPTER 7

APPLICATION TO ADVANCED CLADDING CONCEPTS

All of the proceeding chapters have focused on the standard UO_2-Zircaloy fuel system due to the wider availability of experimental data regarding those materials under irradiation. However, since Fukushima in March 2011, significant research has been undertaken in exploring alternative materials for the cladding to increase coping time in the event of a LOCA. The primary purpose of changing the cladding material is to reduce high temperature oxidation kinetics and the production of hydrogen. Two of the leading candidate materials, which have been irradiated in lead test rods and assemblies (LTRs and LTAs) are chromium (Cr)-coated Zircaloy and FeCrAl. In this chapter, an overview of the differences in material properties between Zircaloy, chromium coatings, and FeCrAl as available in Bison are presented. The majority of material models for all ATF concepts available in Bison was completed by the author of this dissertation in support of his employment at INL. A qualitative comparison of the burst behavior of the different materials is also provided.

7.1 CHROMIUM-COATED ZIRCALOY

All LWR fuel vendors in the United States have a chromium-coated Zircaloy cladding concept being explored for use as a replacement of the existing Zircaloy alloys in fuel rods. Typically this coating is applied to the existing as fabricated Zircaloy substrate resulting in a slightly larger cladding thickness than currently used. The thickness of the cladding alloy is usually in the tens of microns ($10\ \mu\text{m} < t_{coat} < 100\ \mu\text{m}$). Industry partners have publicly stated at conferences that the balloon (not rupture) sizes in Cr-coated cladding tubes was smaller than uncoated tubes under identical loading conditions without providing any

experimental evidence. Gamble [32] performed a numerical experiment including a comprehensive parametric analysis to confirm whether or not the claim of smaller balloons was plausible. It was found that the reduction in balloon size at any given time during the transient was more or less linearly related to the coating thickness. Larger coatings resulting in smaller balloons. This was attributed to the fact that by adding the coating to the outside of the as-fabricated bare cladding tubes resulted in tube with a larger overall thickness, which requires a larger pressure differential or (longer time under the same pressure differential) to induce the same balloon size.

Bison contains a preliminary suite of empirical models for pure chromium, consisting of correlations for thermal creep, elasticity, oxidation, plasticity, thermal conductivity, specific heat, and thermal expansion. The correlations for the models have been summarized in the links available in the table in Appendix C as well as numerous other publications [32, 123]. Here, comparisons of the correlations available in Bison for Zircaloy and pure Cr are presented to highlight differences in behavior and the potential convergence issues that may be encountered due to discontinuities at the substrate coating interface.

7.1.1 Elasticity

The elastic constants for pure chromium are compared against Zircaloy-4 in Figure 7.1. As can be seen both materials are subjected to a decrease in Young's modulus as temperature increases. The values for chromium for the elastic modulus are a factor of two larger, which may lead to stress concentrations at the cladding coating interface under certain loading conditions. This type of concentration in the numerical analysis may lead to convergence issues. The Poisson's ratio for chromium is assumed constant for all temperatures. The relatively flat portion above 1000 K for the Zircaloy Poisson's ratio is due to the α to β phase transition.

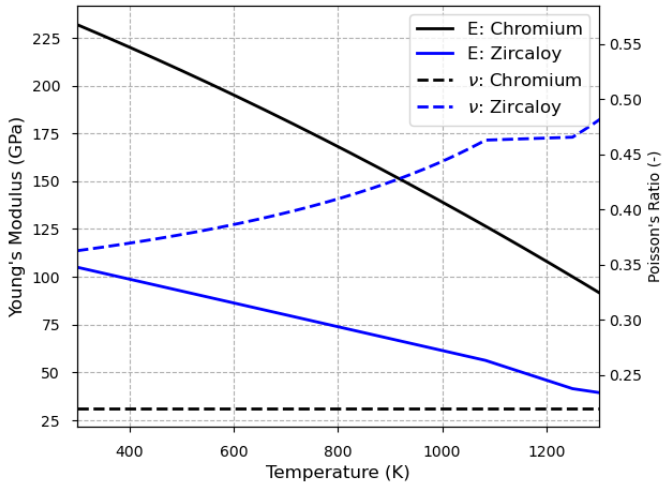

Figure 7.1: Comparisons of the chromium and Zircaloy-4 elastic constants over the temperature range where the chromium correlations are valid (300–1300 K).

7.1.2 Thermal Properties

The behavior of the thermal properties as a function of temperature are vastly different when comparing the coating and Zircaloy-4 cladding substrate. The trends are opposite when it comes to thermal conductivity evolution as a function of temperature with Zircaloy conductivity increasing and chromium decreasing. Although the specific heat capacity does not play much of a role during a LOCA transient there is a significant difference between the two materials. Notably there is a significant increase in the specific heat of Zircaloy during the α to β phase transition as a large amount of energy is needed to facilitate change in microstructure. Overall, the differences in thermal properties are not expected to have an influence on ballooning behavior of the tubes given that the thermal conductivity is high for both materials.

7.1.3 Thermal Expansion

Thermal expansion is the stress free change in dimensions of a material due to an applied thermal load, unless the specimen is fully constrained. For chromium, the thermal expansion coefficient is provided as a mean value and applied isotropically. Care must be taken when using those values in finite element analysis because sometimes the reference temper-

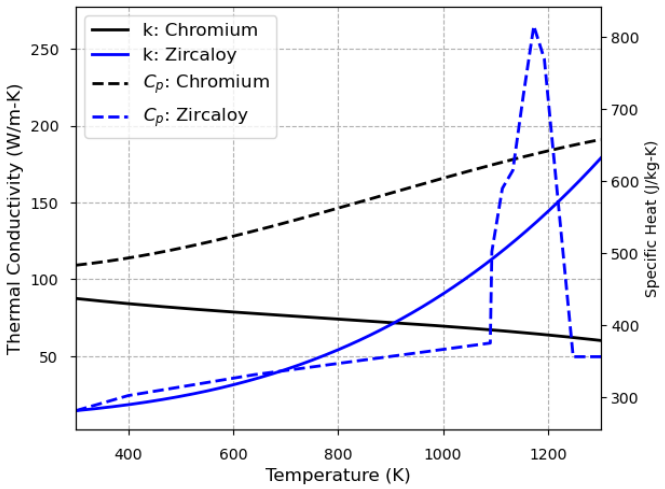

Figure 7.2: Comparisons of the chromium and Zircaloy-4 thermal conductivity and specific heat over the temperature range where the chromium correlations are valid (300–1300 K).

ature and stress-free temperatures can be different. On the other hand the Zircaloy-4 model reports the strain directly (see the appropriate model listed in Chapter C) and has different amounts of thermal strain depending upon whether it is in the axial or diametrical directions as shown in Figure 7.3.

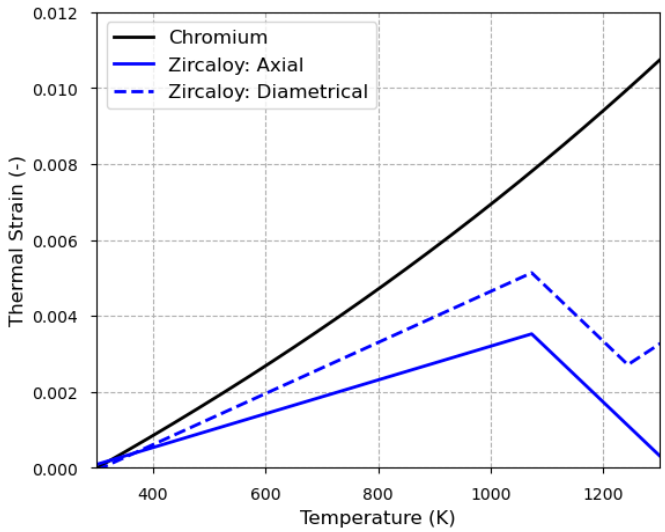

Figure 7.3: Comparisons of the thermal strain for chromium and Zircaloy-4 assuming a reference and stress free temperature of 300 K.

7.1.4 CREEP

High temperature creep is what drives the deformation during the LOCA analyses studied in this dissertation. Figure Figure 7.4 illustrates the secondary (thermal) creep rate for Zircaloy-4 and chromium at 2 different effective stresses. For both stress conditions, Zircaloy-4 creeps at a higher rate for a given temperature. This may play a role in limiting ballooning behavior in coated Zircaloy-4 tubes due to the cladding being less likely to deform inelastically due to instantaneous plasticity (see Section 7.1.5) requiring higher loads to induce displacement.

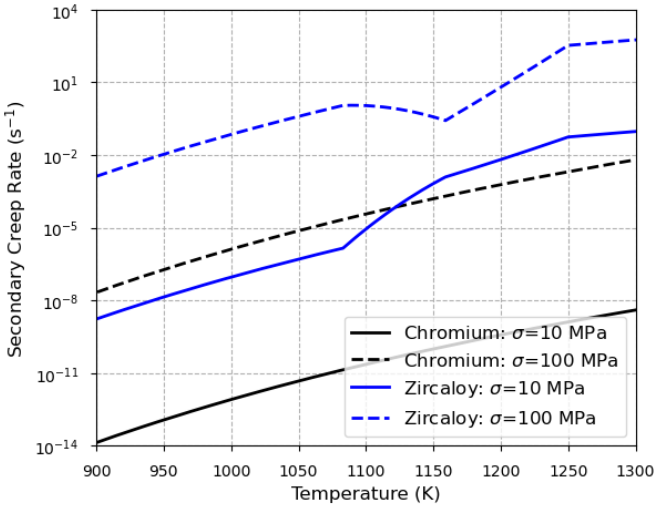

Figure 7.4: Comparisons of the thermal creep rate for chromium and Zircaloy-4 over the temperature range where the chromium correlations are valid (300–1300 K).

7.1.5 INSTANTANEOUS PLASTICITY

Instantaneous plasticity is the inelastic deformation of a material due to stresses exceeding the yield stress of the material. The temperature evolution of the yield stress for chromium is shown in Figure 7.5 for two different fast neutron fluences. The instantaneous plasticity model for Zircaloy-4 is not included on this plot as in any LOCA analyses utilizing the Zircaloy-4 high temperature creep model would double count the plasticity contributions. This is due to the fact that derivations of the Zircaloy-4 creep model accounted for all high

temperature deformation including those from instantaneous plasticity. As expected, irradiation causes hardening of the material, resulting in an increased yield stress. Physically, it is unclear why there is a local maximum in the yield stress around 1000 K due to the fact that there is no phase change or other microstructure effects ongoing. However, the literature from which the model was obtained [123] states that the validity range was 300–1300 K.

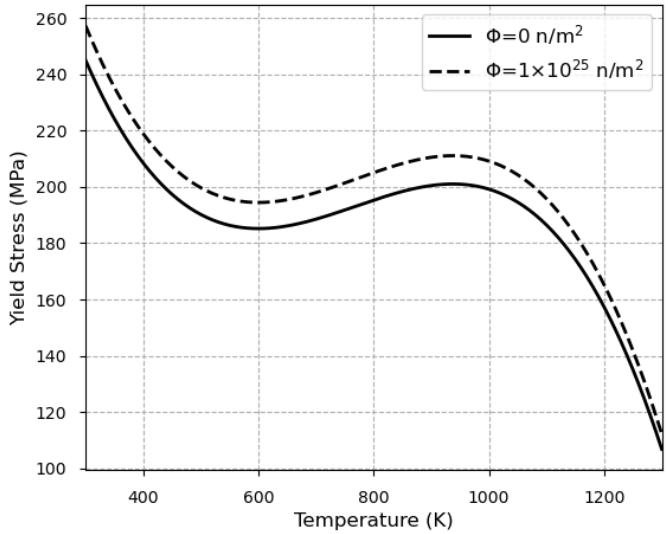

Figure 7.5: Illustration of the yield stress evolution of chromium over its range of applicability. Unirradiated and irradiated curves are shown.

7.1.6 FAILURE

No failure model exists in the literature for pure chromium. Since it is a thin coating on the Zircaloy substrate, the same failure models as for Zircaloy are assumed, in particular, the plastic instability model is used. Overall, the presence of the coating and the differences in thermal creep rate will influence the time to failure between the coated and uncoated Zircaloy tubes.

7.2 IRON-CHROMIUM-ALUMINUM (FECRAL) ALLOYS

FeCrAl cladding alloys are ATF cladding concepts being pursued by General Electric [92] with active development and research being conducted on various FeCrAl alloys by ORNL [114, 115, 116, 29]. FeCrAl is being pursued as a potential replacement to Zircaloy due to its increased strength and significantly reduced oxidation kinetics. Unfortunately, disadvantages include a higher thermal neutron absorption cross-section necessitating the need for a thinner cladding potentially increasing fuel cost and enrichment [114]. The reduced thickness may be compensated by the increased strength offered. Burst studies have been conducted over the years on first generation [66] and more recently second generation [37] FeCrAl alloys. The results were contradictory with the first generation alloys having much larger rupture openings than their Zircaloy counterparts, whereas the recent studies showed favorable FeCrAl rupture sizes.

Development on FeCrAl concepts in Bison began in 2015 with the first publication using Bison appearing in the literature by Gamble et al. [34]. Since then, the FeCrAl handbook [29] was published that summarized additional data and presented correlations for different alloys under development at ORNL (C06M, C35M, C36M) as well as the commercial alloy Kanthal APMT. Plots of the correlations in the [29] illustrate very limited variation amongst the alloys when it comes to elasticity, thermal properties, and thermal expansion. The primary difference comes in the form of the thermal creep correlation where C35M has its own correlation and the others use a general creep equation that encompasses the average behavior of many different alloys. In the studies completed in this chapter, the C35M alloy is used exclusively. In addition to the properties outlined below that can be compared to Zircaloy, FeCrAl experiences volumetric swelling under irradiation due to its cubic structure, unlike Zircaloy, with its hexagonal closed-pack structure which experiences irradiation growth. Irradiation induced-swelling results in a change in volume of the material, whereas irradiation growth results in an increase in axial length but a reduction in diameter to maintain a constant volume. Details of the correlations for C35M can be found

in the appropriate online documentation pages linked to in Appendix C.

7.2.1 Elasticity

As with chromium, FeCrAl has a higher Young's modulus than Zircaloy-4. As the temperature range is increased from 1300–1500 when going from chromium to FeCrAl's range of applicability, one notices that the Poisson's ratio obtained by the MATPRO [100] correlation for Zircaloy-4 becomes unphysical (>0.5) in Figure 7.6. Fortunately, in all studies completed in this work and in the comparison between Zircaloy-4 and FeCrAl, the temperatures remain in the physical value range. FeCrAl also exhibits an increasing Poisson's ratio with temperature.

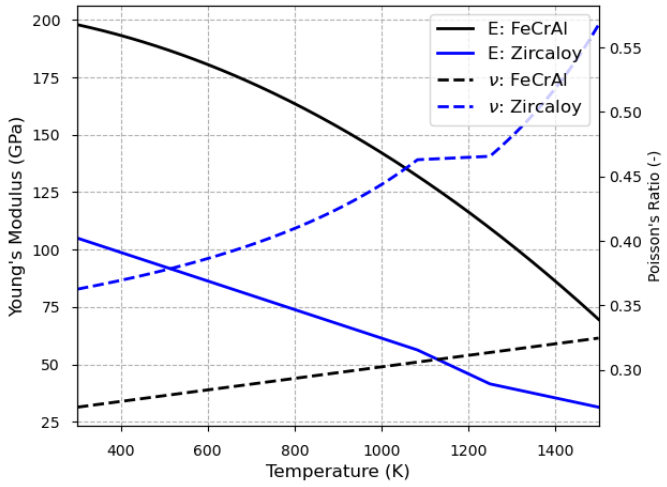

Figure 7.6: Comparisons of the FeCrAl and Zircaloy-4 elastic constants over the temperature range where the FeCrAl correlations are valid (300–1500 K).

7.2.2 Thermal Properties

The thermal properties of FeCrAl behave similarly as Zircaloy-4 as they both have a large peak in specific heat as shown in Figure 7.7. For FeCrAl the location of the peak corresponds to the Curie temperature above which it loses all of its magnetic properties. As before, given that both materials are metallic, their thermal conductivities are high enough that any changes should as a function of temperature should not effect the results.

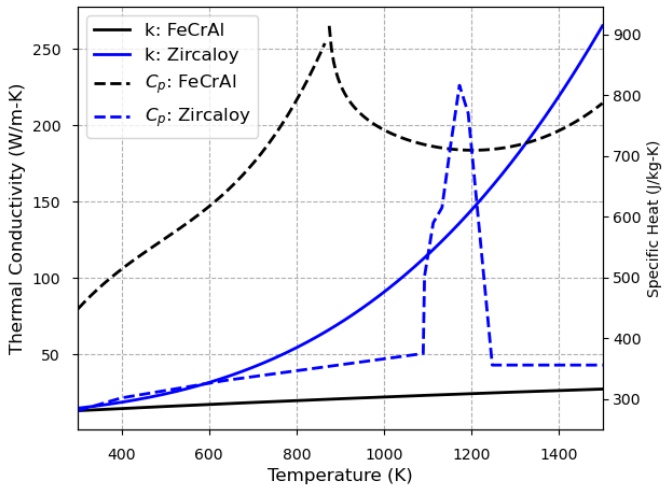

Figure 7.7: Comparisons of the FeCrAl alloy C35M and Zircaloy-4 thermal conductivity and specific heat over the temperature range where the chromium correlations are valid (300–1500 K).

7.2.3 Thermal Expansion

Figure 7.8 highlights the differences in thermal strain between FeCrAl and Zircaloy-4. At high temperatures FeCrAl experiences significantly more thermal expansion (> a factor of 2). Since the modeling approach for predicting rupture aborts the simulation and the temperature is not reduced at the end of the simulation, large differences in thermal expansion may impact the rupture behavior.

7.2.4 Creep

Comparisons of the secondary creep rate between FeCrAl and Zircaloy-4 are presented in Figure 7.9. Similarly to the chromium comparisons FeCrAl always exhibits creep rates that are 2 or more orders of magnitudes less than Zircaloy for all temperatures and for both stress conditions presented. Since FeCrAl has a lower creep rate and a higher elastic modulus, it is likely that higher stresses will form in the cladding at smaller balloon sizes which may lead to large catastrophic like rupture openings as shown in Figure 1.3 as the rapidly increasing stresses exceed the failure threshold (see Section 7.2.5).

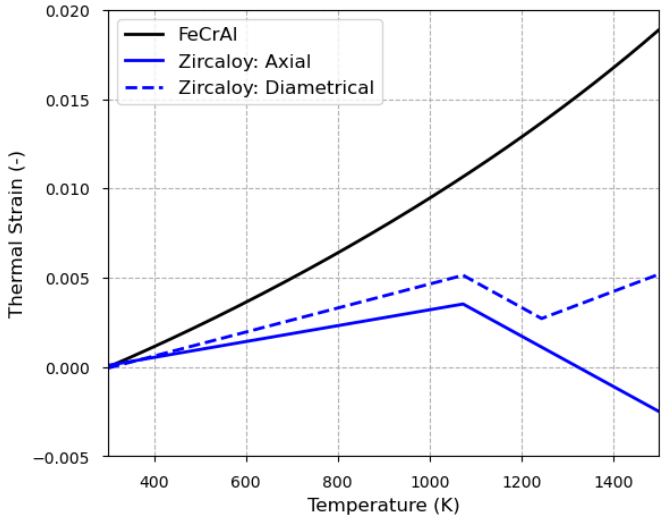

Figure 7.8: Comparisons of the thermal strain for FeCrAl alloy C35M and Zircaloy-4 assuming a reference and stress free temperature of 300 K.

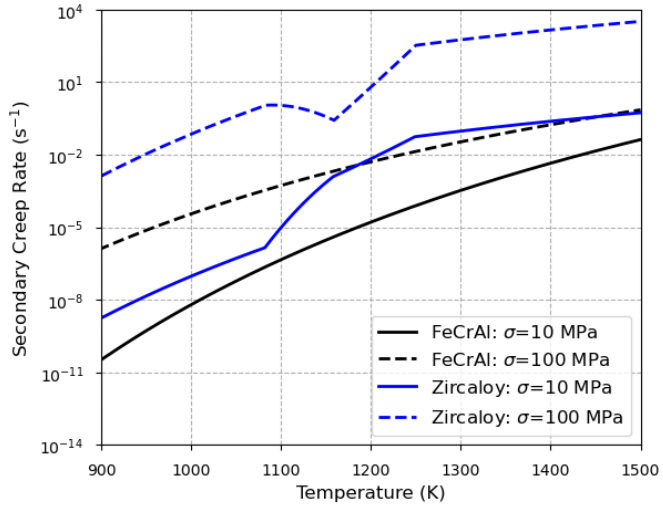

Figure 7.9: Comparisons of the thermal creep rate for FeCrAl alloy C35M and Zircaloy-4 over the temperature range where the FeCrAl correlations are valid (300–1500 K).

7.2.5 FAILURE

Two developed burst stress failure models for FeCrAl are illustrated in Figure 7.10 alongside the overstress criterion for Zirclay-4 assuming no oxidation component. It is observed that Zircaloy is unlikely to rupture by the overstress method while in the α-phase given the large stresses that are necessary to induce rupture. Therefore when comparing to rupture behavior amongst the claddings, the combined overstress and plasticity instability criterion is used

for Zircaloy-4. At high temperatures the rupture stresses for both mateirals are fairly similar. The INL developed model shown on the plot was developed based off of first generation FeCrAl alloys [34], whereas the UTK model was developed off of second generation FeCrAl alloys. Neither studies were specific to the C35M alloy used in this work, but the model is nevertheless applied to the alloy.

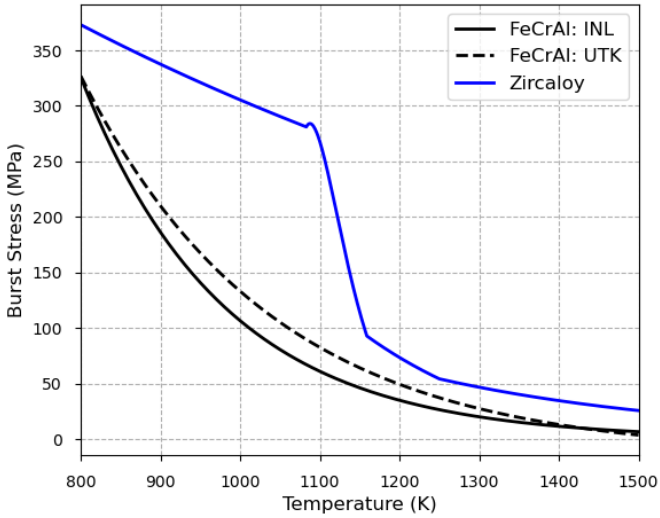

Figure 7.10: Illustration of the burst stress that must be exceeded to determine failure of FeCrAl alloy C35M over its range of applicability. Both the INL and University of Tennessee, Knoxville (UTK) correlations are shown.

7.3 Rupture behavior compared to Zircaloy

Limited experimental data exists for ruptured FeCrAl and Cr-coated Zircaloy tubes. For FeCrAl, almost all of the data was used to develop the empirical models that have been incorporated into Bison. For pure chromium, much of the correlations are developed off of old data applications outside of an LWR irradiation environment. To provide a qualitative comparison between the various cladding types and their rupture behavior the demonstration study completed for Zircaloy in Section 6.6 was used for both FeCrAl and Cr-coated Zircaloy tubes. Slight differences in the geometries of the tubes were required to account for features inherent to the ATF concepts. All tubes maintained the same inner cladding di-

ameter, with the FeCrAl tubes being thinner to account for the neutronic penalty associated with its use, and the pure Cr coating is added onto the bare Zircaloy outer diameter used in the Zircaloy demonstration case. This leads to small diameter tubes of inner/outer diameters of 8.36/9.54 mm and 8.36/9.13 mm for Cr-coated and FeCrAl tubes, respectively. The large diameter tubes for Cr-coated and FeCrAl analyses were 9.30/10.79 mm and 9.30/10.27 mm, respectively.

Tables 7.1 and 7.2 presents tabulated results of the rupture time, rupture width, and two measures of the rupture area for the ATF concepts. The same rupture area schematics as in Section 6.6 are presented for Cr-coated Zircaloy in Figure 7.11. FeCrAl rupture contours are not shown because they are almost invisible to the naked eye. As with the Zircaloy-4 study the same trends are observed in both the Cr-coated and FeCrAl cases. In particular, increasing rod internal pressure leads to earlier rupture times with increasing rupture areas and the rupture length increases. Comparing both ATF cladding concepts to the Zircaloy-4 behavior in Section 6.6 it can be noticed the the rupture areas for a given combination of pressure and rupture length are generally much smaller. For FeCrAl, this is in contrast to the early data on first generation FeCrAl alloys by Massey et al. [66] who showed pictures of rupture width (see Figure 7 in the reference), particularly at the high over pressures for rupture lengths of approximately 20 mm. Newer data by Garrison et al. [37] also shows rupture areas in second generation FeCrAl alloys that are larger than calculated in this demonstration problem. The discrepancy is not attributed to the loading conditions since both the Massey et al. and Garrison et al. models were completed in the SATS facility for which the rupture model predicted reasonably well on Zircaloy tubes (see Table 6.4). Further work is needed to investigate rupture opening in materials that experience a more brittle like fracture mode of failure. Based upon the rupture time differences between Zircaloy FeCrAl does provide slightly more coping time in these analyses, which confirms some of the posulated benefit for the material. This observation is different then the previous study by [34]. The main difference in the two studies is the use of the newer failure criterion based upon 2nd

generation FeCrAl alloys.

The modeling approach for predicting cladding rupture in this work uses the high temperature thermal creep of the material and the depressurization rate to drive rupture opening (ductile failure). Recall from Figure 7.9 that the creep rates for FeCrAl is many orders of magnitude less than Zircaloy at the same temperature and loading condition. Therefore, it would be expected based upon the material models available for FeCrAl that the calculated rupture opening using the developed method would be smaller, even when the cladding thicknesses are much smaller. In the case of a Cr-coated, which also has a significantly lower creep rate at high temperatures than Zircaloy, a suppressed rupture area is observed at lower internal pressures. Once the crack lengths become long enough and the pressures high enough large rupture openings begin to be predicted. It is encouraging to capture the reduced ballooning and rupture sizes in Cr-coated Zircaloy-4 tubes as it should enable a more coolable geometry as flow channels around the tubes would not be as restricted.

Figure 7.12 presents the calculated rupture areas from the demonstration problems for Zircaloy, Cr-coated tubes, and FeCrAl as a function of the rupture length. This plot simply combines the rupture areas from the three different tubes for easy comparison. At crack lengths of 5 and 10 mm all except the large Zircaloy tube experienced very small rupture openings. As the crack lengths increase to 15 and 20 mm in length the Zircaloy and Cr-coated Zircaloy cases have increasing rupture areas.

7.4 SUMMARY

ATF cladding concepts are being pursued for replacement in LWRs for increased coping time and reduced hydrogen production in the event of a LOCA. In this chapter a comparison of the material models available for two potential concepts in the Bison fuel performance code to that of traditional Zircaloy-4 was provided. Then, the demonstration analysis for the rupture model shown Section 6.6 was repeated for Cr-coated Zircaloy and FeCrAl. It was found that both ATF cladding concepts predicted much smaller balloons and rupture areas

Table 7.1: Results of parametric analysis to demonstrate the rupture model on Cr-coated cladding tubes.

Clad ID/ Clad OD (mm)	Rupture Length (mm)	Rod Internal Pressure (MPa)	Rupture Time (s)	Rupture Width (mm)	Rhombus Rupture Area (mm^2)	Ellipse Rupture Area (mm^2)
8.36/9.54	5	2	189.307	2.33×10^{-3}	0.006	0.009
	10	2	189.307	5.34×10^{-3}	0.027	0.042
	15	2	189.307	0.0152	0.114	0.179
	20	2	189.307	0.0174	0.174	0.273
	5	4	175.963	6.50×10^{-3}	0.016	0.026
	10	4	175.963	0.0204	0.102	0.160
	15	4	175.963	0.107	0.803	1.261
	20	4	175.963	0.238	2.380	3.738
	5	6	166.875	6.81×10^{-3}	0.017	0.027
	10	6	166.875	0.0192	0.096	0.151
	15	6	166.875	0.15	1.125	1.767
	20	6	166.875	1.08	10.800	16.965
	5	8	156.323	0.0242	0.061	0.095
	10	8	156.323	0.106	0.530	0.833
	15	8	156.323	1.85	13.875	21.795
	20	8	156.323	5.36	53.600	84.195
9.30/10.79	5	2	190.373	2.48×10^{-3}	0.006	0.010
	10	2	190.373	5.51×10^{-3}	0.028	0.043
	15	2	190.373	0.0137	0.103	0.161
	20	2	190.373	0.0182	0.182	0.286
	5	4	177.419	8.18×10^{-3}	0.020	0.032
	10	4	177.419	0.0169	0.085	0.133
	15	4	177.419	0.110	0.825	1.296
	20	4	177.419	0.263	2.630	4.131
	5	6	168.317	1.19×10^{-3}	0.003	0.005
	10	6	168.317	0.0394	0.197	0.309
	15	6	168.317	0.486	3.645	5.726
	20	6	168.317	0.924	9.240	14.514
	5	8	159.675	0.0262	0.141	0.221
	10	8	159.675	0.0936	0.468	0.735
	15	8	159.675	0.988	7.410	11.640
	20	8	159.675	2.45	24.500	38.485

for the same pressure and initial crack lengths. In the case of FeCrAl, the small rupture openings appear to be in contract to the experimental observations of Massey et al. [66] (see Figure 1.3. In addition, the time to rupture was longer for the same loading conditions.

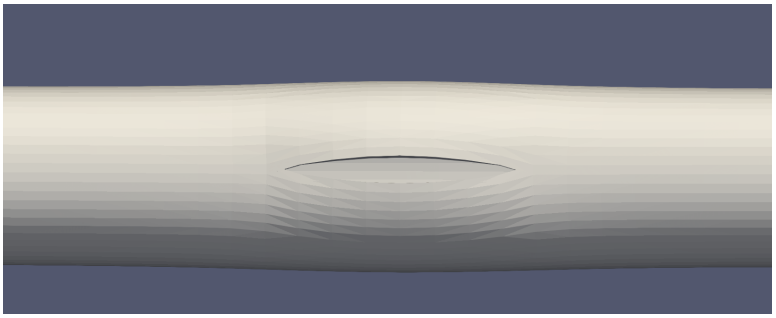

(a)

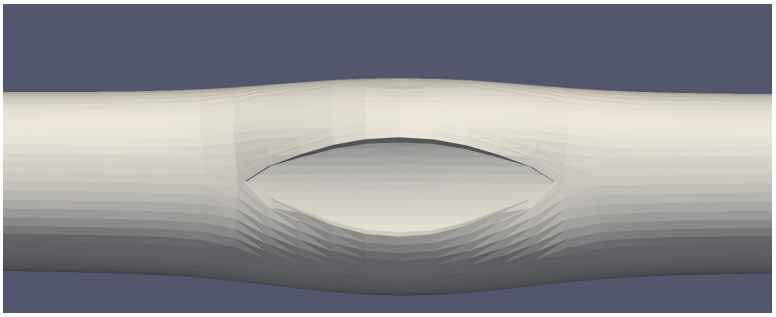

(b)

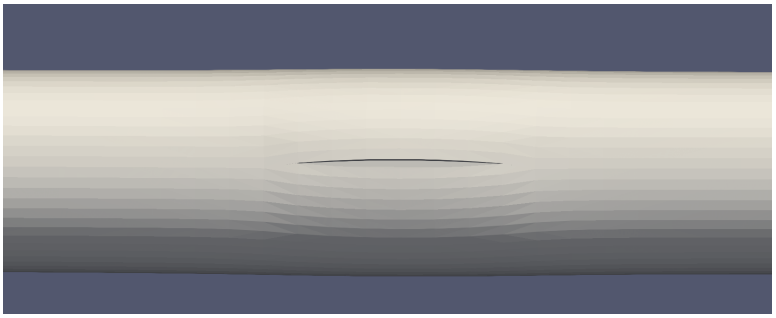

(c)

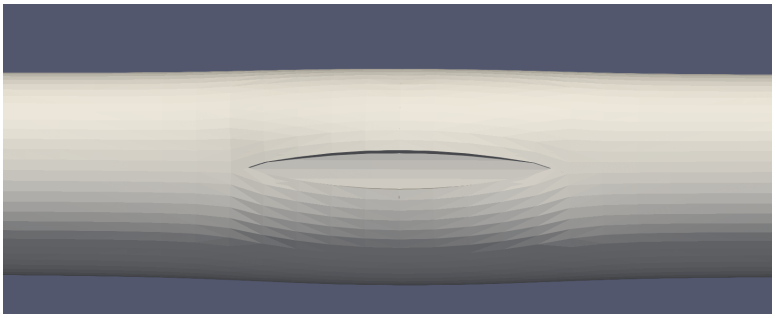

(d)

Figure 7.11: Visualizations of the rupture opening for the Cr-coated Zircaloy demonstration cases with 5 MPa loading for (a) small diameter $l_b = 15$mm, (b) small diameter $l_b = 20$mm, (c) large diameter $l_b = 15$mm, (d) large diameter $l_b = 20$mm.

Table 7.2: Results of parametric analysis to demonstrate the rupture model on FeCrAl cladding tubes.

Clad ID/ Clad OD (mm)	Rupture Length (mm)	Rod Internal Pressure (MPa)	Rupture Time (s)	Rupture Width (mm)	Rhombus Rupture Area (mm^2)	Ellipse Rupture Area (mm^2)
8.36/9.13	5	2	198.106	2.37×10^{-4}	0.001	0.001
	10	2	198.106	4.24×10^{-4}	0.002	0.003
	15	2	198.106	8.62×10^{-4}	0.006	0.010
	20	2	198.106	1.09×10^{-3}	0.011	0.017
	5	4	173.765	2.45×10^{-3}	0.006	0.010
	10	4	173.765	3.67×10^{-3}	0.018	0.029
	15	4	173.765	5.02×10^{-3}	0.038	0.059
	20	4	173.765	4.84×10^{-3}	0.048	0.076
	5	6	160.939	2.01×10^{-3}	0.005	0.008
	10	6	160.939	1.74×10^{-3}	0.009	0.014
	15	6	160.939	8.07×10^{-3}	0.061	0.095
	20	6	160.939	0.0637	0.637	1.001
	5	8	152.026	0.0203	0.051	0.080
	10	8	152.026			
	15	8	152.026	0.0204	0.153	0.240
	20	8	152.026	0.151	1.510	2.372
9.30/10.27	5	2	202.461	3.02×10^{-4}	0.001	0.001
	10	2	202.461	7.09×10^{-4}	0.004	0.006
	15	2	202.461	1.71×10^{-3}	0.013	0.020
	20	2	202.461	2.20×10^{-3}	0.022	0.035
	5	4	177.635	5.19×10^{-4}	0.001	0.002
	10	4	177.635	1.18×10^{-3}	0.006	0.009
	15	4	177.635	3.03×10^{-3}	0.023	0.036
	20	4	177.635	7.25×10^{-3}	0.073	0.114
	5	6	164.629	5.57×10^{-4}	0.001	0.002
	10	6	164.629	1.47×10^{-3}	0.007	0.012
	15	6	164.629	-[†]	-	-
	20	6	164.629	0.0283	0.283	0.445
	5	8	155.742	2.34×10^{-3}	0.006	0.009
	10	8	155.742	4.22×10^{-3}	0.021	0.033
	15	8	155.742	4.44×10^{-3}	0.033	0.052
	20	8	155.742	0.0857	0.857	1.346

[†] obscure I/O failure.

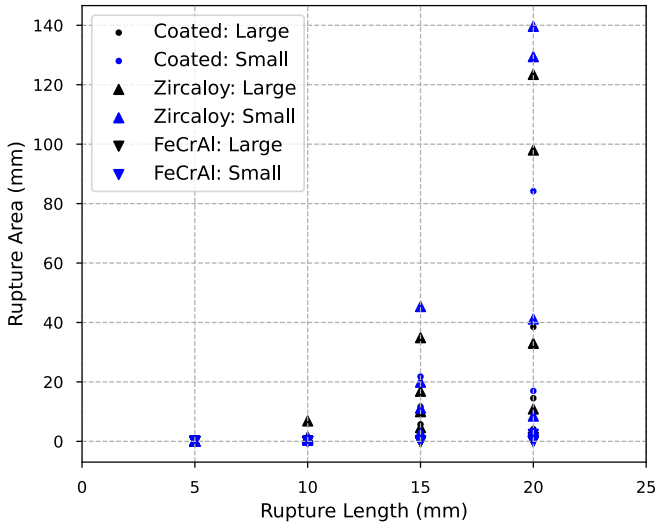

Figure 7.12: Rupture area assuming an elliptical shape for Zircaloy, Cr-coated Zircaloy, and FeCrAl tubes as a function of rupture length.

If these two observations hold true, they are important conclusions for industry stakeholders who are seeking increased coping time and to maintain a coolable geometry.

CHAPTER 8

CONCLUSIONS

The LOCA is an important case study in the nuclear engineering community. Renewed interest in the LOCA scenario in LWRs has been sparked by the Fukushima accident and industry's desire to extend the operating cycle lengths and discharge burnups of the fuel. The IFA-650.4 experiment in the Halden reactor identified that FFRD is likely to occur as the burnup is increased. This work was undertaken to explore multiple facets of the FFRD process with an emphasis on developing a predictive modeling capability for the rupture location and area in failed cladding tubes. This work includes the novel use of existing advanced modeling and simulation techniques to analyze problems in ways that have never been done before as well as developing new capabilities to enhance the fidelity of FFRD analyses. The contributions and findings of this work are:

1. A comprehensive study of fuel fracture was completed incorporating effects never before see in the open literature. A large sensitivity study including material strength randomization, criteria for strength randomization, mesh density, power ramping rates and irradiation (burnup) effects was completed. The results were compared to empirical correlations developed based solely on functions of rod average burnup and maximum power supplied to the fuel. It was found that the volume-weighted Weibull distribution is the most appropriate strength randomization approach. The empirical correlations were also found be acceptable for use given the high uncertainty obtained from the mechanistic modeling.

2. A first-of-its-kind Layered2D framework was developed for the Bison fuel perfor-

mance code that utilizes the discrete axial layers that are capable of accommodating azimuthal boundary conditions. The framework was verified to properly calculate important features necessary for fuel performance modeling. A model originally developed for Layered1D analyses was extended to work within the Layered2D framework. It was found if the maximum balloon size is the same in the Layered1D versus a Layered2D analysis, that less fuel will relocate in the Layered2D case. If the maximum balloon size is larger in Layered2D, any differences in fuel movement predictions will come down the cross-sectional area of the respective layers.

3. A large sensitivity study was completed to assess the impact of the empirical fragmentation model as well as a wide variety of axial relocation model parameters on the predictions of cladding diameter and mass relocation for a handful of Halden IFA-650 LOCA experiments. Cases with single and double balloons were analyzed alongside a case that experienced large strain with no failure.

4. A simplistic approach to capturing consumption of the cladding due to waterside oxidation was developed and verified. Despite its impact in the small fabricated regression tests, it was found that impact of mechanical degradation on rupture behavior is small. A Layered2D analysis including azimuthally varying temperature conditions was completed to demonstrate the ability to compute circumferentially varying oxide thicknesses.

5. A discrete modeling approach for predicting cladding rupture was presented. This is to the authors best knowledge the first time rupture has been discrete modeled in failed cladding tubes during a LOCA. The model primarily focuses on whether or not all of the more detailed modeling capabilities for fuel fragmentation and axial relocation are able to accurately capture the width of the rupture opening as the length is prescribed. This is because fuel cannot disperse if the width remains below the characteristic length of the fuel fragments within the cladding.

6. The rupture model was applied to two accident tolerant cladding concepts of interest by the nuclear community, Cr-coated Zircaloy and FeCrAl. It was found that time to rupture and the rupture areas were much smaller for the same loading conditions in the ATF concepts than conventional Zircaloy-4.

CHAPTER 9

FUTURE WORK

The work accomplished in this dissertation has resulted in contributions to many areas of research that influence the fuel rod behavior during LOCA conditions, including fragmentation, axial relocation, cladding oxidation, and cladding rupture. This work provides the underlying computational framework and methodologies for future work in these areas that will continue to further the state-of-the-art of modeling fuel rod behavior during LOCAs and support industry's desired burnup extension and use of accident tolerant fuel concepts in LWRs. Areas of continued research include:

- The discrete fracture study focused on UO_2 and verified existing empirical correlation for the number of radial fragments that form by incorporating uncertainty analysis. Randomization of the material tensile strength, ramp rates, and burnup effects illustrated that a more physics based approach to modeling fuel fragmentation can predict within uncertainty, the experiments on which the empirical correlations were fitted. Therefore, the discrete modeling capabilities could be used to develop a correlation with associated uncertainty for materials for which experiments do not exist (e.g., U_3Si_2 fuel, Cr_2O_3-doped UO_2 fuel).

- The Jernkvist and Massih [53] model used as the basis of axial relocation modeling improvements in this work has additional limitations not addressed or explored here. This includes the ability to treat the system of fragment sizes as a distribution, rather than a simple binary system of large and small fragments. Experimental data from the SATS and Studsvik tests [18, 30] provide distributions of particle sizes such that

a correlation could be developed.

- With oxidation, comes hydrogen pickup, diffusion, precipitation and dissolution of hydrogen and zirconium hydrides. These hydrides can embrittle the cladding causing an increase in strength but reduction in ductility. Bison contains models to account for these effects [78] but their application to LOCA analyses is limited. These features should be added to LOCA analyses and evaluate the impact on results. In particular, dissolved hydrogen has been found to influence the α to $\alpha+\beta$ and β to $\alpha+\beta$ transition temperatures, which will impact the creep behavior of the cladding.

- Fuel dispersal was briefly discussed in this work. Follow-on work on the post-rupture behavior including coolant ingress leading to double-sided oxidation as well as dispersed fuel movement within the primary coolant system upon reflood should be explored.

BIBLIOGRAPHY

[1] Studsvik AB. *What is SCIP?* 2021. URL: https://www.studsvik.com/scip-project/what-is-scip/.

[2] B. M. Adams et al. *Dakota, A Multilevel Parallel Object-Oriented Framework for Design Optimization, Parameter Estimation, Uncertainty Quantification, and Sensitivity Analysis: Version 6.0 User's Manual*. Tech. rep. SAND2014-4633 Version 6.3. Sandia National Laboratories, 2015.

[3] International Atomic Energy Agency. *Fuel Modeling in Accident Conditions (FUMAC) Final: Final Report of a Coordinated Research Project*. Tech. rep. IAEA-TECDOC-1889. International Atomic Energy Agency, 2019.

[4] L. Alva et al. "Experimental study of thermo-mechanical behavior of SiC composite tubing under high temperature gradient using solid surrogate". In: *Journal of Nuclear Materials* 466 (2015), pp. 698–711.

[5] N. Vu-Bac et al. "A Phantom-Node Method with Edge-Based Strain Smoothing for Linear Elastic Fracture Mechanics". In: *Journal of Applied Mathematics* 2013 (2013), pp. 1–12.

[6] Louis Bailly-Salins et al. "Modeling of High-Temperature Corrosion of Zirconium Alloys Using the eXtended Finite Element Method (X-FEM)". In: *Corrosion Science* 189 (2021), p. 109603. ISSN: 0010-938X. DOI: https://doi.org/10.1016/j.corsci.2021.109603. URL: https://www.sciencedirect.com/science/article/pii/S0010938X21003693.

[7] S. Balay et al. *PETSc Web page*. 2017. URL: http://www.mcs.anl.gov/petsc.

[8] M. Bales et al. *Interpretation of Research on Fuel Fragmentation, Relocation, and Dispersal at High Burnup*. Tech. rep. RIL 2021-13. United States Nuclear Regulatory Commission, 2021.

[9] T. Barani et al. "Isotropic softening model for fuel cracking in BISON". In: *Nuclear Engineering and Design* 342 (2019), pp. 257–263.

[10] T. Belytschko and T. Black. “Elastic crack growth in finite elements with minimal remeshing”. In: *International Journal for Numerical Methods in Engineering* 45 (1999), pp. 601–620.

[11] R. A. Berry et al. *RELAP-7 Theory Manual*. Tech. rep. INL/EXT-14-31366 Rev. 1. Idaho National Laboratory, 2014.

[12] A. Bianco et al. “Experimental investigation on the causes for pellet fragmentation under LOCA conditions”. In: *Journal of Nuclear Materials* 465 (2015), pp. 260–267.

[13] J. Bischoff et al. “Development of Cr-coated Zirconium Alloy Cladding for Enhanced Accident Tolerance”. In: *Proceedings of TopFuel2016*. Boise, ID, USA, 2016.

[14] J. C. Brachet et al. “Behavior under LOCA conditions of Enhanced Accident Tolerant Chromium Coated Zircaloy-4 Claddings”. In: *Proceedings of TopFuel2016*. Boise, ID, USA, 2016.

[15] S. Bragg-Sitton et al. *Advanced Fuels Campaign Light Water Reactor Accident Tolerant Fuel Performance Metrics*. Tech. rep. INL/EXT-13-29957. Idaho National Laboratory, 2014.

[16] N. Capps et al. “A Critical Review of High Burnup Fuel Fragmentation, Relocation, and Dispersal under Loss-Of-Coolant Accident Conditions”. In: *Journal of Nuclear Materials* 546 (2021), p. 152750. ISSN: 0022-3115. DOI: https://doi.org/10.1016/j.jnucmat.2020.152750. URL: https://www.sciencedirect.com/science/article/pii/S0022311520313581.

[17] N. Capps et al. “Engineering Assessment of UO_2 and Cladding Behavior under High Burnup LOCA Conditions”. In: (Sept. 2021). DOI: 10.2172/1822042. URL: https://www.osti.gov/biblio/1822042.

[18] N. Capps et al. “Integral LOCA fragmentation test on high-burnup fuel”. In: *Nuclear Engineering and Design* 367 (2020), p. 110811.

[19] N. Capps et al. “PCI analysis of a commercial PWR using BISON fuel performance code”. In: *Nuclear Engineering and Design* 324 (2017), pp. 131–142.

[20] J. V. Cathcart et al. *Zirconium metal-water oxidation kinetics, IV, reaction rate studies*. Tech. rep. ORNL/NUREG-17. Oak Ridge National Laboratory, 1977.

[21] Y. C. Chiew and E. D. Glandt. “The effect of structure on the conductivity of a dispersion”. In: *Journal of Colloid and Interface Science* 91.1 (1983), pp. 90–104.

[22] F. Bole du Chomont. *LOCA Testing at Halden; The Ninth Experiment IFA-650.9*. Tech. rep. HWR-917. OECD Halden Reactor Project, 2009.

[23] O. Coindreau, F. Fichot, and J. Fleurot. "Nuclear fuel rod fragmentation under accidental conditions". In: *Nuclear Engineering and Design* 255 (2013), pp. 68–76.

[24] Nuclear Regulatory Commission. *NRC: 10 CFR 50.46 Acceptance criteria for emergency core cooling systems for light-water nuclear power reactors*. 2017. URL: https://www.nrc.gov/reading-rm/doc-collections/cfr/part050/part050-0046.html.

[25] S. J. Dagbjartsson et al. *Axial Gas Flow in Irradiated PWR Fuel Rods*. Tech. rep. TREE-NUREG-1158. Idaho National Engineering Laboratory, 1977.

[26] C. P. Deck et al. "Characterization of SiC-SiC composites for accident tolerant fuel cladding". In: *Journal of Nuclear Materials* 466 (2015), pp. 667–681.

[27] F. J. Erbacher et al. "Burst Criterion of Zircaloy Fuel Claddings in a Loss-of-Coolant Accident". In: *Zirconium in the Nuclear Industry: Fifth Conference, ASTM STP 754*. 1982.

[28] A. G. Evans and R. W. Davidge. "The strength and fracture of stoichimetric polycrystalline UO_2". In: *Journal of Nuclear Materials* 33 (1969), pp. 249–260.

[29] K. G. Field et al. *Handbook on the Material Properties of FeCrAl Alloys for Nuclear Power Production Applications*. Tech. rep. ORNL/SPR-2018/905 Rev. 1. Oak Ridge National Laboratory, 2018.

[30] M. Flanagan and P. Askeljung. "Observations of Fuel Fragmentation, Mobility and Release in Integral High-Burnup, Fueled LOCA Tests". In: *Enlarged Halden Program Group Meeting 2011*. 2011.

[31] R. A. Freeman et al. "Analysis of Thermal Creep for Uranium Silicide Fuel using Bison". In: *Proceedings of ICAPP 2018*. 2018.

[32] K. A. Gamble. "Investigation of coated cladding ballooning behavior using Bison". In: *Procedings of "Top Fuel" 2019*. Seattle, USA, 2019.

[33] K. A. Gamble et al. *Advancements in modeling fuel pulverization and cladding behavior during a LOCA*. Tech. rep. INL/EXT-21-64705. Idaho National Laboratory, 2021.

[34] K. A. Gamble et al. "An investigation of FeCrAl cladding behavior under normal operating and loss of coolant conditions". In: *Journal of Nuclear Materials* 491 (2017), pp. 55–66.

[35] K. A. Gamble et al. “Mechanistic verification of empirical UO_2 fuel fracture models”. In: *Journal of Nuclear Materials* 556 (2021), p. 153163. DOI: 10.1016/j.jnucmat.2021.153163.

[36] K. A. L. Gamble. “Modeling of three-dimensional deformation mechanisms in CANDU reactor fuel elements”. MA thesis. Royal Military College of Canada, 2014.

[37] B. Garrison et al. “Burst characteristics of advanced accident-tolerant FeCrAl cladding under temperature transient testing”. In: *Journal of Nuclear Materials* 560 (2022), p. 153488. DOI: 10.1016/j.jnucmat.2021.153488.

[38] F. Garzarolli et al. *Review of PWR fuel rod waterside corrosion behavior*. Tech. rep. EPRI NP-2789 Project 1250 Final Report. Kraftwerk Union A. G. and Combustion Engineering Inc., 1982.

[39] J.-M. Gatt et al. “Experimental and numerical study of fracture mechanisms in UO_2 nuclear fuel”. In: *Engineering Failure Analysis* 47 (2015), pp. 299–311.

[40] K. J. Geelhood et al. *FRAPCON 4.0: A Computer Code for the Calculation of Steady-State, Thermal-Mechanical Behavior of Oxide Fuel Rods for High Burnup*. Tech. rep. PNNL-19418, Vol. 1 Rev. 2. Pacific Northwest National Laboratory, 2015.

[41] K. J. Geelhood et al. *FRAPTRAN 2.0: A Computer Code for the Transient Analysis of Oxide Fuel Rods*. Tech. rep. PNNL-19400, Vol. 1 Rev. 2. Pacific Northwest National Laboratory, 2016.

[42] T.J. Gerczak et al. “Restructuring in high burnup UO_2 studied using modern electron microscopy”. In: *Journal of Nuclear Materials* 509 (2018), pp. 245–259. DOI: 10.1016/j.jnucmat.2018.05.077.

[43] P. M. Gilmore, H. H. Klepfer, and J. M. Sorensen. *EPRI PWR fuel cladding corrosion (PFCC) model volume 1: theory and user’s manual*. Tech. rep. TR-105387-V1. Electric Power Research Institute, 1995.

[44] K. Govers and M. Verwerft. “An insight on fuel fragmentation, relocation and dispersla during loss-of-coolant accidents from computer simulations”. In: *Proceedings of Topfuel 2015*. 2015.

[45] J. D. Hales et al. “Validation of the BISON 3D Fuel Performance Code: Temperature Comparisons for Concentrically and Eccentrically Located Fuel Pellets”. In: *Enlarged Halden Programme Group Meeting: Proceedings of the Fuels and Materials Sessions*. Vol. HPR-378. OECD Halden Reactor Project. Storefjell Resort Hotel, Norway, 2013.

[46] A. Hansbo and P. Hansbo. “A finite element method for the simulation of strong and weak discontinuities in solid mechanics”. In: *Computer Methods in Applied Mechanics and Engineering* 193 (2004), pp. 3523–3540.

[47] M. Helin and J. Flygare. *NRC LOCA tests at Studsvik, Design and construction of test train device and tests with unirradiated cladding material*. Tech. rep. STUDSVIK/N-11/130. Studsvik, 2012.

[48] Y. Hu et al. “Thermomechanical peridynamic analysis with irregular non-uniform domain discretization”. In: *Engineering Fracture Mechanics* 197 (2018), pp. 92–113.

[49] H. Huang, B. Spencer, and J. Hales. “Discrete element method for simulation of early-life thermal fracturing behavior in ceramic nuclear fuel pellets”. In: *Nuclear Engineering and Design* 278 (2014), pp. 515–528.

[50] T. Ikonen. “Comparison of global sensitivity analysis methods - Application to fuel behavior modeling”. In: *Nuclear Engineering and Design* 297 (2016), pp. 72–80.

[51] L. O. Jernkvist. *Cladding tube rupture under LOCA: Data and models for rupture opening size*. Tech. rep. 2021:05. Swedish Radiation Safety Authority, 2021.

[52] L. O. Jernkvist. *Computational assessment of LOCA simulation tests on high burnup fuel rods in Halden and Studsvik*. Tech. rep. 2017:12. Swedish Radiation Safety Authority, 2017.

[53] L. O. Jernkvist and A. Massih. *Models for axial relocation of fragmented and pulverized fuel pellets in distending fuel rods and its effects on fuel rod heat load*. Tech. rep. 2015:37. Quantum Technologies AB, 2015.

[54] W. Jiang, B. W. Spencer, and J. E. Dolbow. “Ceramic nuclear fuel fracture modeling with the extended finite element method”. In: *Engineering Fracture Mechanics* 223 (2020), p. 106713.

[55] L. Kekkonen. *LOCA Testing at Halden; The Fourth Experiment IFA-650.4*. Tech. rep. HWR-838. OECD Halden Reactor Project, 2007.

[56] G. Khvostov et al. “Some insights into the role of axial gas flow in fuel rod behaviour during the LOCA based on Halden tests and calculations with the FALCON-PSI code”. In: *Nuclear Engineering and Design* 241 (2011), pp. 1500–1507.

[57] B. S. Kirk et al. “libMesh: A C++ Library for Parallel Adaptive Mesh Refinement/-Coarsening Simulations”. In: *Engineering with Computers* 22.3–4 (2006), pp. 237–254.

[58] D. A. Knoll and D. E. Keyes. “Jacobian-free Newton-Krylov methods: a survey of approaches and applications”. In: *Journal of Computational Physics* 193 (2004), pp. 357–397.

[59] S. Kondo et al. “Effect of irradiation damage on hydrothermal corrosion of SiC”. In: *Journal of Nuclear Materials* 464 (2015), pp. 36–42.

[60] K. Kulacsy. “Mechanistic model for the fragmentation of the high-burnup structure during LOCA”. In: *Journal of Nuclear Materials* 466 (2015), pp. 409–416.

[61] T. R. G. Kutty et al. “Fracture toughness and fracture surface energy of sintered uranium dioxide fuel pellets”. In: *Journal of Materials Science Letters* 6 (1987), pp. 260–262.

[62] S. Leistikow et al. “Comprehensive presentation of extended Zircaloy-4/steam oxidation results 600-1600 °C”. In: *CSNI/IAEA specialists meeting on water reactor fuel safety and fission product release in off-normal and accident conditions*. 1983.

[63] Z. Ma et al. “A three-dimensional axial fuel relocation framework with discrete element method to support burnup extension”. In: *Journal of Nuclear Materials* 541 (2020), p. 152408.

[64] V. Di Marcello et al. “The TRANSURANUS mechanical model for large strain analysis”. In: *Nuclear Engineering and Design* 276 (2014), pp. 19–29.

[65] M. E. Markiewicz and F.J. Erbacher. *Experiments on ballooning in pressurized and transiently heated Zircaloy-4 tubes*. Tech. rep. KfK 4343. Kernforschungszentrum Karlsruhe, Germany: Kernforschungszentrum Karlsruhe GmbH (Germany, 1988.

[66] C. P. Massey et al. “Cladding burst behavior of Fe-based alloys under LOCA”. In: *Journal of Nuclear Materials* 470 (2016), pp. 128–138. DOI: 10.1016/j.jnucmat.2015.12.018.

[67] Total Materia. *Corrosion of Zirconium Alloys: Part One*. 2015. URL: http://www.totalmateria.com/page.aspx?ID=CheckArticle&site=ktn&NM=354.

[68] K. A. Maupin, L. P. Swiler, and N. W. Porter. “Validation Metrics for Deterministic and Probabilistic Data”. In: *Journal of Verification, Validation and Uncertainty Quantification* 3 (2018), p. 031002. DOI: https://doi.org/10.1115/1.4042443.

[69] Computational Mechanics and Materials Department Idaho National Laboratory. *BISON: A Finite Element-Based Nuclear Fuel Performance Code*. https://mooseframework.inl.gov/bison/.

[70] R. Mella and M. R. Wenman. "Modelling explicit fracture of nuclear fuel pellets using peridynamics". In: *Journal of Nuclear Materials* 467 (2015), pp. 58–67.

[71] N. Moes, J. Dolbow, and T. Belytschko. "A finite element method for crack growth without remeshing". In: *International Journal for Numerical Methods in Engineering* 46 (1999), pp. 131–150.

[72] R. Montgomery and R. N. Morris. "Measurement and modeling of the gas permeability of high burnup pressurized water reactor fuel rods". In: *Journal of Nuclear Materials* 523 (2019), pp. 206–215.

[73] A. Motta and D. Olander. *Light Water Reactor Materials, Volume I: Fundamentals*. 1st ed. American Nuclear Society, 2017. ISBN: 978-0-89448-461-2.

[74] Westinghouse Nuclear. *Integral Fuel Burnable Absorber (IFBA) Fuel Cycles and IFBA/Gad Hybrid Fuel Cycles*. 2018. URL: https://www.westinghousenuclear.com/Portals/0/operating%5C%20plant%5C%20services/fuel/fuel%5C%20products/NFCM-0015%5C%20IFBA.pdf.

[75] M. Oguma. "Cracking and Relocation behavior of Nuclear Fuel Pellets during Rise to Power". In: *Nuclear Engineering and Design* 76 (1983), pp. 35–45.

[76] M. Oguma. "Microstructure Effects on Fracture Strength of UO_2 Fuel Pellets". In: *Journal of Nuclear Science and Technology* 19.12 (1982), pp. 1005–1014.

[77] S. Oterkus and E. Madenci. "Peridynamic modeling of fuel pellet cracking". In: *Engineering Fracture Mechanics* 176 (2017), pp. 23–37.

[78] F. Passelaigue et al. "Implementation and Validation of the Hydride Nucleation-Growth-Dissolution (HNGD) model in BISON". In: *Journal of Nuclear Materials* 544 (2021), p. 152683.

[79] G. Pastore et al. "Analysis of fuel rod behavior during loss-of-coolant accidents using the BISON code: Cladding modeling developments and simulation of separate-effects experiments". In: *Journal of Nuclear Materials* 543 (2021), p. 152537. DOI: https://doi.org/10.1016/j.jnucmat.2020.152537.

[80] G. Pastore et al. "Analysis of fuel rod behavior during loss-of-coolant accidents using the BISON code: Fuel modeling developments and simulation of integral experiments". In: *Journal of Nuclear Materials* 545 (2021), p. 152645. DOI: 10.1016/j.jnucmat.2020.152645.

[81] G. Pastore et al. "Uncertainty and sensitivity analysis of fission gas behavior in engineering-scale fuel modeling". In: *Journal of Nuclear Materials* 456 (2015), pp. 398–408.

[82] C. J. Permann et al. "MOOSE: Enabling massively parallel multiphysics simulation". In: *SoftwareX* 11 (2020), p. 100430.

[83] B. A. Pint et al. "Material Selection for Accident Tolerant Fuel Cladding". In: *Metallurgical and Materials Transactions E* 2E (2015), pp. 190–196.

[84] D. Pizzocri et al. "A semi-empirical model for the formation and depletion of the high burnup structure in UO_2". In: *Journal of Nuclear Materials* 487 (2017), pp. 23–29. DOI: 10.1016/j.jnucmat.2017.01.053.

[85] D. A. Powers and R. O. Meyer. *Cladding Swelling and Rupture Models for LOCA analysis*. Tech. rep. NUREG-0630. Nuclear Regulatory Commission, 1980.

[86] J. T. Prater and E. L. Courtright. *Zircaloy-4 oxidation at 1300 to 2400 °C*. Tech. rep. NUREG/CR-4889. Pacific Northwest National Laboratory, 1987.

[87] A. Prudil et al. "Development and testing of the FAST fuel performance code: Normal operating conditions (Part 1)". In: *Nuclear Engineering and Design* 282 (2015), pp. 158–168.

[88] K. C. Radford. "Effect of Fabrication parameters and Microstructure on the Mechanical Strength of UO_2 Fuel Pellets". In: *Journal of Nuclear Materials* 84 (1979), pp. 222–236.

[89] A. Raftery et al. *In-cell Re-fabrication and Loss-of-coolant Accident (LOCA) Testing of High Burnup Commercial Spent Fuel*. Tech. rep. ORNL/TM-2018/891. Oak Ridge National Laboratory, 2018.

[90] P. Raynaud and I. Porter. "Predictions of Fuel Dispersal During a LOCA". In: *Proceedings of WRFPM 2014*. 2014.

[91] P. A. C. Raynaud. *Fuel Fragmentation, Relocation, and Dispersal During the Loss-of-Coolant Accident*. Tech. rep. NUREG-2121. United States Nuclear Regulatory Commission, 2012.

[92] R. Rebak et al. *GE Final Technical and Scientific Report*. Tech. rep. DE-NE0008221. General Electric Global Research, 2018. URL: https://www.osti.gov/servlets/purl/1488931.

[93] I.G. Ritchie. *Waterside corrosion of zirconium alloys in nuclear power plants*. Tech. rep. IAEA TECDOC 996. International Atomic Energy Agency, 1998.

[94] V. Rondinella et al. *Measurement of gas permeability along the axis of a spent fuel rod*. European Nuclear Society, 2015, pp. 217–225. ISBN: 978-92-95064-23-

2. URL: http://www.euronuclear.org/events/topfuel/topfuel2015/transactions.htm.

[95] G. Rossiter. "Development of the ENIGMA Fuel Performance Code for whole Core Analysis and Dry Storage Assessments". In: *Nuclear Engineering and Technology* 43.6 (2011), pp. 489–498.

[96] G. Schanz. *Recommendations and supporting information on the choice of Zirconium oxidation models in severe accident codes*. Tech. rep. FZKA 6827, SAM-COLOSS-P043. Institut für Materialforschung, 2003.

[97] J. Sercombe, I. Aubrun, and C. Nonon. "Power ramped cladding stresses and strains in 3D simulations with burnup-dependent pellet-clad friction". In: *Nuclear Engineering and Design* 242 (2012), pp. 164–181.

[98] J. A. Sethian. *Level Set Methods and Fast Marching Methods Evolving Interfaces in Computational Geometry, Fluid Mechanics, Computer Vision, and Materials Science*. Cambridge University Press, 1999. ISBN: 9780521645577.

[99] L. J. Siefken. "Fuel axial relocaiton in ballooning fuel rods". In: *International Conference on Structural Mechanics in Reactor Technology*. 1983.

[100] L. J. Siefken et al. *SCDAP/RELAP5/MOD 3.3 Code Manual: MATPRO - A Library of Materials Properties for Light-Water-Reactor Accident Analysis*. Tech. rep. NUREG/CR-6150, Volume 4, Revision 2. Idaho National Engineering and Environmental Laboratory, 2001.

[101] M. A. Snead et al. "Severe Accident Test Station Design Document". In: (Sept. 2015). DOI: 10.2172/1252142. URL: https://www.osti.gov/biblio/1252142.

[102] H. Sonnenburg et al. *Report on Fuel Fragmentation, Relocation, and Dispersal*. Tech. rep. NEA/CSNI/R(2016)16. Organisation for Economic Co-operation and Development, Nuclear Energy Agency, Committee on the Safety of Nuclear Installations, 2016.

[103] B. W. Spencer et al. "3D modeling of missing pellet surface defects in BWR fuel". In: *Nuclear Engineering and Design* 307 (2016), pp. 155–171.

[104] B. W. Spencer et al. "Discrete modeling of early-life thermal fracture in ceramic nuclear fuel". In: *Proceedings of WRFPM2014*. 2014.

[105] B. N. L. Srinivas. "Experimental evaluation of oxide growth in binary zirconium alloys along with pure zirconium and Zircaloy-2 by steam corrosion testing". MA thesis. Royal Institute of Technology (KTH), 2012.

[106] R. E. Stachowski et al. “Progress of GE Development of Accident Tolerant Fuel FeCrAl Cladding”. In: *Proceedings of TopFuel2016*. 2016.

[107] J. G. Stone et al. “Stress analysis and probabilistic assessment of multi-layer SiC-based accident tolerant nuclear fuel cladding”. In: *Journal of Nuclear Materials* 466 (2015), pp. 682–697.

[108] O.E. Strack, R.B. Leavy, and R.M. Brannon. “Aleatory uncertainty and scale effects in computational damage models for failure and fragmentation”. In: *International Journal for Numerical Methods in Engineering* 102.3-4 (2015), pp. 468–495. DOI: 10.1002/nme.4699.

[109] J. Stuckert et al. *On the thermo-physical properties of Zircaloy-4 and ZrO_2 at high temperature*. Tech. rep. FZKA 6739. Forschungszentrum Karlsruhe GmbH, 2002.

[110] V. I. Tarasov and M. S. Veshchunov. “Modelling of as-fabricated porosity in UO_2 fuel by MFPR code”. In: *EPJ Nuclear Science and Technology* 2.19 (2016). DOI: 10.1051/eppjn/2016013.

[111] MOOSE Development Team. *MultiApp System*. 2020. URL: https://mooseframework.org/syntax/MultiApps/index.html.

[112] MOOSE Development Team. *Transfers System*. 2020. URL: https://mooseframework.org/syntax/Transfers/index.html.

[113] Massachusetts Institute of Technology. *Thermophysical Properties of Water and Steam*. 2018. URL: https://cran.r-project.org/web/packages/IAPWS95/IAPWS95.pdf.

[114] K. A. Terrani, S. J. Zinkle, and L. L. Snead. “Advanced oxidation-resistant iron-based alloys for LWR fuel cladding”. In: *Journal of Nuclear Materials* 448 (2014), pp. 420–435.

[115] K. A. Terrani et al. “Hydrothermal corrosion of SiC in LWR coolant environments in the absence of irradiation”. In: *Journal of Nuclear Materials* 465 (2015), pp. 488–498.

[116] K. A. Terrani et al. “Uniform corrosion of FeCrAl alloys in LWR coolant environments”. In: *Journal of Nuclear Materials* 479 (2016), pp. 36–47.

[117] N. Todreas. *Loss of Coolant Accidents (LOCA) in PWRs: Deterministic View, Course 22.39 Lecture 9*. 2005. URL: https://dspace.mit.edu/bitstream/handle/1721.1/45533/22-39Fall-2005/NR/rdonlyres/Nuclear-Engineering/22-39Fall-2005/9ABDFB04-CDB9-402B-B5BB-4E9263DF1C7E/0/lec9_nt.pdf.

[118] M. R. Tonks et al. “Multiscale development of a fission gas thermal conductivity model: Coupling atomic, meso and continuum level simulations”. In: *Journal of Nuclear Materials* 440 (2013), pp. 193–200.

[119] R. Tradotti. *LOCA Testing at Halden; The BWR Fuel Experiment IFA-650.14*. Tech. rep. HWR-1084. OECD Halden Reactor Project, 2014.

[120] J. A. Turnbull et al. “An Assessment of The Fuel Pulverization Threshold During LOCA-Type Temperature Transients”. In: *Nuclear Science and Engineering* 179 (2015), pp. 477–485.

[121] K. Une, S. Kashibe, and A. Takagi. “Fission Gas Release Behavior from High Burnup UO_2 Fuels under Rapid Heating Conditions”. In: *Journal of Nuclear Science and Technology* 43.9 (2006), pp. 1161–1171.

[122] H. Wadell. “Volume, Shape, and Roundness of Quartz Particles”. In: *Journal of Geology* 43 (1935), pp. 250–280.

[123] Malik Wagih et al. “Fuel performance of chromium-coated zirconium alloy and silicon carbide accident tolerant fuel claddings”. In: *Annals of Nuclear Energy* 120 (2018), pp. 304–318. ISSN: 0306-4549. DOI: 10.1016/j.anucene.2018.06.001. URL: https://www.sciencedirect.com/science/article/pii/S0306454918303037.

[124] L. A. Walton and D. L. Husser. “Fuel pellet fracture and relocation”. In: *IAEA Specialists Meeting on Water Reactor Fuel Element Performance Computer Modelling*. 1983.

[125] L. A. Walton and J. E. Matheson. “FUMAC - A new model for light water reactor fuel relocation and pellet-cladding interaction”. In: *Nuclear Technology* 64 (1984), pp. 127–138.

[126] Y. Wang, X. Zhou, and M. Kou. “Peridynamic investigation on thermal fracturing behavior of ceramic nuclear fuel pellets under power cycles”. In: *Ceramics International* 44 (2018), pp. 11512–11542.

[127] Y. Wang et al. “Hybrid P_N-S_N with Lagrange multiplier and upwinding for the multiscale transport capability in Rattlesnake”. In: *Progress in Nuclear Energy* 101 (2017), pp. 391–393.

[128] A. E. R. Westman. “The packing of particles: Empirical equations for intermediate diameter ratios”. In: *Journal of the American Ceramic Society* 76.11 (1936), pp. 127–129.

[129] W. Wiesenack, L. Kekkonen, and B. Oberänder. “Axial gas transport and loss of pressure after ballooning rupture of high burnup-fuel rods subjected to LOCA conditions”. In: *International Conference on the Physics of Reactors "Nuclear Power: A Sustainable Resource"*. Interlaken, Switzerland, 2008.

[130] A. F. Williams and S. Yatabe. “An ANSYS-based 3-dimensional thermomechanical model of a CANDU fuel pin”. In: *CNL Nuclear Review* 6.2 (2016), pp. 199–214. DOI: 10.12943/CNR.2016.00029.

[131] R. L. Williamson and D. A. Knoll. “Simulating Dynamic Fracture in Oxide Fuel Pellets Using Cohesive Zone Models”. In: *20th International Conference on Structural Mechanics in Reactor Technology (SMiRT 20)*. 2009.

[132] R. L. Williamson et al. “BISON: A Flexible Code for Advanced Simulation of the Performance of Multiple Nuclear Fuel Forms”. In: *Nuclear Technology* 207.7 (2021), pp. 954–980. DOI: 10.1080/00295450.2020.1836940.

[133] R. L. Williamson et al. “Validating the BISON Fuel Performance Code to LWR Experiments”. In: *Journal of Nuclear Materials* 301 (2016), pp. 232–244.

[134] S. Yagnik et al. *Fuel Analysis and Licensing Code: FALCON MOD01: Volume 1: Theoretical and Numerical Bases*. Tech. rep. 1011307. EPRI, 2004.

[135] Y. Yamamoto et al. “Development and property evaluation of nuclear grade wrought FeCrAl fuel cladding for light water reactors”. In: *Journal of Nuclear Materials* 467 (2015), pp. 703–716.

[136] J.A. Yingling et al. “UPDATED U3SI2 thermal creep model and sensitivity analysis of the U3SI2-SIC accident tolerant FUEL”. In: *Journal of Nuclear Materials* 543 (2021), p. 152586. ISSN: 0022-3115. DOI: https://doi.org/10.1016/j.jnucmat.2020.152586. URL: https://www.sciencedirect.com/science/article/pii/S0022311520311946.

[137] F. W. Zok. “On weakest link theory and Weibull statistics”. In: *Journal of the American Ceramic Society* 100.4 (2017), pp. 1265–1268.

APPENDIX A

STATISTICAL DATA USED IN THE FRAGMENTATION STUDY

In the fragmentation study completed in Chapter 3 values of d_i^2, the Euclidean distance, and d_{ne}, the total normalized Euclidean distance ($\bar{d}_{ne}$) are required to compute the average total normalized Euclidean distance presented in Tables 3.2–3.4. This Appendix provides the data tables for d_i^2 at rise to power as well as 10, 20, 30, and 40 MWd/kgU for each of the empirical models, Barani et al. [9], Coindreau et al. [23], and Walton and Matheson [125]. A table for d_{ne} is also provided. The symbols C, M, and F within the tables, correspond to the coarse, medium, and fine meshes, respectively. Table A.1 presents the average Euclidean distance from the fragmentation study described in Chapter 3 for the uniform initial strength randomization, to the three empirical correlations for every combination of ramping rate, and mesh density. Table A.2 shows the data for the volume-weighted Weibull initial strength randomization.

Table A.1: The average Euclidean distance compared to the three empirical correlations for the uniform initial strength randomization.

Correlation	1%/h			3%/h			5%/h		
	C	M	F	C	M	F	C	M	F
[9]	8.84	14.62	10.18	5.82	11.63	9.05	6.05	10.91	10.23
[23]	30.35	38.38	31.95	22.65	33.73	29.53	22.27	31.49	30.07
[125]	21.73	26.68	21.56	15.77	23.29	19.12	15.23	21.19	18.62

A.1 EUCLIDEAN DISTANCE DATA TO BARANI ET AL. CORRELATION

Tables A.3–A.7 present the Euclidean distance between the fragmentation study predictions for the Barani et al. empirical correlation. A value is tabulated for each combination of the

Table A.2: The average Euclidean distance compared to the three empirical correlations for the volume-weighted Weibull initial strength randomization.

Correlation	1%/h			3%/h			5%/h		
	C	M	F	C	M	F	C	M	F
[9]	11.47	25.03	25.49	8.09	19.23	22.31	7.13	16.09	18.14
[23]	32.65	60.19	65.38	28.03	55.06	62.21	27.08	49.83	60.67
[125]	22.91	42.42	45.68	19.49	39.09	43.00	18.81	35.60	43.24

method of initial randomization of the fuel strength, the power ramping rate, mesh density, and maximum power level.

Table A.3: The Euclidean distance between the fragmentation study calculations and the Barani et al. [9] empirical correlation at rise to power.

Max. Linear Power (kW/m)	Uniform								
	1%/h			3%/h			5%/h		
	C	M	F	C	M	F	C	M	F
5	Nan	Nan	Nan	Nan	Nan	Nan	Nan	Nan	Nan
10	0.90	0.97	0.16	0.14	0.31	0.00	0.11	0.24	0.004
15	0.96	1.92	0.46	0.76	1.53	0.319	0.42	0.85	0.12
20	2.35	4.90	2.08	1.20	3.54	1.40	0.90	2.55	0.77
25	1.96	3.91	4.24	1.06	3.38	2.22	0.75	2.03	0.42
30	2.60	13.58	3.25	0.94	5.88	0.16	1.01	5.12	0.77
35	3.53	5.00	5.96	1.60	2.99	3.39	1.78	5.38	2.25
40	4.51	10.70	0.30	1.86	6.61	4.68	2.80	6.30	3.76
Max. Linear Power (kW/m)	Weibull								
	1%/h			3%/h			5%/h		
	C	M	F	C	M	F	C	M	F
5	Nan	Nan	Nan	Nan	Nan	Nan	Nan	198.01	0.12
10	0.50	3.52	3.70	0.23	3.97	4.26	0.20	2.36	0.17
15	2.34	9.62	12.00	1.86	7.70	4.97	1.94	4.42	0.94
20	3.85	13.23	11.78	2.08	8.13	9.27	0.90	4.15	1.12
25	4.24	25.23	18.33	2.08	15.46	10.34	1.28	3.85	1.24
30	5.35	23.28	26.80	2.04	13.89	16.12	1.25	6.28	2.93
35	5.44	31.74	32.89	2.48	17.75	26.57	1.69	12.43	3.41
40	8.51	40.07	41.83	3.46	21.27	36.47	3.28	10.24	3.57

Table A.4: The Euclidean distance between the fragmentation study calculations and the Barani et al. [9] empirical correlation at 10 MWd/kgU.

Max. Linear Power (kW/m)	Uniform								
	1%/h			3%/h			5%/h		
	C	M	F	C	M	F	C	M	F
5	Nan	Nan	Nan	Nan	Nan	Nan	Nan	Nan	Nan
10	0.90	1.02	0.17	0.16	0.31	0.00	0.11	0.24	0.00
15	0.96	1.92	0.51	0.65	1.53	0.32	0.42	0.65	0.12
20	2.37	13.35	2.26	1.19	3.54	1.30	0.91	2.45	0.81
25	1.96	3.91	4.25	1.04	3.21	2.20	0.73	1.50	0.41
30	2.61	13.16	3.23	0.99	5.90	1.44	1.14	5.01	0.70
35	3.83	9.06	6.68	1.62	6.11	4.10	1.76	9.89	4.00
40	4.70	12.64	6.22	2.09	6.79	7.14	2.71	7.11	2.05
Max. Linear Power (kW/m)	Weibull								
	1%/h			3%/h			5%/h		
	C	M	F	C	M	F	C	M	F
5	Nan	Nan	Nan	Nan	Nan	Nan	Nan	198.01	0.12
10	0.50	3.52	3.70	0.23	3.97	4.26	0.38	3.36	3.97
15	2.18	9.62	12.00	1.87	7.65	4.97	1.51	7.08	7.12
20	3.85	13.23	11.78	2.07	8.13	9.27	2.10	6.66	8.37
25	4.24	25.56	18.24	2.00	15.46	10.28	1.35	7.19	11.33
30	5.37	23.28	26.77	2.04	13.89	16.12	1.60	11.01	15.41
35	5.41	32.01	38.36	2.48	18.27	27.49	1.93	13.72	27.22
40	8.54	47.78	43.36	3.48	20.15	33.57	2.98	18.44	30.37

A.2 Euclidean Distance Data to Coindreau et al. Correlation

Tables A.8–A.12 present the Euclidean distance between the fragmentation study predictions for the Coindreau et al. empirical correlation. A value is tabulated for each combination of the method of initial randomization of the fuel strength, the power ramping rate, mesh density, and maximum power level.

Table A.5: The Euclidean distance between the fragmentation study calculations and the Barani et al. [9] empirical correlation at 20 MWd/kgU.

Max. Linear Power (kW/m)	Uniform								
	1%/h			3%/h			5%/h		
	C	M	F	C	M	F	C	M	F
5	Nan	Nan	Nan	Nan	Nan	Nan	Nan	Nan	Nan
10	0.89	1.02	0.17	0.17	0.31	0.00	0.10	0.24	0.00
15	1.15	1.92	0.51	0.69	1.53	0.32	0.46	0.65	0.12
20	2.25	4.04	2.26	1.13	3.52	1.29	1.05	2.45	0.81
25	2.70	3.84	4.25	0.81	3.17	2.20	0.92	1.50	0.41
30	2.30	12.04	4.39	0.85	5.61	1.46	1.08	5.21	0.93
35	3.38	8.51	5.59	1.58	6.89	5.29	2.09	8.62	4.52
40	6.03	29.60	16.25	3.07	9.59	17.30	2.79	14.26	69.63
Max. Linear Power (kW/m)	Weibull								
	1%/h			3%/h			5%/h		
	C	M	F	C	M	F	C	M	F
5	Nan	Nan	Nan	Nan	Nan	Nan	Nan	198.01	0.12
10	0.66	3.52	3.70	0.25	3.97	4.26	0.42	3.36	3.97
15	2.17	9.62	12.00	1.89	7.65	4.97	1.68	7.08	7.12
20	3.71	13.23	11.73	2.69	8.13	9.27	2.02	6.61	8.37
25	4.25	25.64	18.24	1.92	15.42	10.28	1.49	7.19	11.33
30	5.61	23.72	27.21	2.10	13.80	17.10	1.61	11.67	16.63
35	6.66	29.54	35.82	2.53	17.52	26.81	1.97	12.20	24.23
40	8.10	48.63	47.47	3.35	17.91	13.58	3.22	14.82	7.69

A.3 Euclidean Distance Data to Walton and Matheson Correlation

Tables A.13–A.17 present the Euclidean distance between the fragmentation study predictions for the Walton and Matheson empirical correlation. A value is tabulated for each combination of the method of initial randomization of the fuel strength, the power ramping rate, mesh density, and maximum power level.

Table A.6: The Euclidean distance between the fragmentation study calculations and the Barani et al. [9] empirical correlation at 30 MWd/kgU.

Max. Linear Power (kW/m)	Uniform								
	1%/h			3%/h			5%/h		
	C	M	F	C	M	F	C	M	F
5	Nan	Nan	Nan	Nan	Nan	Nan	Nan	Nan	Nan
10	0.88	1.02	0.17	0.17	0.31	0.00	0.10	0.23	0.00
15	1.34	1.91	0.51	0.68	1.53	0.32	0.57	0.91	0.12
20	2.48	4.10	2.26	1.15	3.50	1.29	1.07	2.43	0.81
25	3.35	3.82	4.30	0.98	3.13	2.45	0.89	1.52	0.38
30	2.38	11.34	3.74	0.77	8.02	1.93	1.35	4.94	1.25
35	5.17	8.25	8.28	1.69	15.89	11.85	2.63	5.28	7.08
40	Nan	Nan	Nan	Nan	Nan	Nan	Nan	Nan	Nan
Max. Linear Power (kW/m)	Weibull								
	1%/h			3%/h			5%/h		
	C	M	F	C	M	F	C	M	F
5	Nan	Nan	Nan	Nan	Nan	Nan	Nan	198.01	0.12
10	0.68	3.49	3.70	0.25	3.97	4.26	0.40	3.36	3.97
15	2.16	9.62	12.00	2.20	7.61	4.97	1.70	7.25	7.13
20	4.02	13.23	11.73	2.60	8.26	9.27	2.20	6.46	8.37
25	4.54	25.64	18.24	1.99	15.36	10.28	1.49	7.19	11.33
30	5.82	24.31	28.94	2.44	13.43	18.67	1.26	11.46	15.76
35	5.18	18.35	42.58	3.25	15.68	105.70	1.93	14.44	31.09
40	Nan	Nan	Nan	Nan	Nan	Nan	Nan	Nan	Nan

Table A.7: The Euclidean distance between the fragmentation study calculations and the Barani et al. [9] empirical correlation at 40 MWd/kgU.

Max. Linear Power (kW/m)	Uniform								
	1%/h			3%/h			5%/h		
	C	M	F	C	M	F	C	M	F
5	Nan	Nan	Nan	Nan	Nan	Nan	Nan	Nan	Nan
10	0.90	1.02	0.17	0.16	0.31	0.00	0.11	0.23	0.00
15	1.37	1.91	0.51	0.77	1.53	0.32	0.58	0.91	0.12
20	2.59	4.09	2.26	1.63	3.50	1.29	1.44	2.43	0.81
25	3.35	3.60	4.19	0.94	3.79	2.68	1.10	1.34	0.45
30	1.51	15.79	3.95	1.37	11.52	3.18	2.68	16.54	1.02
35	Nan	Nan	Nan	Nan	Nan	Nan	Nan	Nan	Nan
40	Nan	Nan	Nan	Nan	Nan	Nan	Nan	Nan	Nan
Max. Linear Power (kW/m)	Weibull								
	1%/h			3%/h			5%/h		
	C	M	F	C	M	F	C	M	F
5	Nan	Nan	Nan	Nan	Nan	Nan	Nan	198.01	0.12
10	0.68	3.49	3.70	0.25	3.97	4.26	0.42	3.36	3.97
15	2.27	9.62	12.00	2.18	7.61	4.97	1.70	7.25	7.13
20	3.90	13.23	11.73	2.51	8.22	9.27	2.13	6.57	8.37
25	4.34	25.13	21.48	2.07	16.64	10.53	1.67	7.14	11.14
30	6.44	24.94	26.05	2.53	8.88	15.49	1.15	10.38	23.85
35	Nan	Nan	Nan	Nan	Nan	Nan	2.01	Nan	Nan
40	Nan	Nan	Nan	Nan	Nan	Nan	Nan	Nan	Nan

Table A.8: The Euclidean distance between the fragmentation study calculations and the Coindreau et al. [23] empirical correlation at rise to power.

Max. Linear Power (kW/m)	Uniform								
	1%/h			3%/h			5%/h		
	C	M	F	C	M	F	C	M	F
5	Nan	Nan	Nan	Nan	Nan	Nan	Nan	Nan	Nan
10	1.45	1.52	0.36	0.32	0.56	0.021	0.24	0.45	0.01
15	1.12	2.22	0.60	0.89	1.79	0.434	0.51	1.01	0.19
20	3.22	6.65	3.21	1.77	5.09	2.38	1.40	3.75	1.49
25	3.68	7.24	8.90	2.38	6.82	5.37	1.85	4.42	1.68
30	6.35	29.35	9.33	3.23	15.03	0.47	3.46	13.78	3.75
35	11.02	14.93	20.93	6.40	10.54	15.14	7.44	18.39	11.19
40	17.21	37.06	1.32	9.24	26.37	25.06	13.68	26.38	22.46
Max. Linear Power (kW/m)	Weibull								
	1%/h			3%/h			5%/h		
	C	M	F	C	M	F	C	M	F
5	Nan	Nan	Nan	Nan	Nan	Nan	Nan	619.31	0.97
10	0.84	4.91	5.23	0.43	5.59	5.99	0.38	3.37	0.33
15	2.64	10.73	13.57	2.14	8.68	5.75	2.22	5.00	1.10
20	5.21	17.44	16.03	3.04	11.19	13.15	1.40	5.78	1.84
25	7.53	41.63	31.78	4.49	27.71	20.57	3.00	7.26	3.22
30	12.63	48.05	58.49	6.52	31.88	40.87	4.63	15.23	8.67
35	16.26	80.69	89.55	10.15	50.44	81.04	7.95	37.17	12.99
40	31.23	124.85	140.90	16.75	73.59	136.82	16.89	39.09	17.45

Table A.9: The Euclidean distance between the fragmentation study calculations and the Coindreau et al. [23] empirical correlation at 10 MWd/kgU.

Max. Linear Power (kW/m)	Uniform								
	1%/h			3%/h			5%/h		
	C	M	F	C	M	F	C	M	F
5	Nan	Nan	Nan	Nan	Nan	Nan	Nan	Nan	Nan
10	19.46	19.57	9.49	8.23	9.64	4.53	6.55	8.49	4.11
15	5.19	9.51	5.72	3.98	8.41	4.61	2.95	4.41	3.37
20	7.10	35.84	9.30	4.43	12.17	7.10	3.89	9.04	5.94
25	5.65	11.00	14.49	3.98	10.34	9.21	3.20	5.54	3.43
30	7.42	32.68	11.06	4.07	17.64	7.12	4.53	15.95	4.57
35	11.53	25.36	22.68	6.28	19.94	17.68	7.13	31.45	18.37
40	15.37	38.65	24.49	8.61	23.73	29.63	11.29	25.99	11.74
Max. Linear Power (kW/m)	Weibull								
	1%/h			3%/h			5%/h		
	C	M	F	C	M	F	C	M	F
5	Nan	Nan	Nan	Nan	Nan	Nan	Nan	4553.39	12.26
10	12.34	42.03	46.70	8.68	49.36	52.34	10.48	42.95	50.04
15	9.10	35.68	50.82	9.01	31.54	25.33	7.34	29.26	34.67
20	11.11	35.34	34.56	7.41	24.71	30.70	7.52	20.92	28.51
25	11.22	60.26	46.52	7.14	41.46	32.23	5.78	20.70	35.59
30	14.68	54.67	67.10	7.83	36.80	47.80	7.03	30.85	48.56
35	15.74	79.25	101.52	9.82	50.60	82.52	8.05	39.95	85.94
40	27.17	129.28	129.47	14.40	61.31	113.41	13.42	57.67	107.86

Table A.10: The Euclidean distance between the fragmentation study calculations and the Coindreau et al. [23] empirical correlation at 20 MWd/kgU.

Max. Linear Power (kW/m)	Uniform								
	1%/h			3%/h			5%/h		
	C	M	F	C	M	F	C	M	F
5	Nan	Nan	Nan	Nan	Nan	Nan	Nan	Nan	Nan
10	64.31	64.07	34.49	30.01	33.36	18.99	23.57	29.78	17.67
15	15.94	25.70	19.03	11.56	23.58	16.01	8.65	13.07	12.88
20	14.52	25.58	22.76	10.18	27.74	18.95	10.21	21.16	17.20
25	13.84	20.01	28.53	6.89	19.79	19.35	8.09	11.18	8.45
30	10.42	44.56	23.64	6.06	26.84	12.76	7.21	26.94	10.19
35	14.04	31.51	26.33	8.69	30.65	31.46	11.50	37.75	29.76
40	21.92	100.39	66.83	13.50	37.01	72.62	13.51	54.98	286.41
Max. Linear Power (kW/m)	Weibull								
	1%/h			3%/h			5%/h		
	C	M	F	C	M	F	C	M	F
5	Nan	Nan	Nan	Nan	Nan	Nan	Nan	12633.95	37.94
10	49.14	128.03	143.55	32.39	151.37	160.16	36.39	132.33	153.83
15	23.01	87.34	130.75	24.32	80.34	69.32	21.19	74.58	93.54
20	23.07	72.46	73.62	20.62	53.72	69.20	16.99	45.90	65.01
25	20.27	103.47	82.08	13.25	74.42	61.59	13.09	38.33	68.07
30	23.23	81.03	101.72	13.25	55.40	79.15	11.71	49.84	82.81
35	25.45	93.57	126.53	13.47	64.41	109.30	11.96	48.23	105.42
40	30.39	150.67	157.85	15.95	64.75	54.76	16.64	55.77	33.72

Table A.11: The Euclidean distance between the fragmentation study calculations and the Coindreau et al. [23] empirical correlation at 30 MWd/kgU.

Max. Linear Power (kW/m)	Uniform								
	1%/h			3%/h			5%/h		
	C	M	F	C	M	F	C	M	F
5	Nan	Nan	Nan	Nan	Nan	Nan	Nan	Nan	Nan
10	135.08	134.20	75.10	64.80	71.34	43.38	51.53	63.80	40.70
15	34.90	49.59	40.10	22.48	46.39	34.11	19.40	33.86	28.56
20	27.14	44.81	42.14	18.11	49.49	36.58	19.47	38.08	34.31
25	25.87	31.75	47.46	12.98	32.12	36.72	13.35	18.94	15.25
30	14.96	58.91	31.56	8.50	55.49	25.05	12.87	38.03	20.91
35	25.85	38.10	41.94	11.11	71.21	79.17	16.56	31.85	61.14
40	Nan	Nan	Nan	Nan	Nan	Nan	Nan	Nan	Nan
Max. Linear Power (kW/m)	Weibull								
	1%/h			3%/h			5%/h		
	C	M	F	C	M	F	C	M	F
5	Nan	Nan	Nan	Nan	Nan	Nan	Nan	24750.51	77.73
10	104.71	259.55	293.40	69.73	309.10	326.73	76.67	270.71	314.40
15	43.22	161.75	247.76	52.03	150.79	135.01	40.38	143.22	180.94
20	41.49	122.77	127.60	35.37	94.90	123.15	32.07	79.15	116.33
25	33.28	157.78	127.67	21.88	116.84	100.37	21.78	61.36	110.98
30	33.99	113.10	150.14	21.93	76.40	123.90	15.62	69.98	114.74
35	26.97	74.44	185.34	20.13	71.84	508.92	16.22	68.77	149.68
40	Nan	Nan	Nan	Nan	Nan	Nan	Nan	Nan	Nan

Table A.12: The Euclidean distance between the fragmentation study calculations and the Coindreau et al. [23] empirical correlation at 40 MWd/kgU.

Max. Linear Power (kW/m)	Uniform								
	1%/h			3%/h			5%/h		
	C	M	F	C	M	F	C	M	F
5	Nan	Nan	Nan	Nan	Nan	Nan	Nan	Nan	Nan
10	234.74	229.98	131.30	111.42	123.58	77.71	88.69	110.83	73.19
15	57.75	81.50	68.93	40.30	76.84	59.13	32.28	56.64	50.16
20	42.83	68.57	67.44	37.03	77.74	59.94	36.77	60.12	57.27
25	37.39	43.98	69.11	18.61	57.14	58.02	22.96	26.29	26.51
30	14.02	108.30	42.34	16.91	109.03	43.37	31.31	149.56	21.12
35	Nan	Nan	Nan	Nan	Nan	Nan	Nan	Nan	Nan
40	Nan	Nan	Nan	Nan	Nan	Nan	Nan	Nan	Nan
Max. Linear Power (kW/m)	Weibull								
	1%/h			3%/h			5%/h		
	C	M	F	C	M	F	C	M	F
5	Nan	Nan	Nan	Nan	Nan	Nan	Nan	40903.05	131.64
10	178.61	438.16	496.23	120.61	522.53	552.08	135.25	458.09	531.76
15	72.78	258.90	401.84	84.24	243.95	222.39	66.05	231.65	296.95
20	61.75	186.26	196.33	53.20	145.92	192.54	48.97	124.26	182.49
25	46.16	218.27	212.76	33.19	180.01	153.50	35.68	89.08	163.74
30	51.02	150.66	186.98	32.04	70.16	139.15	20.60	86.73	218.83
35	Nan	Nan	Nan	Nan	Nan	Nan	20.90	Nan	Nan
40	Nan	Nan	Nan	Nan	Nan	Nan	Nan	Nan	Nan

Table A.13: The Euclidean distance between the fragmentation study calculations and the Walton and Matheson [125] empirical correlation at rise to power.

Max. Linear Power (kW/m)	Uniform								
	1%/h			3%/h			5%/h		
	C	M	F	C	M	F	C	M	F
5	Nan	Nan	Nan	Nan	Nan	Nan	Nan	Nan	Nan
10	0.16	0.20	0.00	0.00	0.02	0.12	0.00	0.01	0.15
15	0.23	0.54	0.00	0.16	0.36	0.00	0.06	0.14	0.05
20	0.70	1.56	0.26	0.22	0.79	0.05	0.10	0.48	0.00
25	0.50	1.06	0.68	0.11	0.66	0.15	0.04	0.27	0.04
30	0.79	5.33	0.65	0.10	1.62	0.03	0.11	1.24	0.00
35	1.29	1.95	1.80	0.38	0.90	0.62	0.38	1.70	0.30
40	2.03	5.28	0.12	0.62	2.84	1.40	0.95	2.57	0.95
Max. Linear Power (kW/m)	Weibull								
	1%/h			3%/h			5%/h		
	C	M	F	C	M	F	C	M	F
5	Nan	Nan	Nan	Nan	Nan	Nan	Nan	0.01	0.24
10	0.07	1.32	1.33	0.01	1.44	1.56	0.01	0.80	0.00
15	0.86	4.00	4.23	0.55	2.81	1.33	0.60	1.56	0.25
20	1.24	4.88	3.68	0.42	2.37	2.25	0.11	1.13	0.07
25	1.31	9.73	6.13	0.29	4.66	2.13	0.11	0.98	0.04
30	1.76	9.92	10.33	0.29	4.85	4.52	0.09	1.95	0.54
35	2.12	15.30	14.57	0.56	7.44	10.08	0.27	4.85	0.89
40	3.98	21.69	21.18	1.19	10.51	16.69	1.04	4.60	1.21

Table A.14: The Euclidean distance between the fragmentation study calculations and the Walton and Matheson [125] empirical correlation at 10 MWd/kgU.

Max. Linear Power (kW/m)	Uniform								
	1%/h			3%/h			5%/h		
	C	M	F	C	M	F	C	M	F
5	Nan	Nan	Nan	Nan	Nan	Nan	Nan	Nan	Nan
10	13.37	13.54	6.25	5.43	6.50	2.77	4.30	5.68	2.48
15	2.24	4.25	1.91	1.64	3.61	1.43	1.16	1.75	0.88
20	2.14	12.21	1.95	1.05	3.14	1.08	0.78	2.15	0.63
25	0.97	1.99	1.75	0.37	1.41	0.69	0.21	0.56	0.02
30	0.95	5.84	0.83	0.16	1.97	0.12	0.20	1.49	0.01
35	1.21	3.25	1.66	0.29	1.65	0.53	0.28	2.82	0.41
40	1.46	4.42	1.33	0.40	1.88	1.34	0.50	1.79	0.12
Max. Linear Power (kW/m)	Weibull								
	1%/h			3%/h			5%/h		
	C	M	F	C	M	F	C	M	F
5	Nan	Nan	Nan	Nan	Nan	Nan	Nan	4399.97	11.79
10	8.42	30.01	33.22	5.80	35.14	37.30	7.11	30.52	35.59
15	4.37	18.02	24.24	4.07	15.22	11.19	3.30	14.10	15.61
20	3.49	12.10	10.66	1.83	7.32	8.25	1.85	5.97	7.43
25	2.29	15.29	10.20	0.78	8.25	4.67	0.41	3.57	5.14
30	2.08	11.12	11.72	0.40	5.62	5.45	0.21	4.08	4.67
35	1.81	13.88	15.06	0.42	6.67	8.73	0.28	4.61	7.86
40	2.80	20.06	15.74	0.66	7.10	9.88	0.45	6.22	8.12

Table A.15: The Euclidean distance between the fragmentation study calculations and the Walton and Matheson [125] empirical correlation at 20 MWd/kgU.

Max. Linear Power (kW/m)	Uniform								
	1%/h			3%/h			5%/h		
	C	M	F	C	M	F	C	M	F
5	Nan	Nan	Nan	Nan	Nan	Nan	Nan	Nan	Nan
10	47.49	47.46	25.03	21.81	24.44	13.42	17.07	21.76	12.43
15	10.38	16.80	11.57	7.42	15.23	9.59	5.50	8.27	7.47
20	8.29	14.66	11.93	5.44	15.22	9.35	5.38	11.40	8.06
25	6.60	9.49	12.41	2.78	8.82	7.74	3.23	4.71	2.72
30	4.19	19.89	8.70	1.95	10.48	3.76	2.40	10.12	2.73
35	4.96	12.03	8.58	2.56	10.37	8.85	3.40	12.89	7.87
40	7.58	36.65	21.03	4.03	12.23	22.50	3.76	18.18	90.15
Max. Linear Power (kW/m)	Weibull								
	1%/h			3%/h			5%/h		
	C	M	F	C	M	F	C	M	F
5	Nan	Nan	Nan	Nan	Nan	Nan	Nan	10430.02	30.82
10	36.25	96.23	107.70	23.65	113.62	120.27	26.77	99.23	115.41
15	15.38	59.30	87.13	15.95	53.74	45.15	13.93	49.87	61.25
20	13.28	42.88	42.29	11.37	30.53	38.36	9.20	25.82	35.76
25	9.92	53.88	41.03	5.71	36.26	27.82	5.24	18.02	30.72
30	9.77	37.78	45.16	4.52	23.69	31.44	3.74	20.63	31.69
35	9.51	39.69	49.83	4.06	24.69	39.11	3.32	17.61	36.15
40	10.26	59.04	58.53	4.50	22.50	17.50	4.41	18.79	10.11

Table A.16: The Euclidean distance between the fragmentation study calculations and the Walton and Matheson [125] empirical correlation at 30 MWd/kgU.

Max. Linear Power (kW/m)	Uniform								
	1%/h			3%/h			5%/h		
	C	M	F	C	M	F	C	M	F
5	Nan	Nan	Nan	Nan	Nan	Nan	Nan	Nan	Nan
10	81.61	81.39	44.44	38.42	42.70	24.91	30.42	38.05	23.25
15	20.82	29.59	22.49	13.20	27.38	18.90	11.37	19.73	15.43
20	15.94	26.32	23.24	10.17	28.15	19.39	10.77	21.40	17.62
25	14.50	17.55	24.98	6.64	17.11	18.44	6.71	9.78	6.84
30	7.95	32.89	15.67	3.99	28.82	11.39	6.23	19.27	9.09
35	13.46	20.35	21.75	5.33	38.40	37.84	8.05	15.67	27.27
40	Nan	Nan	Nan	Nan	Nan	Nan	Nan	Nan	Nan
Max. Linear Power (kW/m)	Weibull								
	1%/h			3%/h			5%/h		
	C	M	F	C	M	F	C	M	F
5	Nan	Nan	Nan	Nan	Nan	Nan	Nan	15854.12	48.42
10	63.24	160.25	180.74	41.56	190.52	201.51	46.08	166.67	193.68
15	26.31	99.92	150.44	31.26	91.87	80.31	24.25	87.28	108.16
20	24.56	73.74	74.99	20.21	55.38	70.56	18.17	45.81	66.30
25	18.84	92.49	72.93	11.53	65.67	53.93	10.98	33.76	59.59
30	18.41	65.04	83.84	10.74	41.65	65.01	7.17	37.47	58.90
35	13.87	41.48	100.89	9.83	38.46	268.20	7.28	36.36	78.88
40	Nan	Nan	Nan	Nan	Nan	Nan	Nan	Nan	Nan

Table A.17: The Euclidean distance between the fragmentation study calculations and the Walton and Matheson [125] empirical correlation at 40 MWd/kgU.

Max. Linear Power (kW/m)	Uniform								
	1%/h			3%/h			5%/h		
	C	M	F	C	M	F	C	M	F
5	Nan	Nan	Nan	Nan	Nan	Nan	Nan	Nan	Nan
10	117.25	115.33	64.10	54.46	61.08	36.72	43.25	54.57	34.41
15	30.24	42.62	33.90	20.79	39.75	28.74	16.59	28.91	23.81
20	23.61	37.74	35.07	19.75	41.54	30.10	19.39	31.79	27.99
25	21.15	24.56	37.15	9.80	31.06	30.25	12.02	13.86	12.71
30	8.02	65.17	23.69	9.27	62.17	23.46	17.30	85.90	10.86
35	Nan	Nan	Nan	Nan	Nan	Nan	Nan	Nan	Nan
40	Nan	Nan	Nan	Nan	Nan	Nan	Nan	Nan	Nan
Max. Linear Power (kW/m)	Weibull								
	1%/h			3%/h			5%/h		
	C	M	F	C	M	F	C	M	F
5	Nan	Nan	Nan	Nan	Nan	Nan	Nan	21044.55	65.47
10	89.18	224.16	253.23	59.35	266.82	282.09	67.20	233.61	271.36
15	38.88	140.31	213.92	44.37	130.31	115.93	34.77	123.78	155.57
20	34.21	104.65	108.09	28.56	79.81	103.58	26.07	67.50	97.69
25	26.28	128.12	122.41	17.90	102.24	83.77	18.63	49.61	89.27
30	29.95	92.80	111.62	17.51	41.20	80.01	10.77	50.46	125.40
35	Nan	Nan	Nan	Nan	Nan	Nan	11.66	Nan	Nan
40	Nan	Nan	Nan	Nan	Nan	Nan	Nan	Nan	Nan

APPENDIX B

DERIVATION OF SPHERICITY AND VOLUME EQUATIONS

In the Jernkvist and Massih [53] axial relocation model, used as the basis of further developments in axial relocation modeling in this work, the sphericity and volume of the fragments and pulvers play an important role in determining the effective packing fraction (ϕ) of the binary mixture. In the model, fragments are assumed to be prismatic with a characteristic length given by l_f and pulvers are assumed to be octahedral with a default characteristic length given by l_p. In Chapter 4 values were given for the sphericity and equations for the volume of these particle types. Here, the derivation of these values are provided for completeness.

Wadell [122] defined sphericity as a measure of how closely the shape of an object (in this case particles) represent a sphere. Non-spherical shapes have a sphericity < 1.0. The mathematical definition of sphericity is given by the ratio of the surface area of a sphere that has the same volume of the particle of interest to the surface area of the particle:

$$\psi = \frac{SA_s}{SA_p} \tag{B.1}$$

where SA_s is the surface area of the sphere with the same volume of the particle and SA_p is the surface area of the particular particle. Starting with surface area one can relate it to the volume of an arbitrary particle via:

$$SA_s = 4\pi r^2 \implies SA_s^3 = 4^3\pi^3 r^6 = 4\pi 3^2 \left(\frac{4^2\pi^2 r^6}{3^2}\right) = 36\pi \left(\frac{4\pi r^3}{3}\right)^2 \tag{B.2}$$

where r is the radius of the sphere. The term $\left(\frac{4\pi r^3}{3}\right)$ is the volume of a sphere. In order to have the surface area of the sphere have the same volume of the particle of interest one

simply replaces the volume term with the volume of the particle (V_p):

$$36\pi V_p^2 \implies SA_s = 36^{1/3}\pi^{1/3}V_p^{2/3} = \pi^{1/3}\left(6V_p\right)^{2/3} \tag{B.3}$$

This results in the equation for sphericity to become

$$\psi = \frac{\pi^{1/3}\left(6V_p\right)^{2/3}}{SA_p} \tag{B.4}$$

For a prismatic particle, the shape is a triangular prism those height is equal to the length of the sides of the equilateral triangular face. This length is the characteristic length of the particle. For this type of particle the volume is given by:

$$V_p = \frac{1}{2}bhL \tag{B.5}$$

where b is the length of the base of the triangular surfaces, h is the perpendicular height of the triangular surface, and L is the height of the prism. Here $b{=}\frac{\sqrt{3}}{2}l_f$ and $h{=}L{=}l_f$. Therefore,

$$V_p = \frac{\sqrt{3}}{4}l_f^3 = 0.4330l_f^3 \tag{B.6}$$

as given in section 4. The surface area of such a particle is given by:

$$SA_p = 2\frac{1}{2}bh + 3L^2 = \frac{\sqrt{3}}{2}l_f^2 + 3l_f^2 = \left(\frac{\sqrt{3}}{2} + 3\right)l_f^3 \tag{B.7}$$

Then subbing Equation B.6 and Equation B.7 into Equation B.4 one obtains the sphericity of fragments used in the axial relocation model:

$$\psi = \frac{\pi^{1/3}\left(6\left(0.4330l_f^3\right)\right)^{2/3}}{\left(\frac{\sqrt{3}}{2} + 3\right)l_f^3} = 0.716 \tag{B.8}$$

Similarly, for octahedral particles (pulvers) the volume is four times that of a tetrahedron. A tetrahedron, begin a pyramid with a triangular base has volume given by the area of the base (equilateral triangle) multiplied by the perpendicular height of the pyramid.

$$V_p = 4\frac{bhH}{3} \tag{B.9}$$

where b is the length of the side of the triangular base, h is the perpendicular height of the triangular base and H is the perpendicular height of the tetrahedron. Here $b=\frac{\sqrt{3}}{2}l_f$, $h=l_f$, and $H=\frac{\sqrt{6}}{3}l_f$. Therefore,

$$V_p = \frac{\sqrt{2}}{3}l_f^3 = 0.4714 l_f^3 \tag{B.10}$$

The surface area of an octahedral particle is given by:

$$SA_p = 2\sqrt{3}l_f^2 \tag{B.11}$$

Finally, upon subbing Equation B.10 and Equation B.11 into Equation B.4 one obtains the sphericity of pulvers used in the axial relocation model:

$$\psi = \frac{\pi^{1/3}\left(6\frac{\sqrt{2}}{3}l_f^3\right)^{2/3}}{2\sqrt{3}l_f^2} = 0.846 \tag{B.12}$$

APPENDIX C

MATERIAL AND BEHAVIOR MODELS

Throughout this dissertation many Bison simulations were performed. Each chapter focused on simulations related to improvements in the area of which the Chapters are focused. Therefore, the details of the computational models described in those Chapters tend to focus on the models specifically relevant to the phenomenon being explored (i.e., fragmentation, axial relocation, oxidation, cladding rupture). However, to support fuel performance analysis, which in this work focuses on the solving of the stress divergence and heat conduction partial differential equations additional models are necessary. This Appendix summarizes the MOOSE objects used in the Bison analyses completed throughout this dissertation. The details of these objects and the references from which they are obtained are readily available in the Bison online documentation (see Bison Documentation). To prevent duplication of these details, the models are tabulated in Table C.1. The table consists of columns containing a description of what the model does, the MOOSE object type, the model name (as a hyperlink to the appropriate Bison theory and user page), and a list of problems in this dissertation in which the models were used. Models developed and added to Bison as part of this work (some with funding from the DOE programs NEAMS and CASL) have their row colored cyan. Models that already existed but needed to be modified to support the studies in this work are colored green.

A brief glossary of the MOOSE objects highlighted in the table is provided. Some of the definitions (e.g., AuxVariables) are defined as they typically are used in Bison. Note that many other MOOSE objects exist for a wide variety of other physics and computational capabilities. These have been omitted from the glossary since they are not used in this work.

Action: A MOOSE object used to simply input file syntax for users. Typically creates numerous other MOOSE objects behind the scenes.

AuxKernels: MOOSE objects that act upon AuxVariables. Usually compute field variables used for output visualization or in other down stream calculations (e.g., stress, strain, flux)

AuxScalarKernels: MOOSE objects that act on scalar variables. These are used extensive in the Layered1D and Layered2D formulations to compute the reference residual contrtibutions.

AuxVariables: Variables that hold the outputs calculated by AuxKernels. Variable types are typically nodal or elemental. Nodal variables store values at the nodes. Elemental variables store a single value per element.

BCs: MOOSE objects that specify the boundary conditions on the finite element domain. Can be of the nodal or integrated type where nodal BCs set a value on the boundary (e.g., Dirichlet) and integrated BCs apply a value to the surface (e.g., a flux)

Controls: A MOOSE system that allows other MOOSE objects to be disabled and enabled based on specified criteria. An example turning on and off boundary conditions at specified times.

Dampers: MOOSE objects that can be applied to primal variables help limit the change in the primary variable over a linear iteration.

Executioner: A MOOSE object that defines the convergence tolerances, type of analysis (steady or transient), minimum and maximum timestep sizes, the start and end times of the calculation, the finite element quadrature rule, and a timestepper that defines how the timestep evolves.

Functions: MOOSE objects that allow the definition of constant or spatial or temporal function for use in other MOOSE objects (e.g., PiecewiseLinear, Parsed).

GlobalParams: A MOOSE object that allows the specification of common Input-Parameters used in a variety of MOOSE Objects to reduce input file length. The GlobalParams can be overwritten locally in specific MOOSE objects.

ICs: MOOSE objects that specify the initial condition of a Variable or AuxVariable.

Kernels: MOOSE objects that operate on primal variables. These are the operators found in partial differential equations (e.g., time derivatives, Laplacian, etc.).

Materials: MOOSE objects that are evaluated at the quadrature points within the finite element domain. Typically, as the name implies, these objects are material properties of the materials used in the analysis (e.g., thermal conductivity, elastic constants).

Mesh: A MOOSE object that defines the finite element domain used for a particular analyses. These meshes can be generated using external third party software (e.g., Cubit) or built internally using mesh generators.

Outputs A set of MOOSE objects used to define the a variety of outputs available for postprocessing and creation of figures. Examples include ExodusII files (for creating contour plots and movies) as well as CSV files for scatter and line plots. Another option is the creation of Checkpoint files to enable restarting of a simulation if it fails or to follow a base irradiation by a transient such as a LOCA.

Postprocessors: MOOSE objects that return a single scalar value for use in other MOOSE objects or for creation of line plots. Examples include rod internal pressure and fission gas release.

Problem: A MOOSE object that defines the coordinate system for the analysis (i.e., Cartesian, 2D-RZ) as well as other details related to partitioning of the mesh in parallel and some methods of solve convergence criteria.

UserObjects: The most flexible MOOSE object from a developers perspective. These are designed to perform a wide variety of calculations at the nodes, elements, or just a general lookup type calculation. This work resulted in the development of many UserObjects.

Variables: The MOOSE object that defines the names, order, and family of the primal variables.

VectorPostprocessors (VPPs): A family of MOOSE objects to provide vectors of scalar variables in space and over time. Examples where VectorPostprocessors are used include obtaining a radial temperature profile or an end of life cladding diameter.

Table C.1: Other models and MOOSE objects used in analyses in this work. Underlined model names are hyperlinks to associated online documentation pages in the electronic version of this dissertation. Cyan colored rows denote models either fully developed as part of this work and green colored rows denote models modified to accommodate new features introduced by this work.

Model Name	Model Type	Brief Description	Chapters used[†]
AxialRelocation	Action	An object used to create all of the materials, AuxVariables, AuxKernels, Postprocessors, and UserObjects necessary for simulating fuel relocation during a LOCA	AR, O, CR, AC
AxialRelocationUserObject	UserObject	The object that tracks fuel movement to lower layers in a Layered1D or Layered2D simulation	AR, O, CR, AC
BoundingValueNodalDamper	Damper	An object that ensures that the calculated value of a primary variable in a nonlinear iteration remains between the upper and lower bounds provided.	FF, AR, O, CR, AC
Burnup	Action	An object that creates the necessary functions, AuxVariables, and AuxKernels to compute the evolution of burnup as a function of irradiation including the radial power factor. The local fission rate is also computed.	FF, AR, O, CR, AC
Checkpoint	Output	An object to output checkpoint files to be used when restarting or recovering a simulation.	AR, O, CR, AC
ChromiumCreepUpdate	Material	A thermal and irradiation creep model for pure chromium.	AC
ChromiumElasticityTensor	Material	Computes the isotropic Young's modulus and Poisson's ratio for pure chromium.	AC

Continued on next page

Table C.1 – *Continued from previous page*

Model Name	Model Type	Brief Description	Chapters used[†]
Oxidation	Material	Computes the weight gain and scale thickness due to oxidation of pure chromium.	AC
ChromiumPlasticityUpdate	Material	Computes the yield stress and permanent deformation associated with instantaneous plasticity for pure chromium.	AC
ChromiumThermal	Material	Computes the thermal conductivity and specific heat of pure chromium as a function of temperature.	AC
ChromiumThermalExpansionEigenstrain	Material	Computes the instantaneous thermal expansion coefficient for pure chromium from mean values.	AC
CladdingAxialPressureFunction	Function	Computes the axial pressure that needs to be applied to the cladding for Layered1D and Layered2D simulations due to the plenum and coolant pressures.	AR, O, CR, AC
ComputeFiniteStrainElasticStress	Material	A stress calculator that computes finite deformation due to large strain calculations in Cartesian geometries.	FF, AR, O, CR, AC
CompositeFunction	Function	Multiplies multiple functions together.	FF, AR, O, CR, AC

Continued on next page

Table C.1 – *Continued from previous page*

Model Name	Model Type	Brief Description	Chapters used[†]
ComputeIsotropicElasticityTensor	Material	An object that computes the elasticity tensor of an isotropic material given any two elastic constants (i.e., Young's modulus, Poisson's ratio, shear modulus, bulk modulus, or Lamé's constant).	FF, AR, O, CR, AC
ComputeMultipleInelasticStress	Material	A stress calculate the computes large deformation including contributions from inelastic models such as creep and instantaneous plasticity.	FF, AR, O, CR, AC
ComputeThermalExpansionEigenstrain	Material	Computes the change in volume due to a constant instantaneous thermal expansion coefficient.	FF, AR, O, B
Contact	Action	An object that creates all of the necessary AuxVariables, AuxKernels, and Constraints necessary to enforce mechanical contact between surfaces.	FF, AR, O, CR, AC
ConvectiveFluxBC	BC	A flux boundary condition computed due to convection as a function of surface temperature, far temperature, and ramping rate.	FF
CoolantChannel	Action	An object that creates the necessary Materials, UserObjects, and BCs for the one-dimensional coolant channel on the outside of fuel rods.	AR, O, CR, AC
CSV	Output	An object used to output all of the Postprocessors or individual VectorPostprocessors to comma separated value files.	FF, AR, O, CR, AC

Continued on next page

Table C.1 – *Continued from previous page*

Model Name	Model Type	Brief Description	Chapters used[†]
Density	Material	Computes the evolving density of a material due to dimensional changes given an initial density.	FF, AR, O, CR, AC
DirichletBC	BC	A boundary condition that applies a constant value of a variable at a boundary or boundaries of a domain.	FF, AR, O, CR, AC
ElementAverageValue	Postprocessor	An object that loops over all elements in the specified block (or mesh if no block is specified) and computes the average value of the variable (Aux or primal) supplied.	FF, AR, O, CR, AC
ElementIntegralFisGasBoundarySifgrs	Postprocessor	An object that outputs the total fission gas content located a grain boundaries in moles when using the Sifgrs fission gas model.	FF
ElementIntegralFisGasGeneratedSifgrs	Postprocessor	An object that outputs the total fission gas content generated within the fuel in moles when using the Sifgrs fission gas model.	FF
ElementIntegralFisGasGrainSifgrs	Postprocessor	An object that outputs the total fission gas content located inside grains in moles when using the Sifgrs fission gas model.	FF
ElementIntegralFisGasReleasedSifgrs	Postprocessor	An object that outputs the total fission gas content released from the fuel in moles when using the Sifgrs fission gas model.	FF
ElementIntegralPower	Postprocessor	Computes the total power supplied to the fuel. Typically used as cross check on the input power.	FF, AR, O, CR, AC

Continued on next page

Table C.1 – *Continued from previous page*

Model Name	Model Type	Brief Description	Chapters used[†]
ElementExtremeValue	Postprocessor	Loops over the supplied block (or mesh if no block specified) and returns the extreme value type selected (maximum or minimum) for a given variable.	FF, AR, O, CR, AC
Exodus	Output	An output object used to create contour plots.	AR, O, CR, AC
FastNeutronFluenceAux	AuxKernel	An object used to compute the fast neutron fluence for use in cladding creep models. This is the time integrated fast neutron flux.	FF, AR, O, CR, AC
FastNeutronFluxAux	AuxKernel	An object used to compute the fast neutron flux as a function of power.	FF, AR, O, CR, AC
FeCrAlCladdingFailure	Material	A failure model for FeCrAl.	AC
FeCrAlCreepUpdate	Material	A thermal creep model for FeCrAl.	AC
FeCrAlElasticityTensor	Material	Commputes the temperature dependent elasticity tensor for FeCrAl.	AC
FeCrAlOxidation	Material	Computes normal operating and high temperature mass gain and scale thickness formation due to oxidation of FeCrAl	AC
FeCrAlPlasticityUpdate	Material	Computes the temperature dependentt yield stress and permanent deformation due to instantaneous plasticity of FeCrAl given a linear or constant hardening slope.	AC

Continued on next page

Table C.1 – *Continued from previous page*

Model Name	Model Type	Brief Description	Chapters used[†]
FeCrAlPowerLawHardeningStressUpdate	Material	Computes temperature dependent permanent deformation following a power law formulation for FeCrAl.	AC
FeCrAlThermal	Material	Computes the thermal conductivity and specific heat of FeCrAl.	AC
FeCrAlThermalExpansionEigenstrain	Material	Computes the instantaneous thermal expansion coefficient for FeCrAl.	AC
FeCrAlVolumetricSwellingEigenstrain	Material	Computes the estimiated volume change due to irradiation-induced swelling of FeCrAl.	AC
FGRPercent	Postprocessor	An object that reports the total fission gas released as a percentage of generated.	FF, AR, O, CR, AC
FileMeshGenerator	MeshGenerator	An mesh generator that reads in an external mesh file. Typically in the ExodusII format.	CR, AC
FunctionAux	AuxKernel	An object that creates a sets the value of an AuxVariable to the results of input MOOSE function.	FF, AR, O, CR, AC
FunctionDirichletBC	BC	A boundary condition that applies a value to a boundary or boundaries of a domain that varies as prescribed by a MOOSE function.	FF, AR, O, CR, AC
FunctionValuePostprocessor	Postprocessor	An object that reports a single value for a function as a postprocessor. Typically used for time varying functions.	FF, AR, O, CR, AC

Continued on next page

Table C.1 – *Continued from previous page*

Model Name	Model Type	Brief Description	Chapters used[†]
GeneralizedPlaneStrainReferenceResidual	ScalarAux Kernel	Computes the reference residual to be used for the out-of-plane strains in Layered1D and Layered2D geometries when checking convergence of the scalar variables when ReferenceResidualProblem is used.	FF, AR, O, CR, AC
GrainRadiusAux	AuxKernel	Computes the grain growth in UO_2 as a function of temperature.	FF, AR, O, CR, AC
HeatConduction	Kernel	Computes the residual and Jacobian terms for the gradient of thermal conductivity term in the heat conduction equation.	FF, AR, O, CR, AC
HeatConductionMaterial	Material	Provides a thermal conductivity and specific heat to a block. Can be constant or a function of temperature.	FF, AR, O, CR, AC
HeatConductionTimeDerivative	Kernel	Computes the residual and Jacobian terms for the time-dependent term in the heat conduction equation.	FF, AR, O, CR, AC
HighBurnupStructureFormation	Material	A model to compute the local volume fraction of UO_2 that has restructured into the high burnup structure.	AR, O, CR, AC
InternalVolume	Postprocessor	An object used to compute the volume bounded by a specified boundary.	FF, AR, O, CR, AC

Continued on next page

Table C.1 – *Continued from previous page*

Model Name	Model Type	Brief Description	Chapters used[†]
IterationAdaptiveDT	Timestepper	A flexible timestepper that grows or shrinks the timestep based upon convergence as well as allow a function and or postprocessor to be supplied to force certain times or timestep size	FF, AR, O, CR, AC
Layered1DAction	Action	An object that creates the primal displacement variables, stress and strain output AuxKernels, strain calculator, and stress divergence kernels for mechanical analyses for Layered1D geometries.	AR, O, CR, AC
Layered1DFuelPinGeometry	UserObject	An object that reads input geometric information from a Layered1D mesh for use in other objects that depend upon geometric quantities.	AR, O, CR, AC
Layered1DMeshGenerator	Mesh	An object that enables the creation of Layered1D geometries. Numerous options and customization is available including interior liners and coatings.	AR, O, CR, AC
Layered2DAction	Action	An object that creates the primal displacement variables, stress and strain output AuxKernels, strain calculator, and stress divergence kernels for mechanical analyses for Layered2D geometries.	FF, AR, O, CR, AC
Layered2DFuelPinGeometry	UserObject	An object that reads input geometric information from a Layered2D mesh for use in other objects that depend upon geometric quantities.	FF, AR, O, CR, AC

Continued on next page

Table C.1 – *Continued from previous page*

Model Name	Model Type	Brief Description	Chapters used[†]
Layered2DMeshGenerator	Mesh	An object that enables the creation of Layered2D geometries. Numerous options and customization is available including interior liners and coatings.	FF, AR, O, CR, AC
LayeredAverage	UserObject	An object that computes the element average of a variable over user-defined layers.	AR, O, CR, AC
LayeredAxialRelocationEigenstrain	UserObject	Used with the axial relocation algorithm to compute the eigenstrain necessary to move crumbled layers towards the cladding at each layer. An eigenstrain of zero indicates that the mesh is not moved as the layer has not crumbled. This strain is irreversible.	AR, O, CR, AC
LayeredElementIntegralFisGasBoundarySifgrsPostprocessor	Postprocessor	An object that outputs the total fission gas content located a grain boundaries in moles when using the Sifgrs fission gas model for Layered1D or Layered2D geometries.	AR, O, CR, AC
LayeredElementIntegralFisGasGeneratedSifgrsPostprocessor	Postprocessor	An object that outputs the total fission gas produced in moles when using the Sifgrs fission gas model for Layered1D or Layered2D geometries.	AR, O, CR, AC
LayeredElementIntegralFisGasGrainSifgrsPostprocessor	Postprocessor	An object that outputs the total fission gas content located in the grains in moles when using the Sifgrs fission gas model when using Layered1D or Layered2D geometries.	AR, O, CR, AC

Continued on next page

Table C.1 – *Continued from previous page*

Model Name	Model Type	Brief Description	Chapters used[†]
LayeredElementIntegralFisGasReleasedSifgrsPostprocessor	Postprocessor	An object that outputs the total fission gas content released in moles when using the Sifgrs fission gas model when using Layered1D or Layered2D geometries.	AR, O, CR, AC
LayeredNodalExtremeValue	UserObject	An object that returns the extreme value (e.g. maximum or minimum) of a variable in each layer defined by the user.	AR, O, CR, AC
LayeredInternalVolume	UserObject	Computes the internal volume encapsulated by a boundary over user-defined layers.	AR, O, CR, AC
LayeredInternalVolumePostprocessor	Postprocessor	Computes the total internal volume in a simulation using a Layered1D or Layered2D representation of the geometry.	AR, O, CR, AC
LayeredPlenumTemperature	Action	Computes the gas temperature in the fuel-to-cladding gap in each user-defined layer.	AR, O, CR, AC
LayeredSideAverage	UserObject	Computes the average value on a boundary of a variable over user-defined layers.	AR, O, CR, AC
LayeredSideAverageValuePostprocessor	Postprocessor	Computes the average value on a boundary of a variable for Layered1D or Layered2D geometries.	AR, O, CR, AC
LayeredVariableIntegral	UserObject	Computes the integral some of a variable over user-defined layers.	AR, O, CR, AC
LineValueSampler	VPP	An object that outputs the value of a variable along a line with the given starting and end points as well as the total number of points to sample.	AR, O, CR, AC

Continued on next page

Table C.1 – *Continued from previous page*

Model Name	Model Type	Brief Description	Chapters used[†]
MaterialRealAux	AuxKernel	Populates an elemental AuxVariable with the average value of the specified material property at each finite element.	FF, AR, O, CR, AC
MaterialTensorIntegral	Postprocessor	A postprocessor that performs an volume integral of a material property on a block. This can be used to verify the computation of the out-of-plane scalar strain variables used in Layered1D or Layered2D formulations.	FF
MaterialTimeStepPostprocessor	Postprocessor	An object that queries the inelastic increments (i.e., creep and/or plasticity) relative to the maximum inelastic increment allowed on the specified blocks to limit the timestep size.	AR, O, CR, AC
MaxIncrement	Damper	An object that limits the increment in the specified variable during a nonlinear iteration. Smaller values may improve convergence, but will also increase simulation run time.	FF, AR, O, CR, AC
NeutronHeatSource	Kernel	Computes the volumetric heat generation due to fission given a linear power and axial peaking factors supplied to the fuel rod.	FF, AR, O, CR, AC
NodalExtremeValue	Postprocessor	An object that returns the extreme value chosen (i.e., maximum or minimum) for a given nodal variable at each timestep.	FF, AR, O, CR, AC
NodalValueSampler	VPP	Outputs a vector of values of a specified variable along a boundary of the domain.	FF, AR, O, CR, AC

Continued on next page

Table C.1 – *Continued from previous page*

Model Name	Model Type	Brief Description	Chapters used[†]
NumNonlinearIterations	PostProcessor	Reports the total number of nonlinear iterations for each timestep.	FF, AR, O, CR, AC
ParsedFunction	Function	Defines a function that can be a function of position, time, postprocessors, other functions, scalar variables, and common mathematical functions (e.g., sin).	FF, AR, O, CR, AC
PiecewiseBilinear	Function	Creates a piece-wise bilinear function of user supplied data. Typically used in this work to create the axial peaking factors as a function of time.	FF, AR, O, CR, AC
PiecewiseConstant	Function	Creates a function that assumes a constant value between the given points. The user can specify whether the point to the left or right of the interpolated point is used.	AR, O, CR, AC
PiecewiseLinear	Function	Defines a piece-wise function with linear interpolation between provided values.	FF, AR, O, CR, AC
PlenumPressure	Action	Computes the internal pressure of nuclear fuel rods. Can account for fission gas release, refabrication, and integral fuel burnable absorbers (IFBA).	FF, AR, O, CR, AC

Continued on next page

Table C.1 – *Continued from previous page*

Model Name	Model Type	Brief Description	Chapters used[†]
Pressure	Action	An object that creates pressure boundary conditions for each of the coordinate directions on a surface. For a pressure boundary condition in one of the coordinate directions (e.g., for a tensile test) the `Pressure` BC object can be used.	FF, AR, O, CR, AC
RadialCrackCounter	VPP	Groups the total number of radial cracks in a 2D plane-strain model into user-defined bins that define the crack length ranges for the bins.	FF
Radius	AuxKernel	Computes the current radius of points on a boundary from a user-specified central axis.	AR, O, CR, AC
RandomIC	IC	Initializes a variable using randomly generated numbers using a user defined distribution.	FF
RankTwoScalarAux	AuxKernel	Extracts a specified tensor component from a supplied rank two tensor into an elemental AuxVariable.	FF, AR, O, CR, AC
ReferenceResidualProblem	Problem	Defines that convergence of the primary variables is achieved when the individual residuals are within the nonlinear convergence criteria specified in the Executioner block.	FF, AR, O, CR, AC
RodAverageBurnup	Postprocessor	Queries the burnup function created by the `Burnup` action and extracts the rod average burnup.	FF, AR, O, CR, AC
SideAverageValue	Postprocessor	Calculates the average value of the supplied variable on a specified boundary.	FF, AR, O, CR, AC

Continued on next page

Table C.1 – *Continued from previous page*

Model Name	Model Type	Brief Description	Chapters used[†]
SideDiffusiveFluxIntegral	Postprocessor	Computes the flux through a boundary due to diffusive processes of a specified variables.	FF, AR, O, CR, AC
Sifgrs	Material	A sophisticated model for the computation of fission gas behavior and swelling in UO_2 fuel.	FF, AR, O, CR, AC
SpatialUserObjectAux	AuxKernel	An object used to output the computation completed inside of a UserObject to a field variable for visualization purposes.	AR, O, CR, AC
TensorMechanicsAction	Action	Generates numerous objects behind the scenes for mechanics analysis.	FF, AR, O, CR, AC
Terminator	UserObject	An object that gracefully terminates a simulation when a specified criterion is met. This criterion is a function of one or more postprocessors in the simulation.	FF, AR, O, CR, AC
ThermalContactLWRAction	Action	An object that creates all the necessary constraints, material properties, boundary conditions, AuxVariables and AuxKernels to enforce thermal contact in LWR applications. The model accounts for gas conductance (including fission gases), solid-to-solid conductance after pellet-cladding mechanical contact, and radiation.	FF, AR, O, CR, AC

Continued on next page

Table C.1 – *Continued from previous page*

Model Name	Model Type	Brief Description	Chapters used[†]
ThermalZryDegraded	Material	Selects the appropriate material property on either side of the metal-oxide interface for thermal properties.	O
TimeExtremeValue	Postprocessor	An object that reports the chosen extreme value (maximum or minimum) of another postprocessor over time.	AR, O, CR, AC
TimePeriod	Control	An object that allows the enabling and disabling of boundary conditions and other objects over certain periods of time.	AR, O, CR, AC
TimestepSize	Postprocessor	Reports the timestep size for every converged timestep.	FF, AR, O, CR, AC
Transient	Executioner	Denotes that a transient simulation is to be solved. Typically used for pseudo-steady-state cases as well (e.g., ramping a load to steady-state).	FF, AR, O, CR, AC
UO2AxialRelocationEigenstrain	Material	Applies the necessary movement to the layers in a Layered1D or Layered2D simulation after crumbling during axial fuel relocation.	AR, O, CR, AC
UO2CreepUpdate	Material	A thermal and irradiation creep model for UO_2	FF, AR, O, CR
UO2ElasticityTensor	Material	Computes a temperature dependent elasticity tensor for UO_2. Young's modulus and Poisson's ratio are the elastic constants that are defined.	FF, AR, O, CR

Continued on next page

Table C.1 – *Continued from previous page*

Model Name	Model Type	Brief Description	Chapters used[†]
UO2Pulverization	Material	Determines whether a particular material point is deemed to have pulverized (finely fragmented) based upon the local temperature and burnup using the Turnbull [120] threshold.	AR, O, CR
UO2Thermal	Material	Computes the thermal conductivity and specific heat of UO_2 as a function of temperature, burnup, porosity, and gadolinia content.	FF, AR, O
UO2VolumetricSwellingEigenstrain	Material	Computes the change in volume of UO_2 due to solid and gaseous fission products as well as densification under the high temperature and pressure in the reactor early in life.	FF, AR, O, CR
XFEM	Action	Specifies details related to the extended finite element method.	FF, CR, AC
XFEMRankTwoTensorMarkerUserObject	UserObject	Mark elements to be cut by XFEM based on a scalar extracted from a RankTwoTensor (e.g., hoop stress).	FF, CR, AC
ZrO2ElasticityTensor	Material	Computes the elastic properties of zirconium dioxide.	O
ZrO2Thermal	Material	Computes the thermal conductivity and specific heat of zirconium dioxide as a function of temperature.	O
ZrO2ThermalExpansionEigenstrain	Material	Computes the linear strain associated with thermal expansion of zirconium dioxide.	O
ZrPhase	Material	Computes the phase of Zircaloy claddings as a function of heating rate.	AR, O, CR, AC

Continued on next page

Table C.1 – *Continued from previous page*

Model Name	Model Type	Brief Description	Chapters used[†]
ZryCladdingFailure	Material	A failure model for Zircaloy claddings. Six options are available: overstress, plastic instability, combined overstress and plastic instability, overstrain, combined overstress and overstrain, and rupture temperature.	AR, O, CR, AC
ZryCreepLimbackHoppeUpdate	Material	A thermal and irradiation creep model for Zircaloy claddings under normal operating conditions.	FF
ZryDegradedElasticityTensor	Material	Selects the appropriate material property on either side of the metal-oxide interface for the elasticity tensor.	O
ZryDegradedThermalExpansionEigenstrain	Material	Selects the appropriate material property on either side of the metal-oxide interface for thermal expansion.	O
ZryCreepLOCAErbacherLimbackHoppeUpdate	Material	A thermal and irradiation creep model for Zircaloy claddings under LOCA conditions.	AR, O, CR, AC
ZryIrradiationGrowthEigenstrain	Material	Computes the dimensional changes due to irradiation of Zircaloy claddings. Axial growth occurs with a shrinkage in the radial and azimuthal directions, resulting in a total conservation of volume.	FF, AR, O, CR, AC

Continued on next page

Table C.1 – *Continued from previous page*

Model Name	Model Type	Brief Description	Chapters used[†]
ZryOxidation	Material	A model that computes the mass gain and oxide scale thickness of Zircaloy claddings under all operating conditions. Note that certain commercial claddings (e.g., M5 and Zirlo) are not present in this model due to the fact that the oxidation kinetics of these materials are not publically available.	FF, AR, O, CR, AC
ZryThermal	Material	Computes the thermal conductivity and specific heat of Zircaloy claddings as a function of temperature.	FF, AR, O, CR, AC
ZryThermalExpansionMATPROEigenstrain	Material	Computes the volumetric change due to thermal expansion as a function of temperature using the model from the MATPRO [100] library for Zircaloy claddings.	FF, AR, O, CR, AC

[†]FF: Fuel Fragmentation; AR: Axial Relocation; O: Oxidation; CR: Cladding Rupture; AC: Advanced Cladding

APPENDIX D

SAMPLE INPUT FILE

Below is a sample Bison input for the IFA-650.4 LOCA transient (part2 of the analysis) that uses the overstrain failure criterion, the Barani fragmentation models for large fragments and a axial mesh density of thirty layers. Parameters with around the parameter names are varied as part of the sensitivity study.

Listing D.1: Sample Input

```
[GlobalParams]
  density = 10452.96
  initial_porosity = 0.048
  order = SECOND
  family = LAGRANGE
  displacements = disp_x
  temperature = temperature
  energy_per_fission = 3.2e-11 #J/fission
[]

[Problem]
  type = ReferenceResidualProblem
  coord_type = RZ
  reference_vector = 'ref'
  extra_tag_vectors = 'ref'
  acceptable_multiplier = 10
  restart_file_base = '../IFA_650_4_part1_checkpoint_cp/LATEST'
[]

[Mesh]
  [layered1D_mesh]
    type = Layered1DMeshGenerator
    slices_per_block = 30
    pellet_outer_radius = 4.565e-3
    clad_gap_width = 0.085e-3
    clad_thickness = 0.725e-3
    fuel_height = 0.480
    plenum_height = 0.291185
    pellet_mesh_density = customize
    clad_mesh_density = customize
    nx_p = 11
    nx_c = 5
```

```
  []
  patch_update_strategy = auto
  partitioner = centroid
  centroid_partitioner_direction = y
[]

[Variables]
  [disp_x]
  []
  [temperature]
    initial_condition = 295.0
  []
[]

[Functions]
  [power_history]
    type = PiecewiseLinear
    data_file = ../power_history.csv
    scale_factor = 1.0
    format = columns
  []
  [axial_peaking_factors]
    type = PiecewiseBilinear
    data_file = ../axial_peaking_factors.csv
    axis = 1
    scale_factor = 1
  []
  [pressure_ramp]
    type = PiecewiseLinear
    data_file = ../coolant_pressure.csv
    scale_factor = 1
    format = columns
  []
  [average_htc]
    type = PiecewiseLinear
    data_file = ../average_coolant_htc.csv
    format = columns
    scale_factor = 1
  []
  [q]
    type = CompositeFunction
    functions = 'power_history axial_peaking_factors'
  []
  [forced_times]
    type = PiecewiseLinear
    data_file = ../timestep_limiting.csv
    scale_factor = 1
    format = columns
  []
  [heat_sink_temperature]
    type = PiecewiseBilinear
    data_file = ../heater_temp.csv
    scale_factor = 1
    axis = 1
```

```
  []
  [clad_outer_temperature]
    type = PiecewiseBilinear
    data_file = ../clad_surface_temp.csv
    scale_factor = 1
    axis = 1
  []
  [heat_transfer_mode]
     type = PiecewiseConstant
     x = '-200 172489073 172489661'
     y = '9 9 8 '
     direction = 'right'
  []
  [clad_axial_pressure]
    type = CladdingAxialPressureFunction
    plenum_pressure = plenum_pressure
    coolant_pressure = pressure_ramp
    coolant_pressure_scaling_factor = 1.0
    fuel_pin_geometry = fuel_pin_geometry
  []
  [fuel_axial_pressure]
    type = ParsedFunction
    value = plenum_pressure
    vars = plenum_pressure
    vals = plenum_pressure
  []
[]

[AuxVariables]
  [disp_y]
  []
  [disp_z]
  []
  [fast_neutron_flux]
    block = clad
  []
  [fast_neutron_fluence]
    block = clad
  []
  [grain_radius]
    block = fuel
    initial_condition = 5.0e-6
  []
  [hoop_stress]
    order = CONSTANT
    family = MONOMIAL
  []
  [effective_creep_strain]
    block = clad
    order  = CONSTANT
    family = MONOMIAL
  []
  [fract_beta_phase]
    order  = CONSTANT
```

```
    family = MONOMIAL
  []
  [oxide_thickness]
    order  = CONSTANT
    family = MONOMIAL
  []
  [bursted]
    order  = CONSTANT
    family = MONOMIAL
  []
  [gap_conductance]
    order = CONSTANT
    family = MONOMIAL
  []
  [coolant_htc]
    order = CONSTANT
    family = MONOMIAL
  []
  [creep_rate]
    order = CONSTANT
    family = MONOMIAL
  []
  [gap_thermal_conductivity]
    order = CONSTANT
    family = MONOMIAL
  []
  [layered_maximum_clad_radius]
    order = CONSTANT
    family = MONOMIAL
  []
  [strain_yy_0]
    order = CONSTANT
    family = MONOMIAL
  []
[]

[Kernels]
  [heat]
    type = HeatConduction
    variable = temperature
    extra_vector_tags = 'ref'
  []
  [heat_ie]
    type = HeatConductionTimeDerivative
    variable = temperature
    extra_vector_tags = 'ref'
  []
  [heat_source]
    type = NeutronHeatSource
    variable = temperature
    block = fuel
    burnup_function = burnup
    axial_relocation_object = axial_relocation
    extra_vector_tags = 'ref'
```

```
  []
[]

[Modules]
  [TensorMechanics]
    [Layered1DMaster]
      [fuel]
        add_scalar_variables = true
        out_of_plane_strain_name = strain_yy
        fuel_pin_geometry = fuel_pin_geometry
        out_of_plane_pressure = fuel_axial_pressure
        strain = finite
        block = fuel
        eigenstrain_names = 'fuel_thermal_strain
                             fuel_swelling_strain
                             fuel_relocation_strain
                             axial_relocation_eigenstrain'
        decomposition_method = EigenSolution
        generate_output = 'stress_xx stress_yy stress_zz
                           vonmises_stress'
        extra_vector_tags = 'ref'
        group_scalar_vars_in_reference_residual = true
        mesh_generator = layered1D_mesh
      []
      [clad]
        add_scalar_variables = true
        out_of_plane_strain_name = strain_yy
        fuel_pin_geometry = fuel_pin_geometry
        strain = finite
        out_of_plane_pressure = clad_axial_pressure
        block = clad
        eigenstrain_names = 'clad_thermal_strain
                             clad_irradiation_strain'
        generate_output = 'stress_xx stress_yy stress_zz vonmises_stress
                           strain_zz creep_strain_zz'
        decomposition_method = EigenSolution
        extra_vector_tags = 'ref'
        group_scalar_vars_in_reference_residual = true
        mesh_generator = layered1D_mesh
      []
    []
  []
[]

[Burnup]
  [burnup]
    block = fuel
    rod_ave_lin_pow = power_history
    axial_power_profile = axial_peaking_factors
    num_radial = 80
    num_axial = 11
    fuel_pin_geometry = fuel_pin_geometry
    fuel_volume_ratio = 1.0
    order = CONSTANT
```

```
    family = MONOMIAL
    RPF = RPF
    i_enrich = '0.035 0.965 0 0 0 0'
  []
[]

[AuxKernels]
  [fast_neutron_flux]
    type = FastNeutronFluxAux
    block = clad
    variable = fast_neutron_flux
    rod_ave_lin_pow = power_history
    axial_power_profile = axial_peaking_factors
    factor = 3e13
    execute_on = timestep_begin
  []
  [fast_neutron_fluence]
    type = FastNeutronFluenceAux
    block = clad
    variable = fast_neutron_fluence
    fast_neutron_flux = fast_neutron_flux
    execute_on = timestep_begin
  []
  [grain_radius]
    type = GrainRadiusAux
    block = fuel
    variable = grain_radius
    temperature = temperature
    execute_on = linear
  []
  [hoop_stress]
    type = RankTwoScalarAux
    rank_two_tensor = stress
    variable = hoop_stress
    scalar_type = HoopStress
    execute_on = timestep_end
  []
  [effective_creep_strain]
    type = MaterialRealAux
    block = clad
    variable = effective_creep_strain
    property = effective_creep_strain
    execute_on = 'timestep_end'
  []
  [fract_bphase]
    type = MaterialRealAux
    block = clad
    variable = fract_beta_phase
    property = fract_beta_phase
    execute_on = 'initial linear'
  []
  [oxide_thickness]
    type = MaterialRealAux
    boundary = 2
```

```
    variable = oxide_thickness
    property = oxide_scale_thickness
    execute_on = 'initial linear'
  []
  [hasbursted]
    type = MaterialRealAux
    boundary = 2
    variable = bursted
    property = failed
    execute_on = timestep_end
  []
  [conductance]
    type = MaterialRealAux
    boundary = 10
    property = gap_conductance
    variable = gap_conductance
    execute_on = 'initial linear'
  []
  [coolant_htc]
    type = MaterialRealAux
    property = coolant_channel_htc
    variable = coolant_htc
    boundary = 2
    execute_on = 'initial linear'
  []
  [creep_rate]
    type = MaterialRealAux
    block = clad
    variable = creep_rate
    property = creep_rate
    execute_on = timestep_end
  []
  [gas_th_cond]
    type = MaterialRealAux
    variable = gap_thermal_conductivity
    property = gap_conductivity
    boundary = 10
    execute_on = 'initial linear'
  []
[]

[AxialRelocation]
  mesh_generator = layered1D_mesh
  fragmentation_model = BARANI
  linear_heat_rate_function = power_history
  axial_direction = y
  fuel_blocks = fuel
  clad_blocks = clad
  contact_pressure_variable = contact_pressure
  out_of_plane_strain_variable = strain_yy
  penetration_variable = penetration
  clad_inner_volume_addition = 3.189382e-6
  burnup_variable = burnup
  gap_thickness_threshold = {gap_thickness_threshold}
```

```
  nonrelocatable_fuel_fraction = {nonrelocatable_fuel_fraction}
  pulver_characteristic_length = {pulver_characteristic_length}
  axial_relocation_output_options = MASS_FRACTION
[]

[CoolantChannel]
  [convective_clad_surface]
    boundary = 2
    variable = temperature
    heat_transfer_mode = heat_transfer_mode
    heat_transfer_coefficient = average_htc
    inlet_temperature = heat_sink_temperature    # K
    effective_emissivity {effective_emissivity}
    # inlet_temperature = 580 # K
    # inlet_pressure = 15.3e6 # Pa
    # inlet_massflux = 3800 # kg/m^2-sec
    rod_diameter = 0.01075 # m
    rod_pitch = 1.26e-2 # m
    compute_enthalpy = false
    linear_heat_rate = power_history
    axial_power_profile = axial_peaking_factors
    output_properties = 'coolant_channel_htype coolant_channel_hmode'
  []
[]

[Contact]
  [pellet_clad_mechanical]
    primary = 5
    secondary = 10
    penalty = 1e7
    formulation = kinematic
    model = frictionless
  []
[]

[ThermalContact]
  [thermal_contact]
    type = GapHeatTransferLWR
    variable = temperature
    primary = 5
    secondary = 10
    initial_gas_fractions = '0.05 0.95 0. 0. 0. 0. 0. 0. 0. 0.'
    initial_moles = initial_moles
    gas_released = fis_gas_released
    plenum_pressure = plenum_pressure
    contact_pressure = contact_pressure
    jump_distance_model = KENNARD
    roughness_coef = 3.2
    refab_gas_fractions = '0.05 0.95 0. 0. 0. 0. 0. 0. 0. 0.'
    refab_time = 172387800
    refab_type = 0
  []
[]
```

```
[BCs]
  [no_x_all]
    type = DirichletBC
    variable = disp_x
    boundary = 12
    value = 0.0
  []
  [Pressure]
    [coolantPressure]
      boundary = 2
      function = pressure_ramp
      factor = 1.0
    []
  []
  [clad_outer_temp]
    type = FunctionDirichletBC
    boundary = 2
    variable = temperature
    function = clad_outer_temperature
  []
  [PlenumPressure]
    [plenumPressure]
      boundary = 9
      initial_pressure = 2.0e6
      startup_time = 0
      R = 8.3143
      output_initial_moles = initial_moles
      temperature = plenum_temp
      volume = 'clad_volume pellet_volume'
      material_input = fis_gas_released
      output = plenum_pressure
      refab_time = 172387800
      refab_pressure = 4.0e6
      refab_temperature = 295.0
      refab_volume = 2.15e-05
    []
  []
[]

[LayeredPlenumTemperature]
  [plenum_temp]
    boundary = 5
    fuel_pin_geometry = fuel_pin_geometry
    out_of_plane_strain = strain_yy
    use_current_slice_heights = true
    inner_surfaces = '5'
    outer_surfaces = '10'
    temperature = temperature
    execute_on = 'initial timestep_end'
  []
[]

[Controls]
  [period1]
```

```
    type = TimePeriod
    disable_objects = 'BCs/clad_outer_temp'
    start_time = 172489043
    end_time = 172489661
  []
[]

[UserObjects]
  [terminator]
    type = Terminator
    expression = 'bursted > 0'
    execute_on = timestep_end
  []
[]

[Materials]
  [fuel_thermal]
    type = ThermalFuel
    block = fuel
    thermal_conductivity_model = STAICU
    hbs_porosity_correction = KAMPF
    model_hbs_formation = true
    temperature = temperature
    burnup_function = burnup
    axial_relocation_object = axial_relocation
    gap_thermal_conductivity = layered_average_gap_conductivity
  []
  [relocation]
    type = UO2RelocationEigenstrain
    block = fuel
    burnup_function = burnup
    rod_ave_lin_pow = power_history
    axial_power_profile = axial_peaking_factors
    fuel_pin_geometry = fuel_pin_geometry
    burnup_relocation_stop = 0.024
    relocation_activation1 = 5000.0
    relocation_model = ESCORE_modified
    eigenstrain_name = fuel_relocation_strain
  []
  [fuel_thermal_strain]
    type = ComputeThermalExpansionEigenstrain
    block = fuel
    thermal_expansion_coeff = 10.0e-6
    stress_free_temperature = 295.0
    eigenstrain_name = fuel_thermal_strain
  []
  [fuel_swelling]
    type = UO2VolumetricSwellingEigenstrain
    gas_swelling_model_type = SIFGRS
    block = fuel
    burnup_function = burnup
    initial_fuel_density = 10430.0
    eigenstrain_name = fuel_swelling_strain
  []
```

```
[fission_gas_release]
  type = Sifgrs
  block = fuel
  temperature = temperature
  burnup_function = burnup
  grain_radius = grain_radius
  transient_option = 1
  diff_coeff_option = 3
  gbs_model = true
[]
[fuel_elasticity_tensor]
  type = UO2IsotropicDamageElasticityTensor
  block = fuel
  temperature = temperature
  rod_ave_lin_pow = power_history
  rod_average_burnup = average_burnup
  fragmentation_model = BARANI
  axial_relocation_object = axial_relocation
  crumbling_scale_factor = 0.1
[]
[fuel_stress]
  type = ComputeMultipleInelasticStress
  tangent_operator = elastic
  inelastic_models = 'fuel_creep'
  block = fuel
[]
[fuel_creep]
  type = UO2CreepUpdate
  block = fuel
  temperature = temperature
  burnup_function = burnup
  initial_grain_radius = 5.0e-6
[]
[HBS]
  type = HighBurnupStructureFormation
  burnup_function = burnup
  temperature = temperature
  output_properties = 'hbs_volume_fraction'
[]
[clad_elasticity_tensor]
  type = ZryElasticityTensor
  block = clad
[]
[stress]
  type = ComputeMultipleInelasticStress
  tangent_operator = elastic
  inelastic_models = 'zrycreep'
  block = clad
[]
[zrycreep]
  type = ZryCreepLOCAErbacherLimbackHoppeUpdate
  fast_neutron_flux = fast_neutron_flux
  fast_neutron_fluence = fast_neutron_fluence
  model_irradiation_creep = true
```

```
  model_primary_creep = true
  model_thermal_creep = true
  max_inelastic_increment = {max_inelastic_increment}
  zircaloy_material_type = stress_relief_annealed
  block = clad
[]
[thermal_expansion]
  type = ZryThermalExpansionMATPROEigenstrain
  block = clad
  stress_free_temperature = 295.0
  eigenstrain_name = clad_thermal_strain
[]
[irradiation_swelling]
  type = ZryIrradiationGrowthEigenstrain
  block = clad
  fast_neutron_fluence = fast_neutron_fluence
  zircaloy_material_type = stress_relief_annealed
  eigenstrain_name = clad_irradiation_strain
[]
[clad_phase]
  type = ZrPhase
  block = clad
  temperature = temperature
  numerical_method = 2
[]
[clad_oxidation]
  type = ZryOxidation
  boundary = 2
  temperature = temperature
  clad_inner_radius = 4.65e-03
  clad_outer_radius = 5.375e-03
  normal_operating_temperature_model = epri_kwu_ce
  high_temperature_model = cathcart
  use_coolant_channel = true
[]
[clad_failure_criterion]
  type = ZryCladdingFailure
  boundary = 2
  failure_criterion = overstrain
  hoop_stress = hoop_stress
  hoop_creep_strain = creep_strain_zz
  effective_strain_rate_creep = creep_rate
  temperature = temperature
  fraction_beta_phase = fract_beta_phase
[]
[clad_thermal]
  type = ThermalZry
  block = clad
  temperature = temperature
[]
[fuel_density]
  type = Density
  block = fuel
[]
```

```
  [clad_density]
    type = Density
    block = clad
    density = 6551.0
  []
[]

[Postprocessors]
  [ave_temp_interior]
    type = LayeredSideAverageValuePostprocessor
    boundary = 9
    variable = temperature
    execute_on = 'initial linear'
    fuel_pin_geometry = fuel_pin_geometry
  []
  [pellet_volume_2]
    type = LayeredInternalVolumePostprocessor
    boundary = 8
    component = 0
    fuel_pin_geometry = fuel_pin_geometry
    out_of_plane_strain = strain_yy
    execute_on = 'initial linear'
  []
  [avg_clad_temp]
    type = LayeredSideAverageValuePostprocessor
    boundary = 7
    variable = temperature
    fuel_pin_geometry = fuel_pin_geometry
    execute_on = 'initial linear'
  []
  [fis_gas_produced]
    type = LayeredElementIntegralFisGasGeneratedSifgrsPostprocessor
    block = fuel
    fuel_pin_geometry = fuel_pin_geometry
  []
  [fis_gas_released]
    type = LayeredElementIntegralFisGasReleasedSifgrsPostprocessor
    block = fuel
    fuel_pin_geometry = fuel_pin_geometry
  []
  [fis_gas_grain]
    type = LayeredElementIntegralFisGasGrainSifgrsPostprocessor
    block = fuel
    fuel_pin_geometry = fuel_pin_geometry
  []
  [fis_gas_boundary]
    type = LayeredElementIntegralFisGasBoundarySifgrsPostprocessor
    block = fuel
    fuel_pin_geometry = fuel_pin_geometry
  []
  [fisson_gas_release]
    type = FGRPercent
    fission_gas_released = fis_gas_released
    fission_gas_generated = fis_gas_produced
```

```
  []
  [average_coolant_htc]
    type = LayeredSideAverageValuePostprocessor
    boundary = 2
    variable = coolant_htc
    execute_on = 'initial linear'
    fuel_pin_geometry = fuel_pin_geometry
  []
  [average_burnup]
    type = RodAverageBurnup
    burnup_function = burnup
    execute_on = 'initial timestep_end'
  []
  [temp_clad_max]
    type = NodalExtremeValue
    block = clad
    value_type = max
    variable = temperature
    execute_on = 'initial timestep_end'
  []
  [betaph_fract_max]
    type = ElementExtremeValue
    value_type = max
    variable = fract_beta_phase
    block = clad
    execute_on = 'initial timestep_end'
  []
  [bursted]
    type = ElementExtremeValue
    value_type = max
    variable = bursted
    block = clad
    execute_on = 'initial timestep_end'
  []
  [timestep_material]
    type = MaterialTimeStepPostprocessor
    block = clad
    execute_on = 'initial timestep_end'
  []
[]

[Dampers]
  [limitT]
    type = BoundingValueNodalDamper
    variable = temperature
    max_value = 3200.0
    min_value = 0.0
  []
  [limitX]
    type = MaxIncrement
    max_increment = 1e-5
    variable = disp_x
  []
[]
```

```
[Executioner]
  type = Transient
  solve_type = 'PJFNK'

  petsc_options = '-snes_ksp_ew'
  petsc_options_iname = '-pc_type -pc_factor_mat_solver_package
                         -ksp_gmres_restart'
  petsc_options_value = 'lu       superlu_dist      51'

  line_search = 'none'

  l_max_its = 50
  l_tol = 1e-3
  nl_max_its = 100
  nl_rel_tol = 1e-4
  nl_abs_tol = 1e-8
  dtmax = 5e5
  dtmin = 1e-5
#  end_time = 172387800 # End base irradiation
#  end_time = 172489043 # Begin Blowdown
 end_time = 172489661 # End

  [TimeStepper]
    type = IterationAdaptiveDT
    dt = 200
    timestep_limiting_postprocessor = timestep_material
    optimal_iterations = 20
    iteration_window = 4
    linear_iteration_ratio = 100
    timestep_limiting_function = forced_times
    force_step_every_function_point = true
    max_function_change = 2000
    time_t  = '172387800 172388043 172488043 172489043 172489073
               172489661'
    time_dt = '1.0e04 1.0e04 10.0 5.0 3.0 5.0'
  []
[]

[VectorPostprocessors]
  [clad_radial_disp]
    type = NodalValueSampler
    variable = disp_x
    boundary = 2
    sort_by = y
    outputs = 'outfile_2'
  []
  [clad_out_temp]
    type = NodalValueSampler
    variable = temperature
    boundary = 2
    sort_by = y
    outputs = 'outfile_temp_2'
  []
```

```
  [mass_fraction]
    type = LineValueSampler
    start_point = '0 0.01124 0'
    end_point = '0 0.47524 0'
    num_points = 30
    sort_by = y
    variable = layered_mass_fraction
    outputs = 'outfile_mass_2'
  []
[]

[PerformanceMetricOutputs]
[]

[Outputs]
  csv = true
  color = false
  exodus = false
  execute_on = 'initial timestep_end'
  perf_graph = true
  [outfile_2]
    type = CSV
    execute_on = 'FINAL'
    create_final_symlink = true
  []
  [outfile_temp_2]
    type = CSV
    execute_on = 'FINAL'
    create_final_symlink = true
  []
  [outfile_mass_2]
    type = CSV
    execute_on = 'FINAL'
    create_final_symlink = true
  []
[]
```

APPENDIX E

CURRICULUM VITAE

Kyle Allan Lawrence Gamble

Contact Information

Permanent Address: 2860 Sunlight Dr. Idaho Falls, ID, 83401 Mobile: (208)-206-6513
Email: Kyle.Gamble@inl.gov
gambkyle@gmail.com

Education

PhD Candidate, Nuclear Engineering, APOGEE (distance) Program Aug. 2015 - present
University of South Carolina, Columbia, SC, USA
"Mechanistic Multiphysics Modeling of Cladding Rupture in Nuclear Fuel Rods during Loss of Coolant Accident Conditions"
Advised by: Dr. Travis W. Knight

M.A.Sc., Chemistry and Chemical Engineering (Nuclear Specialization) Sept. 2012 - June 2014
Royal Military College of Canada, Kingston, ON, Canada
"Modeling Three-Dimensional Deformation Mechanisms in CANDU Reactor Fuel Elements"
Advised by: Prof. Paul K. Chan (RMCC) and Dr. Anthony F. Williams (CNL formerly AECL)

B.Sc., Engineering Physics, Mechanical Engineering Option Sept. 2008 – June 2012
Queen's University, Kingston, ON, Canada
Senior Thesis: "Fresh air cooling system for Computer Rooms" Advised by: Prof. Lawrence Widrow

Honours and Awards

- R&D 100 Award winner for the Bison fuel performance code, Idaho National Laboratory (2021
- Expanded Recognition Award, Idaho National Laboratory (2020-2021)
- Exceptional Contributions Program Award, Idaho National Laboratory (2015-2017)
- Gold Governor General's Medal, Royal Military College of Canada (nominated) (2015)
- National Sciences and Engineering Research Council of Canada (NSERC) Undergraduate Student Research Award (USRA) (2012)
- Dean's Scholar (2009-2012)
- Queen's University Excellence Scholarship (2008, 2009)

Work Experience

Computational Scientist June 2014 - present
Fuel Modeling and Simulation Department, Idaho National Laboratory, Idaho Falls, ID, USA

- Work package manager on multiple projects ranging in scope of funding levels.
- Develop new capabilities within the MOOSE/BISON framework including accident tolerant fuel concepts, Loss of Coolant Accident models, numerical methods, and mesh generation.
- Perform validation simulations with BISON against existing experimental data.
- Technical writing

- Provide user support and training

Attached Staff May 2013 - Apr. 2014
Fuel and Fuel Channel Safety Branch, Chalk River Laboratories, Chalk River, ON, Canada

- Conducted advanced finite element modeling of a CANDU fuel element to assess the capabilities of Idaho National Laboratory's MOOSE/BISON framework.
- Investigated material properties, fuel-to-sheath gap heat transfer, pellet-to-pellet and pellet-to-sheath contact in three dimensions for a CANDU fuel element.
- Determined the scalability of MOOSE on multiple processors.
- Compared fuel performance parameters to ELESTRES-IST and ANSYS simulations.
- Analyzed the flexural rigidity and thermal bowing of a CANDU fuel element using MOOSE/BISON.
- Compared fuel element deflection with ongoing and existing experiments, and ANSYS simulations.
- Presented modeling and simulation results to colleagues.

Research Assistant May 2012 - Aug. 2012
Department of Mechanical and Aerospace Engineering, Royal Military College of Canada, Kingston, ON, Canada

- Developed corner crack growth models using centred, non-centred, and rotated ellipses as the crack front approximation.
- Coupled the finite element software StressCheck to Microsoft Excel to assess crack growth in military aircraft for the Directorate of Technical Airworthiness and Engineering Support.
- Created user and theory manuals for the modules.
- Completed a small literature review on the applications and analysis of the Arctic Boundary Layer.
- Completed both of the above projects as part of the NSERC USRA program.

Engineering Summer Student May 2011 - Aug. 2011
Engineering Department, Gay Lea Foods Co-operative, Weston, ON, Canada

- Developed Process and Instrumentation Diagrams (P&IDs) for the utilities (water, natural gas, glycol, compressed air, steam, and sprinklers) in the plant under the supervision of the engineering manager.
- Completed colour-coded labelling of the flow direction of all utility pipes for easy identification.
- Created a streamlined purchase order database in Microsoft Access to expedite purchasing requests for the engineering department.
- Supervised contractors during the installation of a new production line.

Professional Associations

- Engineer in Training, Professional Engineers of Ontario (2012 - 2019)

- Canadian Nuclear Society (2012 – 2014)
- American Nuclear Society (2015 – present)
- Reviewer for TopFuel Conference 2015
- Reviewer for ICAPP Conference 2016
- Reviewer for ANS Annual Meeting (2016 – present)
- Reviewer for Journal of Nuclear Engineering and Design (5 papers)
- Reviewer for Journal of Nuclear Materials (10 papers)
- Reviewer for Annals of Nuclear Energy (3 papers)
- Reviewer for Progress in Nuclear Energy (2 papers)
- Reviewer for European Journal of Physics N (1 paper)

Technical Skills

Computational

- *Numerical Modeling and Simulation:* Thermodynamics, heat transfer, structural mechanics, thermal-hydraulics, multi-scale multiphysics
- *Scientific Software:* MOOSE, BISON, Dakota, Cubit (Trelis), ParaView, SolidEdge, Maple, Matlab, StressCheck, ANSYS Mechanical, FactSage
- *Software Development:* Doxygen, LLDB, Git
- *Programming Languages:* C++, Visual Basic, Python (limited)
- *Operating Systems:* Windows, Linux (Ubuntu), Mac OSX
- *Miscellaneous Software:* Microsoft Office (Word, Excel, Access, PowerPoint)
- *Computing Clusters:* User of INL's Falcon and Lemhi Machines

Publications

Refereed Journal Papers

1. **K. A. Gamble**, T. W. Knight, E. Roberts, J. D. Hales, B. W. Spencer, "Mechanistic Verification of Empirical UO_2 Fracture Models," *Journal of Nuclear Materials*, 556 (2021), 153163.
2. M. W. D. Cooper, **K. A. Gamble**, L. Capolungo, C. Matthews, D. A. Andersson, B. Beeler, C. R. Stanek, K. Metzger, "Irradiation-enhanced diffusion and diffusion-limited creep in U_3Si_2," *Journal of Nuclear Materials,* 555 (2021), 153129.
3. **K. A. Gamble**, G. Pastore, M. W. D. Cooper, D. A. Andersson, C. Matthews, B. Beeler, L. K. Aagesen, T. Barani, D. Pizzocri, "Improvement of the BISON U_3Si_2 modeling capabilities based on multiscale developments to modeling fission gas behavior," *Journal of Nuclear Materials*, 555 (2021), 153097.
4. W. Jiang, J. D. Hales, B. W. Spencer, B. P. Collin, A. E. Slaughter, S. R. Novascone, A. Toptan, **K. A. Gamble**, R. Gardner, "TRISO particle fuel performance and failure analysis with BISON," *Journal of Nuclear Materials*, 548 (2021), 152795.
5. J. D. Hales, W. Jiang, A. Toptan, **K. A. Gamble**, "Modeling fission product diffusion in TRISO fuel particles with BISON, *Journal of Nuclear Materials*, 548 (2021), 152840.
6. G. Pastore, **K. A. Gamble**, R. L. Williamson, S. R. Novascone, R. J. Gardner, J. D. Hales, "Analysis of fuel rod behavior during loss-of-coolant accidents using the BISON code: Fuel

modeling development and simulation of integral experiments," *Journal of Nuclear Materials*, 545 (2021), 152645.

7. G. Pastore, R. L. Williamson, R. J. Gardner, S. R. Novascone, J. B. Tompkins, **K. A. Gamble**, J. D. Hales, "Analysis of fuel rod behavior during loss-of-coolant accidents using the BISON code: Cladding modeling developments and simulation of separate-effects experiments," *Journal of Nuclear Materials*, 543 (2021), 152537.
8. M. W. D Cooper, G. Pastore, and Y. Che, C. Matthews, A. Forslund, C. R. Stanek, K. Shirvan, T. Tverberg, **K. A. Gamble**, B. Mays, D. A. Andersson, "Fission Gas Diffusion and Release for Cr_2O_3-Doped UO_2: From the Atomic to the Engineering Scale," *Journal of Nuclear Materials* (2020).
9. J. A. Yingling, **K. A. Gamble**, E. Roberts, R. A. Freeman, T. W. Knight, "Updated U_3SI_2 Thermal Creep Model and Sensitivity analysis of the U_3Si_2-SiC Accident Tolerant Fuel," *Journal of Nuclear Materials* (2020).
10. L. K. Aagesen, D. Andersson, B. W. Beeler, M. W. D. Cooper, **K. A. Gamble**, Y. Miao, G. Pastore, M. R. Tonks, "Phase-field simulations of intergranular fission gas bubble behavior in U_3Si_2 nuclear fuel," *Journal of Nuclear Materials*, 541 (2020), 152415.
11. T. Barani, G. Pastore, D. Pizzocri, D. A. Andersson, C. Matthews, A. Alfonsi, **K. A. Gamble**, P. Van Uffelen, L. Luzzi, J. D. Hales, "Multiscale modeling of fission gas behavior in U_3Si_2 under LWR conditions," *Journal of Nuclear Materials*, 522 (2019), p. 97-110
12. S. Stimpson, J. Powers, K. Clarno, R. Pawlowski, R. Gardner, S. Novascone, **K. Gamble**, R. Williamson, "Pellet-clad mechanical interaction screening using VERA applied to Watts Bar Unit 1, Cycles 1-3," *Journal of Nuclear Engineering and Design,* 327 (2018), p. 172-186
13. Y. Miao, **K. A. Gamble**, D. Andersson, Z-G Mei, A. M. Yacout, "Rate theory scenarios study on fission gas behavior of U_3Si_2 under LOCA conditions in LWRs," *Journal of Nuclear Engineering and Design*, 326 (2018), p. 371-282
14. Y. Miao, **K. A. Gamble**, D. Andersson, B. Ye, Z-G Mei, G. Hofman, A. M. Yacout, "Gaseous Swelling of U_3Si_2 during Steady-State LWR Operation: a Rate Theory Investigation," *Journal of Nuclear Engineering and Design*, 322 (2017), p. 336-344
15. **K. A. Gamble**, T. Barani, D. Pizzocri, J. D. Hales, K. A. Terrani, G. Pastore, "An investigation of FeCrAl cladding behaviour under normal operating and loss of coolant conditions," *Journal of Nuclear Materials*, 491 (2017), p. 55-66
16. R. L. Williamson, **K. A. Gamble**, D. M. Perez, S. R. Novascone, G. Pastore, R. J. Gardner, J. D. Hales, W. Liu, A. Mai, "Validating the BISON fuel performance code to integral LWR experiments," *Journal of Nuclear Engineering and Design,* 301 (2016), p. 232-244
17. **K. A. Gamble**, A. F. Williams, P. K. Chan, D. Wowk, "A feasibility study on the use of the MOOSE computational framework to simulate three-dimensional deformation of CANDU reactor fuel elements," *Journal of Nuclear Engineering and Design,* 293 (2015), p. 385-394
18. D. Wowk, **K. Gamble**, R. Underhill, "Influence of p-method finite element parameters on predictions of crack front geometry," *Journal of Finite Element in Analysis and Design*, 73 (2013), p. 1-10.

Conference Proceedings

1. **K. A. Gamble**, G. Pastore, M. W. D. Cooper, A. Andersson, "BISON Capability and Validation for U3Si2, Cr2O3-doped UO2, FeCrAl, and Cr-coated Zircaloy ATF Concepts," *Proceedings of ANS Virtual Winter Meeting* (November 2020)

2. **K. A. Gamble**, "Investigation of coated cladding ballooning behavior using Bison, "*Proceedings of Top Fuel 2019,"* Seattle, USA (September 2019)
3. **K. A. Gamble**, "Modeling Axial Relocation of Fragmented Fuel during Loss of Coolant Conditions using the Bison Fuel Performance Code, "*Proceedings of Top Fuel 2019,"* Prague, Czech Republic (October 2018)
4. **K. A. Gamble**, J. D. Hales, G. Pastore, T. Barani, D. Pizzocri, K. A. Terrani, "Fuel Performance Modeling of FeCrAl Cladding Failure during Loss of Coolant Conditions," *Proceedings of the 2017 Water Reactor Fuel Performance Meeting*, Jeju Island, South Korea (September 2017)
5. **K. A. Gamble**, J. D. Hales, "Preliminary Modeling of Accident Tolerant Fuel Concepts under Accident Conditions, *Proceedings of TopFuel 2016*, Boise, USA (September 2016)
6. **K. A. Gamble**, L. P. Swiler, "Uncertainty Quantification and Sensitivity Analysis Applications to Fuel Performance Modeling," *Proceedings of TopFuel 2016*, Boise, USA (September 2016)
7. **K. A. Gamble**, J. D. Hales, "Investigating Accident Tolerant Fuel Concepts using the BISON Fuel Performance Code," *Proceedings of the Nuclear Fuels and Structural Materials Embedded Topical – ANS Annual Meeting*, New Orleans, LA, USA (June 2016)
8. J. D. Hales, **K. A. Gamble**, "Preliminary evaluation of FeCrAl cladding and U-Si fuel for accident tolerant fuel concepts," *Proceedings of TopFuel 2015*, Zurich, Switzerland (September 2015)
9. **K. A. Gamble**, "Overview of the BISON Fuel Performance Code," *Proceedings of the ANS Annual Meeting*, San Antonio, TX, USA (June 2015)
10. **K. A. Gamble**, A.F. Williams, P.K. Chan, "Development of a Three-Dimensional Thermo-Mechanical Deformation Model of a Horizontal Nuclear Fuel Element," *Proceedings of the 19th Pacific Basin Nuclear Conference*, Vancouver, BC, Canada (August 2014)
11. **K. Gamble**, A.F. Williams, P.K. Chan, "A Three-Dimensional Analysis of the Stresses and Strains at the Pellet Ridges in a Horizontal Nuclear Fuel Element," *Proceedings of the 22nd International Conference on Nuclear Engineering*, Prague, Czech Republic (July 2014)
12. **K. Gamble**, A.F. Williams, P.K. Chan, "Feasibility Study of Modeling a CANDU Fuel Element using a Multiphysics Object-Oriented Simulation Environment," *Proceedings of the 12th International Conference on CANDU Fuel,* Kingston, ON, Canada (September 2013)
13. **K. Gamble**, A.F. Williams, P.K. Chan, "Advanced Finite Element Modeling of a Horizontal Nuclear Fuel Element using a Multiphysics Object-Oriented Simulation Environment," *37th Annual CNS/CNA Student Conference,* Toronto, ON, Canada (June 2013)

Invited Talks

1. **K. A. Gamble**, "Application of the BISON nuclear fuel performance code," *University of South Carolina*, Columbia, SC, USA (May 2019)
2. **K. Gamble**, "Examining the Capabilities of MOOSE/BISON to Model CANDU Fuel Pin and Bundle Deformation," *Idaho National Laboratory,* Idaho Falls, ID, USA (November 2013)

Technical Documents

1. **K. A. Gamble**, L. K. Aagesen, S. Biswas, W. Jiang, A. M. Recuero, J. D Hales, D. Van Wasshenova, M. W. D. Cooper, N. Capps, R. Sweet, "Advancements in modeling fuel pulverization and cladding behavior during a LOCA, Technical Report, Idaho National Laboratory, INL/EXT-21-647705 Rev. 001 (September 2021)
2. **K. A. Gamble**, M. W. D. Cooper, "Multiscale Modeling of Cr_2O_3-doped UO_2 Creep and Fracture," Technical Report, Idaho National Laboratory, INL/EXT-21-64733 (September 2021)

3. **K. A. Gamble**, A. Toptan, P.-C. A. Simon, "PCMI as a Potential Failure Mechanism During a Control Rod Drop Accident in a BWR," Technical Report, Idaho National Laboratory, INL/LTD-21-64690 (September 2021)
4. **K. A. Gamble**, A. Toptan, "FY21 BISON BWR Fuel Modeling Capability: Sensitivity Analysis During Normal Operation," Technical Report, Idaho National Laboratory, INL/LTD-21-62647 (April 2021)
5. A. Toptan, **K. A. Gamble**, "BISON High Burnup Structure Modeling Capabilities Validated with a Selection of the Halden IFA-650 Rods," Technical Report, Idaho National Laboratory, INL/EXT-20-60778 (November 2020)
6. A. Toptan, **K. A. Gamble**, G. Pastore, "BISON Capabilities for LWR Fuel Behavior Analysis During Accident and High-burnup Conditions," Technical Report, Idaho National Laboratory, INL/EXT-20-59392 (July 2020)
7. **K. A. Gamble**, "ATF Material model development and validation for priority cladding concepts," Technical Report, CASL, CASL-U-2019-1892 (August 2019)
8. **K. A. Gamble**, G. Pastore, D. Andersson, M.W.D. Cooper, "ATF Material model development and validation for priority fuel concepts," Technical Report, CASL, CASL-U-2019-1870 (July 2019)
9. **K. A. Gamble**, G. Pastore, "Investigate Accident Tolerant Fuel Concepts," Technical Report, Idaho National Laboratory, INL/EXT-18-51326 (September 2018)
10. **K. A. Gamble**, "Axial Relocation Model Extension in Bison," Technical Report, CASL, CASL-U-2018-1662 (August 2018)
11. G. Pastore, **K. A. Gamble**, J. D. Hales, "Modeling Benchmark for FeCrAl Cladding in the IAEA CRP ACTOF: FeCrAl-C35M Material Models and Benchmark Cases Specifications," Technical Report, Idaho National Laboratory, INL/EXT-17-43695 (October 2017)
12. **K. A. Gamble**, J. D. Hales, D. M. Perez, G. Pastore, "Nuclear Energy Advanced Modeling and Simulation (NEAMS) Accident Tolerant Fuels High Impact Problem: Engineering Scale Models and Analysis, Technical Report, Idaho National Laboratory, INL/EXT-17-43388 (September 2017)
13. **K. A. Gamble**, R. J. Gardner, R. L. Williamson, "BISON FY17 Accident Capability Development," Technical Report, CASL, CASL-U-2017-1389-000 (July 2017)
14. **K. A. Gamble**, J. D. Hales, G. Pastore, T. Barani, D. Pizzocri, "Behavior of U_3Si_2 Fuel and FeCrAl Cladding under Normal Operating and Accident Reactor Conditions, Technical Report, Idaho National Laboratory, INL/EXT-16-40059 (September 2016)
15. J. D. Hales, R. L. Williamson, S. R. Novascone, G. Pastore, B. W. Spencer, D. S. Stafford, **K. A. Gamble**, D. M. Perez, W. Liu, "BISON Theory Manual: The Equations Behind Nuclear Fuel Analysis, BISON Release 1.2," Technical Report, Idaho National Laboratory, INL/MIS-13-29930 Rev. 3 (September 2015)
16. J. D. Hales, **K. A. Gamble**, B. W. Spencer, S. R. Novascone, G. Pastore, W. Liu, D. S. Stafford, R. L. Williamson, D. M. Perez, R. J. Gardner, "BISON User's Manual, BISON Release 1.2," Technical Report, Idaho National Laboratory, INL/MIS-13-30307 Rev. 3 (September 2015)
17. **K. A. Gamble**, J. D. Hales, J. Yu, Y. Zhang, X. Bai, D. Andersson, A. Patra, W. Wen, C. Tomé, M. Baskes, E. Martinez, C. R. Stanek, Y. Miao, B. Ye, G. L. Hofman, A. M. Yacout, W. Liu, "Multiscale Multiphysics Developments for Accident Tolerant Fuel Concepts," Technical Report, Idaho National Laboratory, INL/EXT-15-36761 (September 2015)
18. **K. Gamble**, R. Williamson, D. Schwen, Y. Zhang, S. Novascone, P. Medvedev, "BISON and MARMOT Development for Modeling Fast Reactor Fuel Performance," Technical Report, Idaho National Laboratory, INL/EXT-15-36440 (September 2015)

19. M.H.A. Piro, J.J. Bashcuk, **K. Gamble**, B.W. Leitch, A.F. Williams, "Multi-Physics Software Comparison Between ANSYS and MOOSE/BISON/MARMOT," *AECL Memo,* Chalk River, ON, Canada, F&FCSB-13-060 (December 2013)

Workshops, Seminars and Training

- OECD/NEA UAM-LWR-10 Benchmark, Paul Scherrer Institut, Villigen, Switzerland (May 2016)
- Iodine Induced Stress Corrosion Cracking (I-SCC) Workshop, Chalk River, Canada (October 2015)
- OECD/NEA UAM-LWR-9 Benchmark, Madrid, Spain (May 2015)
- RAVEN Training Workshop, Sun Valley, ID, USA (May 2015)
- Materials Models for the Simulation of Nuclear Fuels Workshop (MMSNF), Chicago, IL, USA (October 2013)
- COG CNSC Seminar: COG S&L and IST Programs, Ottawa, ON, Canada (May 2013)
- MOOSE Training Workshop, Chicago, IL, USA (January 2013)
- BISON Training Workshop, Idaho Falls, ID, USA (December 2012)
- ASSERT-IST Training, Deep River, ON, Canada (June 2012)

References

Available Upon Request